Development of multi-material phantoms and implanted monopole antennas for bone fracture monitoring

Symeon Symeonidis

Thesis submitted to Loughborough University for the degree of Doctor of Philosophy in the Faculty of Engineering

Wolfson School of Mechanical, Electrical and Manufacturing Engineering

Loughborough University

Epinal Way, Loughborough LE11 3TU, UK

July 2018

ABSTRACT

This thesis presents a novel method for monitoring the healing of severe bone fractures. This would be particularly useful during the first two to four weeks after trauma where x-ray and computerised tomography scanning cannot provide an accurate indication regarding the healing status of the fractured bone. The technique involves measuring the radiofrequency transmission from one bone-implanted monopole to another, each one located on either side of the bone fracture. Throughout this thesis, it is envisaged that the monopoles will also act as the screws of an external fixation implanted into patients for the stabilization and alignment of the bone fragments. To replicate a simplified version of a human limb, several multi-material semi-solid phantoms were developed to represent bone marrow, bone cortical, blood and muscle. Medical literature indicates that the amount of blood found at the initial stage of a bone fracture decreases as bone regeneration takes place towards the healed state. The rate of change of the S_{21} of the implanted monopoles over time was shown to provide a tool that allowed the estimation of the amount of blood (hematoma) inside any bone fracture. In this thesis it has been shown that as the effective dielectric properties of the investigated fractured area shifted from the dielectric properties of blood towards the properties of bone, the S_{21} of the monopoles increased, thus, this technique can be used to indicate bone healing. The simulated results were validated in measurements using several multi-material phantoms and a real lamb joint. Finally, an analytical model on the approximation of the S_{21} of the monopoles in the near field inside the multi-material phantoms was developed. The results showed good agreement over the frequency spectrum of 1 to 4GHz and reasonable agreement over the parametric investigation of separation distance between them for the range of 1 to 7cm. This will potentially allow the application of the proposed technique for special types of fractures where the screws of the external fixation are separated by different distances.

ACKNOWLEDGEMENTS

I would like to express my sincere and foremost gratitude to my supervisors, Dr. Chinthana Panagamuwa and Dr. William Whittow for their guidance and valuable discussions throughout this work. I would also like to thank Dr. Athanasios Goulas for his invaluable assistance with the measurements and Prof. Massimiliano Zecca for his wisdom and ideas on this project. I am also grateful to Prof. Stelios Mitilineos, George Drimaropoulos and Rania Karantani for their continuous encouragement throughout my years of study and through the process of researching and writing this thesis. Finally, last but by no means least, I would like to thank my friends and family for providing me with unfailing support.

PUBLICATIONS

1. S. Symeonidis, W. G. Whittow, M. Zecca, and C. J. Panagamuwa, *"Bone fracture monitoring using implanted antennas in the radius, tibia and phalange heterogeneous bone phantoms,"* Biomedical Physics & Engineering Express, vol. 4, no. 4, pp. 1–36, 2018.

2. S. Symeonidis, W. G. Whittow, C. J. Panagamuwa, and M. Zecca, *"An Implanted Antenna System for the Monitoring of the Healing of Bone Fractures,"* in 2015 Loughborough Antennas & Propagation Conference (LAPC), 2015, pp. 1–4.

3. S. Symeonidis, W. G. Whittow, and C. J. Panagamuwa, *"Characterisation of an Antenna System Implanted Into a Limb Phantom for Monitoring of Bone Fracture Healing,"* in Loughborough Antennas & Propagation Conference (LAPC), 2016.

4. S. Symeonidis, W. G. Whittow, and C. Panagamuwa, *"Design and characterization of a three material anatomical bone phantom for implanted antenna applications,"* in Loughborough Antennas & Propagation Conference (LAPC), 2017, pp. 4–8.

5. S. Symeonidis, C. Torres-Sanchez, C. Panagamuwa, and W. G. Whittow, "*An Implanted Antenna System for the Monitoring of Bioresorbability of a Biocompatible Scaffold Embedded into a Bone Fracture,"* in MOBIHEALTH'15 Proceedings of the 5th EAI International Conference on Wireless Mobile Communication and Healthcare, 2015, pp. 1–4.

ACRONYMS

ABS	Acrylonitrile butadiene styrene
CT	Computerized x-ray tomography
CAD	Computer-aided design
CST	Computer simulation technology microwave studio®
dB	Decibels
E	Electric
EM	Electromagnetic
FDTD	Finite-difference time-domain
GPS	Global positioning system
H	Magnetic
PLA	Biocompatible plastic polymer
PEC	Perfect electrical conductor
RMS	Root mean square
SAR	Specific absorption rate

LIST OF NOTATIONS

D	Length of the largest monopole dimension (*m*)
d	Monopole separation distance (*m*)
δ	Skin depth
E	Electric field intensity (*V/m*)
E_0	Amplitude of electric field
ε_r	Relative permittivity
ε_0	Permittivity of vacuum (*F/m*)
ε_w^*	Complex relative permittivity of deionized water
ε'	Real part of the complex relative permittivity
ε''	Imaginary part of the complex relative permittivity
ε_∞	Relative permittivity at high frequencies
ε_s	Static relative permittivity at low frequencies
e_{rad}	Radiated antenna efficiency
f	Frequency (Hz)
$\vec{f}_{r,t}$	Normalized far fields
φ	Azimuthal angle of the far field (*degrees*)
θ	Polar angle of the far field (*degrees*)
G	Realized gain of the antenna (dBi)
Γ_m^*	Measured complex reflection coefficients
H	Magnetic field intensity (*A/m*)
k	Wavenumber (*1/cm*)
k_{lossy}	Wavenumber of lossy media (*1/cm*)
μ_r	Relative permeability
μ_0	Permeability of vacuum (*H/m*)
η	Intrinsic impedance (*Ohm*)
P_{abs}	Power absorption *(W)*
P_{rad}	Radiated power *(W)*
P_{source}	Power of the source of the antenna *(W)*
p	Mass density of the medium ($^{kg}/_{m^3}$)

R_s	Reflectance (s-polarization)
R_p	Reflectance (p-polarization)
SAR	Specific absorption rate (W/kg)
σ	Conductivity (*S/m*)
$tan\delta$	Loss tangent
τ	Relaxation time (*sec*)
Z	Impedance (*Ohm*)
ω	Angular velocity (*Hz*)

CONTENTS

LIST OF FIGURES

LIST OF TABLES

Chapter 1

Introduction

1.1 Summary

The first implanted electronic devices in the history of medicine were the pacemakers in the beginning of the 1960's [1]. Their use was to regulate the rate of the heart's beats for patients that suffered from syncope, congestive heart failure and hypertrophic cardiomyopathy. Those implants consisted of two parts. The first part consisted of the lead wires that were wrapped around the veins of the heart and the second part was a pulse generator consisting of a battery and a small electronic chip that generated electrical pulses. The pulses were transferred via the lead wires to the heart's veins.

Nowadays, the technology for implanted devices has improved greatly although there are still challenging tasks for the designers to overcome. Some of the most common impediments include the difficulty of transmitting information between implants inside the body or from the inside of the body to external sources and vice versa. In addition to that, there are limitations in terms of free space inside the body while the biocompatibility of the materials that constitute the implants is compulsory. In most cases an approach involving scientists from several fields, such as electronics, electromagnetics and biology is required in order for an implanted device to be designed and tested properly. Acknowledging these prerequisites, this thesis presents results of a study on monitoring severe bone fracture healing using an in-body Radiofrequency (RF) monopole antenna system.

Robust healing of severe fractures in bones is a complicated biological process requiring continuous monitoring, evaluation and mechanical assistance for the restoration of the bone to its original state [2]. Healing in bones requires 4 to 40 weeks depending on the number and the size of fractures, the age of the patient and the type of the bone. According to the literature there is no standard defining when a fracture is healed, therefore the evaluation of a healing fracture is based on predetermined time points [3]. The development of an implanted antenna system for monitoring healing could provide orthopaedic professionals with a continuous indicator of the bone's condition. This could play a crucial part in managing the healing process as it could determine if further treatment is required and also greatly reduce the number of X-rays and CT scanning required for a proper evaluation of the bone's condition.

1.2 The six major design considerations for implanted antennas

Implanting radiating devices inside the body is by no means a trivial task. There are six major aspects that need to be considered from an engineering, as well as a biological, point of view.

In-body channel propagation:

Channel propagation is the characterisation of the electromagnetic (EM) wave propagation usually as a function of frequency or distance and it is typically used to predict path loss along a link. An investigation on channel propagation is important due to the multipath propagation of the transmitted EM waves and the attenuation that is introduced by the lossy multi-material structure of the human body.

Implanted antennas:

Due to limitations of space inside the body, the design of implanted antennas should be able to provide the best possible trade-off between size and efficiency. This requires careful study of the body part in terms of relative permittivity, conductivity, depth and available space that will host the implant. For example, resonators based on the electric dipole are easily affected by their surroundings in terms of efficiency than spiral antennas that are based on the magnetic dipole principles [4]. Therefore, careful consideration of the type of antenna used is also necessary.

The human body:

The human body is a lossy medium for EM propagation. Although lossy mediums broaden antenna bandwidth, most of the time they significantly reduce antenna efficiency [5]. This wider bandwidth phenomenon is a result of the dissipation of the near field of the radiator into the medium. This results in more power being absorbed due to the losses than being reflected back to the source, thus producing wideband behaviours and limited efficiencies for the antennas. Therefore, careful consideration of the electromagnetic properties of the tissues of the human body is important when designing efficient radiators [6]. Testing the implants on anatomical body phantoms or on in-vitro and in-vivo animals might provide a better insight on the design of the implants.

Insulation covering the radiators:

Insulation is essential for the protection and correct operation of electronic parts of an implant that is embedded in tissues. The insulation material must be biocompatible to avoid adverse

reactions in the tissues that surround it. The insulation must also be well tuned for the enhancement of the EM propagation. This can be achieved by carefully selecting a material that its impedance matches the antenna's impedance and its thickness has the maximum allowed value considering the geometrical limitations of the area of implantation [1], [7]. That way the unwanted coupling of the antenna's near field with the surrounding tissues can be minimized [8].

Implanted device:

The metallic construction if the implant housing the sensors, processors and power supply, can itself negatively affect EM propagation. This often requires further investigation on how to position the device in the body. It is worth mentioning that, power supplies like batteries consist of non-biocompatible chemicals, therefore, their use can only be temporary. Other techniques for powering, configuring and data downloading from the implant through an induction loop can be found in literature and can offer a more suitable solution for permanently implanted applications [9]–[11].

Characterisation and experiments:

Before designing a system that can be implanted in human tissue, further tests of compatibility should be considered. Simulations in single- and multi- material phantoms can offer the designer a greater insight on the behaviour of the implant, but measurements on in-vitro and in-vivo animals can provide more accurate results. This is due to the complex nature of the body tissues. In real life body parts for instance, it is common for the muscle layer to be randomly inhomogeneous due to fat that is located in-between the muscle fibres. This causes

inhomogeneities that can affect the operation of an implant considering that the dielectric characteristics of fat are lower compared to muscle. This contrasts to measurements which generally use homogeneous phantoms. Therefore, proper characterization of an implant often requires investigations both in phantoms and in in-vitro test-beds.

1.3 Scope

The aim of this thesis is to develop a system that monitors the healing of severe bone fractures by measuring the change in power received between two monopole antennas implanted either side of the fracture. It is envisaged that the fixator screws already used for immobilising the bone will have a secondary purpose of acting as the Radio Frequency (RF) monopoles. The functionality of this system will be tested in several in-house developed multi-material limb phantoms and a lamb joint. In addition, the theory and mechanism behind the simulated and measured results will be used for the definition of the principles of operation of this monitoring system.

1.4 Novel contributions

This thesis presents a novel technique for monitoring the healing of severe bone fractures using a pair of RF monopoles implanted in the bone. The novel contributions include:

- Development of low-cost and easy to produce phantom recipes of bone cortical, bone marrow, muscle and blood after careful examination of the dielectric properties of human body tissues.

- The recipes were used for the development of multi-material semi-solid geometrical human body phantoms. The phantoms provided good agreement with their real life equivalents in the frequency range of 0.5 to 4GHz.

- A pair of monopole antennas was designed to represent the screws of an external fixation implanted into patients for the stabilization and alignment of the bone fragments. The rate of change of the S_{21} of the monopoles provided a tool that can be used for the estimation of the healing of any bone fracture.

- It has been shown that the change of the dielectric properties of the bone fracture during the healing period will alter the S_{21} between the implanted monopoles. These simulated results using anatomical phantoms have been verified in measurements using three in-house developed multi-material phantoms and a lamb joint

- Preliminary research on an analytical model of the approximation of the S_{21} of the monopoles in the near field inside multi-material phantoms has been extended from a free space version to work inside multi-layered lossy dielectric media. The results exhibited an agreement over the frequency spectrum of 1 to 4GHz and also for the parametric investigation of separation distances between 1 to 7cm.

1.5 An overview of this thesis

Chapter 2 will give a brief summary of the theoretical basis that is necessary for the design of implanted antennas applications; the natural process of bone healing in the human body and the existing techniques used by the doctors to monitor bone unification. Chapter 3 provides a

detailed approach about the development and validation of bone marrow, bone cortical, muscle and blood phantom recipes for the frequency spectrum of 0.5 to 4GHz.

In Chapter 4 the designs of two multi-material phantoms are presented. The first one consisted of bone cortical and muscle and the second consisted of bone marrow, bone cortical and muscle. Two radiofrequency monopoles were simulated in these heterogeneous phantoms and validated by measurements using the phantoms. Additionally, a specific absorption rate (SAR) simulation was carried out in the two phantoms. At the end of this chapter, the designs of two versions of the proposed external medical metal plate are presented and their load bearing capabilities are investigated using the Solidworks 3D CAD simulator.

Chapter 5 shows the comparisons of the proposed technique between simulations of voxel models of an arm (radius), a finger (phalange) and a leg (tibia) and measurements of three geometrical phantoms with bone dimensions according to their corresponding investigated voxel model equivalents. The results were validated using an ex-vivo lamb joint measurement.

An approximate method for the near field coupling calculation inside multilayer phantoms is presented in Chapter 6. The method has been extended from a free space version to work inside multi-layered lossy dielectric media. The model uses the near field counterpart of the Friis transmission equation and it is envisioned to provide an analytical approach which reduces the calculation time of mutual coupling of implanted monopole antennas for the separation distances of 1 to 7cm by minimizing the number of necessary CST simulations inside multi-material human body phantoms.

Chapter 7 is included as a final chapter in order to summarise and conclude the research considered in this thesis.

References

[1] F. Merli, “Implantable Antennas for Biomedical Applications,” PhD Thesis, Ecole Polytechnique Federale de Lausanne, 2011.

[2] K. D. Hankenson, G. Zimmerman, and R. Marcucio, “Biological perspectives of delayed fracture healing,” *Injury*, vol. 45, pp. S8–S15, 2014.

[3] P. Augat *et al.*, “Biomechanical methods for the assessment of fracture repair,” *Injury*, vol. 45, pp. S32–S38, 2014.

[4] F. Merli, B. Fuchs, J. R. Mosig, and A. K. Skrivervik, “The effect of insulating layers on the performance of implanted antennas,” *IEEE Transactions on Antennas and Propagation*, vol. 59, no. 1, pp. 21–31, 2011.

[5] N. Qasem and R. Seager, “Overcoming the influence of people shadowing and enhancing MIMO capacity systems via modified environments,” in *LAPC 2012 Loughborough Antennas and Propagation Conference*, 2012, pp. 1–4.

[6] M. W. Abdullah, X. Fafoutis, M. Klemm, and G. S. Hilton, “Radiation pattern analysis of single and multi-antenna wearable systems,” in *IEEE Vehicular Technology Conference*, 2017, pp. 1–5.

[7] P. S. Hall and Y. Hao, “Antennas and propagation for body centric communications,” *European Space Agency, (Special Publication) ESA SP*, vol. 626 SP, 2006.

[8] T. Dissanayake, K. P. Esselle, and M. R. Yuce, “Dielectric loaded impedance matching for wideband implanted antennas,” *IEEE Transactions on Microwave Theory and Techniques*, vol. 57, no. 10, pp. 2480–2487, 2009.

[9] S. Rao *et al.*, “Miniature implantable and wearable on-body antennas: Towards the new

era of wireless body-centric systems," *IEEE Antennas and Propagation Magazine*, vol. 56, no. 1, pp. 271–291, 2014.

[10] B. Kibret, A. K. Teshome, and D. T. H. Lai, "Analysis of the Human Body as an Antenna for Wireless Implant Communication," *IEEE Transactions on Antennas and Propagation*, vol. 64, no. 4, pp. 1466–1476, 2016.

[11] A. Kiourti, K. A. Psathas, and K. S. Nikita, "Implantable and ingestible medical devices with wireless telemetry functionalities: A review of current status and challenges," *Bioelectromagnetics*, vol. 35, no. 1, pp. 1–15, 2014.

Chapter 2

Review of implanted antennas in lossy media and bone fractures

2.1 Summary

In the first part of this chapter, a literature overview regarding the principles of operation and applications of implanted antennas into lossy media is presented. In the second part of this chapter a literature review regarding the characteristics of bone fractures and the types of implants used by the doctors to facilitate correct bone healing is summarised. The chapter is organised as follows: In Section 2.2 the design principles of antennas in lossy media are reported. Section 2.3 details the electromagnetic properties of lossy media, such as the human body, that need consideration when designing efficient implanted radiators. In Section 2.4 the nature, causes, types and healing of bone fractures is presented. Section 2.5 is a summarisation of the techniques used by doctors in order to assist proper bone union. Section 2.6 discusses the techniques for bone healing monitoring during the first four weeks after the trauma that are available in the literature. Further on in this section, the proposed technique that is thoroughly investigated in this thesis is presented. Finally, in Section 2.7 the concluding remarks of this chapter are presented.

2.2 Design principles of antennas in lossy media

The human body is a lossy medium, therefore antennas that operate at lower frequencies are more preferable to engineers due to their effectiveness in terms of the skin depth penetration and propagation through the lossy material. This naturally requires bigger antenna geometries, which are challenging to implement due to the limited available space inside the human body. Over the last ten years, multiple authors have addressed these challenges in the literature and have proposed a variety of optimised antenna geometries for various applications. A good trade-off between frequency of operation, antenna efficiency and size was established in the Medical Devise Radiocommunications Service (MedRadio) frequency band at the 401 – 406MHz range [1]–[3] and the Industrial, Scientific and Medical (ISM) radio bands at the 2.44 to 2.46GHz range [4]–[6]. Most of the proposed applications in the literature include incorporation of the antenna under the skin, fat or muscle tissues [7]–[9]. Others include implants beneath the skull for monitoring brainwave signals [10], intraocular implementation of antennas for retinal prosthesis [11], ingestible capsule antennas for the monitoring human intestines [12] and antennas operating in the Global Positioning System (GPS) frequency range for the localization of people suffering from Alzheimer's disease [13].

The principles of consideration when designing implanted antennas are presented in the following sections. In order for a radiator to be effective, the electromagnetic properties of the medium, the required efficiency, the desired radiation pattern, the bandwidth, the specific absorption rate (SAR) and the coupling between the implants need to be carefully studied.

2.3 The electromagnetic properties of the medium

Permittivity ε, permeability μ and conductivity σ of homogenous, linear and isotropic phantoms are complex quantities defined by the following formulas [14]:

$$\varepsilon = \varepsilon_0(\varepsilon_r' - j\varepsilon_r'') \; F/m \tag{2.1}$$

$$\mu = \mu_0(\mu_r' - j\mu_r'') \; H/m \tag{2.2}$$

$$\sigma = \sigma' - j\sigma'' \; S/m \tag{2.3}$$

Where:

$$\varepsilon_0 = 8.854187817 \times 10^{-12} F \cdot m^{-1} \tag{2.4}$$

$$\mu_0 = 4\pi \times 10^{-7} \; H/m \tag{2.5}$$

ε_0 and μ_0 correspond to the permittivity and permeability of vacuum. ε_r'' and μ_r'' account for the loses due to the damping of the vibrating dipole moments. ε_r' and μ_r' are the relative permitivitty and relative permeability of a medium with respect to the permittivity and permeability of vacuum.

The values of ε, μ, and σ are frequency dependent. Therefore $\varepsilon = \varepsilon(\omega)$, $\sigma = \sigma(\omega)$ and $\mu = \mu(\omega)$ for $\omega = 2\pi f$.

The human body does not possess any magnetic properties ($\mu_r' = 1$, $\mu_r'' = 0$), as a result the definition of real effective permittivity ε_e' and conductivity σ_e' can be given as follows:

$$\varepsilon_e' = \varepsilon_r' - \frac{\sigma''}{\omega\varepsilon_0} \tag{2.6}$$

$$\sigma_e' = \sigma' + \omega\varepsilon_0\varepsilon_r'' \tag{2.7}$$

The definition of the complex effective permittivity ε_e is given by the substitution of the above formulas as follows:

$$\varepsilon_e = \varepsilon_0\,(\varepsilon_e' - j\varepsilon_e'') = \varepsilon_0(\varepsilon_e' - j\frac{\sigma_e'}{\omega\varepsilon_0}) \tag{2.8}$$

The dissipation of the EM power inside a medium can be given by the loss tangent *tanδ* [15], as shown below:

$$\tan\delta = -\frac{Re\,\{\varepsilon_e\}}{Im\{\varepsilon_e\}} = \frac{\sigma_e'}{\omega\varepsilon_0\varepsilon_e'} \qquad \delta = \sqrt{\frac{2}{\mu\omega\sigma_e'}} \tag{2.9}$$

δ corresponds to the skin depth for $\sigma_e' \gg \omega\varepsilon_0\varepsilon_e'$

The spatial frequency of the propagated wave inside a lossy medium is given by the wave number k_e:

$$k_e = \omega\sqrt{\mu_0\varepsilon_0}\sqrt{\varepsilon_e' - j\frac{\sigma_e'}{\omega\varepsilon_0}} \tag{2.10}$$

The wavelength λ_ε inside the medium is given by:

$$\lambda_\varepsilon = \frac{2\pi}{\omega\sqrt{\mu_0\varepsilon_0}}\,Re\,\{\sqrt{\frac{\omega\varepsilon_0}{\omega\varepsilon_0\varepsilon_e' - \sigma_e' j}}\,\} \tag{2.11}$$

2.3.1 Efficiency and radiated power

The radiation efficiency of an antenna is the ratio between the power radiated from the antenna to the power delivered at the feed of the antenna. Highly efficient antennas have most of the total power delivered from the source, radiated to their environment. Low efficiency antennas have most of the total power absorbed or reflected back to the source [16].

The average power, P_{rad}, flowing through a spherical surface S_r of volume *V* is given by the following equations found in [17]:

$$P_{source} = P_{rad} + P_{abs} = \oint_{S_r} Re\,\{S * \hat{r}\}dS + \frac{\omega}{2}\int_V \varepsilon_0\varepsilon_e''|E|^2 dV \quad (2.12)$$

Where P_{abs} is the power absorption and *S* the pointing vector equal to $(\frac{1}{2}\bar{E}x\bar{H})$.

Further expanding the equation above:

$$P_{source} = \oint_{S_r} Re\,\left\{S\left(1/r^2\right) + S\left(1/r^n\right)\right\} * \hat{r}dS + \frac{\omega}{2}\int_V \varepsilon_0\varepsilon_e''[|E|^2\left(1/r^2\right) + |E|^2(1/r^n)]dV =$$

$$= P_{rad-FF} + P_{rad-NF} + P_{abs-FF} + P_{abs-NF} \quad (2.13)$$

The $1/r^2$ dependency identifies exclusively the far-field component, while $1/r^n$, with n >2, refers to the near-field components of the electromagnetic radiation. The power terms P_{rad-FF}, P_{rad-NF}, P_{abs-FF} and P_{abs-NF} can be defined to separate the radiated and absorbed power with respect of the nature ($1/r^n$ dependency) of the EM field. Obviously, P_{rad-NF} is only appreciable within a small distance from the source.

The limitations of space inside the body in implanted applications, makes radiators prone to near field coupling with the surrounding tissue-materials, having as a result low radiation

efficiencies and increased power loss [18]. A way to reduce this coupling effect is by the use of insulators between the tissue and the antenna.

The radiated efficiency of the antenna is given by the equation below:

$$e_{rad} = \frac{P_{rad}}{P_{source}} \tag{2.14}$$

As observed in Figure 2.1, as the insulation increases in thickness, the efficiency of the antenna increases accordingly. All e_{rad} values where measured for the same antenna depth inside the body phantom.

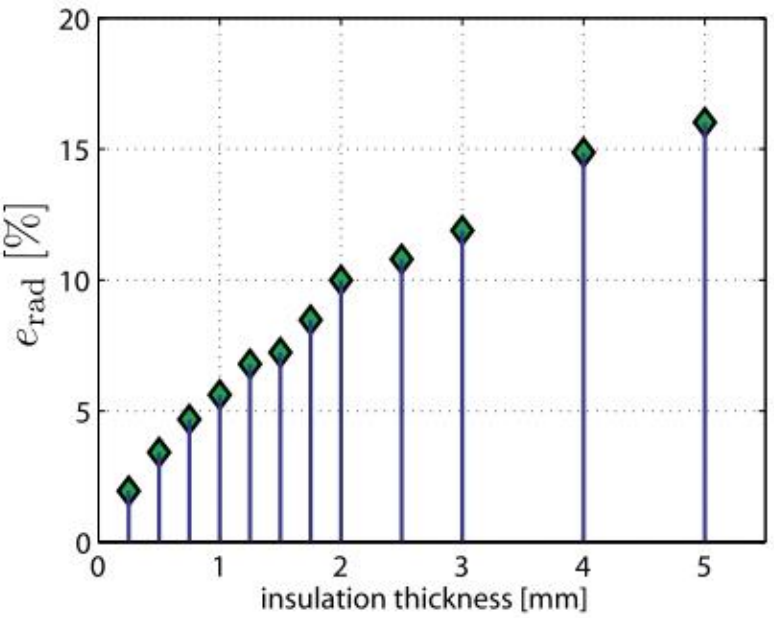

Figure 2.1: e_{rad} values for different insulation thicknesses inside a body phantom [1]

For implanted antennas, radiation from different parts of the conductor is not attenuated evenly. This is a result of the unique dielectric properties of the tissues around the antenna and the uneven geometry of the human body [19]. An example of this can be shown in Figure 2.2. In this example an antenna was implanted into two different phantoms that differ in geometry. It can be seen that at the maximum radiation, there is a 45° difference of the radiation pattern. Therefore the precise representation of the investigated body part is important for accurate prediction of the radiation pattern is crucial in terms of designing an efficient radiator.

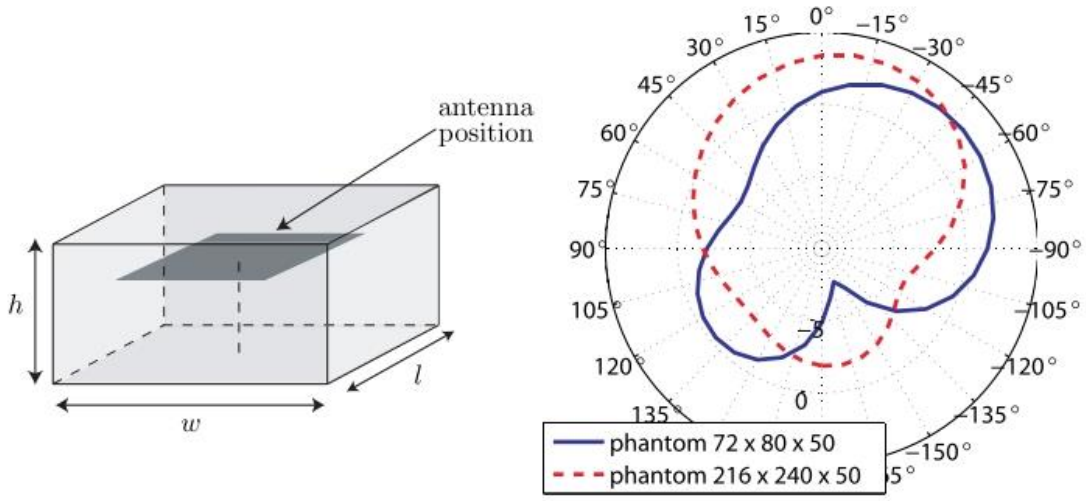

Figure 2.2: An implanted antenna's directivity simulated in two different phantom geometries taken from [14]

2.3.2 Bandwidth

The bandwidth in antenna theory describes the frequency range in which the antenna can properly radiate or receive energy and it is directly depended on the propagation medium [20]. For lossy media like the human body, a wider bandwidth phenomenon can be observed. This

phenomenon is a result of the dissipation of the near field of the radiator into the lossy medium. No matter how efficient a radiator may be, most of the provided power will be absorbed by the medium resulting in antennas with wide band characteristics [21], [22]. Figure 2.3 shows an antenna implanted into a lossy and lossless skin phantom.

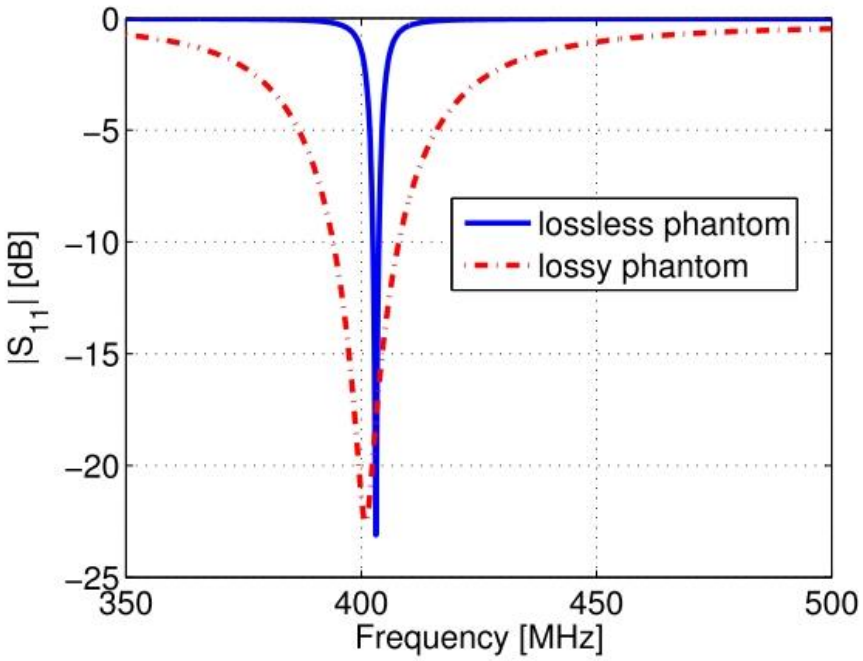

Figure 2.3: The simulation of S_{11} based on the implanted radiator into a lossless and a lossy phantom [1]

2.3.3 Specific absorption rate

The main health hazard for patients that have implanted radiators into their bodies comes from the heating of their biological tissues. This is a result of the lossy nature of the human body as a propagation medium for the implanted antennas. The specific absorption rate (SAR) is a

measure of the dissipating EM power per unit mass. Regulatory bodies around the world set strict SAR limits, such as: 1.6W/kg per 1-g averaging [23] in the USA and 2W/kg per 10-g averaging [24] in Europe. Radiating elements cannot exceed these limits.

The definition of the peak SAR value is given by:

$$\mathrm{SAR}(r_0) = \frac{1}{2}\frac{\sigma_e'(r_0)|E(r_0)|^2}{p(r_0)} \tag{2.22}$$

σ_e' : The conductivity of the medium

p : The mass density of the medium

$\frac{1}{2}\sigma_e'(r_0)|E|^2$: The average power density absorbed

r_0 : The point of observation

E: The RMS electric field strength in the tissue

The spatial - average SAR is computed at every point of the tissue. *R*, *M* and *V* are the average values of a region *R* with mass *M* and volume *V* [23]:

$$\mathrm{SAR(V)} = \frac{1}{M(V)}\int_V SAR(r)\mathrm{dm} = \frac{1}{M(V)}\int_V \frac{\sigma_e'(r_0)|E(r)|^2}{2}\mathrm{dV} \tag{2.23}$$

In order for the SAR values to be calculated with precision in an in-vivo measurement, it is important to know the exact implant location into the body, the fluid dynamics and thermoregulatory biological responses of the tissues that surround it. Tissue simulating liquid phantoms are often used to measure SAR.

2.4 Bone fractures

A bone fracture is a medical condition in which there is damage in the continuity of the bone. The fracture can be a result of high force impact or stress, or an injury as a result of certain medical conditions such as osteoporosis and bone cancer [25].

2.4.1 The natural process of bone healing

The natural process of fracture healing starts when the injured bone and the surrounding tissues haemorrhage, forming a hematoma inside and around the fracture [26]. Within a couple of days, the blood coagulates to form parosteal – endosteal calluses situated between the broken fragments. The new blood vessels bring white blood cells (phagocytes) to the area, which gradually remove the non-viable material [27]. The blood vessels also bring fibroblasts cells that multiply and produce collagen fibres. In this way the blood callus is replaced by a matrix of collagen (intermediate - hard callus). The rubbery consistency of collagen does not allow bone fragments to move unless severe or a persistent force is applied. At this stage, the fibroblasts begin to lay a bone matrix in the form of collagen monomers. The collagen monomers initiate the mineralization of the bone matrix and stiffen it while transforming it into bone [27]. The intermediate bone callus, for cases where a medical metal plate is not used to support the fractured bone, is sufficiently mineralized to show up on X-rays within 6 weeks in adults and less in children on average. This initial spongy bone does not have the strong mechanical properties of a mature bone. By a process of remodelling, the spongy bone is replaced by mature "lamellar" bone [28]. The whole process may take up to 18 months, but in adults, the strength of the healing bone is usually 80% of normal by 3 months after the injury [29]. The healing stages are shown graphically in Figure 2.4.

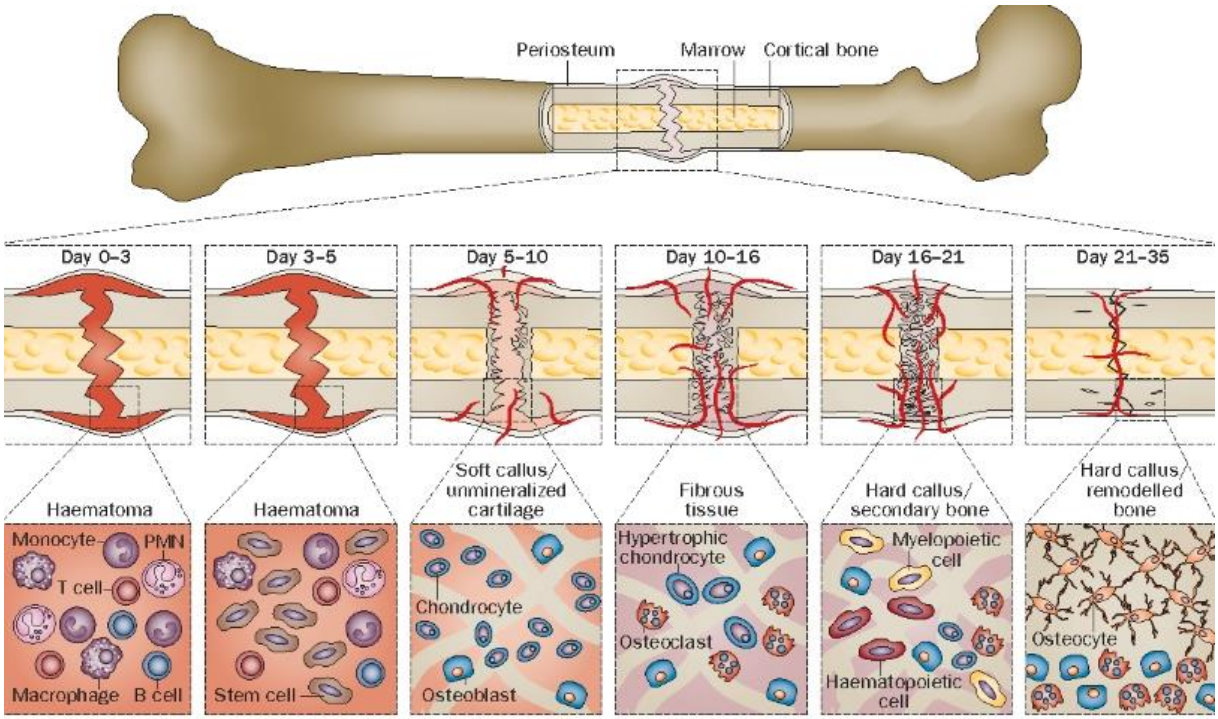

Figure 2.4: The stages of fracture healing taken from [30]

2.4.2 Types of bone fractures

The two main categories of bone fractures regardless of the cause of injury are: simple and compound fractures (see Figure 2.5) [31], [32].

Simple fractures are broken bones that remain within the body and do not penetrate the skin.

Compound fractures are broken bones that penetrate through the skin and expose the bone and deep tissues to the exterior environment.

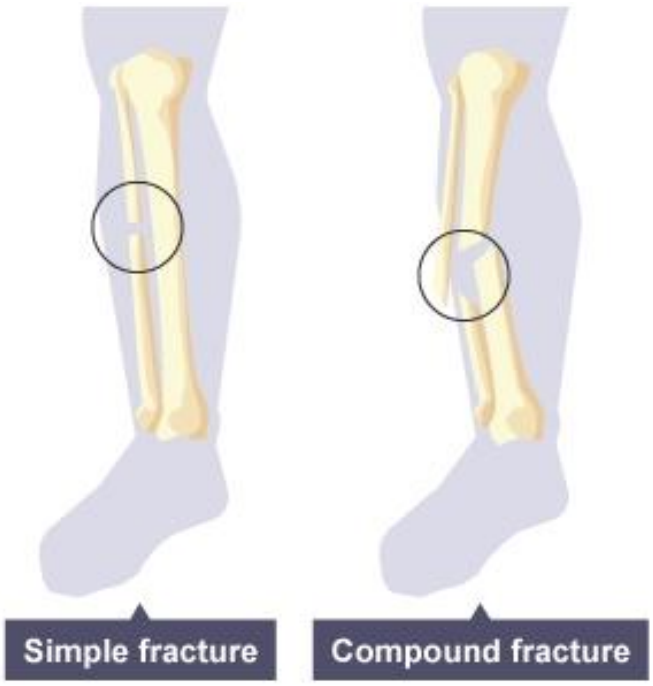

Figure 2.5: Simple and compound fractures, picture taken from [33]

Compound fractures as seen at the right part of Figure 2.5 are considered much more serious than simple fractures mainly due to the high probability of pathogen infection via the surface of the wound. The use of anti-microbial medicine is often necessary in order to prevent infections that will delay fracture healing at best or cause limb amputations at worst [30].

Within the simple and compound fracture categories are many specific types of fractures [34], [35]. These are illustrated in Figure 2.6.

Comminuted fractures are severe fractures where the bone is segmented into several smaller pieces.

Greenstick fractures are caused on one side of the bone by a force perpendicular to the bone's long axis. This fracture type can be observed in children whose developing bones are flexible and tend to bend to a point that they partially break instead of breaking completely.

Avulsion fractures are a result of a segment of bone being torn off from the main bone. This can occur due to an extreme force applied to a ligament or tendon. The main causes of Avulsion fractures can be: Overexertion of muscles and sudden pulling of a body part during an accident [36].

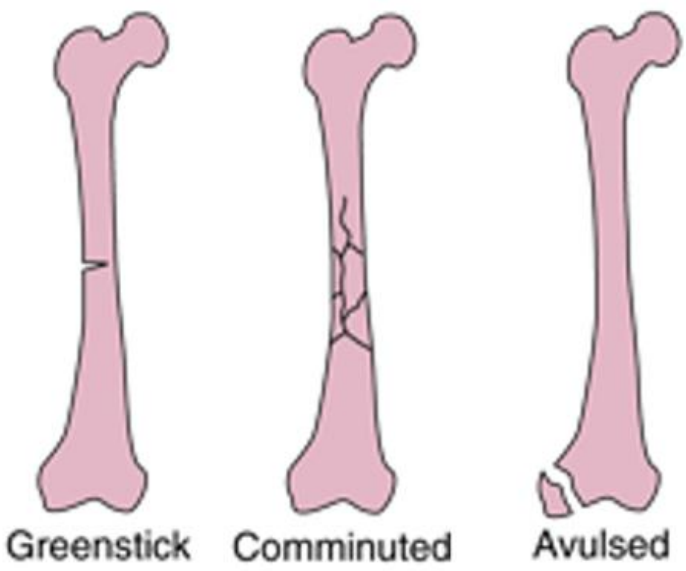

Figure 2.6: Greenstick, Comminuted and Avulsed fractures, picture taken from [36]

The geometry of a bone fracture is dependent on the direction angle in which a force is applied to a bone. The sub-categories depicted in Figure 2.7 and presented bellow correspond to the dependency of a fracture's geometry to the angle of incidence of the applied force along the axis of the bone [35].

Transverse fractures form perpendicular to the long axis of a bone and are the result of a force applied at a right angle to the bone.

Oblique fractures are fractures that occur when a force is applied at any angle other than a right angle to the bone.

Spiral fractures are the result of an extreme twisting force being exerted on a bone, resulting to a spiral bone fracture formation.

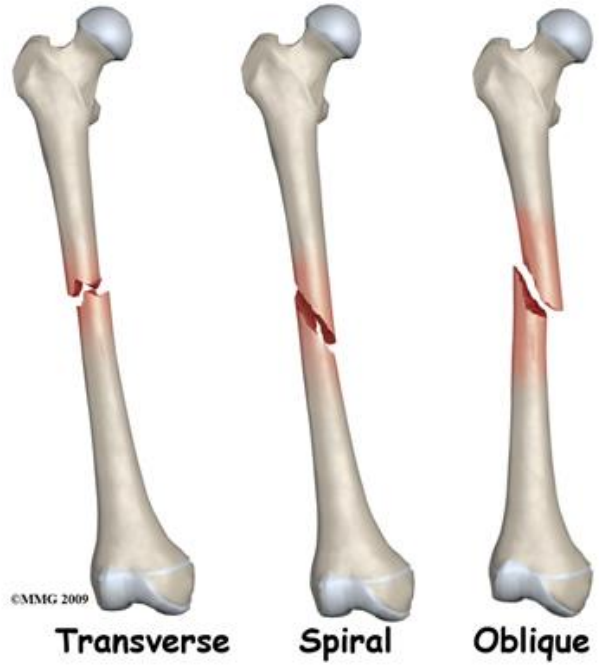

Figure 2.7: Transverse, spiral and oblique fractures, picture taken from [35]

2.4.3 Bone fracture treatment

The period immediately after a bone fracture is critical for the proper repair of to the bone to its initial state. Normally bones begin to heal quickly after a fracture. Bone fragments will knit together with bone tissue forming a callus and eventually new bone tissue until proper union is achieved [29], [30].

The first step in monitoring a bone fracture is an x-ray that will lead to a diagnosis for the classification the fracture according to the degree of displacement and misalignment [34]. The initial aim in treatment is to align the bone fragments in a position so that after the callus

transforms to bone tissue the bone will retain its previous shape. Displaced bone fragments are manually maneuvered back into position either through the skin using an anaesthetic, or by a surgical operation.

Once the fracture has been placed in proper position, the bone is immobilized to allow the broken pieces to reunite. For minor injuries, a rigid plaster is used to immobilize the bones for several weeks and achieve union. In severe cases, such as the cases investigated in this thesis, the fractured bone is fixed in place by metal pins connected to an external fixator. Once the fracture has healed, the pins and frame are removed.

In other cases a surgical operation is performed in order to open up the injury and fasten together the bone pieces with metal screws, nails, plates, rods, or wires (internal fixation). For the prevention of a possible infection, internal fixators are often left permanently inside the body after bone healing is achieved.

The x-ray visibility in cases were the internal or external fixators used are non-ferromagnetic is greatly reduced due to the scattering of the propagated electromagnetic wave at the surface of the fixator's metallic parts [37]. This usually results into insufficient monitoring of the state of the fracture as the doctor's only available alternative is an estimation of the healing process by palpation of the skin that surrounds the fracture.

2.4.4 Factors that affect bone healing

Several factors that may help bone healing can be: an increased calcium intake, an adequate nutrition and weight-bearing stress to the bone after the bone has healed sufficiently to bear the weight [38]. A factor that will negatively affect bone healing is the consumption of any form of nicotine and malnutrition [39]. Generally, the older a person is, the longer it takes for a bone

to heal. Usually, a child will recover within a few weeks and an elderly person may take several months [40]. Regardless the age, some bones will have a higher healing rate than others. It is possible for an arm to heal within a month, but for a leg to take up to six months [41], [42]. In most cases a properly united bone is stronger along the fractured area than it was before the break. Delayed bone union can be experienced by elderly people as well as those in poor health condition, in these cases the bone takes longer than normal to heal [43]–[45]. Healthy people may also be affected by nonunion in cases of infection, severe trauma to the soft tissues surrounding the fracture site or lack of proper medical treatment. These factors may also lead to malunion, a condition where the bone fragments are united but without being anatomically aligned, leading to severe pain and loss of mobility and muscle strength [46].

2.5 Fixators

Stabilization and support of bone fragments are necessary for a damaged bone to return to its pre-fractured state and be able to support the body's weight and movement. The past 100 years, doctors relied on wrapping the fracture with casts and splints externally to support and stabilize the bone. The growth of antibiotic research and sterilisation techniques allowed doctors to use more effective methods to treat bone trauma, both internally and externally [41], [47], [48].

2.5.1 Internal Fixators

The benefits of internal fixators include less hospital stays by enabling the patients to return to function earlier. The probability of non-union and malunion is greatly reduced for severe trauma compared to techniques such as coating the wound externally with plaster (see Figure 2.8) [49]. The implants used for internal fixation are made from stainless steel and titanium, which are

durable, resistant to rust and biocompatible. In the case of joint replacement, these implants can also be made of cobalt and chrome [50].

Figure 2.8: A picture of an internal fixator taken from [46]

2.5.2 Plates

Plates are internal splints used for positioning of bone fragments to a desired direction. Metal plates are attached to the bone with screws. Usually they stay in place after bone union is achieved in order to avoid unnecessary infections by reopening the traumatised area (see Figure 2.8) [49].

2.5.3 Screws

The design of an implanted screw can vary according to the type of fracture and the size of the bone. It can either be used alone to hold the bone fragments of a fracture or simultaneously with plates, rods, or nails (see Figure 2.9) [51], [52].

Figure 2.9: Implanted screws that hold bone fragments taken from [46]

2.5.4 Nails or Rods

For certain types of fractures of the long bones, treatment by inserting a rod or nail through the hollow centre of the bone that normally contains some marrow can be used. Screws at each end of the rod are used to keep the fracture in position by minimizing rotation of the bone fragments (see Figure 2.10) [53].

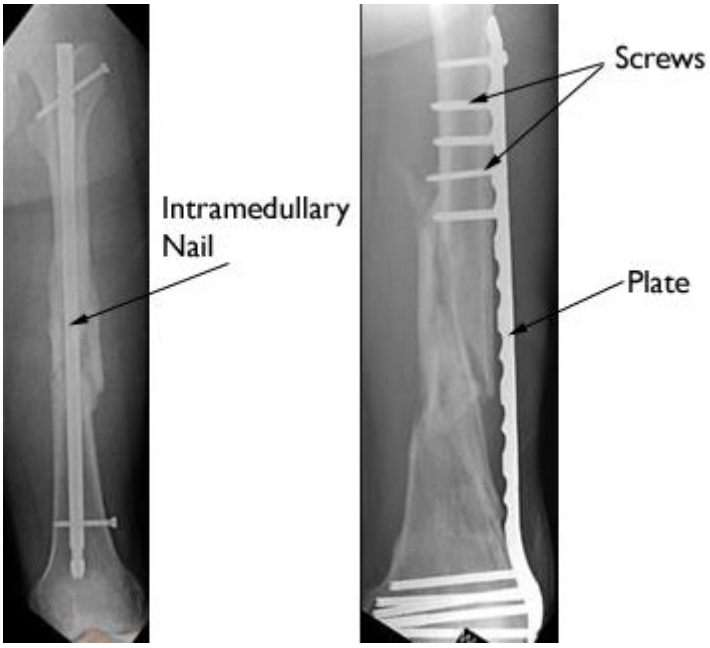

Figure 2.10: X-ray image of: (Left) A healed thighbone fracture treated with intramedullary nailing. (Right) A healed thighbone fracture treated with plates and screws (internal fixator) picture taken from [31]

2.5.5 Wires

Wires are often used to hold in position smaller bone fragments that are difficult to be pierced by screws. Usually, they are used along with other types of internal fixation, and in most cases are removed after bone union (see Figure 2.11) [35].

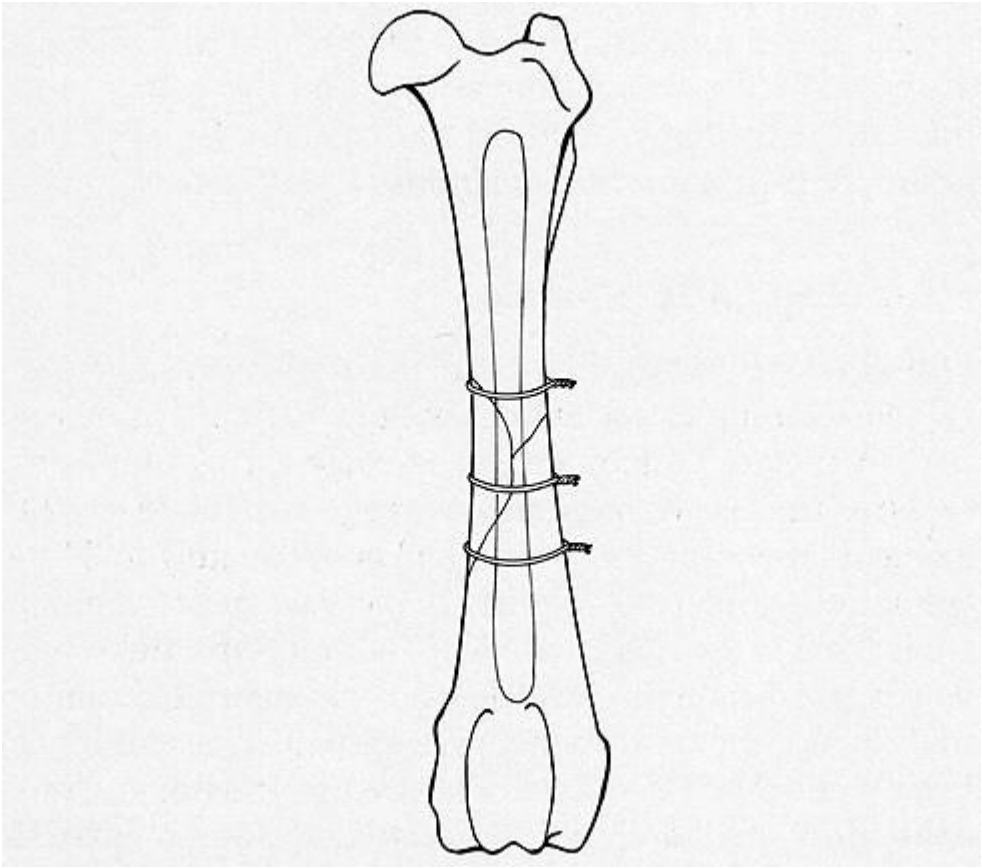

Figure 2.11: Orthopaedic wires used for the positioning of bone fragments taken from [54]

2.5.6 External Fixators

External fixators consist of metallic frames with pins or screws attached. The frame is used for stability of the bone fragments externally and the pins or screws are placed into the bone through small incisions into the skin and muscle (see Figure 2.12).

Until recently, external fixators are the most preferred method used for treating fractures that require implant support. Their benefits compared to other types of fixation techniques include [55]:

1. Rigid fixation of bone fragments for cases where additional treatment of soft tissue wounds is necessary and internal fixators may increase the risk of contamination [56].

2. Direct monitoring of probable infections of the limb and wound at the surface of the skin.

3. Supplementary treatment, such as skin and bone grafting, are possible without disturbing the fracture alignment.

4. Motion of certain degrees of the proximal and distal joints is allowed that contributes to the reduction of edema, muscle atrophy and osteoporosis [57].

5. The pins and frames can be elevated using ropes above the bed that allow pressure reduction on the posterior soft tissue part.

6. Implantation of the frame and pins can be performed under local anaesthesia due to the minimum surgery required compared to internal fixators.

7. External fixation can be used in infected fractures or non-unions which is rarely possible with casting or internal fixation devices [56].

8. Rigid fixation of failed, infected arthroplasties in which joint reconstruction is not possible and in which arthrodesis is desired can be achieved.

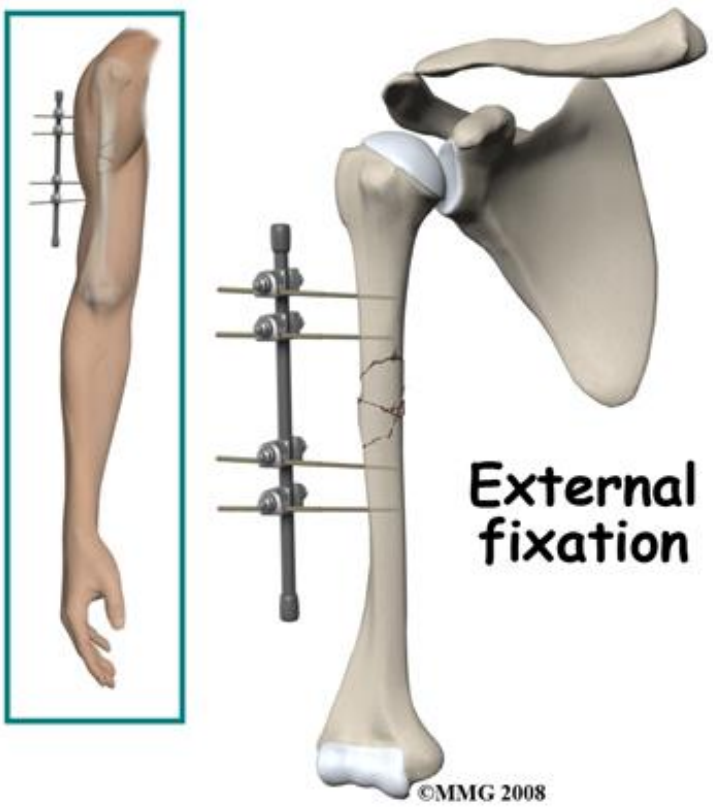

Figure 2.12: Treatment of humerus bone fracture via external fixation, picture taken from [58]

2.6 Analysis of the existing methods to monitor bone healing

According to literature, the reported electrical properties of bones include: capacitance [59], inductance [60], impedance [61], dielectric constant [62] and conductance [63]. This thesis proposes to use these properties to develop a fracture healing monitoring system.

The critical amount of monitoring that is necessary for sufficient evaluation and bone restoration at the first four weeks after the trauma can be difficult to achieve with patients that have surgically implanted metal plates [64]. Due to the limitations of x-ray and CT monitoring in severe trauma cases at the crucial period of callus formation a new monitoring technique is presented in this thesis.

The proposed technique features two monopole antennas embedded into the parts of the pins of a fixator that are screwed perpendicularly into the long axis of a fractured bone. An external fixator was chosen for the application of the proposed technique due to its limited invasiveness, the convenience of surgical implantation and removal, the ease with which an RF signal could be applied to and extracted from the implanted monopoles, and its frequent use by the doctors in severe trauma cases compared to the other reported techniques [65].

Several researchers have proposed similar techniques using AC current at low frequencies. The current is conducted by the implanted pins through the long axis of the fractured bone measuring the variations of the fracture's impedance as a probable healing indicator.

According to [66], an increase in the impedance of the bone fracture of human patients measured at 100Hz is reported in the first 4 weeks after the trauma, the impedance decreased gradually after the fourth week until the bone was restored. The proposed technique of Figure 2.13 uses the ratio of the bone impedances taken at the control parts "1" and "2" vs the impedance measured at the fracture part. However, the results of the impedance fluctuation in Table 2.1 shows an increase (in mΩ) in the impedance of the fracture over a period of 8 weeks after the trauma. This impedance increase is so small that an accuracy of at least two decimal places or more is required in order to be observable. The proximal and distal segments of Table 2.1 correspond to the control parts "1" and "2" of Figure 2.13.

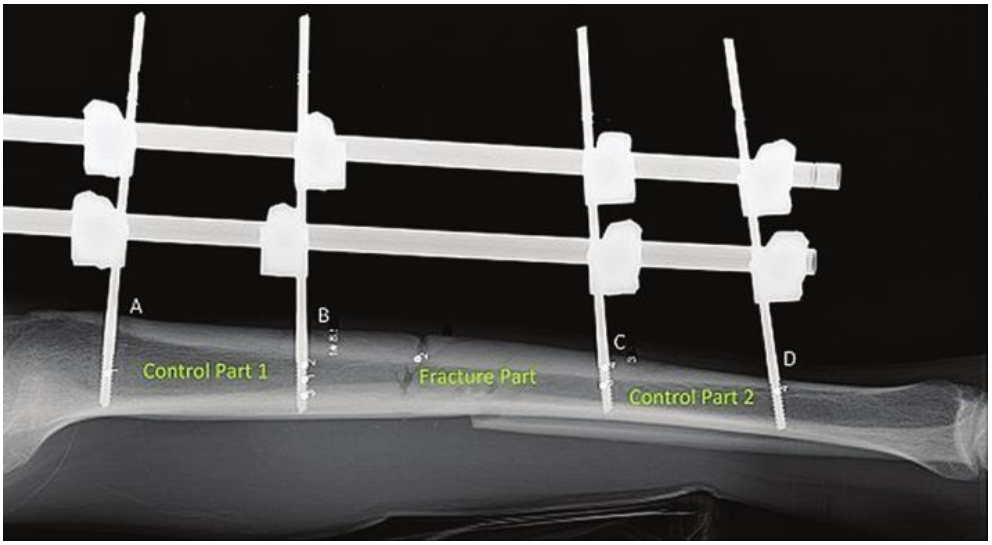

Figure 2.13: Measurement of bone impedance test-bed during fracture healing, picture taken from [66]

Table 2.1: Bone impedance fluctuation during fracture healing, picture taken from [66]

	Bone segments	**Time**			
		Week 1	**Week 4**	**Week 6**	**Week 8**
Mean impedance (in mΩ)	**Proximal segment**	23.16574	23.08505	26.75187	23.18246
	Distal segment	20.02352	20.39869	22.34932	29.78008
	Fractured segment	14.27392	18.34957	19.23854	19.77187

A similar measurement technique can be found in [67] for measurements in an in-vitro buffalo joint at the 50kHz spectrum where it is mentioned that the impedance of the bone increased as the bone was partially and completely fractured.

The bone impedance measurements of Figure 2.14 exhibit a very small increase, 334.2 to 334.7 Ohms, as the fracture site increased in length along the long axis of the bone, this is contradictory to [66] where the fracture's impedance increased as the bone healed. Finally in [68], at 2Hz, the impedance of the fractured bone of a rabbit began increasing at the second week after the fracture when the mineralization process of the bone started (see Figure 2.15).

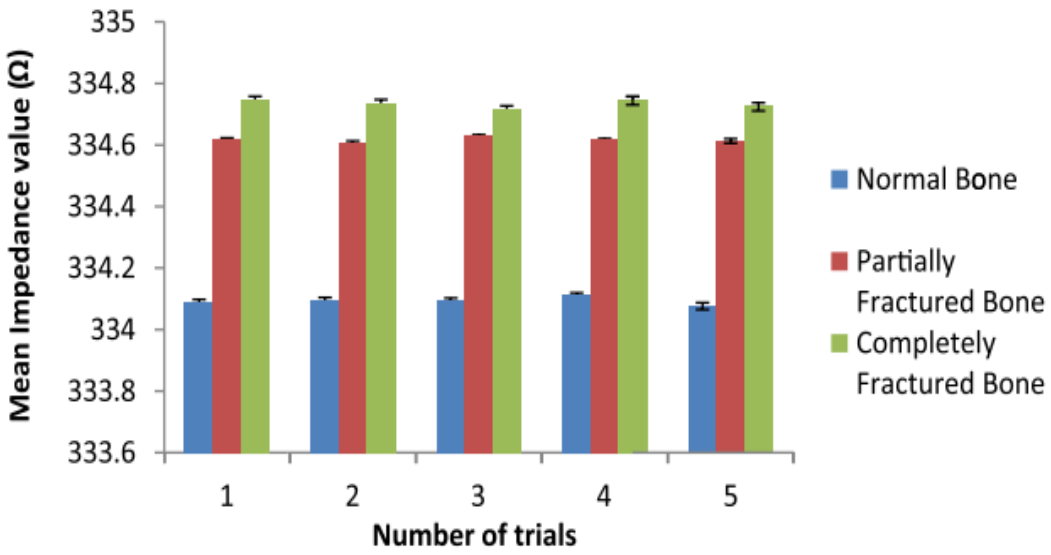

Figure 2.14: Impedance measurements in a buffalo joint, picture taken from [67]

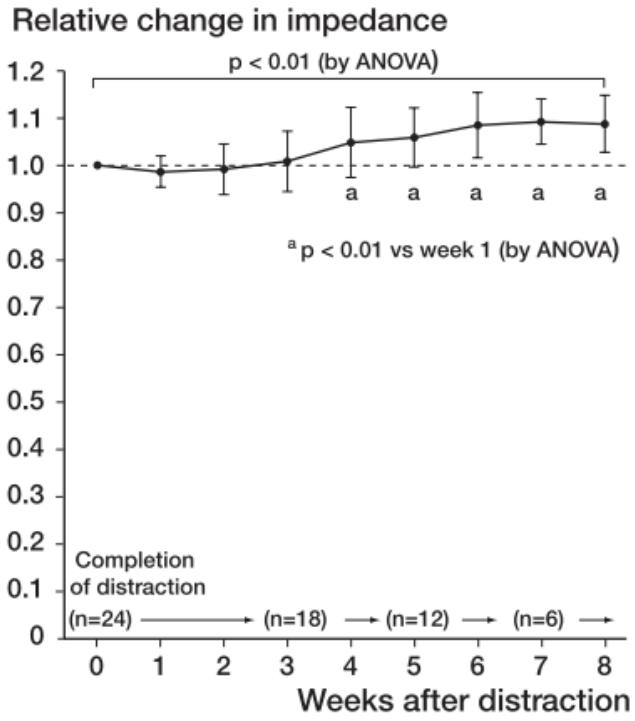

Figure 2.15: Relative impedance change measured at the fractured joint of a rabbit, picture taken from [68]

In Figure 2.15, a small increase in the impedance of the fractured bone as it heals during the period of 8 weeks can be observed, this comes to an agreement with the results presented in [66] (see Table 2.1) but are contradictory to [67] (see Figure 2.14).The major issue with these measurements is that the impedance fluctuation is often very small and can be a result of errors due to the unpredictable volume and geometry of blood inside and around the fracture. The calculation of the imaginary part of the impedance is necessary in order to extract viable conclusions, this is also due to the high conductivity of blood that increases the overall losses of the measured body part. In addition to that, the wavelength of the current in the frequencies used in [66]–[68] is large compared to the dimensions of the investigated bones, limiting its sensitivity to the change of the chemical components of the fracture during the healing process.

An approach that will take into account all the mentioned criteria for the proper evaluation of fracture healing is necessary. The proposed technique uses the pins of an external metal plate as monopoles at the frequency spectrum of 1 to 4GHz. This frequency range was selected due to the well balanced ratio of wave dissipation in the human body versus the wavelength's comparability to the bone's dimensions at the given frequency range. The technique was tested inside several multilayer body phantoms, the recipes for the creation of the phantoms are presented in Chapter 3, and the test – bed of the proposed monopole system is thoroughly analysed in Chapters 4 and 5.

2.7 Conclusions

This chapter has provided details on the most important aspects for consideration when designing antennas that operate inside lossy media and referenced sources that provide more specific information. Details have also been included regarding the nature, causes, types and healing of bone fractures, followed by a summary of the most common techniques that doctors use. It has been shown that monitoring and treating a bone fracture at the period before the fourth week after the trauma can be a difficult task. As reported in this chapter, the limited proposed solutions in the literature exhibit contradictory results that can be unreliable. Thus, the remainder of this thesis is dedicated to the development and validation of a novel technique using a pair of radiofrequency monopoles, for monitoring bone fracture healing. In the following chapter (Chapter 3), the recipes for bone cortical, bone marrow, blood and muscle for the creation of multi material phantoms will be investigated.

References

[1] J. Kim and Y. Rahmat-Samii, “Implanted antennas inside a human body: Simulations, designs, and characterizations,” *IEEE Transactions on Microwave Theory and Techniques*, vol. 52, no. 8, pp. 1934–1943, 2004.

[2] P. Soontornpipit, C. M. Furse, and Y. C. Chung, “Design of implantable microstrip antenna for communication with medical implants,” *IEEE Transactions on Microwave Theory and Techniques*, vol. 52, no. 8, pp. 1944–1951, 2004.

[3] T. Karacolak, A. Z. Hood, and E. Topsakal, “Design of a dual-band implantable antenna and development of skin mimicking gels for continuous glucose monitoring,” *IEEE Transactions on Microwave Theory and Techniques*, vol. 56, no. 4, pp. 1001–1008, 2008.

[4] W. Xia, K. Saito, M. Takahashi, and K. Ito, “Performances of an implanted cavity slot antenna embedded in the human arm,” *IEEE Transactions on Antennas and Propagation*, vol. 57, no. 4, pp. 894–899, 2009.

[5] R. Warty, M. R. Tofighi, U. Kawoos, and A. Rosen, “Characterization of implantable antennas for intracranial pressure monitoring: Reflection by and transmission through a scalp phantom,” *IEEE Transactions on Microwave Theory and Techniques*, vol. 56, no. 10, pp. 2366–2376, 2008.

[6] S. Soora, K. Gosalia, M. S. Humayun, and G. Lazzi, “A comparison of two and three dimensional dipole antennas for an implantable retinal prosthesis,” *IEEE Transactions on Antennas and Propagation*, vol. 56, no. 3, pp. 622–629, 2008.

[7] T. Karacolak, R. Cooper, and E. Topsakal, “Electrical properties of rat skin and design of implantable antennas for medical wireless telemetry,” *IEEE Transactions on*

Antennas and Propagation, vol. 57, no. 9, pp. 2806–2812, 2009.

[8] J. Abadia *et al.*, "3D-spiral small antenna design and realization for biomedical telemetry in the MICS band," *Radioengineering*, vol. 18, no. 4, pp. 359–367, 2009.

[9] E. Y. Chow, C. L. Yang, A. Chlebowski, S. Moon, W. J. Chappell, and P. P. Irazoqui, "Implantable wireless telemetry boards for in Vivo transocular transmission," *IEEE Transactions on Microwave Theory and Techniques*, vol. 56, no. 12, pp. 3200–3208, 2008.

[10] Z. N. Chen, G. C. Liu, and T. S. P. See, "Transmission of RF signals between MICS loop antennas in free space and implanted in the human head," *IEEE Transactions on Antennas and Propagation*, vol. 57, no. 6, pp. 1850–1854, 2009.

[11] K. Gosalia, M. S. Humayun, and G. Lazzi, "Impedance matching and implementation of planar space-filling dipoles as intraocular implanted antennas in a retinal prosthesis," *IEEE Transactions on Antennas and Propagation*, vol. 53, no. 8, pp. 2365–2373, 2005.

[12] P. M. Izdebski, H. Rajagopalan, and Y. Rahmat-Samii, "Conformal ingestible capsule antenna: A novel chandelier meandered design," *IEEE Transactions on Antennas and Propagation*, vol. 57, no. 4, pp. 900–909, 2009.

[13] M. Z. Azad and M. Ali, "A miniature implanted inverted-F antenna for GPS application," *IEEE Transactions on Antennas and Propagation*, vol. 57, pp. 1854–1858, 2009.

[14] F. Merli, "Implantable Antennas for Biomedical Applications," PhD Thesis, Ecole Polytechnique Federale de Lausanne, 2011.

[15] S. Y. Huang, "Loss Tangent," *Notes*, no. 5, pp. 8–9, 2012.

[16] W. G. Scanlon, J. B. Burns, and N. E. Evans, “Radiowave propagation from a tissue-implanted source at 418 MHz and 916.5 MHz.,” *IEEE Transactions on Bio-medical Engineering*, vol. 47, no. 4, pp. 527–34, 2000.

[17] C. A. Balanis, *Modern Antenna Handbook*. New York, NY, USA: Wiley-Interscience, 2008.

[18] Y. Hao, A. Alomainy, P. S. Hall, Y. I. Nechayev, C. G. Parini, and C. C. Constantinou, “Antennas and propagation for body centric wireless communications,” *2005 IEEE/ACES International Conference on Wireless Communications and Applied Computational Electromagnetics*, pp. 588–591, 2005.

[19] R. Moore, “Effects of a surrounding conducting medium on antenna analysis,” *IEEE Transactions on Antennas and Propagation*, vol. 11, no. 3, pp. 216–225, 1963.

[20] A. D. Yaghjian and S. R. Best, “Impedance, bandwidth, and Q of antennas,” *IEEE Transactions on Antennas and Propagation*, vol. 53, no. 4, pp. 1298–1324, 2005.

[21] S. R. Best, “A discussion on electrically small antennas surrounded by lossy dispersive materials,” *European Conference on Antennas and Propagation, EuCAP*, vol. 2006, no. October, 2006.

[22] T. Alves, B. Poussot, and L.-M. Laheurte, “A Simple Method to Estimate the Antenna Efficiency Over a Lossy Medium,” *7th European Conference on Antennas and Propagation (EuCAP)*, vol. 1, no. 3, pp. 3750–3753, 2013.

[23] IEEE Standards Coordinating Committee 28, *IEEE C95. 1-1992: IEEE Standard for Safety Levels with Respect to Human Exposure to Radio Frequency Electromagnetic Fields, 3 kHz to 300 GHz*, no. April. 1999.

[24] IEEE International Committee on Electromagnetic Safety (SCC39), *IEEE Standard for Safety Levels With Respect to Human Exposure to Radio Frequency Electromagnetic Fields, 3 kHz to 300 GHz*, no. April. 2006.

[25] J. F. Kellam, "Musculoskeletal Injury," *Management of Musculoskeletal Injuries in the Trauma Patient*, vol. 1, pp. 3–12, 2014.

[26] J. A. Auer, "Principles of fracture treatment," *Equine Surgery*, pp. 1000–1029, 2006.

[27] M. S. Ghiasi, J. Chen, A. Vaziri, E. K. Rodriguez, and A. Nazarian, "Bone fracture healing in mechanobiological modeling: A review of principles and methods," *Bone Reports*, vol. 6, pp. 87–100, 2017.

[28] C. Qing, "The molecular biology in wound healing & non-healing wound," *Chinese Journal of Traumatology*, vol. 20, no. 4, pp. 189–193, 2017.

[29] I. H. Kalfas;, "Principles of bone healing," *Neurosurgery Focus*, vol. 10, no. 4, pp. 1–4, 2001.

[30] T. A. Einhorn and L. C. Gerstenfeld, "Fracture healing: mechanisms and interventions," *Nature Reviews Rheumatology*, vol. 11, no. 1, pp. 45–54, Jan. 2015.

[31] Stuart James Fischer, "Fractures (Broken Bones)," *American Academy of Orthopaedic Surgeons*, 2012. [Online]. Available: http://orthoinfo.aaos.org/topic.cfm?topic=a00139. [Accessed: 03-Jul-2017].

[32] Jill Weisenberger, "Types of Bone Fractures | Interactive Anatomy Guide," *www.Innerbody.com*, 2017. [Online]. Available: http://www.innerbody.com/image/skel06.html. [Accessed: 03-Jul-2017].

[33] "BBC - GCSE Bitesize Science - Endoskeletons and exoskeletons : Revision, Page 3,"

BBC, 2014. [Online]. Available: http://www.bbc.co.uk/schools/gcsebitesize/science/triple_ocr_gateway/the_living_body/skeletons/revision/3/. [Accessed: 04-Jul-2017].

[34] Graham Lloyd-Jones, "Introduction to Trauma X-ray - Fracture description," *Royal College of Radiologists*, 2016. [Online]. Available: http://www.radiologymasterclass.co.uk/tutorials/musculoskeletal/trauma/trauma_x-ray_page1. [Accessed: 03-Jul-2017].

[35] K. Ambadan, "Classification of Fractures & Compound Fracture Managment," *PowerPoint presentation*, 2014. [Online]. Available: https://www.slideshare.net/kevwired/classification-of-fractures-compound-fracture-managment?from_action=save.

[36] Danielle Campagne, "Overview of Fractures, Dislocations, and Sprains - Injuries; Poisoning," *MSD Manual Professional Edition*, 2017. [Online]. Available: http://www.msdmanuals.com/en-gb/professional/injuries-poisoning/fractures,-dislocations,-and-sprains/overview-of-fractures,-dislocations,-and-sprains. [Accessed: 03-Jul-2017].

[37] P. Elsissy, Y. T. Akpolat, A. Chien, and W. K. Cheng, "MRI evaluation of the knee with non-ferromagnetic external fixators: cadaveric knee model," *European Journal of Orthopaedic Surgery and Traumatology*, vol. 25, no. 5, pp. 933–939, 2015.

[38] D. C. Patterson, J. I. Shin, S. M. Andelman, V. Olujimi, and B. O. Parsons, "Increased risk of 30-day postoperative complications for diabetic patients following open reduction-internal fixation of proximal humerus fractures," *Journal of Shoulder and Elbow Surgery (JSES)*, vol. 1, no. 1, pp. 19–24, 2017.

[39] R. Parviainen, J. Auvinen, T. Pokka, W. Serlo, and J.-J. Sinikumpu, “Maternal smoking during pregnancy is associated with childhood bone fractures in offspring – A birth-cohort study of 6718 children,” *Bone*, vol. 101, pp. 202–205, 2017.

[40] C. Spross, R. Zeledon, V. Zdravkovic, and B. Jost, “How bone quality may influence intraoperative and early postoperative problems after angular stable open reduction - internal fixation of proximal humeral fractures,” *Journal of Shoulder and Elbow Surgery*, pp. 1–7, 2017.

[41] M. B. Leno, S. Y. Liu, C. T. Chen, and H. T. Liao, “Comparison of functional outcomes and patient-reported satisfaction between titanium and absorbable plates and screws for fixation of mandibular fractures: A one-year prospective study,” *Journal of Cranio-Maxillofacial Surgery*, vol. 45, no. 5, pp. 704–709, 2017.

[42] U. K. Meena, M. C. Bansal, P. Behera, R. Upadhyay, and G. C. Gothwal, “Evaluation of functional outcome of pilon fractures managed with limited internal fixation and external fixation: A prospective clinical study,” *Journal of Clinical Orthopaedics and Trauma*, vol. 8, no. 2, pp. S16–S20, 2017.

[43] J. C. Thorud, S. Mortensen, J. L. Thorud, N. Shibuya, Y. M. Maldonado, and D. C. Jupiter, “Effect of Obesity on Bone Healing After Foot and Ankle Long Bone Fractures,” *The Journal of Foot and Ankle Surgery*, vol. 56, no. 2, pp. 258–262, 2017.

[44] W. H. Cheung, T. Miclau, S. K. H. Chow, F. F. Yang, and V. Alt, “Fracture healing in osteoporotic bone,” *Injury*, vol. 47, pp. S21–S26, 2016.

[45] M. Mehta *et al.*, “Influences of age and mechanical stability on volume, microstructure, and mineralization of the fracture callus during bone healing: Is osteoclast activity the key to age-related impaired healing?,” *Bone*, vol. 47, no. 2, pp. 219–228, 2010.

[46] P. J. Harwood, J. B. Newman, and A. L. R. Michael, "(ii) An update on fracture healing and non-union," *Orthopaedics and Trauma*, vol. 24, no. 1, pp. 9–23, 2010.

[47] A. Karakasli, N. Acar, A. Karaarslan, F. Ertem, and H. Havitcioglu, "A novel adjustable dynamic plate for treatment of long bone fractures: An in vitro biomechanical study," *Journal of Clinical Orthopaedics and Trauma*, vol. 7, pp. 177–183, 2016.

[48] N. D. Chakladar, L. T. Harper, and A. J. Parsons, "Optimisation of composite bone plates for ulnar transverse fractures," *Journal of the Mechanical Behavior of Biomedical Materials*, vol. 57, pp. 334–346, 2016.

[49] L. W. N. Ng, Z. J. L. Lim, R. W. Xu, and H. W. D. Hey, "Reduced Incision Surgical Fixation of Diaphyseal Forearm Fractures in Adults through a Minimally Invasive Volar Approach," *Journal of Orthopaedics, Trauma and Rehabilitation*, vol. 23, pp. 34–38, 2017.

[50] C. Dai, J. Sun, K. Chen, and H. Zhang, "Omnidirectional Internal Fixation by Double Approaches for Treating Ruedi- Allgower Type III Pilon Fractures," *The Journal of Foot and Ankle Surgery*, vol. 56, no. 4, pp. 756–761, 2017.

[51] A. P. Shetty, A. Bosco, R. Perumal, J. Dheenadhayalan, and S. Rajasekaran, "Midterm radiologic and functional outcomes of minimally-invasive fixation of unstable pelvic fractures using anterior internal fixator (INFIX) and percutaneous iliosacral screws," *Journal of Clinical Orthopaedics and Trauma*, vol. 1, no. 1, pp. 1–8, 2017.

[52] H. Leonhardt, A. Franke, N. M. H. McLeod, G. Lauer, and A. Nowak, "Fixation of fractures of the condylar head of the mandible with a new magnesium-alloy biodegradable cannulated headless bone screw," *British Journal of Oral and*

Maxillofacial Surgery, vol. 55, no. 6, pp. 623–625, 2017.

[53] Y. Feng, X. Shui, J. Wang, L. Cai, G. Wang, and J. Hong, "Comparison of hybrid fixation versus dual intramedullary nailing fixation for forearm fractures in older children: Case-control study," *International Journal of Surgery*, vol. 30, pp. 7–12, 2016.

[54] Charles D. Newton and David M. Nunamaker, *Textbook of Small Animal Orthopaedics*. Elsevier Health Sciences, 1985.

[55] T. Boutefnouchet, A. S. Lakdawala, and P. Makrides, "Outcomes following the treatment of bicondylar tibial plateau fractures with fine wire circular frame external fixation compared to open reduction and internal fixation: A systematic review," *NeuroImage*, vol. 13, no. 3, pp. 193–199, 2016.

[56] X. Zhao *et al.*, "A meta-analysis of external fixation versus open reduction and internal fixation for complex tibial plateau fractures," *International Journal of Surgery*, vol. 39, pp. 65–73, 2017.

[57] T. A. Horst and J. B. Jupiter, "Stabilisation of distal radius fractures: Lessons learned and future directions," *Injury*, vol. 47, no. 2, pp. 313–319, 2016.

[58] Angela Finn, "A Patient's Guide to Adult Humerus Shaft Fractures," *eOrthopod*, 2017. [Online]. Available: http://www.mplsortho.com/conditions-treatments/ecategory/47/etopic/4e9a2e8d8583ef20c2f7a72ebfa65420/. [Accessed: 04-Jul-2017].

[59] R. S. Lakes, R. A. Harper, and J. L. Katz, "Dielectric relaxation in cortical bone," *Journal of Applied Physics*, vol. 48, no. 2, pp. 808–811, 1977.

[60] C. Goldstein, S. Sprague, and B. A. Petrisor, “Electrical stimulation for fracture healing: current evidence,” *Journal of Orthopaedic Trauma*, vol. 24, no. 3, pp. 62–65, 2010.

[61] R. Pethig and D. B. Kell, “The passive electrical properties of biological systems: their significance in physiology, biophysics and biotechnology.,” *Physics in Medicine and Biology*, vol. 32, no. 8, pp. 933–970, 1987.

[62] T. Hirashima, W.-C. Kim, W.-C. Kim, K. Kawamoto, T. Yoshida, and T. Kubo, “Evaluating bone union of distal radius fractures by measuring impedance values,” *Orthopedics*, vol. 32, no. 1, pp. 1–31, 2009.

[63] R. Wade and J. Richardson, “Outcome in fracture healing: A review,” *Injury*, vol. 32, no. 2, pp. 109–114, 2001.

[64] K. D. Hankenson, G. Zimmerman, and R. Marcucio, “Biological perspectives of delayed fracture healing,” *Injury*, vol. 45, pp. S8–S15, 2014.

[65] D. A. Becker, “A Patient’s Guide to Adult Humerus Shaft Fractures,” *Orthopod*, pp. 1–8, 2010.

[66] K. Gupta, P. Gupta, G. Singh, S. Kumar, R. Singh, and R. Srivastava, “Change in electrical properties of bone as diagnostic tool for measurement of fracture healing,” *Hard Tissue*, vol. 2, no. 1, pp. 1–8, 2013.

[67] M. Khan, S. P. S. M. A. Sirdeshmukh, and K. Javed, “Evaluation of bone fracture in animal model using bio-electrical impedance analysis,” *Perspectives in Science*, vol. 8, pp. 567–569, 2016.

[68] T. Yoshida, W.-C. Kim, Y. Oka, N. Yamada, and T. Kubo, “Assessment of distraction

callus in rabbits by monitoring of the electrical impedance of bone.," *Acta Orthopaedica*, vol. 81, no. 5, pp. 628–633, 2010.

Chapter 3

Development of broadband homogenous tissue-mimicking phantom recipes

3.1 Summary

In the previous chapter a literature review regarding implanted antennas design considerations and bone fractures was conducted. In this chapter, an investigation into recipes for the development of tissue mimicking phantoms for bone marrow, bone cortical, blood and muscle is presented. The materials used for the creation of the recipes are low cost, easily accessible and non-toxic. In total, 12 recipes were made. Bone cortical, bone marrow and muscle were designed to be solid in order to enable the fabrication of bespoke heterogeneous phantoms. Blood was designed to be liquid in order to be injected into the phantoms for the replication of the effect of a bone fracture. Four of the recipes, each one corresponding to the dielectric parameters of real-life bone marrow, bone cortical, blood and muscle accordingly, are broadband with less than 5% error in conductivity and less than 10% error in relative permittivity compared to their target values as defined by the IEEE measurement standards for broadband phantom recipes [1] at 0.5 to 4GHz. This chapter is organised as follows. In Section 3.2, a literature overview is provided on the types of frequency depended tissue-mimicking phantoms that are currently available. In Section 3.3, the dispersion properties of the dielectric parameters of the ingredients used for constructing the phantom recipes is presented. In Section 3.4, a theoretical background is given about the operation of the probe used for the dielectric measurements of each recipe. In Section

3.5, the measurement results of each tissue-mimicking material over the 0.5 to 4GHz frequency spectrum are presented. Finally, in Section 3.6 the concluding remarks of this chapter are discussed.

3.2 Review of tissue-mimicking phantoms

Since the earliest research regarding the interaction between the electromagnetic radiation and the biological tissues, a large amount of body phantoms has been proposed, designed and developed [2]–[10].

The dielectric properties of the human tissues are well known over a wide frequency spectrum (2Hz -100GHz). Most of the research in the microwave range is well established in academia and industry due to the work of Gabriel [11]. To the authors best knowledge, the work of Gabriel et al. is considered the industry's standard regarding measurements of body tissues and it is adopted by multiple organisations such as the Federal Communications Commission [12] and the Foundation for Research on Information Technologies in Society of the Swiss Federal Institute of Technology (ETH) [13]. Gabriel measured the dielectric properties of body tissues by conducting multiple measurements using coaxial probes and averaging the results, thus minimising the error.

According to investigations on the applications conducted in [14], [15] the electromagnetic field radiated out of the body is highly dependent to the geometry and composition of the test-bed phantom. Therefore, when designing a body phantom, it is important to reproduce close approximations of the dielectric properties of the lossy tissues of the human body and geometries for the investigated body section. The novelty of the in-house developed multilayer phantoms presented in this chapter and Chapters 4 and 5 is in the broadband capabilities of its layers in the

frequency spectrum of 0.5 to 4GHz and the adjustability of its dimensions according to the geometry of any human body limb.

In order to properly report the available phantoms proposed in the literature, it is necessary to divide them into two major categories. The first category is geometrical phantoms while the second is anatomical phantoms. Additionally, each category is followed by a sub-section of simulation based and measurement based phantoms.

3.2.1 Geometrical phantoms

The most common geometries used for simulations and measurements of geometrical phantoms are canonical: Cubical [6], cylindrical [7] or spherical [8]. These types are frequently used to emulate parts of the human body in order to validate the electromagnetic propagation of a radiator through a lossy medium.

3.2.2 Simulations of geometrical phantoms

In simulations, geometrical phantoms offer fast results by providing easy to interpret conditions for the measurements of implanted devices. This is due to the simplicity of their geometries. Examples of reported canonical geometries include a cylindrical phantom that was used for the validations of EM wave propagation through sea water in [16] and spherical phantoms for the modeling of the human body in [4], and the human head in [8]–[10]. Another example shown in Figure 3.1 is a simulated cubical phantom found in [17] used for the representation of the human body. Figure 3.2, shows a combination of canonical geometries. This can offer a better imitation of the human body. Additional combinations of canonical geometries based on the human body emulation can be found in [18], [19] for MedRadio band implants and in [20] at 2.4GHz for on-

body applications. Moreover, simulations of canonical geometries offer an easier transition to validations via measurements than anatomical phantom geometries. Each layer takes the shape of the container used, ensuring minimum dimensional error between the simulated and constructed phantoms, along with high repeatability for each experiment (see Figure 3.3).

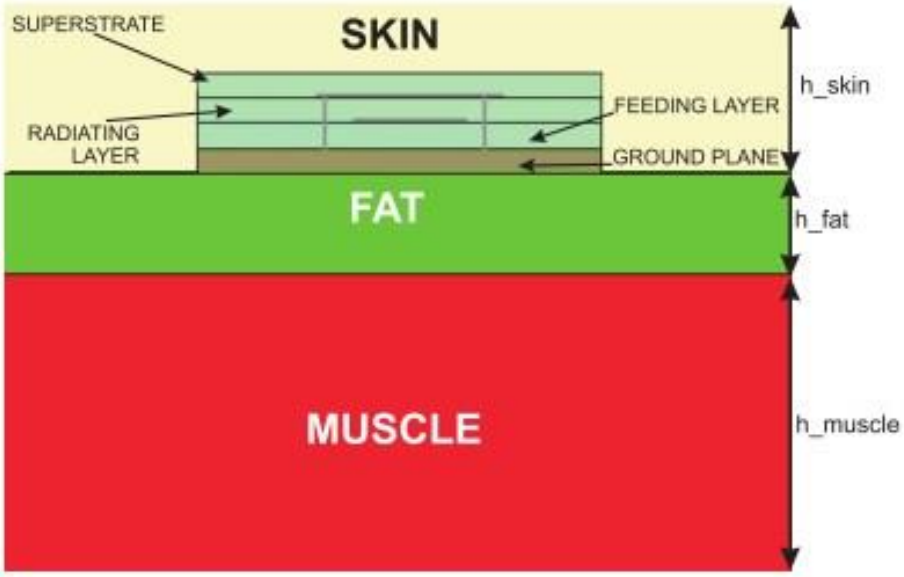

Figure 3.1: A three layer canonical geometry taken from [17]

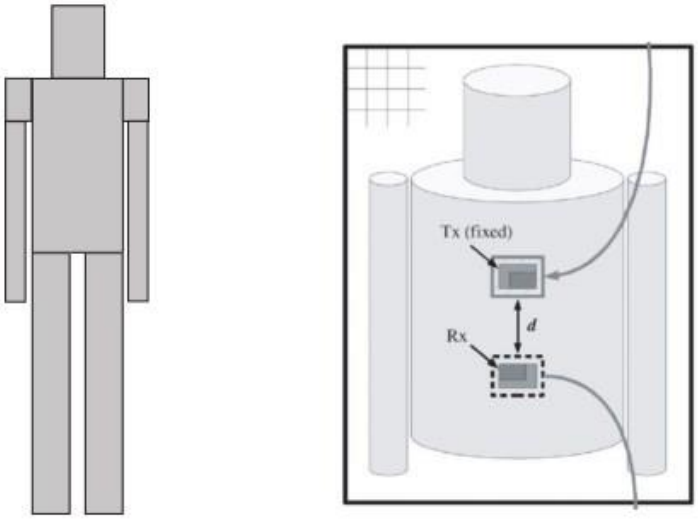

Figure 3.2: Two simulated human body models consisting of a combination of canonical geometries [18], [21]

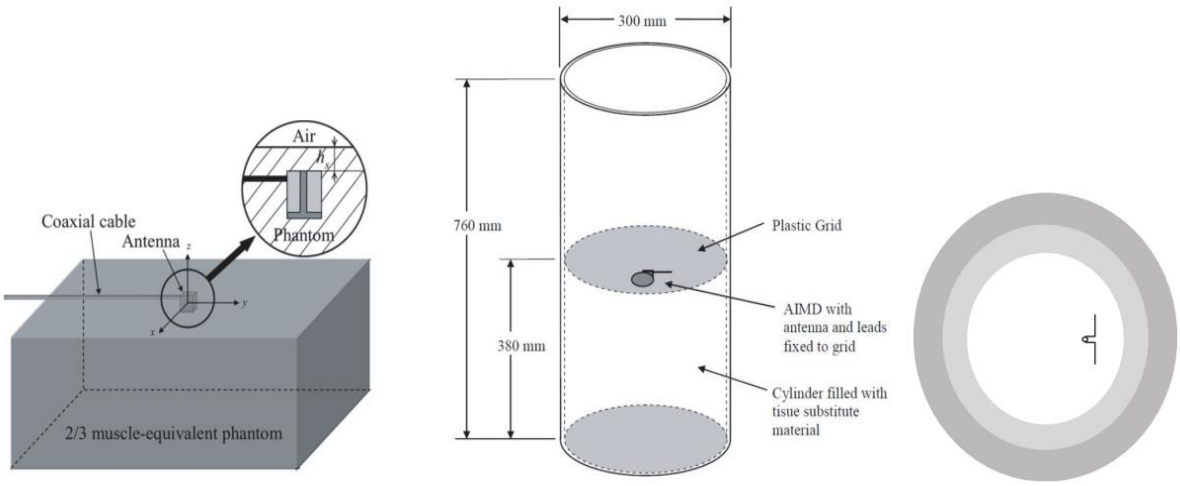

Figure 3.3: An example of cubical, cylindrical and spherical phantom geometries [22]

3.2.3 Measurements of geometrical phantoms

Phantoms with canonical geometries usually consist of homogenized liquids or gels with averaged dielectric properties according to the investigated area of the human head or body. They can be manufactured by mixing deionized water and specific amounts of sugar and/or salt to match the desired relative permittivity and conductivity (see Figure 3.4) [23]–[25].

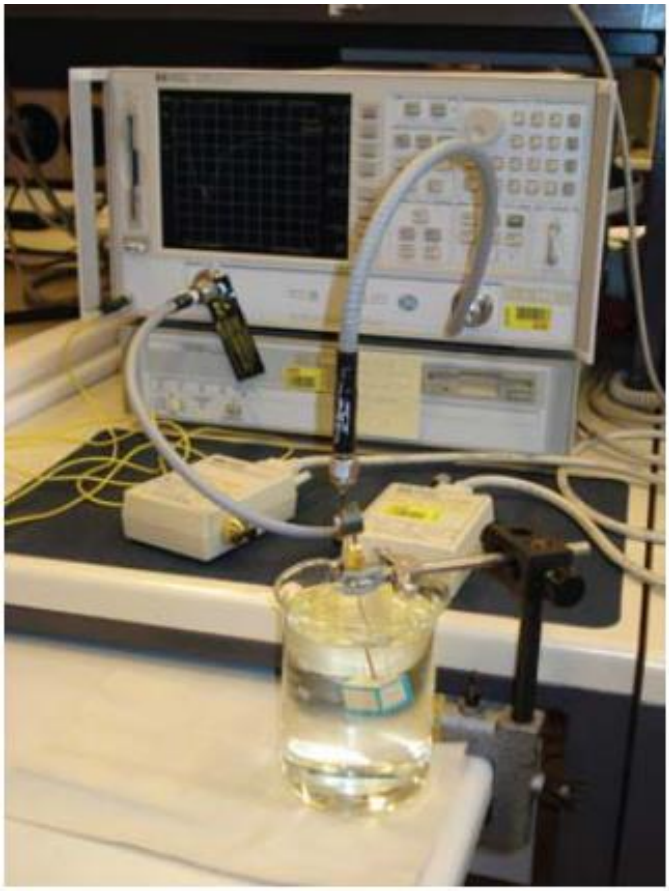

Figure 3.4: An example of a liquid phantom with canonical geometry found in [25]

It is worth mentioning that the chemical components of the recipes require a well-controlled ambient temperature as the fluctuation of the heat from the surrounding environment can affect their dielectric properties, as well as creating ideal conditions for bacteria contaminations. Bactericides are often used in order to avoid these contaminations and increase the lifespan of phantoms [26]. A liquid tissue phantom has been reported to reach over one year long lifetime [27] and gel type phantoms has shown sufficient dielectric consistency for over 40 days [28] [29]. In [30], solutions at 22°C are reported to possess similar dielectric properties to real muscle tissue at 37°C. Finally, in [29], recipes with more robust temperature tolerance are presented.

The main disadvantage of geometrical homogeneous phantoms is the frequent unrealistic approach in terms of dimensions compared to the real human body tissue. The complex geometry

of the human body can contribute to the creation of standing waves in the channel of propagation. This effect can cause several frequency discrepancies of implanted radiators between the comparisons of simulations of a realistic human model and the measurements in a geometrical phantom [31].

3.2.4 Phantoms with realistic dimensions

The realistic dimensions category refers to anatomical phantoms in relation to the targeted body tissue. This type of phantoms possesses complex geometry attributes and are mainly represented by simulations using voxel models.

Selection of realistic dimensions for a body phantom is a very important variable as the efficiency of an implanted radiator is highly dependent on the position that it is placed inside the body [22]. Adding to that is the large variety of different human body types in nature that differ in terms of age, height and weight, making the appropriate choice of phantom a complicated process. These observations highlight the importance of a detailed investigation of anatomical phantoms [32] with designs that will be adjustable to the body type of the person about to receive an implant, such as the phantom presented in this thesis.

3.2.5 Simulations of anatomical phantoms

One of the most frequently reported realistic dimensions model is the Visible Human Project (VHP) Hugo that has been studied thoroughly in literature [33]–[37]. Hugo was an adult male who was frozen, sliced and photographed after execution. The photographs were then combined to produce a detailed 3D model of Hugo, including his internal body structure. The final computer model of Hugo has more than 20 tissue types identified, with each one allocated a

frequency dependant relative permittivity and conductivity. The advantage of this model, and anatomical phantoms in general, is that the electromagnetic propagation and behaviour of the implants inside the body can be studied in more detail. The main disadvantage compared to homogenous phantoms is increased simulation time as a consequence of the phantom's level of detail.

Extended reports of realistic models can be found in [38]–[40]. Results on performance comparisons of implanted radiators found in [8], [41], [42] are presented in [39] and [40]. Other regularly used models are the Japanese male and female body phantoms developed in [43], that allow modification of their postures [44]. These phantoms are also compared with the VHP model in [45] using implanted radiators.

Two of the most detailed models found in literature are the Virtual Family and Virtual Classroom (see Figure 3.5) featuring more than 300 tissues and organs per model and a resolution of $0.5 \times 0.5 \times 0.5\text{mm}^3$ throughout the entire body with the ability to adjust the posture of each model [46]. These models incorporate a complete human family based on magnetic resonance images allowing investigations of different body constitutions according to age and gender.

Virtual Family	Virtual Classroom
Ella: a 26-year-old female adult	*Louis*: a 14-year-old male child
Duke: a 34-year-old male adult	*Eartha*: an 8-year-old female child
Billie: an 11-year-old female child	*Dizzie*: an 8-year-old male child
Thelonius: a 6-year-old male child	*Roberta*: a 5-year-old female child

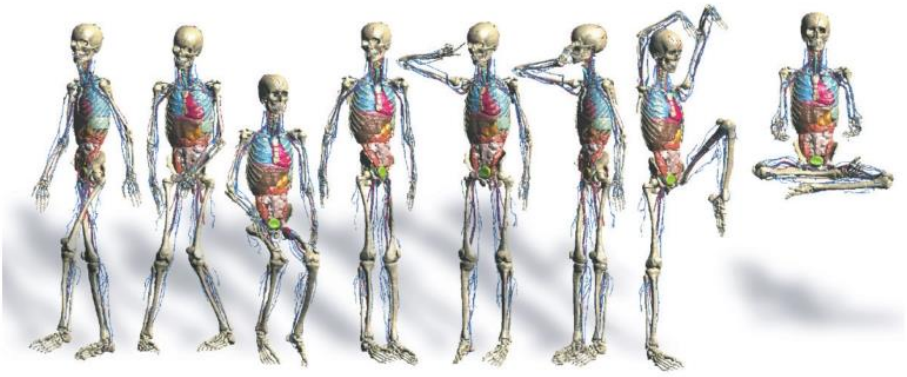

Figure 3.5: The VHP voxel models [46]

3.2.6 Measurements of anatomical phantoms

In order to match the dimensions of the investigated real life tissues, specific animal parts, such as lamb, pork or rabbit joints are often used in literature (see Figure 3.6) [7], [47]–[50]. These animal joints can provide good geometric detail when measuring implanted devices. Due to the process that commercially available meat undergoes (maturation in low humidity and blood draining), a known issue is that the dielectric properties of the investigated part may exhibit minor variations. This usually results in a drop of the average relative permittivity and conductivity of the animal part due to the lack of blood [51]. This may lead to minor differences between the simulated and measured properties of investigated implants [7].

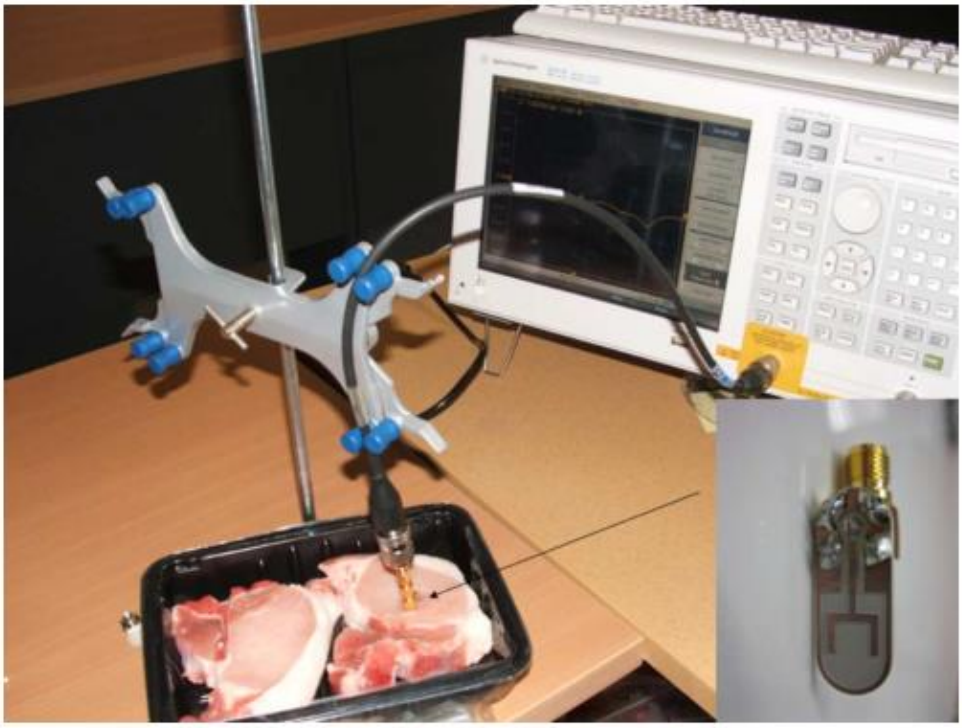

Figure 3.6: Measuring an encapsulated antenna in a pork phantom, picture taken from [7]

3.2.7 Composition of human body phantoms

The composition of tissue-mimicking phantoms is highly reliant on the body part under investigation. For simulations and measurements of body parts in the microwave spectrum where one tissue layer takes up most of the available space, like the brain inside the human head, the most common phantoms used are homogenous [8], [52]. In both simulations and measurements, multilayered phantoms, are used when an investigation of a radiator implanted into a tissue layer with respect to the surrounding tissues is required [53]. Multilayered phantoms usually consist of bone, fat, and muscle layers [28]. The example shown in Figure 3.7 is based on a simulated three layer phantom that was used for the investigation of the performance of a monopole at 2.4GHz that was implanted into three different depths of the fat layer found in [54] and [55] respectively.

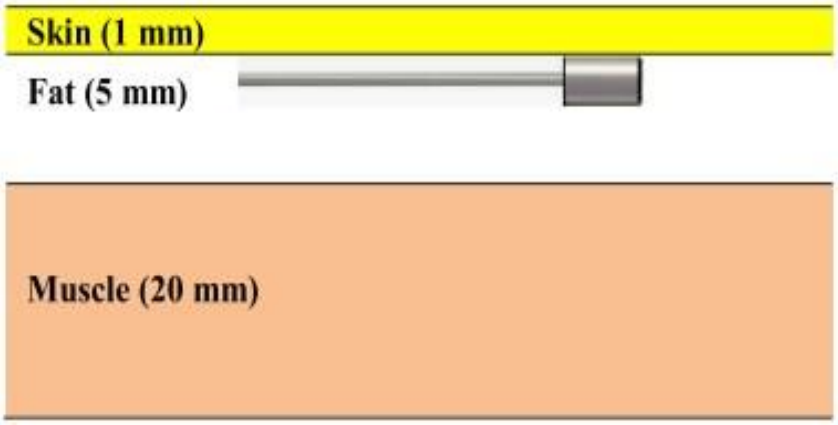

Figure 3.7: A simulation of a monopole implant in the fat layer, investigated for a variant depth [54]

While there is a large variety of simulated body phantoms, there are several limitations in the realisation of a human body phantom in measurements [5]. Several solid phantoms have been reported, as the examples shown in Figure 3.8 that are anatomical and homogenous. The cast used for these measurements is given a human shape and filled with liquids that represent an approximation on the average dielectric properties of the body part.

Figure 3.8: An example of realistic shape phantom featuring ceramic (white coloured) and plastic (black coloured) casts [56]

Due to the large variation of the dielectric properties of human tissues in the microwave frequency range, developing multilayer phantom test-beds with dielectric properties similar to the desired human tissues in a wide frequency band is challenging. Detailed inhomogeneous phantoms with exact human body anatomy is almost impossible to achieve with liquids, and very hard with gels due to the complexity of the geometric characteristics and the multi-layer nature of real life tissues [57].

In the literature, an ultra-wideband multilayer phantom with head equivalent properties can be found in [58] for the 0.2-20GHz frequency range and in [59] featuring blood, fat, wet skin and

muscle layers at 0.3 to 20GHz for the monitoring of blood glucose levels (see Figure 3.9). The phantom was made using specific amounts of deionized water, vegetable oil, salt and sugar for each tissue layer.

Figure 3.9: A four layer tissue phantom featuring blood, muscle, fat, and wet skin tissue layers for the monitoring of blood glucose levels [59]

Such phantoms require the combination of multiple layers, each with a specific recipe and thickness according to its equivalent tissue. The recipes are either gels for high permittivity and conductivity tissues or flour based for lower values. Combining multiple recipes into a phantom can often result to undesirable mixing among the contact area of the layers [57], [59], [60]. This can affect the properties of each layer in a destructive manner. Therefore, the use of high amounts of gelatine for high permittivity and conductivity recipes that require deionized water was followed as a process for the creation of the recipes of this chapter.

This thesis proposes a number of wideband inhomogeneous geometric phantoms. The geometries of the proposed measured in-house developed phantoms consist of bone marrow and bone cortical with realistic dimensions and muscle with canonical dimensions. The dimensions of bone marrow and bone cortical materials match their real life equivalent geometries of bone marrow and bone cortical and can be adjusted to match specific bone sizes and types. This is due to the ductile nature of their constituting materials. All the recipes for each tissue layer of the in-house developed phantoms presented in this chapter are frequency dispersive and wide band according to the IEEE specific absorption rate (SAR) measurement standard for the 0.3 – 2GHz and the 2 – 3GHz frequency spectrum [1].

3.3 Methodology and design of the in-house developed phantom recipes

Combining results from literature along with experimental investigations for specific frequencies, bone marrow, bone cortical, blood and muscle phantom recipes were developed in-house. The dielectric behaviour of each ingredient based on experimentation can be summarized as: Deionized water has the highest permittivity and conductivity values. By adding sugar the permittivity of the mixture reduces. Adding salt (NaCl) will increase its permittivity and conductivity; adding oil, either vegetable or olive, will decrease both these parameters over the desired frequency spectrum. It is important to mention that oil will not dissolve in water because water molecules form a polar covalent bond and oil molecules have non-covalent bonds. In order to mix oil and water, a detergent containing surfactants is required for the reduction of the tension between molecules of oil and water [61]. The detergent used for these measurements was a Fairy Lemon washing up liquid containing 15 – 30% anionic surfactants and 5 – 15% non-anionic surfactants. Gelatine was used as a solidifying agent for the mixture.

3.4 Measurement test-bed for the dielectric parameters of the phantom recipes

For the measurements of the dielectric parameters of the recipes presented in Section 3.5, an open ended 50 ohm RG-402 semi-rigid coaxial cable probe with an SMA connector was used (see Figure 3.10). This technique was chosen due to the low cost coaxial cable required and the accuracy of the results when measuring body tissues [62]. Measurements were taken with an Anritsu MS46524A vector network analyzer that was calibrated over the 0.5 to 4GHz frequency range. The coaxial probe's dimensions were: 3mm diameter and 9.5cm length. As detailed in [63], the relative permittivity and conductivity of a liquid can be calculated by measuring the complex reflection coefficient Γ of three different calibration standards: open, short and deionised water. The open complex reflection coefficient Γ was recorded with the probe left open-ended in free space. The short-circuited Γ was recorded with an aluminium foil pushed against the cleaved end and the deionized water immersed Γ was measured with the probe dipped into the liquid to the depth of 3cm below the surface. This depth was selected to ensure that the wave will be propagated inside the liquid and not on its surface or in the air [64]. A detailed analysis on the operation principles of the probe can be found in [63]. In order to minimize any phase related errors due to the flexible coaxial cable that was used, the probe was calibrated at the exact same position that the materials under measurement were placed. In addition to that, a soldering cable stand was used as the probe holder in close proximity to the materials under measurement. A comparison between CST simulations of the coaxial probe presented in this chapter and Gabriel et al measurements of muscle tissue dielectric properties can be found in Appendix A.

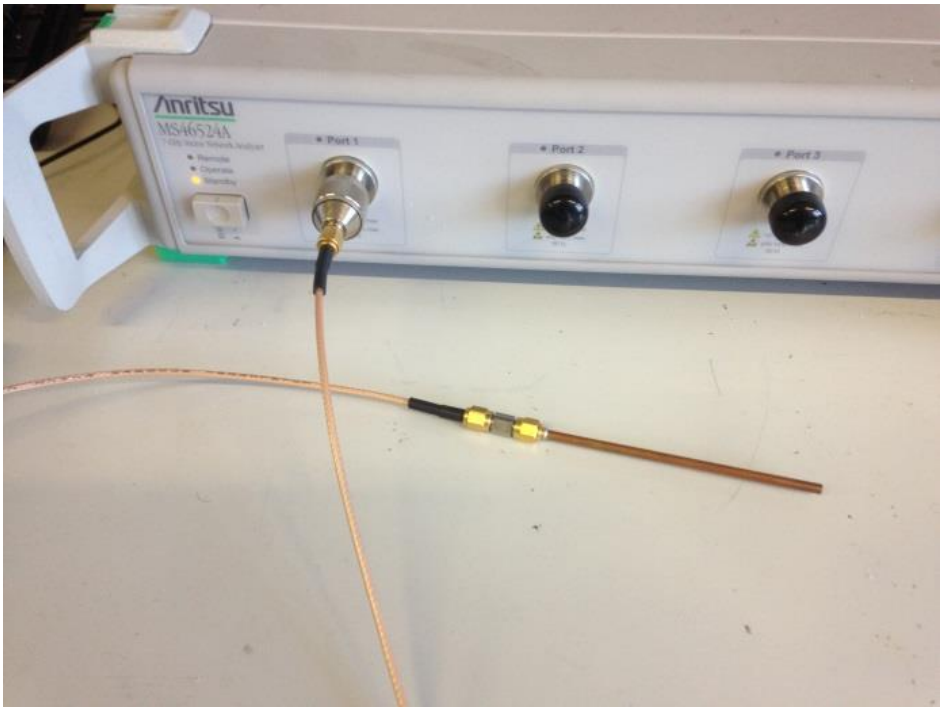

Figure 3.10: The probe used for the dielectric measurements

The complex permittivity of deionized water was calculated using the Debye Equation (3.1) [63]:

$$\varepsilon_w = \varepsilon' + \mathrm{j}\varepsilon'' = \varepsilon_\infty + \frac{\varepsilon_s - \varepsilon_\infty}{1 + j\omega\tau} \tag{3.1}$$

ε_w: Complex relative permittivity of deionized water

ε', ε'': Real and imaginary parts of the complex relative permittivity respectively

ε_∞: Relative permittivity at high frequencies

ε_s: Static relative permittivity at low frequencies

τ: Relaxation time

According to the literature measurements of deionized water at room temperature from [65], [66], ε_∞= 4.6, ε_s = 78.3 and τ = 8.08ps. The complex relative permittivity ε_m and the effective conductivity σ_m can be calculated as:

$$\varepsilon_m = -\frac{\Delta_{m2}\times\Delta_{13}}{\Delta_{m1}\times\Delta_{32}}\varepsilon_w - \frac{\Delta_{m3}\times\Delta_{21}}{\Delta_{m1}\times\Delta_{32}} \quad (3.2)$$

$$\sigma_m = \omega\varepsilon_0\varepsilon'' \quad (3.3)$$

$$\Delta_{ij} = \Gamma_i - \Gamma_j \quad (3.4)$$

Γ_1, Γ_2, Γ_3, Γ_m: Measured complex reflection coefficients for the short, open, deionized water and material under test respectively.

3.5 Measurements of homogenous tissue emulating phantom recipes

Refection coefficient measurements were taken with 300mg of sample (this was applied for both liquids and solid samples) held in a 350ml cylindrical plastic cup of 3.5cm radius. Each measurement was taken by immersing the coaxial probe into the middle of the sample found at 3cm depth from the surface, thus a good contact between the probe and the sample was achieved. The size of the container (350ml, 3.5cm radius) and the depth that the probe was immersed was selected according to [62], [67], [68] in order to ensure all of the radiated waves were confined inside the sample. A Microsoft© Excel spreadsheet produced by the authors of [64] that implemented the formulas (3.1) to (3.4) was used. The real and imaginary values of the probe's S_{11} for the open, short and deionised water were used as an inputs and the relative permittivity and conductivity values of the sample under test were extracted and plotted as a function of frequency.

The procedures given in the flowcharts of Figures Figure 3.11 -Figure 3.14 were followed to produce recipes for bone marrow, bone cortical, blood, and muscle respectively. In these flowcharts, the recipes were compared with the real life values of the equivalent body tissues as measured by Gabriel at [11]. A similar process of ingredient mixing for producing representations of different body tissues, such as the human skin, can be found in [59].

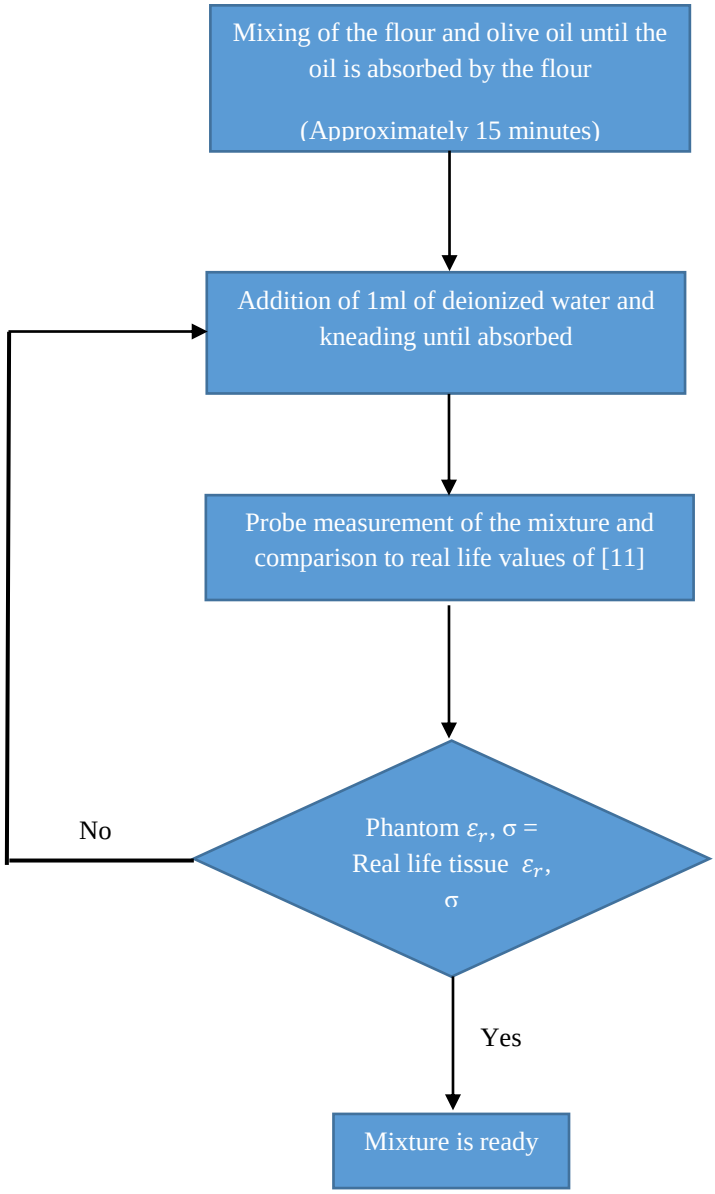

Figure 3.11: Bone marrow and bone cortical recipes development process

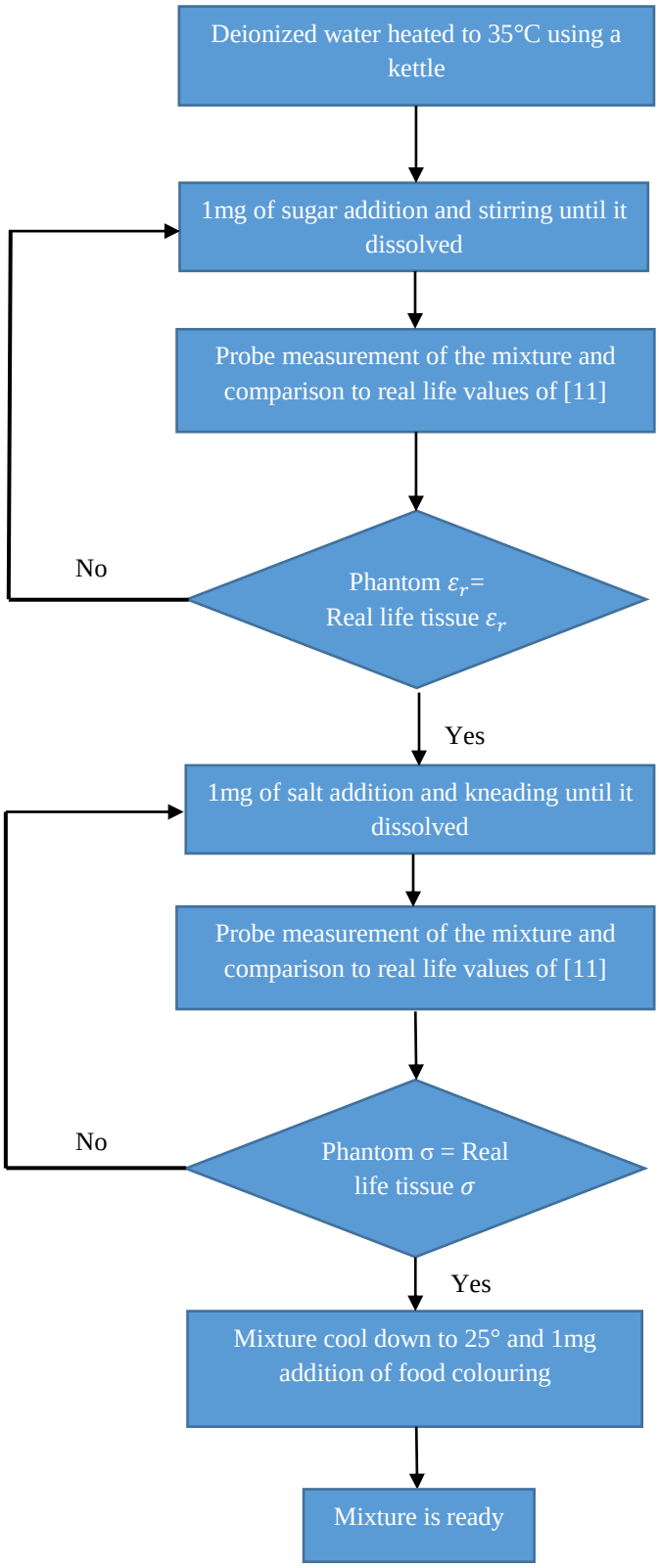

Figure 3.12: Blood emulating liquid recipe development process

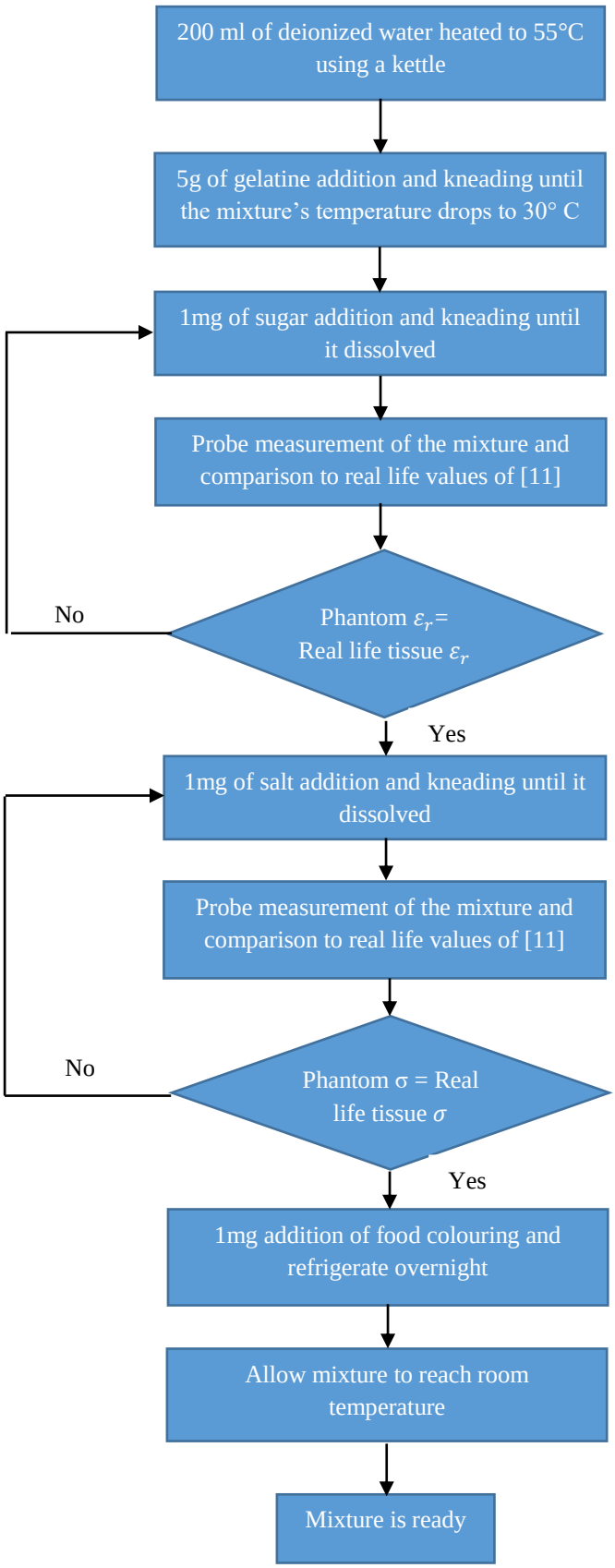

Figure 3.13: Narrow-band muscle recipe development process

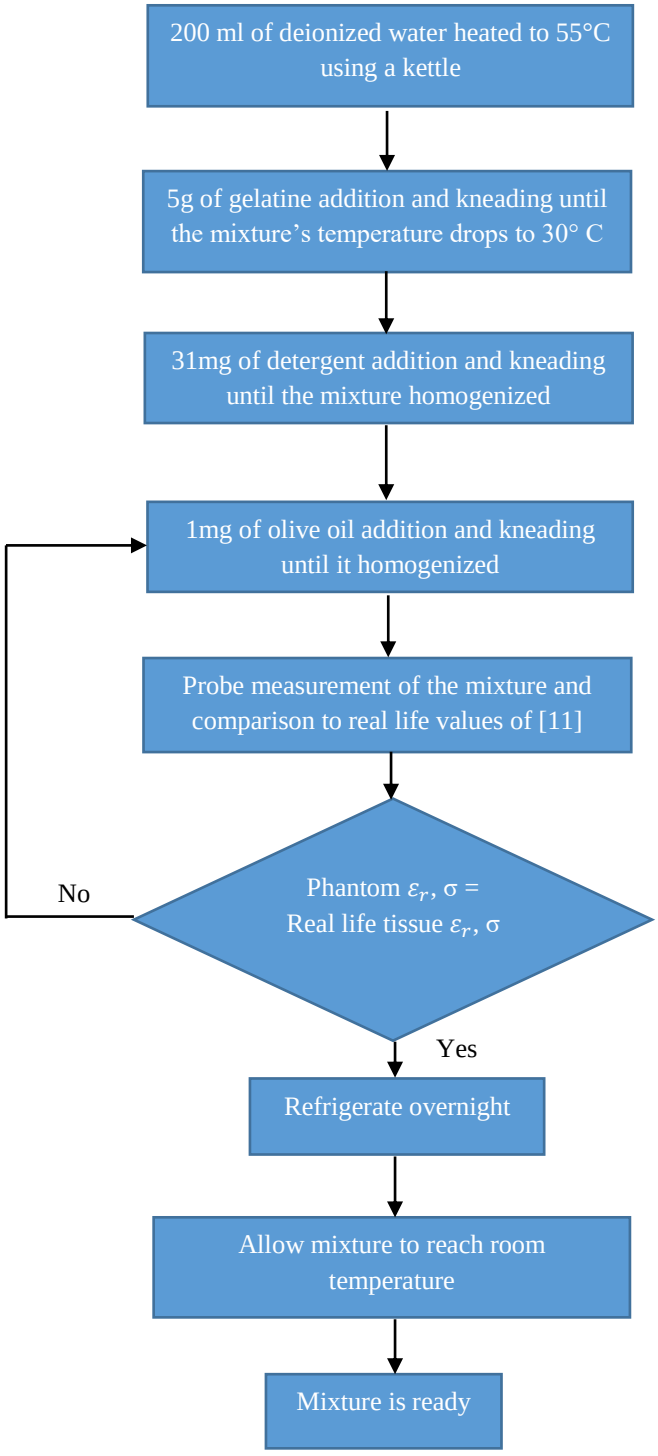

Figure 3.14: Broadband muscle recipe development process

A small amount of blue food colouring (1mg) was used in order to provide the blood emulating liquid a distinct colour. This made it easier to observe the liquid's spread inside the phantom during experiments that will be detailed later in Chapter 5.

Once the mixing was completed, the material was allowed to rest for ten minutes. Then, the S_{11} was measured from 0.5 to 4GHz three times using the probe. The three measurements were input into the Microsoft Excel spreadsheet separately, yielding three sets of relative permittivity and conductivity curves for the material. The average of the three was calculated and compared to the target curves taken from the published literature [11].

Following extensive testing, when the curve finally showed good agreement with the target values, the recipe was complete. The material was then reproduced twice more using that recipe and the S_{11} measurement procedure and proceeding Microsoft© Excel calculations were conducted in the same way. This yielded nine sets of relative permittivity and conductivity curves for the material. The average of all nine sets of relative permittivity and conductivity curves were then calculated and are henceforth referred to as the measured relative permittivity and measured conductivity. These are the values used in all proceeding phantom models of Chapters 4 and 5.

This detailed procedure was used to produce measured relative permittivity and conductivity curves for blood, muscle, bone cortical and bone marrow emulating material. The depiction of the produced samples can be found in Figure 3.15 and Figure 3.16. Table 3.1 to Table 3.4 describe the amounts of ingredients used for each recipe. To cover the full 0.5 to 4GHz frequency band, two or three recipes were needed for each material.

Table 3.1: Bone marrow recipes for 0.5 to 4GHz

Ingredient (g)	**0.5 to 0.8 GHz**	**0.5 to 4 GHz**	**2 to 4 GHz**
Flour	80	80	80
Oil	33	33	33
Deionized water	-	1.5	3
Food colouring	1	1	1

Table 3.2: Bone cortical recipes for 0.5 to 4GHz

Ingredient (g)	**0.5 to 1.5 GHz**	**0.5 to 4 GHz**
Flour	80	80
Oil	30	30
Deionized water	9.6	10.5
Sugar	7.2	7.2

Table 3.3: Blood recipes for 0.5 to 4GHz

Ingredient (g)	**0.5 to 1.5 GHz**	**0.5 to 4 GHz**	**3 to 4 GHz**
Sugar	114	91	70
Salt	2	1	-
Deionized water	164.5	164.5	151.5
Food colouring	1	1	1

Table 3.4: Muscle recipes for 0.5 to 4GHz

Ingredient (g)	**0.5 to 1.5 GHz**	**1.5 to 3 GHz**	**0.5 to 4 GHz**
Sugar	141	90	-
Salt	1	1	-
Deionized water	172	150	200
Gelatine	4.3	3.75	5
Detergent	-	-	31
Oil	-	-	31

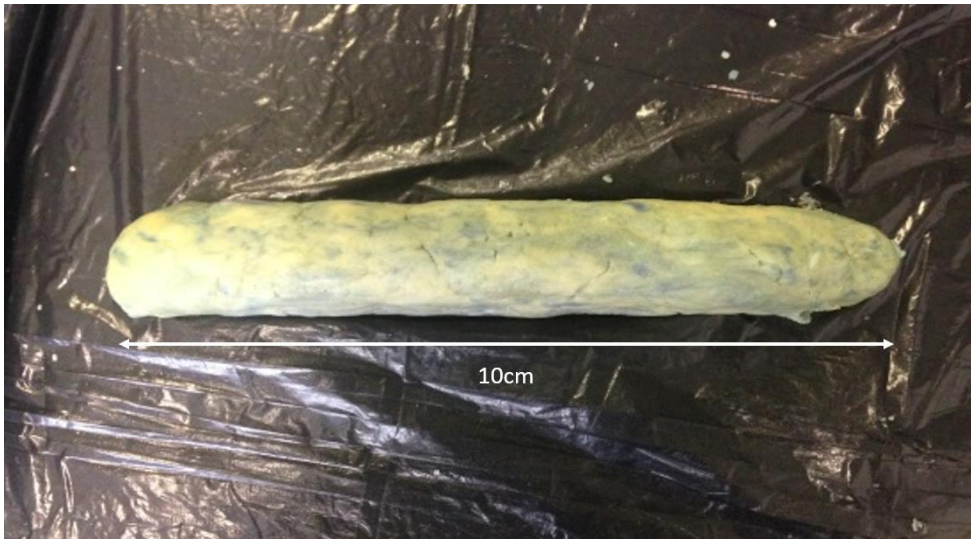

(a)

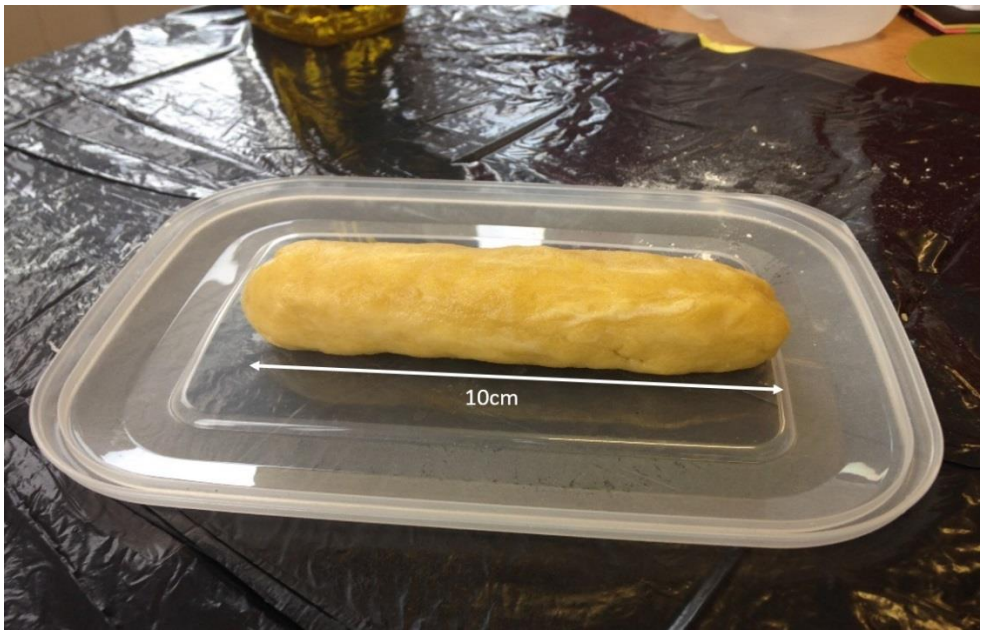

(b)

Figure 3.15: Flour based recipes: a) Bone marrow b) bone cortical

(a)

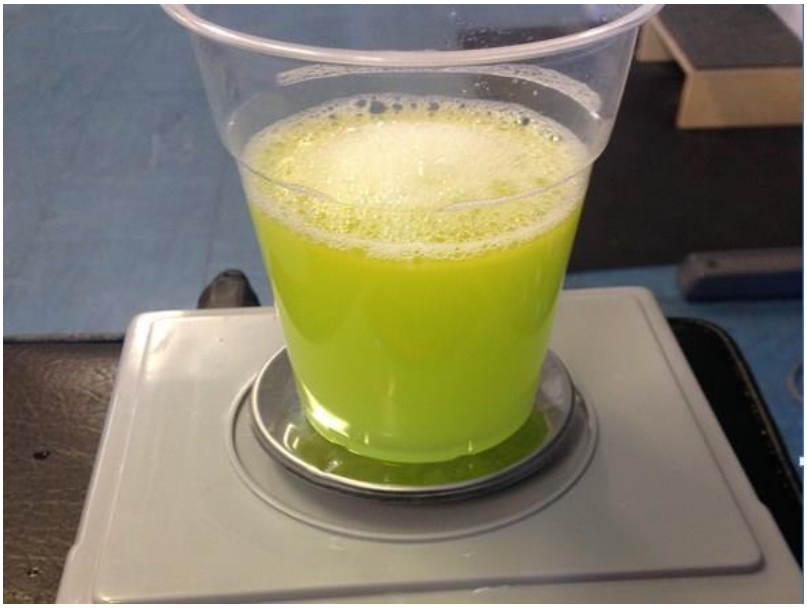

(b)

Figure 3.16: Deionized water based recipes held in a 350ml cylindrical plastic cup of 3.5cm radius: a) blood b) muscle

The measured dielectric parameters (both narrowband and wideband) of blood, muscle, bone cortical and bone marrow are presented in the next series of graphs (see Figure 3.17 Figure 3.27). Data found in literature for the relevant body tissue [69] is also plotted for comparison purposes.

The standard deviation between the nine sets of relative permittivity and conductivity curves for the four materials can be found in Appendix B. In several of the following plots a green shade is used to highlight the narrowband area of interest inside the 0.5 to 4GHz frequency spectrum. In cases of where broadband recipes were investigated, the complete frequency spectrum was targeted and so the green shade is not used.

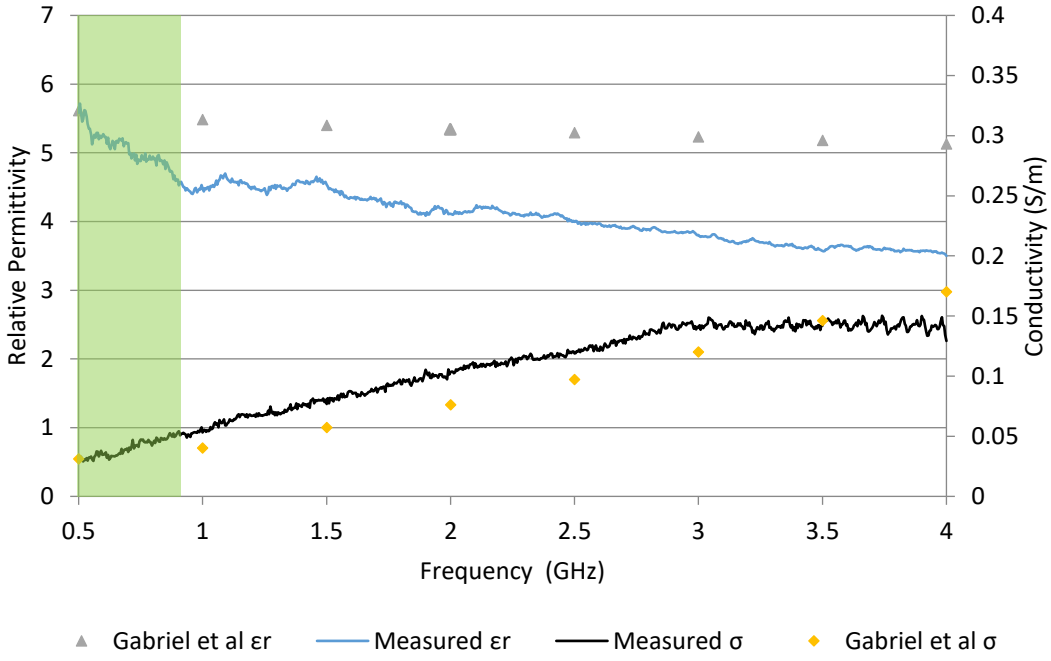

Figure 3.17: Relative permittivity and conductivity measurements compared to literature data for bone marrow at 0.5 to 0.8GHz according to the recipes of Table 3.1

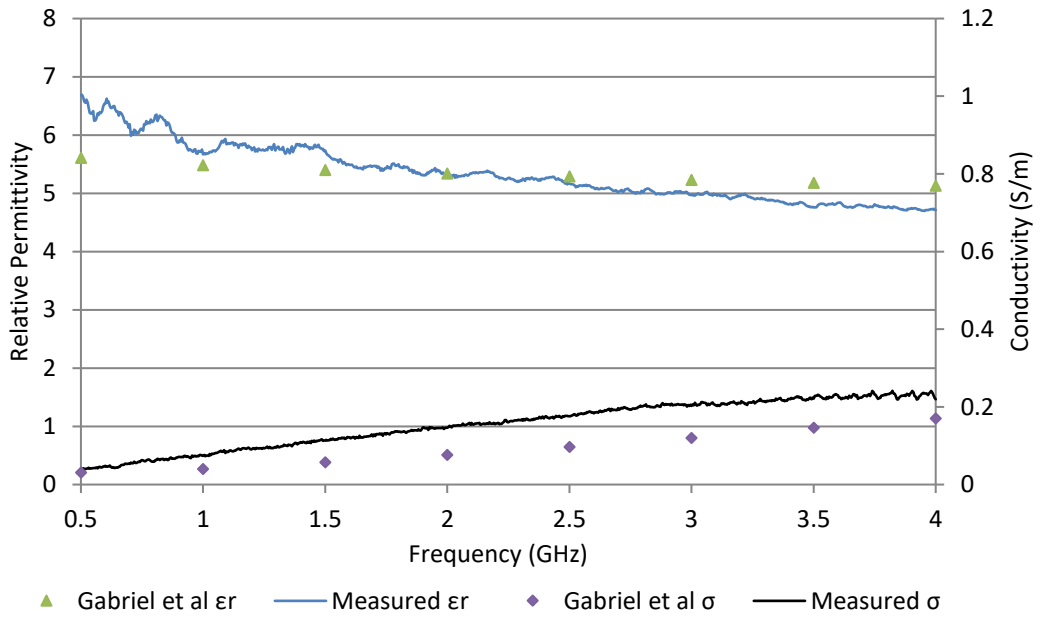

Figure 3.18: Relative permittivity and conductivity measurements compared to literature data for bone marrow at 0.5 to 4GHz according to the recipes of Table 3.1

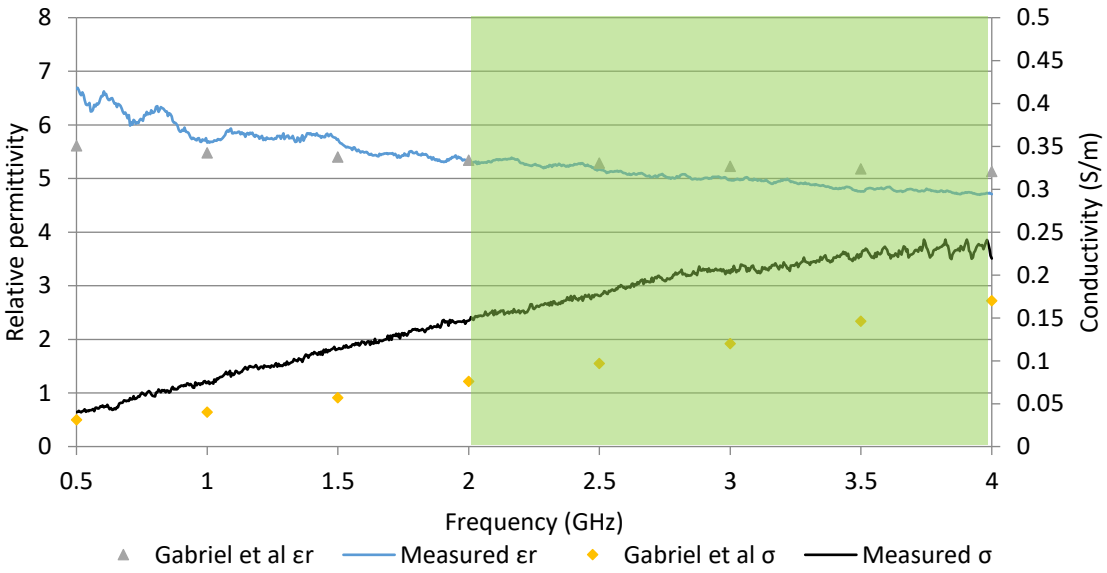

Figure 3.19: Relative permittivity and conductivity measurements compared to literature data for bone marrow at 2 to 4GHz according to the recipes of Table 3.1

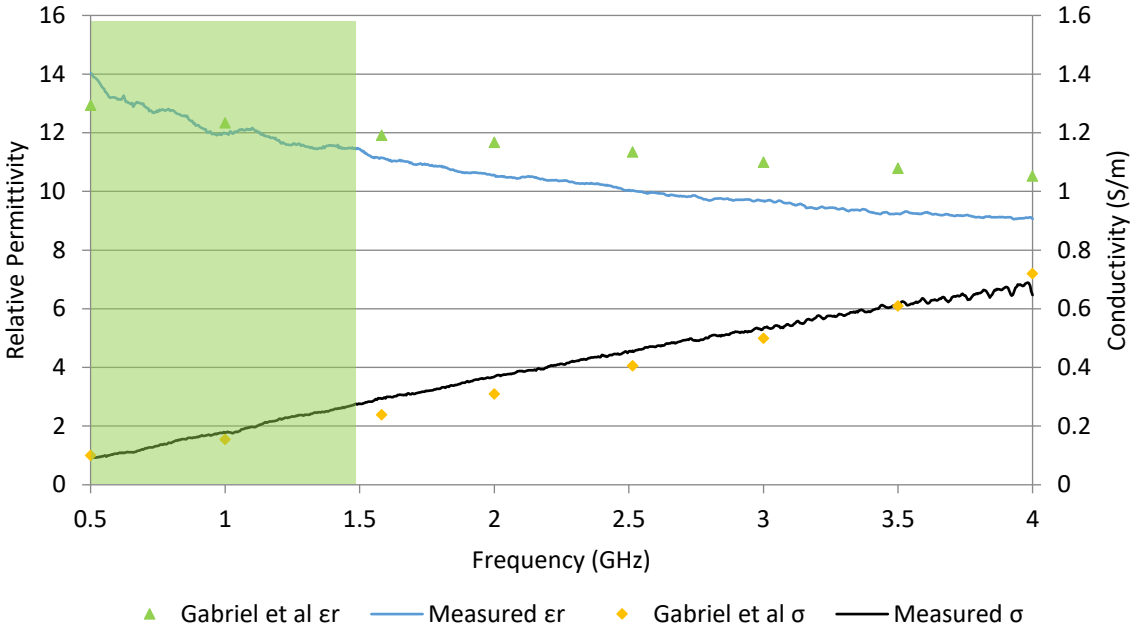

Figure 3.20: Relative permittivity and conductivity measurements compared to literature data for bone cortical at 0.5 to 1.5GHz according to the recipes of Table 3.2

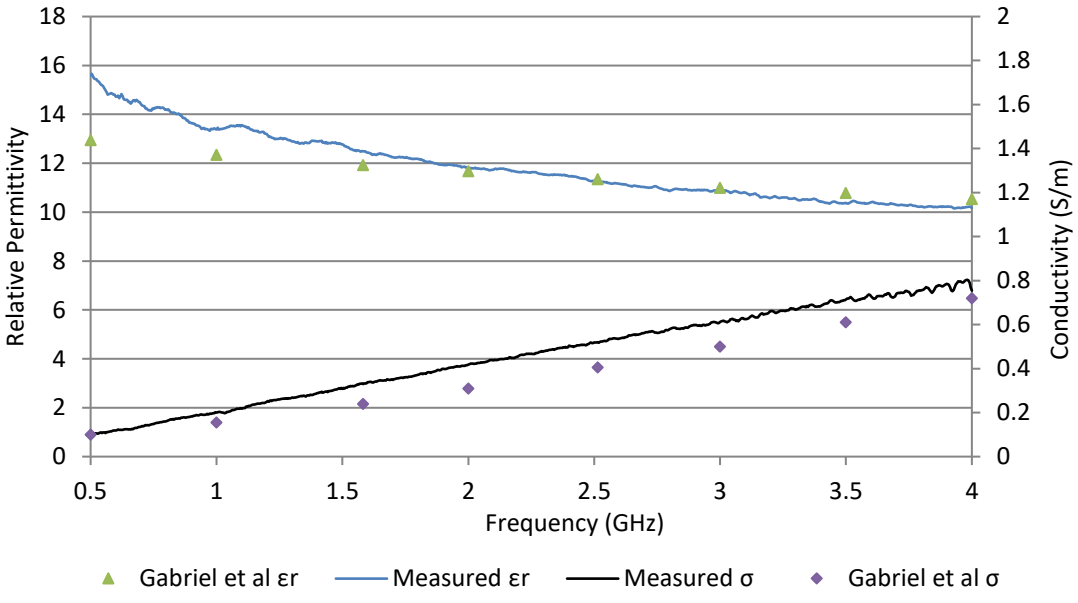

Figure 3.21: Relative permittivity and conductivity measurements compared to literature data for bone cortical at 0.5 to 4GHz according to the recipes of Table 3.2

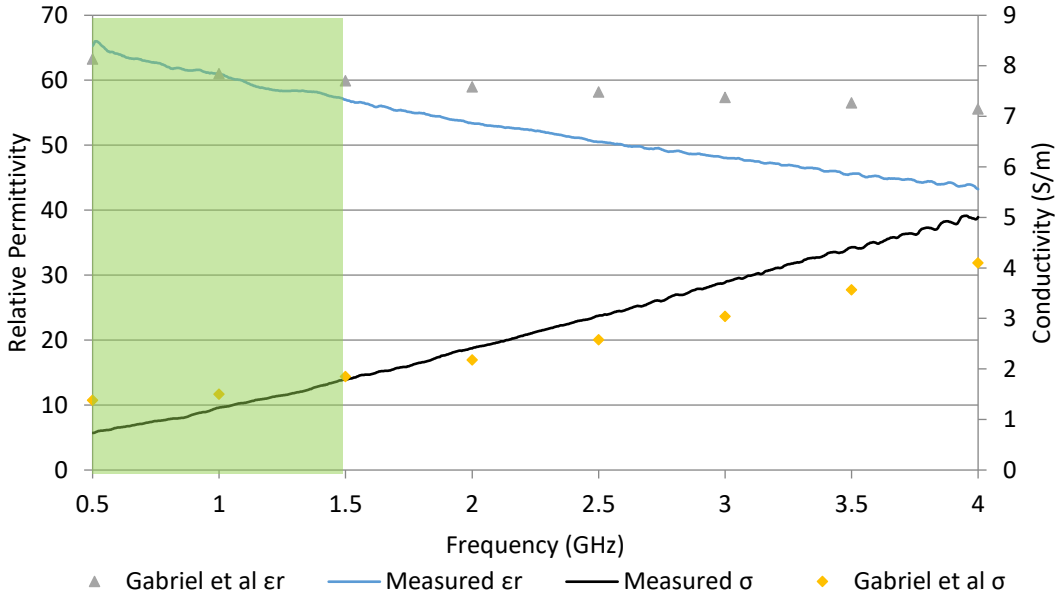

Figure 3.22: Relative permittivity and conductivity measurements compared to literature data for blood at 0.5 to 1.5GHz according to the recipes of Table 3.3

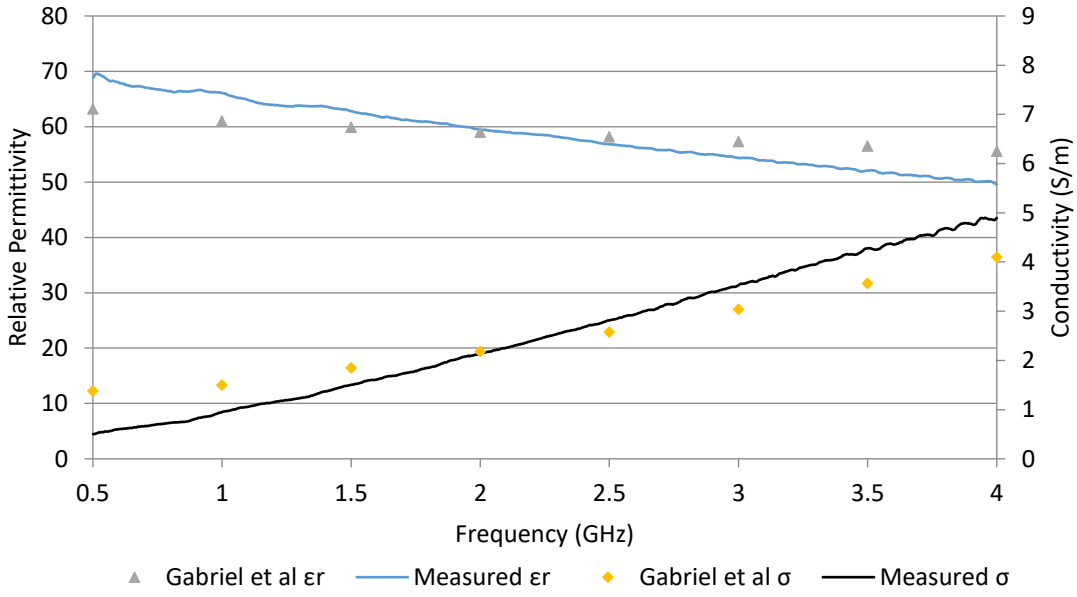

Figure 3.23: Relative permittivity and conductivity measurements compared to literature data for blood at 0.5 to 4GHz according to the recipes of Table 3.3

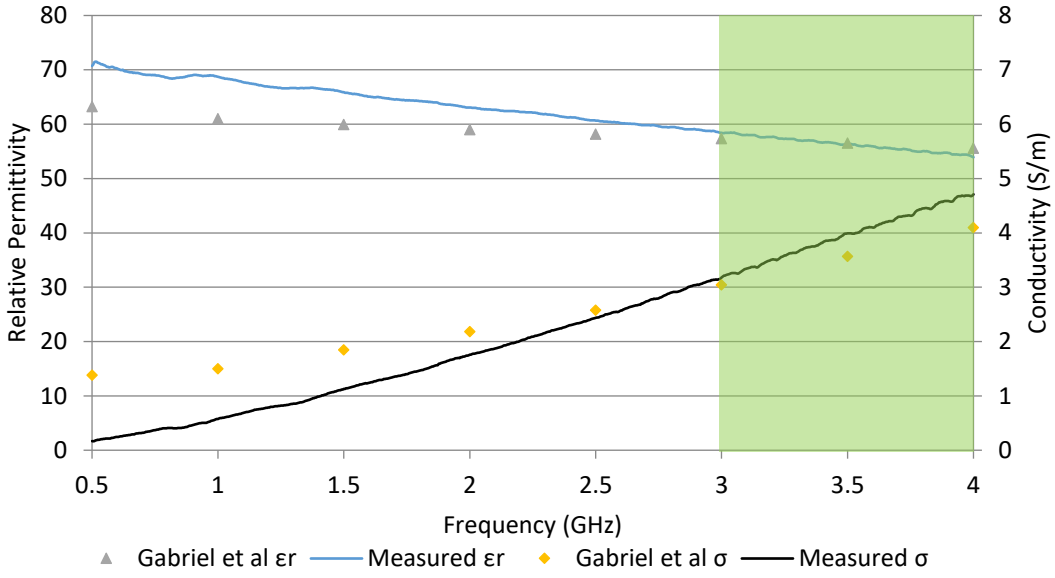

Figure 3.24: Relative permittivity and conductivity measurements compared to literature data for blood at 3 to 4GHz according to the recipes of Table 3.3

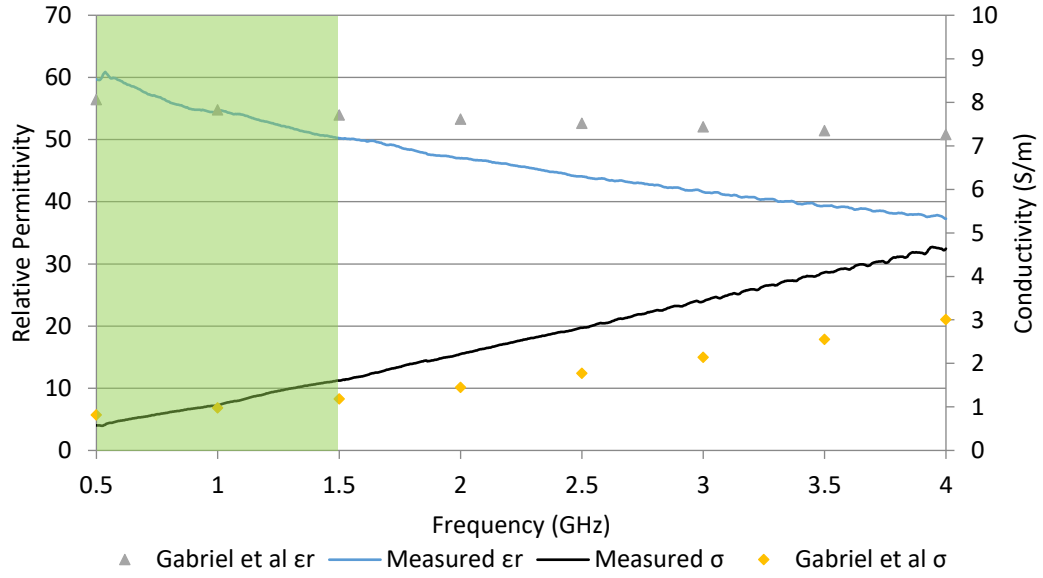

Figure 3.25: Relative permittivity and conductivity measurements compared to literature data for muscle at 0.5 to 1.5GHz according to the recipes of Table 3.4

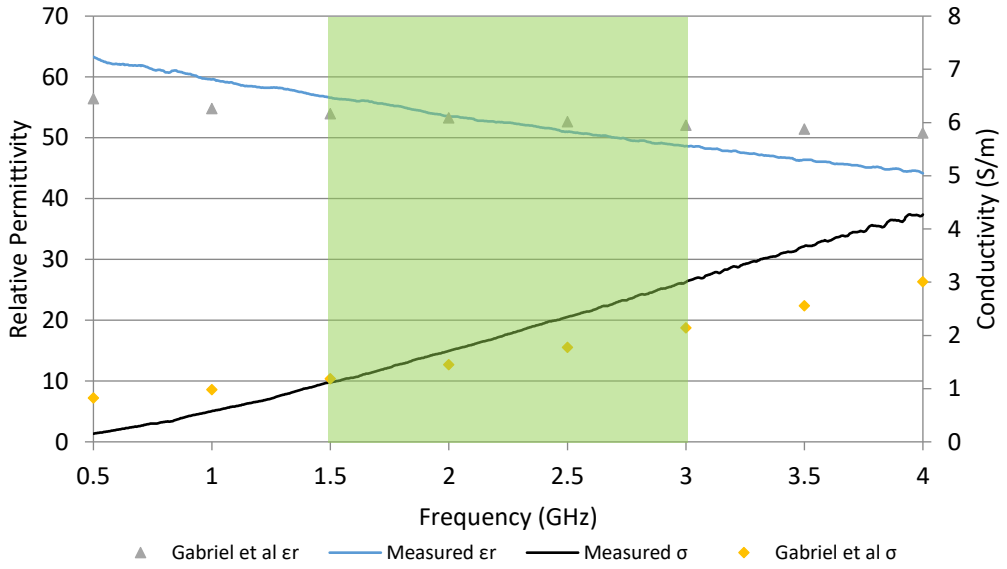

Figure 3.26: Relative permittivity and conductivity measurements compared to literature data for muscle at 1.5 to 3GHz according to the recipes of Table 3.4

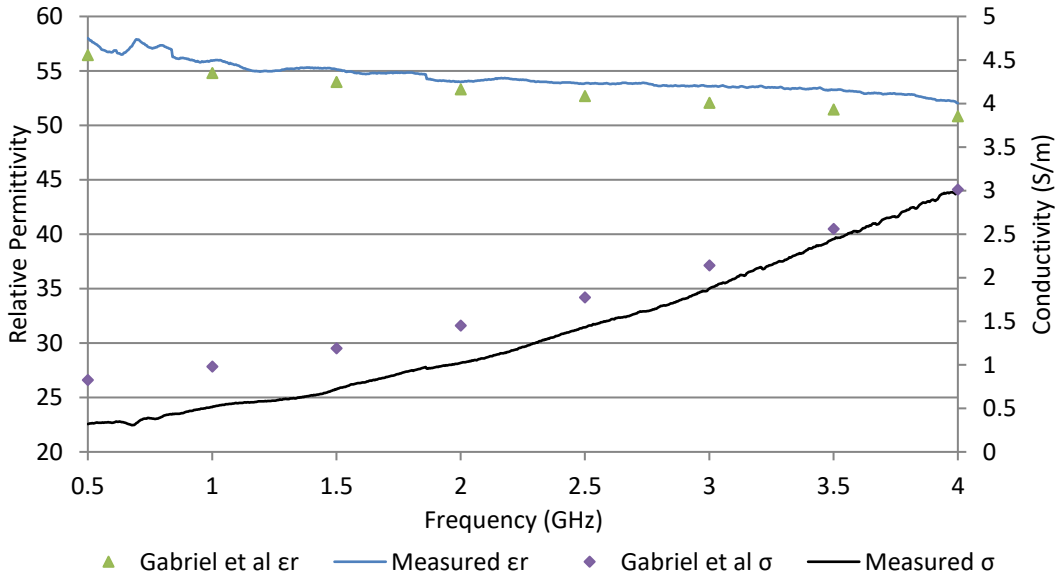

Figure 3.27: Relative permittivity and conductivity measurements compared to literature data for muscle at 0.5 to 4GHz according to the recipes of Table 3.4

Tables 3.5, 3.7, 3.9 and 3.11 describe the mean square error between the twelve phantom recipes that were presented in this section and the measurements of Gabriel et al. [11] for their real-life equivalents. Tables 3.6, 3.8, 3.10 and 3.12 describe the maximum standard deviation error between each average recipe measurement. According to the IEEE SAR measurement standard for broadband phantoms [1], the measured conductivity and relative permittivity of recipes targeted between the 0.3 – 2GHz frequency spectrum, should be within ± 5% of their real-life tissue equivalent values. For the 2 – 3GHz frequency spectrum measured conductivity should be within ± 5% and relative permittivity cannot be more than ±10% from the target values. The mean square error for ε_r and σ of the measured tissue-mimicking phantoms compared to [11] that are found at Tables 3.5, 3.7, 3.9 and 3.11, shows that the recipes of Figures 3.18, 3.21, 3.23 and 3.27 , that correspond to bone marrow, bone cortical, blood and muscle accordingly, exhibit a broadband behaviour at the frequency spectrum of 0.5 to 4GHz [57], [59], [60]. The rest of the recipes found in Figures 3.19, 3.20, 3.22 and 3.24 to 3.26 can be used in measurements where targeting a specific frequency is required.

Table 3.5: The calculated mean square error of the bone marrow phantom versus bone marrow in [11]

Bone marrow phantom	**0.5 to 0.8GHz**	**0.5 to 4GHz**	**2 to 4GHz**
Relative Permittivity	0.09	0.03	0.04
Conductivity (S/m)	0.01	0.01	0.02

Table 3.6: The maximum standard deviation error between each average measurement for the bone marrow phantom

Bone marrow phantom	**0.5 to 0.8GHz**	**0.5 to 4GHz**	**2 to 4GHz**
Relative Permittivity	0.3	0.22	0.22
Conductivity (S/m)	0.01	0.01	0.03

Table 3.7: The calculated mean square error of the bone cortical phantom versus bone cortical in [11]

Bone cortical phantom	**0.5 to 1.5GHz**	**0.5 to 4GHz**
Relative Permittivity	0.24	0.14
Conductivity (S/m)	0.02	0.01

Table 3.8: The maximum standard deviation error between each average measurement for the bone cortical phantom

Bone cortical phantom	**0.5 to 1.5GHz**	**0.5 to 4GHz**
Relative Permittivity	1	1
Conductivity (S/m)	0.03	0.06

Table 3.9: The calculated mean square error of the blood phantom versus blood in [11]

Blood phantom	**0.5 to 1.5GHz**	**1.5 to 3GHz**	**0.5 to 4GHz**
Relative Permittivity	2.77	3.41	1.29
Conductivity (S/m)	0.12	0.13	0.45

Table 3.10: The maximum standard deviation error between each average measurement for the blood phantom

Blood phantom	**0.5 to 1.5GHz**	**1.5 to 3GHz**	**0.5 to 4GHz**
Relative Permittivity	0.88	1.25	1.14
Conductivity (S/m)	0.15	0.15	0.03

Table 3.11: The calculated mean square error of the muscle phantom versus muscle in [11]

Muscle phantom	**0.5 to 1.5GHz**	**1.5 to 3GHz**	**0.5 to 4GHz**
Relative Permittivity	4.99	4.20	1.14
Conductivity (S/m)	0.06	0.43	0.06

Table 3.12: The maximum standard deviation error between each average measurement for the muscle phantom

Muscle phantom	**0.5 to 1.5GHz**	**1.5 to 3GHz**	**0.5 to 4GHz**
Relative Permittivity	0.25	0.41	2.39
Conductivity (S/m)	0.05	0.08	0.11

3.6 Conclusions

In the first part of this chapter, a literature overview was provided on the types of frequency depended tissue-mimicking phantoms that are currently available. It was highlighted that multi-material phantoms with broadband behaviour, without the undesirable mixing of their constituting ingredients is necessary for implanted antenna applications. In the second part of this chapter, twelve different tissue-mimicking phantom recipes have been developed, each approximating the dielectric properties of bone marrow, bone cortical, blood and muscle. The recipe ingredients are easy to source and the procedure for producing the materials is straight forward. The standard deviation calculations confirms the process yields highly repeatable results. The mean-square error calculation has shown that the dielectric properties of four of the proposed phantom recipes exhibited broadband behaviour at the frequency spectrum of 0.5 to 4GHz according to the IEEE standards for phantom development [1]. The rest of the recipes are narrowband and can be used in measurements where targeting a specific frequency is required. The standard deviation between the nine sets of relative permittivity and conductivity curves for the four materials can be found in Appendix B. These recipes will be used in Chapter 4 for the development of two multi-layered anatomical limb phantoms that can be used for the replication

of any bone of the human body in terms of anatomy by combining the bone marrow and bone cortical materials into an inhomogeneous bone in a muscle host.

References

[1] IEEE Standards Coordinating Committee 34, *IEEE Recommended Practice for Determining the Peak Spatial-Average Specific Absorption Rate (SAR) in the Human Head from Wireless Communications Devices: Measurement Techniques,* no. February. The Institute of Electrical and Electronics Engineers, Inc., 2003.

[2] H. P. Schwan, "Interaction of Microwave with Biological Radio Frequency Radiation Systems," *Symposium on Biological Effects and Health Implications of Microwave Radiation,* pp. 146–152, 1971.

[3] A. W. Guy, "Analyses of Electromagnetic Fields Induced in Biological Tissues by Thermographic Studies on Equivalent Phantom Models," *IEEE Transactions on Microwave Theory and Techniques,* vol. 19, no. 2. pp. 205–214, 1971.

[4] J. C. Lin, A. W. Guy, and C. C. Johnson, "Power Deposition in a Spherical Model of Man Exposed to I-20-MHz Electromagnetic Fields," *IEEE Transactions on Microwave Theory and Techniques,* vol. 21, no. 12. pp. 791–797, 1973.

[5] K. Ito, "Human Body Phantoms for Evaluation of Wearable and Implantable Antennas," *The Second European Conference on Antennas and Propagation, EuCAP 2007*. pp. 1–6, 2007.

[6] W. Xia, K. Saito, M. Takahashi, and K. Ito, "Performances of an implanted cavity slot antenna embedded in the human arm," *IEEE Transactions on Antennas and*

Propagation, vol. 57, no. 4, pp. 894–899, 2009.

[7] T. Dissanayake, K. P. Esselle, and M. R. Yuce, "Dielectric loaded impedance matching for wideband implanted antennas," *IEEE Transactions on Microwave Theory and Techniques*, vol. 57, no. 10, pp. 2480–2487, 2009.

[8] J. Kim and Y. Rahmat-Samii, "Implanted antennas inside a human body: Simulations, designs, and characterizations," *IEEE Transactions on Microwave Theory and Techniques*, vol. 52, no. 8, pp. 1934–1943, 2004.

[9] C. M. Rappaport and F. R. Morgenthaler, "Optimal Source Distribution for Hyperthermia at the Center of a Sphere of Muscle Tissue," *IEEE Transactions on Microwave Theory and Techniques*, vol. 35, no. 12. pp. 1322–1327, 1987.

[10] K. S. Nikita, G. S. Stamatakos, N. K. Uzunoglu, and A. Karafotias, "Analysis of the interaction between a layered spherical human head model and a finite-length dipole," *IEEE Transactions on Microwave Theory and Techniques*, vol. 48, no. 11. pp. 2003–2013, 2000.

[11] C. Gabriel, "Compilation of the dielectric properties of body tissues at RF and microwave frequencies," *Environmental Health*, vol. 1, pp. 1–21, 1996.

[12] "Body Tissue Dielectric Parameters | Federal Communications Commission." [Online]. Available: https://www.fcc.gov/general/body-tissue-dielectric-parameters. [Accessed: 29-Oct-2018].

[13] Bryn A. Lloyd, "Dielectric Properties » IT'IS Foundation," *Copyright © 2010–2018 IT'IS Foundation*. [Online]. Available: https://itis.swiss/virtual-population/tissue-properties/database/dielectric-properties/. [Accessed: 29-Oct-2018].

[14] P. S. Hall *et al.*, “Antennas and propagation for on-body communication systems,” *IEEE Antennas and Propagation Magazine*, vol. 49, no. 3. pp. 41–58, 2007.

[15] A. Alomainy *et al.*, “Statistical Analysis and Performance Evaluation for On-Body Radio Propagation With Microstrip Patch Antennas,” *IEEE Transactions on Antennas and Propagation*, vol. 55, no. 1. pp. 245–248, 2007.

[16] W. Blair, “Experimental verification of dipole radiation in a conducting half-space,” *IEEE Transactions on Antennas and Propagation*, vol. 11, no. 3. pp. 269–275, 1963.

[17] C. Sanchez-Fernadez *et al.*, “Dual-Band Implantable Antenna Based on Short-Circuit SRR,” *2010 Proceedings of the Fourth European Conference on Antennas and Propagation (EuCAP)*, pp. 1–4, 2010.

[18] C. Miry, R. Gillard, and R. Loison, “An application of the multi-level DG-FDTD to the analysis of the transmission between a dipole in free-space and an implanted antenna in a simplified body model with various positions,” *2009 3rd European Conference on Antennas and Propagation*, pp. 67–70, 2009.

[19] C. Miry, R. Gillard, and R. Loison, “Multi-level dual-grid finite-difference time-domain approach for the analysis of body implanted antennas,” *IET Microwaves, Antennas & Propagation*, vol. 4, no. May 2009, p. 659, 2010.

[20] C. Miry, T. Alves, R. Gillard, J. M. Laheurte, R. Loison, and B. Poussot, “Analysis of the Transmission Between On-Body Devices Using the Bilateral Dual-Grid FDTD Technique,” *IEEE Antennas and Wireless Propagation Letters*, vol. 9. pp. 1073–1075, 2010.

[21] C. Miry, T. Alves, R. Gillard, J.-M. M. Laheurte, R. Loison, and B. Poussot, “Analysis of the Transmission Between On-Body Devices Using the Bilateral Dual-Grid FDTD

Technique," *IEEE Antennas and Wireless Propagation Letters*, vol. 9, pp. 1073–1075, 2010.

[22] F. Merli, "Implantable Antennas for Biomedical Applications," PhD Thesis, Ecole Polytechnique Federale de Lausanne, 2011.

[23] D. Valderas *et al.*, "Broadband Implanted UHF RFID Antenna," *2010 IEEE Antennas and Propagation Society International Symposium (APSURSI)*, no. 1, pp. 1–4, 2010.

[24] J. Kim and Y. Rahmat-Samii, "SAR reduction of implanted planar inverted F antennas with non-uniform width radiator," in *IEEE Antennas and Propagation Society, AP-S International Symposium (Digest)*, 2006, pp. 1091–1094.

[25] J. Abadia *et al.*, "3D-spiral small antenna design and realization for biomedical telemetry in the MICS band," *Radioengineering*, vol. 18, no. 4, pp. 359–367, 2009.

[26] A. T. Mobashsher and A. M. Abbosh, "Artificial human phantoms: Human proxy in testing microwave apparatuses that have electromagnetic interaction with the human body," *IEEE Microwave Magazine*, vol. 16, no. 6, pp. 42–62, 2015.

[27] G. Hartsgrove, A. Kraszewski, and A. Surowiec, "Simulated biological materials for electromagnetic radiation absorption studies," *Bioelectromagnetics*, vol. 8, no. 1, pp. 29–36, 1987.

[28] K. Ito, K. Furuya, Y. Okano, and L. Hamada, "Development and characteristics of a biological tissue-equivalent phantom for microwaves," *Electronics and Communications in Japan (Part I: Communications)*, vol. 84, no. 4, pp. 67–77, 2001.

[29] K. Fukunaga, S. Watanabe, H. Asou, and K. Sato, "Dielectric properties of non-toxic tissue-equivalent liquids for radiowave safety tests," *IEEE International Conference on*

Dielectric Liquids, 2005. ICDL 2005. pp. 425–428, 2005.

[30] C. K. A Chou, G. W. Chen, A. W. Guy, and K. H. Luk, "Formulas for preparing phantom muscle tissue at various radiofrequencies," *Bioelectromagnetics*, vol. 5, no. 4, pp. 435–41, 1984.

[31] S. Symeonidis, W. G. Whittow, and C. Panagamuwa, "Design and characterization of a three material anatomical bone phantom for implanted antenna applications," in *Loughborough Antennas & Propagation Conference (LAPC)*, 2017, pp. 4–8.

[32] P. B. Johnson, S. R. Whalen, M. Wayson, B. Juneja, C. Lee, and W. E. Bolch, "Hybrid patient-dependent phantoms covering statistical distributions of body morphometry in the u.s. adult and pediatric population," *Proceedings of the IEEE*, vol. 97, no. 12, pp. 2060–2075, 2009.

[33] W. G. Scanlon, J. B. Burns, and N. E. Evans, "Radiowave propagation from a tissue-implanted source at 418 MHz and 916.5 MHz.," *IEEE Transactions on Bio-medical Engineering*, vol. 47, no. 4, pp. 527–34, 2000.

[34] L. C. Chirwa, P. A. Hammond, S. Roy, and D. R. S. Cumming, "Electromagnetic radiation from ingested sources in the human intestine between 150 MHz and 1.2 GHz," *IEEE Transactions on Biomedical Engineering*, vol. 50, no. 4, pp. 484–492, 2003.

[35] A. Alomainy and Y. Hao, "Modeling and Characterization of Biotelemetric Radio Channel From Ingested Implants Considering Organ Contents," *IEEE Transactions on Antennas and Propagation*, vol. 57, no. 4, pp. 999–1005, 2009.

[36] J. H. Jung, S. W. Kim, Y. S. Kim, and S. Y. Kim, "Electromagnetic propagation from the intestine-ingested source in the human body model," *IEEE Transactions on Antennas and Propagation*, vol. 58, no. 5, pp. 1683–1688, 2010.

[37] L. Xu and M. Q. H. Meng, “Effects of dielectric parameters of human body on specific absorption rate for Ingestible Wireless Device at operating frequency of 430 MHz,” *IEEE/ASME International Conference on Advanced Intelligent Mechatronics, AIM*, vol. 56, no. 8, pp. 215–220, 2009.

[38] P. Dimbylow, T. W. Dawson, K. Caputa, and M. A. Stuchly, “Current densities in a 2 mm resolution anatomically realistic model of the body induced by low frequency electric fields,” *Physics in Medicine and Biology*, vol. 45, pp. 1013–1022, 2000.

[39] I. G. Zubal, C. R. Harrell, E. O. Smith, Z. Rattner, G. Gindi, and P. B. Hoffer, “Computerized three-dimensional segmented human anatomy,” *Medical Physics*, vol. 21, no. 2, pp. 299–302, Feb. 1994.

[40] “Center for NMR Research – Penn State College of Medicine Research.” [Online]. Available: https://research.med.psu.edu/departments/center-for-nmr-research/. [Accessed: 06-Jul-2017].

[41] Z. N. Chen, G. C. Liu, and T. S. P. See, “Transmission of RF signals between MICS loop antennas in free space and implanted in the human head,” *IEEE Transactions on Antennas and Propagation*, vol. 57, no. 6, pp. 1850–1854, 2009.

[42] M. Z. Azad and M. Ali, “A miniature implanted inverted-F antenna for GPS application,” *IEEE Transactions on Antennas and Propagation*, vol. 57, pp. 1854–1858, 2009.

[43] T. Nagaoka *et al.*, “Development of realistic high-resolution whole-body voxel models of Japanese adult males and females of average height and weight, and application of models to radio-frequency electromagnetic-field dosimetry,” *Physics in Medicine and Biology*, vol. 49, no. 1, pp. 1–15, 2004.

[44] T. Nagaoka and S. Watanabe, “Postured voxel-based human models for electromagnetic dosimetry,” *Physics in Medicine and Biology*, vol. 53, no. 24, pp. 7047–61, 2008.

[45] A. Sani, A. Alomainy, and Y. Hao, “Numerical Characterization and Link Budget Evaluation of Wireless Implants Considering Different Digital Human Phantoms,” *IEEE Transactions on Microwave Theory and Techniques*, vol. 57, no. 10. pp. 2605–2613, 2009.

[46] A. Christ *et al.*, “The Virtual Family—development of surface-based anatomical models of two adults and two children for dosimetric simulations,” *Physics in Medicine and Biology*, vol. 55, no. 2, pp. N23–N38, 2010.

[47] E. Y. Chow, C.-L. Yang, A. Chlebowski, W. J. Chappell, and P. P. Irazoqui, “Miniature antenna for RF telemetry through ocular tissue,” *2008 IEEE MTT-S International Microwave Symposium Digest*, pp. 1309–1312, 2008.

[48] M. Khan, S. P. S. M. A. Sirdeshmukh, and K. Javed, “Evaluation of bone fracture in animal model using bio-electrical impedance analysis,” *Perspectives in Science*, vol. 8, pp. 567–569, 2016.

[49] T. Yoshida, W.-C. Kim, K. Kawamoto, T. Hirashima, Y. Oka, and T. Kubo, “Measurement of bone electrical impedance in fracture healing.,” *Journal of Orthopaedic Science*, vol. 14, no. 3, pp. 320–329, 2009.

[50] T. Yoshida, W.-C. Kim, Y. Oka, N. Yamada, and T. Kubo, “Assessment of distraction callus in rabbits by monitoring of the electrical impedance of bone.,” *Acta Orthopaedica*, vol. 81, no. 5, pp. 628–633, 2010.

[51] J. L. Damez, S. Clerjon, S. Abouelkaram, and J. Lepetit, “Beef meat electrical impedance spectroscopy and anisotropy sensing for non-invasive early assessment of

meat ageing," *Journal of Food Engineering*, vol. 85, no. 1, pp. 116–122, 2008.

[52] T. Karacolak, A. Z. Hood, and E. Topsakal, "Design of a dual-band implantable antenna and development of skin mimicking gels for continuous glucose monitoring," *IEEE Transactions on Microwave Theory and Techniques*, vol. 56, no. 4, pp. 1001–1008, 2008.

[53] R. King, S. Prasad, and B. Sandler, "Transponder antennas in and near a three-layered body," *Microwave Theory and Techniques*, vol. 28, no. 6, pp. 586–596, 1980.

[54] A. O. Alamoudi, S. Almari, S. Zhu, and R. J. Langley, "Improved Performance of 2.45 GHz Implanted Antenna for Wireless Communication," in *IEEE Asia-Pacific Conference on Applied Electromagnetics*, 2012, pp. 308–312.

[55] S. Almari, R. J. Langley, and A. O. Alamoudi, "Improved Performance of 2.45 GHz Implanted Patch Antenna for Wireless Communication," in *(LAPC) Loughborough Antennas & Propagation Conference*, 2013, pp. 27–30.

[56] "EM Phantoms," *Schmid & Partner Engineering AG*, 2018. [Online]. Available: https://www.speag.com/products/em-phantom/overview/. [Accessed: 03-May-2018].

[57] A. Sani, M. Rajab, R. Foster, and Y. Hao, "Antennas and Propagation of Implanted RFIDs for Pervasive Healthcare Applications," *Proceedings of the IEEE*, vol. 98, no. 9, pp. 1648–1655, 2010.

[58] Y. Okano, K. Ito, I. Ida, and M. Takahashi, "The SAR Evaluation Method by a Combination of Thermographic Experiments and Biological," *IEEE Trans. Microw. Theory Tech.*, vol. 48, no. 11, pp. 2094–2103, 2000.

[59] T. Yilmaz, R. Foster, and Y. Hao, "Broadband Tissue Mimicking Phantoms and a Patch

Resonator for Evaluating Noninvasive Monitoring of Blood Glucose Levels," *IEEE Transactions on Antennas and Propagation*, vol. 62, no. 6, pp. 3064–3075, 2014.

[60] R. Augustine, S. Raman, and A. Rydberg, "Microwave Phantoms For Craniotomy Follow-Up Probe Development," in *2014 IEEE Conference on Antenna Measurements & Applications (CAMA)*, 2014.

[61] J. L. Salager, A. M. Forgiarini, and J. Bullón, "How to attain ultralow interfacial tension and three-phase behavior with surfactant formulation for enhanced oil recovery: A review. Part 1. Optimum formulation for simple surfactant-oil-water ternary systems," *Journal of Surfactants and Detergents*, vol. 16, no. 4, pp. 449–472, 2013.

[62] D. M. Hagl, D. Popovic, S. C. Hagness, J. H. Booske, and M. Okoniewski, "Sensing volume of open-ended coaxial probes for dielectric characterization of breast tissue at microwave frequencies," *IEEE Transactions on Microwave Theory and Techniques*, vol. 51, no. 4 I, pp. 1194–1206, 2003.

[63] T. P. Marsland and S. Evans, "Dielectric measurements with an open-ended coaxial probe," *IEEE Proceedings in Microwaves, Antennas and Propagation*, vol. 134, no. 4, p. 341, 1987.

[64] C. J. Panagamuwa, I. Howells, and W. G. Whittow, "Conductivity and permittivity measurements of children and adult's hands covering mobile communications frequency bands," in *Progress In Electromagnetics Research Symposium (PIERS)*, 2013, pp. 1–5.

[65] H. P. Schwan, R. J. Sheppard, and E. H. Grant, "Complex permittivity of water at 25°C," *The Journal of Chemical Physics*, vol. 64, no. 5, pp. 2257–2259, 1976.

[66] V. Komarov, S. Wang, and J. Tang, "Permittivity and Measurements," *Encyclopedia of RF and Microwave Engineering*, pp. 1–19, 2005.

[67] M. Wolf, R. Gulich, P. Lunkenheimer, and A. Loidl, “Broadband dielectric spectroscopy on human blood.,” *Biochimica et Biophysica Acta*, vol. 1810, pp. 727–740, 2011.

[68] M. H. Moussa, M. A. Abu-Khousa, and N. N. Qaddoumi, “Measurement of liquids dielectric property using monopole probes operating at microwave frequencies,” *Proceedings of the IEEE International Conference on Electronics, Circuits, and Systems*, vol. 3, pp. 1204–1207, 2003.

[69] R. W. Lau and C. Gabriel, “The dielectric properties of biological tissues: III. Parameteric models for the dielectric spectrum of tissues,” *Physics in Medicine and Biology*, vol. 41, pp. 2271–2293, 1996.

Chapter 4

Evaluation of two geometrical multi-layer phantoms

4.1 Summary

Chapter 3 developed the recipes to make solid tissue emulating materials. In this chapter the development and testing of two geometrical human body phantoms based on the recipes that were investigated in Chapter 3 is presented. The first is a two material phantom consisting of bone cortical and muscle layers simulated in Section 4.2 and measured in Section 4.3. The second is a three material geometrical phantom consisting of bone marrow, bone cortical and muscle layers simulated and measured in Sections 4.4 and 4.5 accordingly. A specific absorption rate (SAR) evaluation of the test-bed according to the USA [1], Canada [2] and European Union [3] standards was conducted in Section 4.6. In Section 4.7 the realizations of two versions of the proposed external medical metal plate are presented and their load bearing capabilities investigated using the Solidworks 3D CAD simulator. Finally, the concluding remarks of this Chapter can be found in Section 4.8.

4.2 Simulation of a two layer anatomical phantom

The geometrical characteristics of the bone layer presented in this chapter can be adjusted to fit the geometry of any desired bone in the human body. The bone marrow and bone cortical materials of the presented phantoms have cylindrical shapes and their diameters are the same with the average diameter of a real-life femur bone found in [4]. Multi-material phantoms, such

as the phantoms presented in this chapter, are used when the performance of an implanted radiator with respect to the surrounding tissues is investigated [5]. These types of phantoms usually consist of bone, fat, and muscle layers and their development requires the combination of multiple recipes and can offer a detailed representation of the investigated body part in terms of geometry and electromagnetic characteristics [6]–[8]. The suitability of the phantom has been tested by comparing the results of S_{11} and S_{21} of simulations and measurements of an implanted two-monopole test-bed.

CST Microwave Studio® [9] was used for the simulations of Sections 4.2 and 4.4. The permittivity and conductivity of the simulated phantom materials were frequency dependent and the recipes presented in Chapter 3 that mimick Gabriel's measurements [10] over the frequency range of 0.5 to 4GHz were used to develop them. The dimensions of the muscle layer were 8.5 × 17 × 23cm ($H \times W \times L$). The bone cortical cylinder centred in the muscle layer was 12cm long with 4cm diameter. An antenna test bed consisting of two monopoles was simulated for the investigation of the electromagnetic wave propagation inside the phantom. The same antenna test bed will be used in Chapter 5 where bone fracture monitoring is addressed. The monopoles were implanted into the bone and muscle layers of the simulated two layer phantom. The length of each monopole was 4cm. The monopoles' groundplanes sat at the bottom of the phantom and were in free-space. The dimensions of the groundplanes were chosen to be 8 × 9.5cm (see Figure 4.1a) in order to achieve good support of the monopoles perpendicularly along the bone axis. The groundplanes were attached to the parts of the monopoles that were exposed on the surface of the phantom (see Figure 4.1b). The two groundplanes were covered in plastic tape and were separated from each other by 0.4cm. The monopoles, also covered in plastic tape, were separated from each other by 2cm as it was found to be within the spectrum of screw separation distances in real-life applications of metal plates [11]–[14]. Achieving a

2cm distance between the conductors required the monopoles to be placed 0.8cm off the edge of the ground plane in the x-axis (see Figure 4.1a).

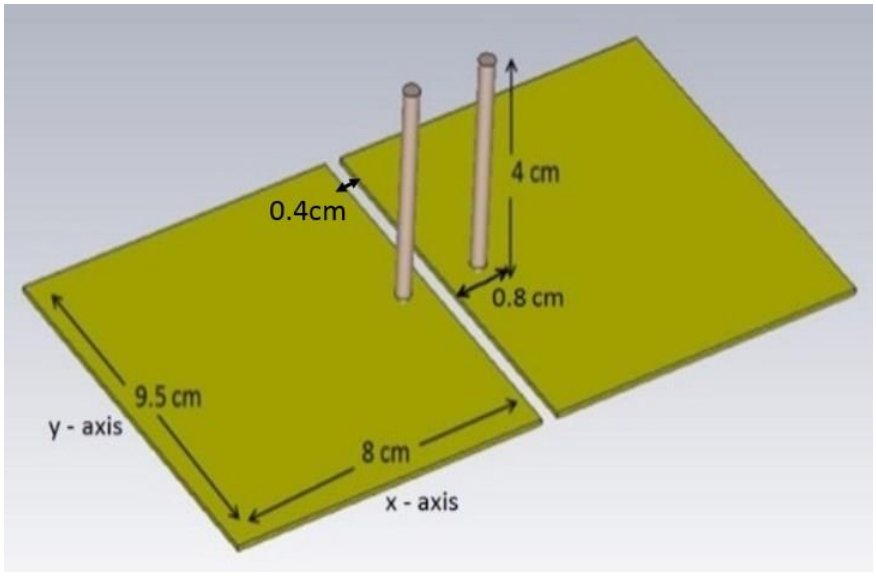

a)

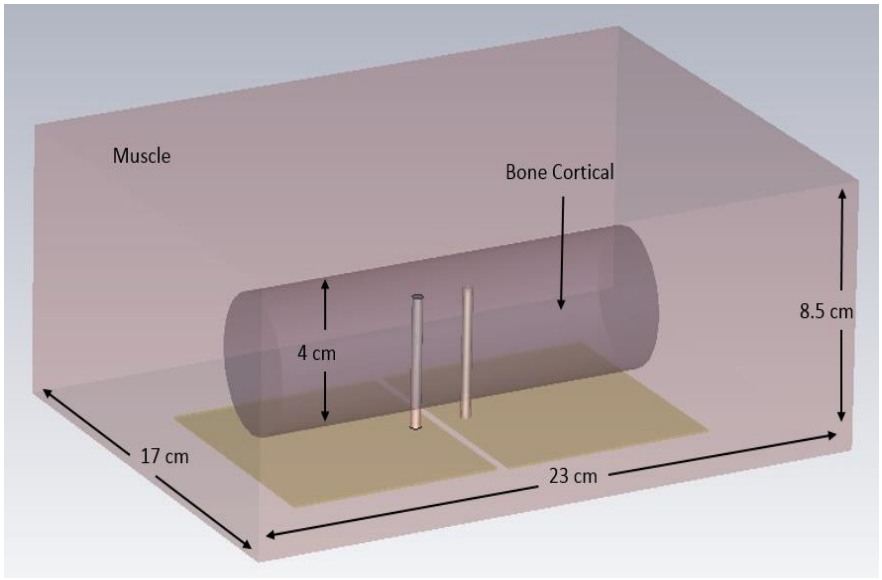

b)

Figure 4.1: a) The two monopole test bed; b) the monopoles in the simulated two material phantom

4.3 Measurement results using a two material phantom

Using the recipes presented in Chapter 3, the phantom layers of bone cortical and muscle were developed (see Table 4.1). Bone cortical was designed to be solid, while muscle had a semi-solid form.

The diameter of bone cortical was 4cm and had a length of 12cm. The dimensions of the muscle layer were 17 × 23cm and 8.5cm high. An area on the top surface at the centre of the muscle layer with dimensions of 4 × 4 × 12cm ($H \times W \times L$) was removed in order to create space for the placement of the bone layer. After the bone layer was in position, the remaining air gaps in the area were carefully filled with parts of the previously removed muscle layer.

Table 4.1: Tissue-mimicking recipes used for the development of the two material phantom

Ingredient (g)	**Bone Cortical**	**Muscle**
Flour	80	-
Oil	30	31
Deionized water	10.5	200
Food colouring	-	-
Sugar	7.2	-
Detergent	-	31

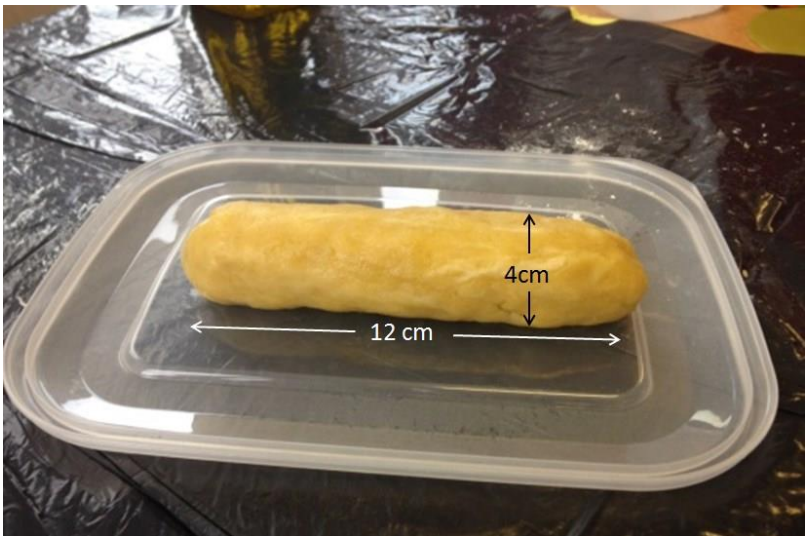

(a)

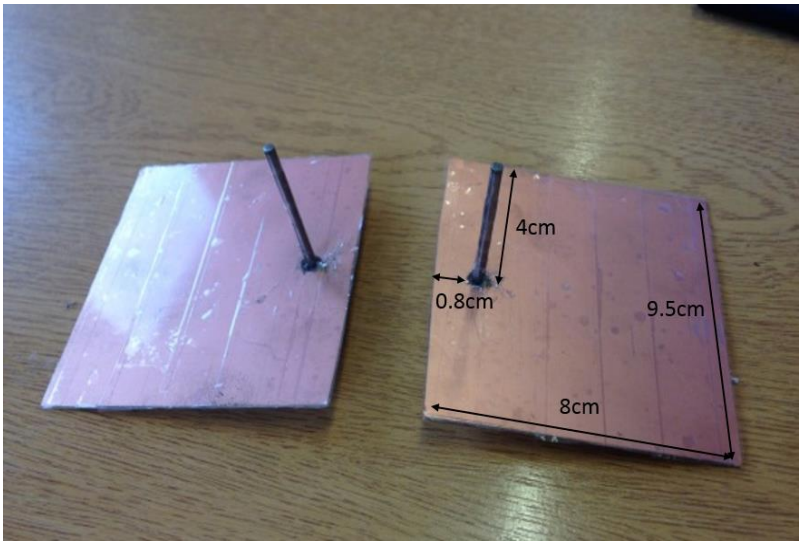

(b)

Figure 4.2: a) Bone cortical layer b) monopole implants

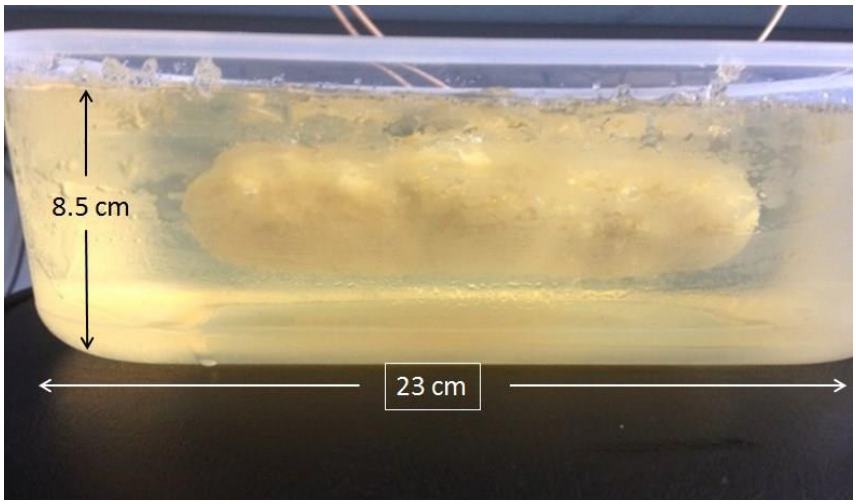

(a)

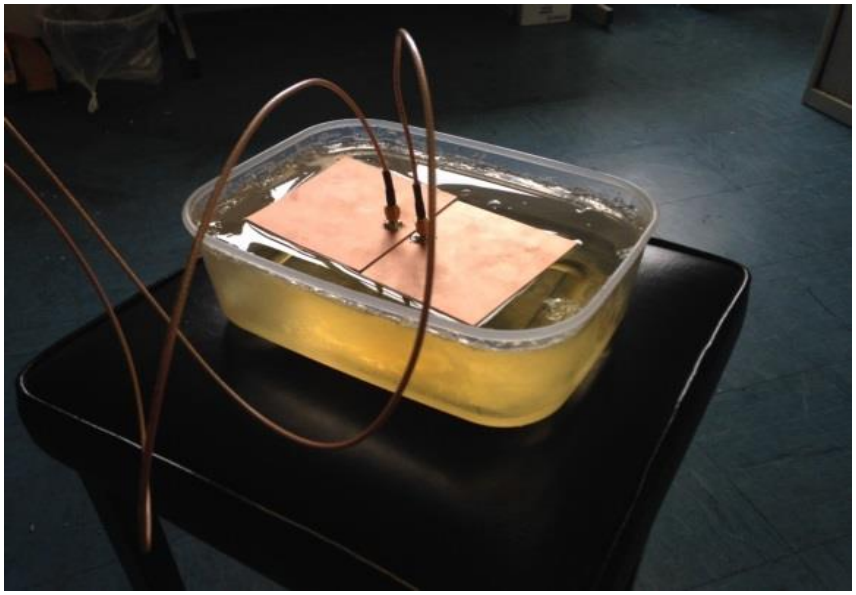

(b)

Figure 4.3: a) Muscle and bone cortical layers b) monopoles implanted into the two-material phantom

Two identical monopoles were implanted on top of the phantom into the bone layer (see Figure 4.2 and Figure 4.3). Two stainless steel rods were used as wire parts of the monopoles coated with a 0.05cm layer of plastic tape to avoid direct contact with the high losses of the muscle layer, and two copper sheets 0.2cm thick were chosen as groundplanes.

Figure 4.4 and Figure 4.5 show the S_{11} and S_{21} comparison of simulated and measured results accordingly. In order to highlight the effect of the channel of propagation inside the phantom, the effect of any mismatch issues has been removed from the S_{21} plot by normalizing it with the S_{11} using the function $\text{Norm}_{S_{21}} = \frac{|S_{21}|}{\sqrt{1-|S_{11}|^2}}$. All calculations were conducted with S_{11} and S_{21} in linear form. Some disagreement can be observed mainly due to each developed recipe's dielectric properties' minor deviation from the simulated body tissue properties provided by the CST microwave studio® above and below the 3GHz frequency point.

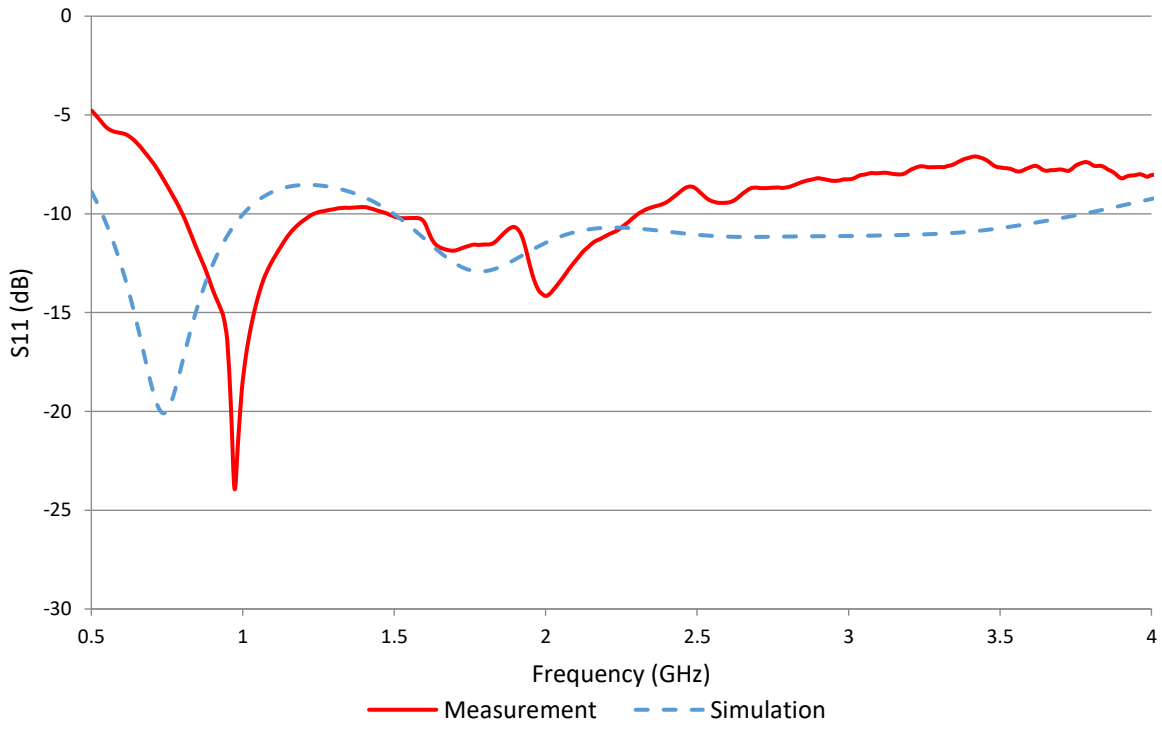

Figure 4.4: Simulated and measured S_{11} of the implanted monopoles inside the two-material phantom

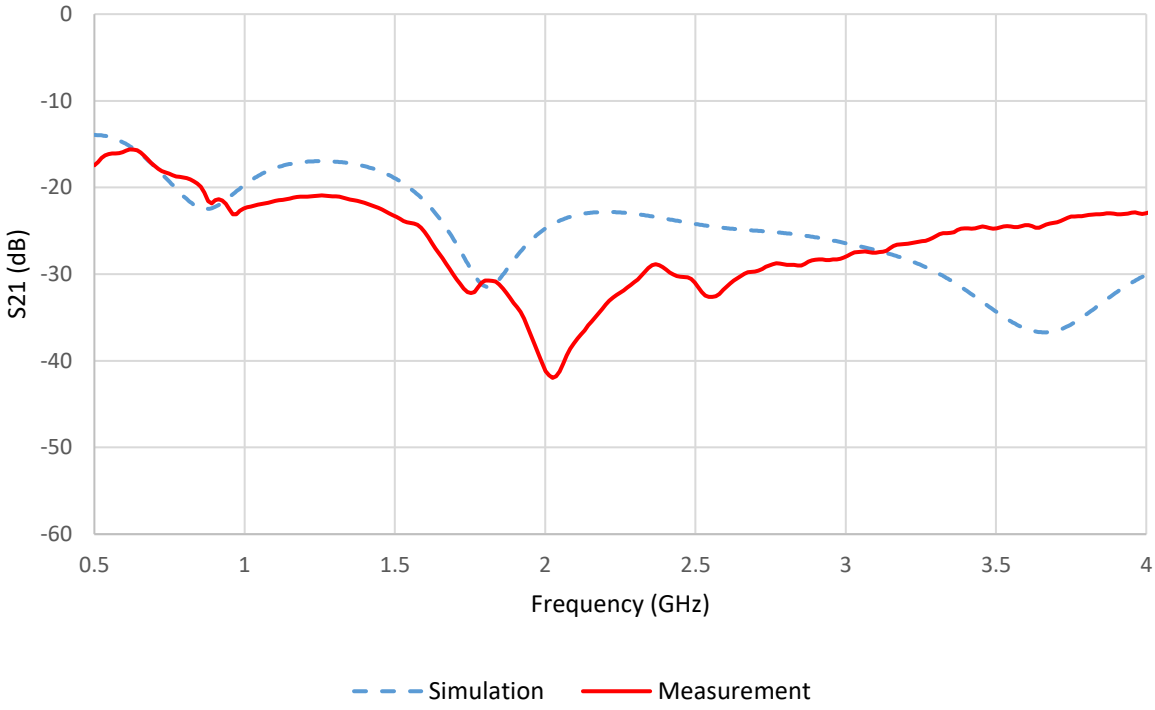

Figure 4.5: Simulated and measured $S_{21}$of the implanted monopoles inside the two-material phantom normalized with S_{11}

One more aspect of consideration is the difficulty in the execution of each of these measurements due to the fragile connection that is formed between the conducting part of each monopole and its groundplane, being a result of the thinness of the connector pin of the SMA launcher. In the occasion that the monopoles are forced into the bone layer, there is a high chance that the connection will fall apart. A solution to this issue is suggested in Section 4.7 of this chapter where two modified external medical metal plates are presented featuring the monopole test-bed and their load bearing capabilities are investigated using the Solidworks 3D CAD simulator.

To further validate the measurement results of Section 4.3, the experiment was repeated in a three material phantom consisting of bone marrow, bone cortical and muscle layers in Sections 4.4 and 4.5.

4.4 Simulation of a three layer anatomical phantom

The dimensions selected for the simulations of the muscle layer were the same as the muscle layer used in Sections 4.2 and 4.3. The bone cortical and bone marrow cylinders were 12cm long and had diameters of 4 cm and 2 cm respectively. The same monopole setup presented in Section 4.2 was used for the simulations of the S_{11} and S_{21} of the three layer anatomical phantom. The complete simulation model is given in Figure 4.6.

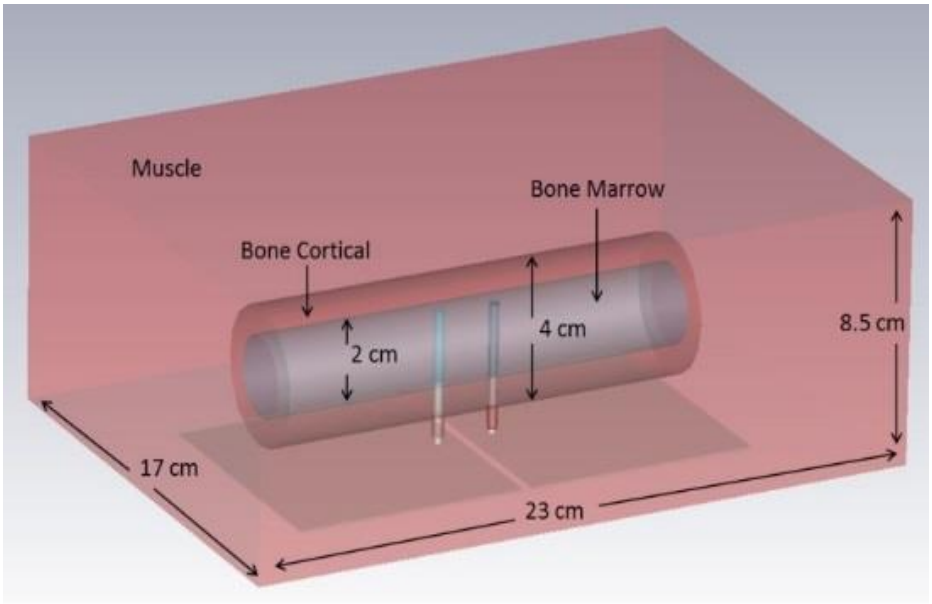

Figure 4.6: The monopoles in the simulated three layer phantom

4.5 Measurement setup using a three-material phantom

For the measurements section, the bone consisted of two layers, bone marrow and bone cortical. The bone cortical layer was flattened to a thickness of 1cm and wrapped around the bone marrow layer (see Figure 4.6). The diameter of the final bone was 4 cm and had a length of

12cm. The dimensions of the muscle layer were 17 × 23cm and 8.5cm high and the same process of inserting the bone into the muscle phantom as in Section 4.3 was followed.

Table 4.2: Tissue-mimicking recipes used for the development of the three-material phantom

Ingredient (g)	**Bone Marrow**	**Bone Cortical**	**Muscle**
Flour	80	80	-
Oil	33	30	31
Deionized water	3	10.5	200
Food colouring	1	-	-
Sugar	-	7.2	-
Detergent	-	-	31

In the same manner as the experiment presented in Section 4.3, the two monopoles were inserted through the top of the muscle into the bone layer (see Figure 4.8). Their geometry and separation distance was the same as in Section 4.3. A 0.05cm layer of plastic tape was wrapped once again around the monopoles and stuck to the grounplanes in order to avoid short circuiting with the highly conductive muscle layer.

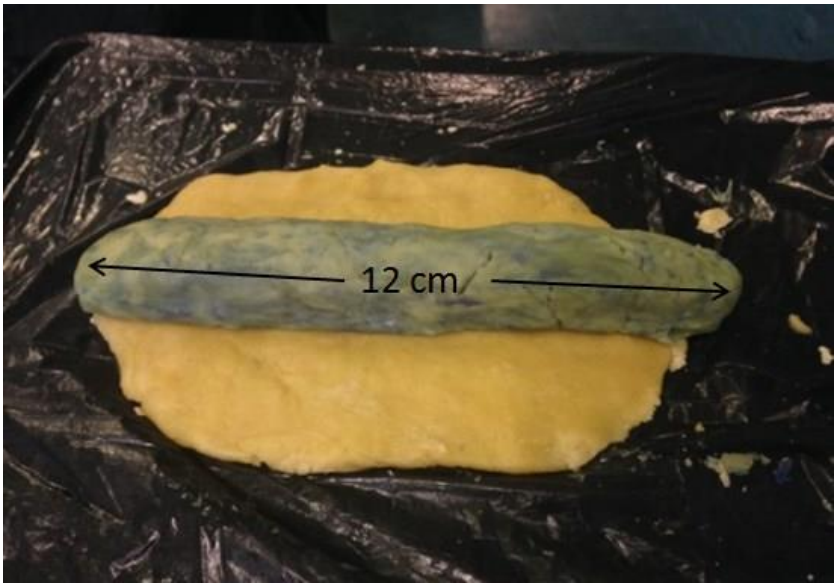

(a)

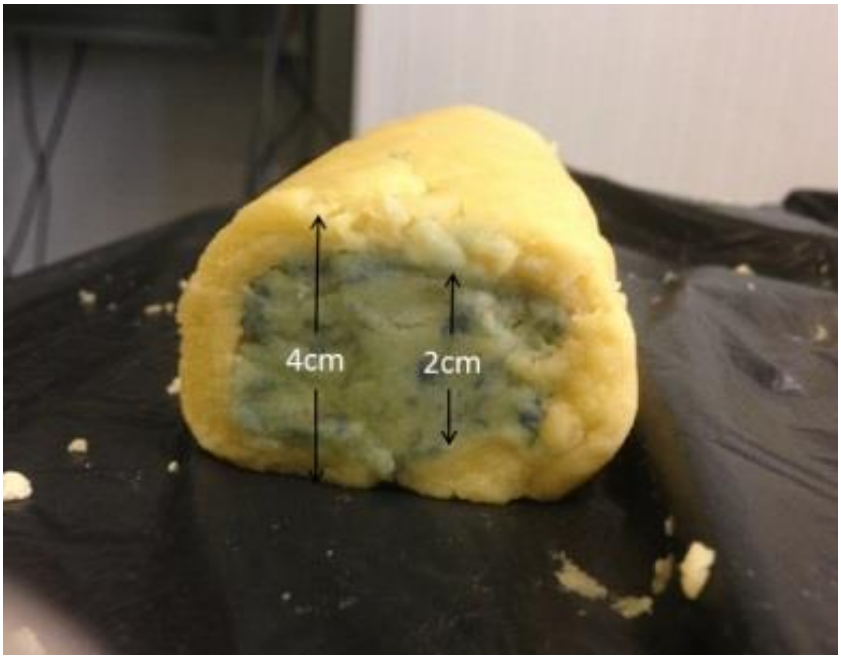

(b)

Figure 4.7: a) Bone marrow and bone cortical (flattened) b) Bone cortical wrapped around bone marrow

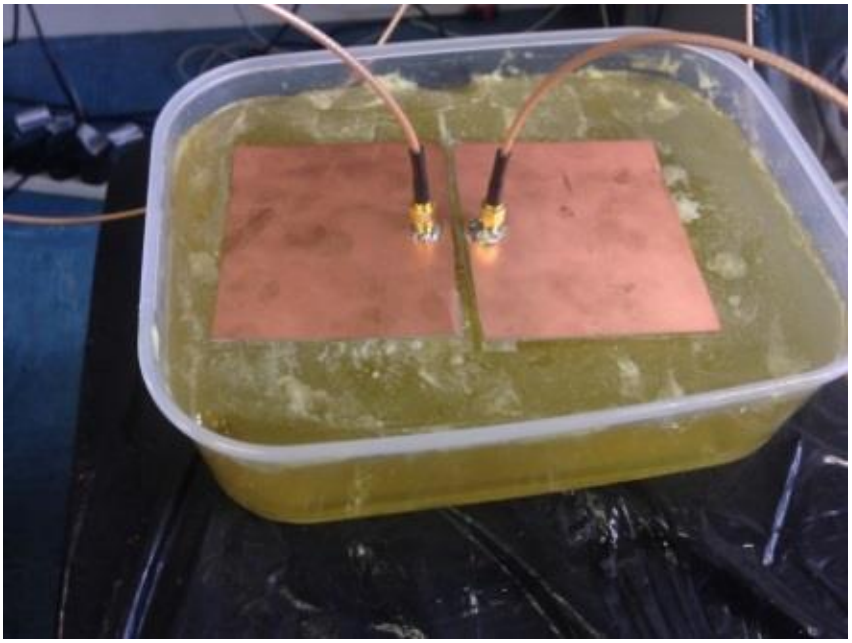

Figure 4.8: Monopoles implanted into the three layer phantom

Figure 4.9 and Figure 4.10 show that there is good agreement in the S_{11} and S_{21} between the simulated and the measured phantom. This is due to the precise replication of the simulated geometry into the measured test-bed that offered a good match between the simulated and the measured power transfer of the two monopoles. Some small deviation of the measured scattering parameters is expected due to the unwanted mixing of the ingredients in the contact area among the layers of the phantom. Yet, due to the high amount of gelatine used for the development of the muscle recipe, these effects are minimal. However, due to the different dielectric properties of each of the materials of the phantom, it is possible for an amount of the propagated wave to be diffracted or reflected at the point of interface between the tissues of the phantom; this effect can cause minor disagreement between the simulated and measured S_{11} and S_{21}. An important aspect that will be addressed in Chapter 5 is the necessity for an insulation improvement for the monopoles that will ensure adequate isolation of their wire parts in occasions where liquids are introduced inside the phantom while achieving better support of the antenna and the SMA launcher.

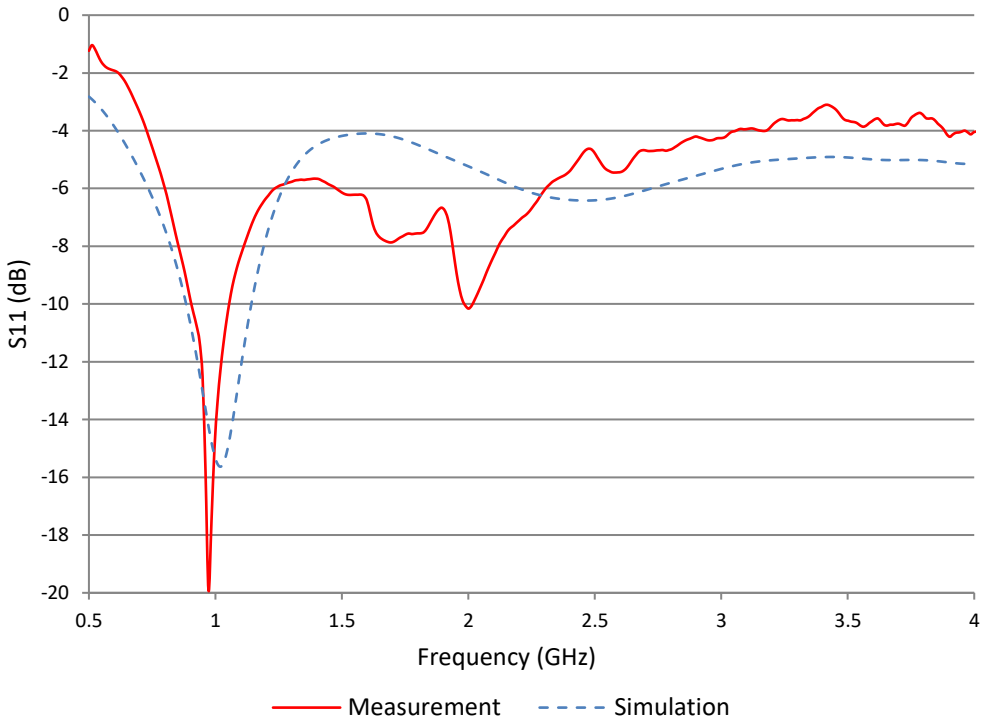

Figure 4.9: Simulated and measured S_{11} of the implanted monopoles inside the three-material phantom

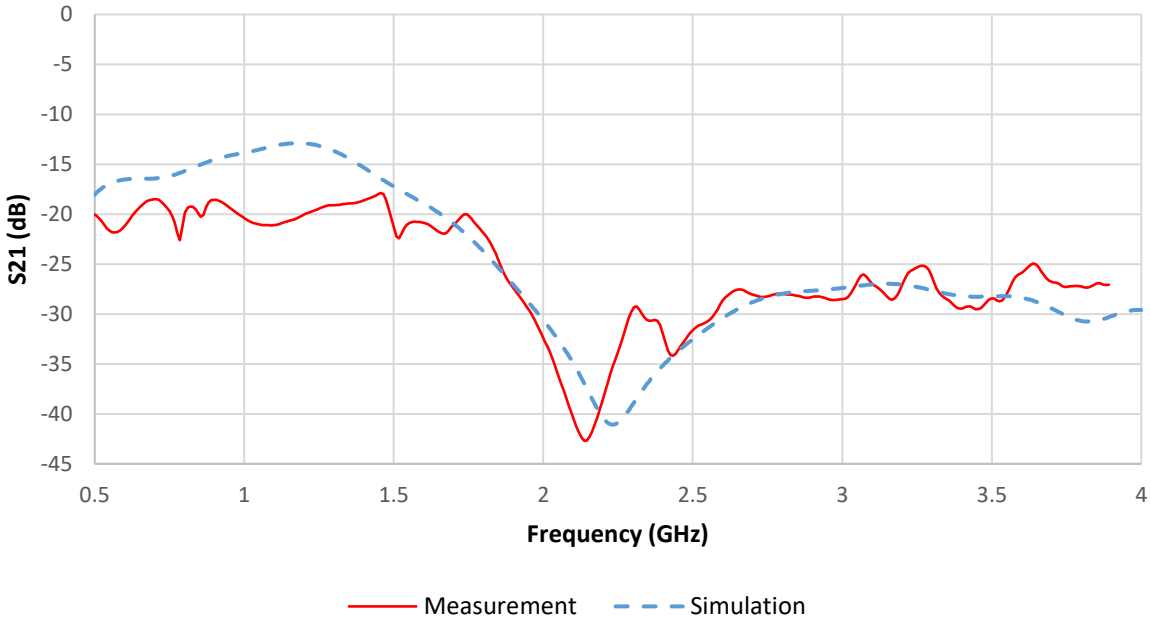

Figure 4.10: Simulated and measured S_{21} of the implanted monopoles inside the three-material phantom normalized with S_{11}

4.6 SAR evaluation of the implanted monopoles inside a three material phantom

According to [15], the power absorbed in the body must be limited to minimize possible adverse health effects This is directly correlated with SAR at the frequency spectrum of 30MHz to 6GHz [16]. SAR is defined as the amount of energy absorption by the human body when exposed to an EM wave and is calculated by:

$$\text{SAR} = \frac{\sigma|E|^2}{p} \text{ (W/kg)} \tag{4.1}$$

Where σ the conductivity of the tissue, p the mass density of the tissue and E the RMS value of the induced electric field. According to equation (4.1) the conductivity of the tissue is directly related to the absorption of the EM wave. Thus, as the conductivity increases throughout the frequency spectrum, the absorption of the EM wave is expected to increase. Accordingly, tissues such as the muscle, that have high losses, are expected to have a higher SAR value compared to bone that has lower losses in any frequency [17].

The purpose of this thesis is to investigate the possibility of monitoring bone fractures in areas of the human body where doctors use external metal plates for treatment. These areas are the human limbs, such as: The arms, the legs and the fingers, thus, all of the phantoms investigated throughout this thesis are limb phantoms. The electromagnetic exposure of human limbs, and the human body in general, with microwave fields leads to an uneven distribution of electromagnetic power. This is due to the multitude of tissue layers in the investigated areas that have different complex permittivity values [18] and thicknesses. Therefore, it is possible that the RF power of the implanted antennas can be unevenly distributed in locations with high electric or magnetic field strengths [19].

According to the International Commission on Non-Ionizing Radiation Protection (ICNIRP) the SAR values are averaged for any period of exposure that is over 6 minutes [19]. It is important to note that the realization of the proposed monopole test bed into an external metal plate will act as a metal plate that enhances support of the bone fragments continuously but will be fed by a power source only at the time of measurement of the scattering parameters. To the authors' best knowledge, connecting two monopoles with an already calibrated vector network analyser and measuring the scattering parameters does not require more than two minutes for a trained operator. With respect to the health and safety regulations for SAR limits, even though the exposure of a patient to EM field radiation cannot exceed this two minute period, the standard SAR limit (6 minute period interval) will be considered. The average localized SAR value for limb measurements for general public exposure is 4W/kg per 10g in the USA, Canada and the European Union [1]–[3]. The 10g average localised SAR has been investigated for two selected frequencies, the 0.5GHz that is the lowest frequency of operation of the antenna test bed where the EM field has the highest penetration potential in the tissues; and at 4GHz that is the highest frequency and the overall conductivity of the phantom has the highest value, thus SAR is expected to be maximum. Figure 4.11 and Figure 4.12 show the average localized SAR at 0.5GHz and 4GHz respectively for the feeding power of 0.3W. The phantom that was used for the SAR simulation was the two material phantom that was simulated in Section 4.2 as all of the real life equivalents of the investigated limbs in the rest of this thesis consist only of bone cortical and do not have bone marrow.

The 0.5GHz frequency band is much lower than the 4GHz. Therefore, the wavelength of the current at 0.5GHz is larger than at 4GHz, $\lambda_{0.5GHz}$= 8cm, λ_{4GHz}= 1cm inside the muscle, for $\lambda = \lambda_{vacuum} \Big/ \sqrt{\varepsilon_{r\ muscle}}$. As expected, it can be observed that the EM field has more penetration into the phantom at 0.5GHz compared to 4GHz. In addition to that, the losses of the two

channels of propagation inside the phantom (bone and muscle) are much lower at 0.5GHz compared to 4GHz, $\sigma_{muscle} = 0.82\ S/m$ and $\sigma_{bone} = 0.10\ S/m$ at 0.5GHz and $\sigma_{muscle} = 3.01\ S/m$ and $\sigma_{bone} = 0.72\ S/m$ at 4GHz. Thus, the propagated wave inside the muscle attenuates more than the propagated wave inside the bone and the overall wave attenuation inside the phantom increases as the frequency increases. It is worth mentioning that the SAR values are much below the allowed safety limit recommended by the standards.

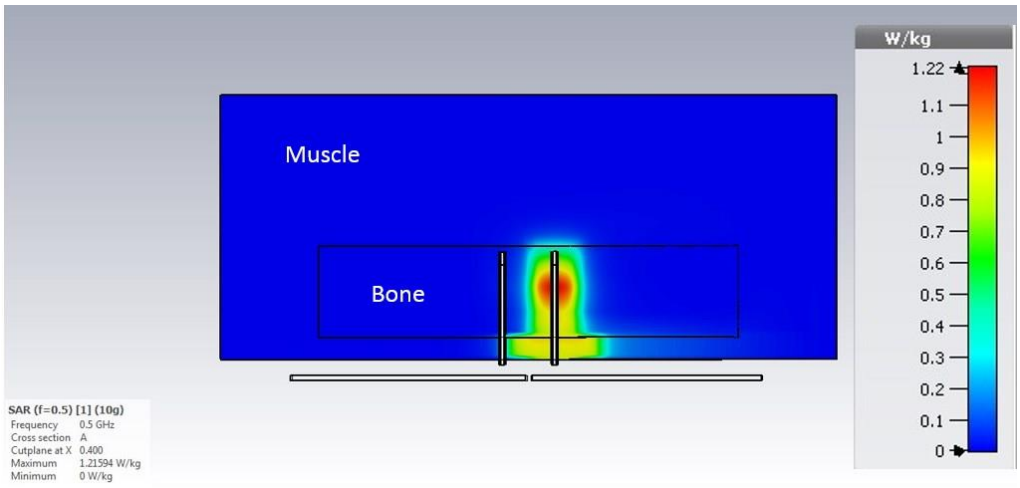

Figure 4.11: 10g SAR simulation at the frequency of 0.5GHz for 0.3W of feeding power

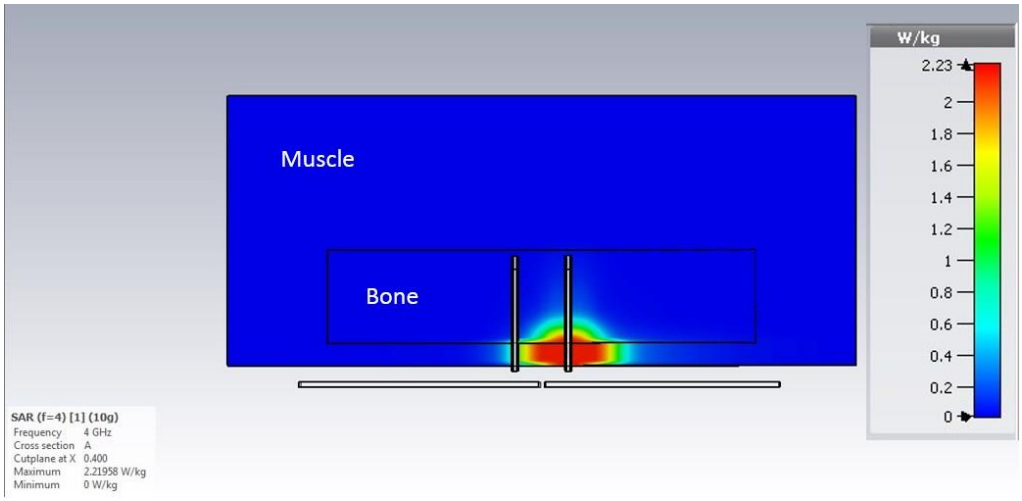

Figure 4.12: 10g SAR simulation at the frequency of 4GHz for 0.3W of feeding power

4.7 CAD model of the external medical metal plate

An important aspect for the integration of the proposed monopole antennas into an existing external medical metal plate is the amount of load that the plate is required to withstand in order to provide adequate support for the bone fragments after its application in real life situations. According to [20] for external fixators that are removed after the limb has been declared fixed such as the one proposed in this thesis, these forces can be up to 30N. Therefore, due to the thinness of the SMA launcher pin (1mm diameter) of the monopoles, it is necessary to use additional support in order to increase the plate's load bearing capability.

Two types of metal plates based on real life external metal plates found in [21] were modified in order to feature the embedded monopoles. The modified metal plates were simulated using the Solidworks 3D CAD design software. The material used for both types was surgical steel 316, which is the most used material for internal and external metal plates and screws [12]. Type A utilized the monopoles of Figure 4.1a that were connected to a 9cm coaxial cable that was embedded to an external fixator bar. In real life metal plates, the supportive clamps are used for the support of the screws perpendicularly to the external fixator bar and can adjust the distance between the screws and the distance between the skin and the external fixator bar (see Figure 4.13). A rectangular piece of Polyvinyl chloride (PVC) plastic with dimensions of 0.5 × 1 × 4cm ($H \times W \times L$) was attached to each groundplane and was envisioned to be used for the support of the monopoles in perpendicular position in real-life situations.

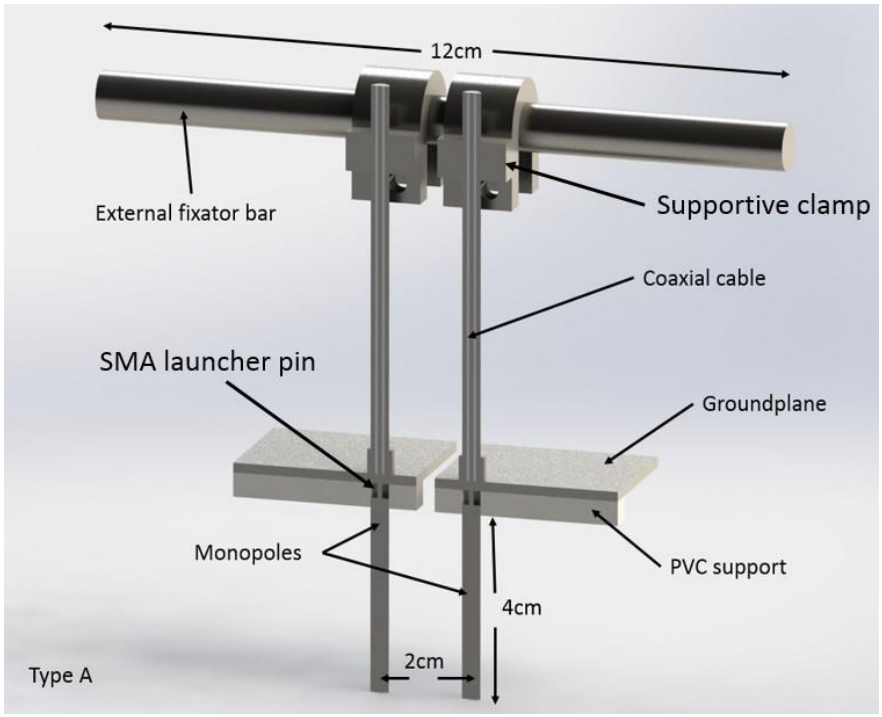
12cm
External fixator bar
Supportive clamp
Coaxial cable
SMA launcher pin
Groundplane
Monopoles
PVC support
4cm
2cm
Type A

(a)

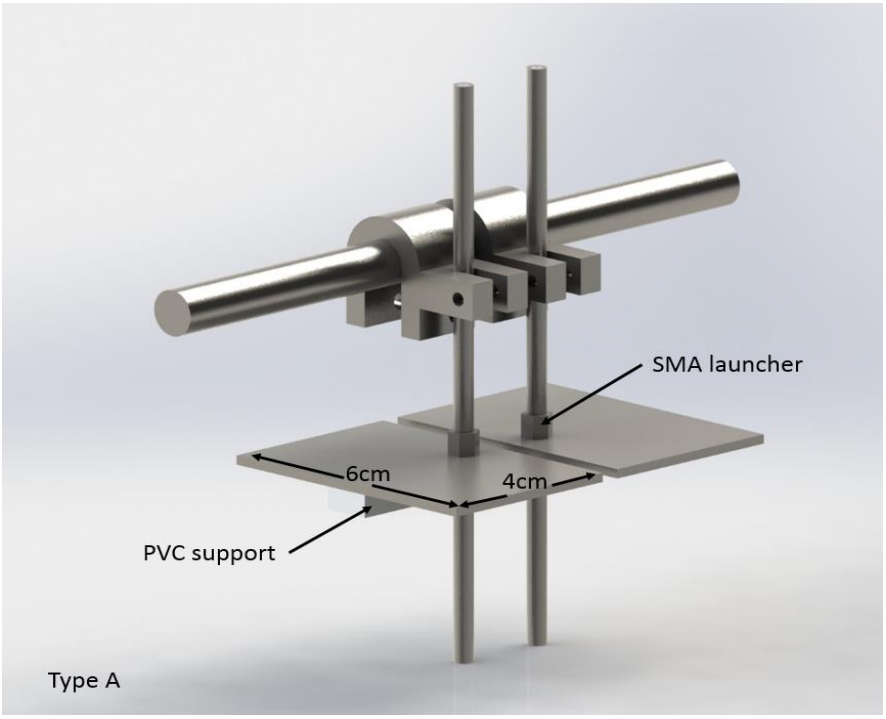
SMA launcher
6cm
4cm
PVC support
Type A

(b)

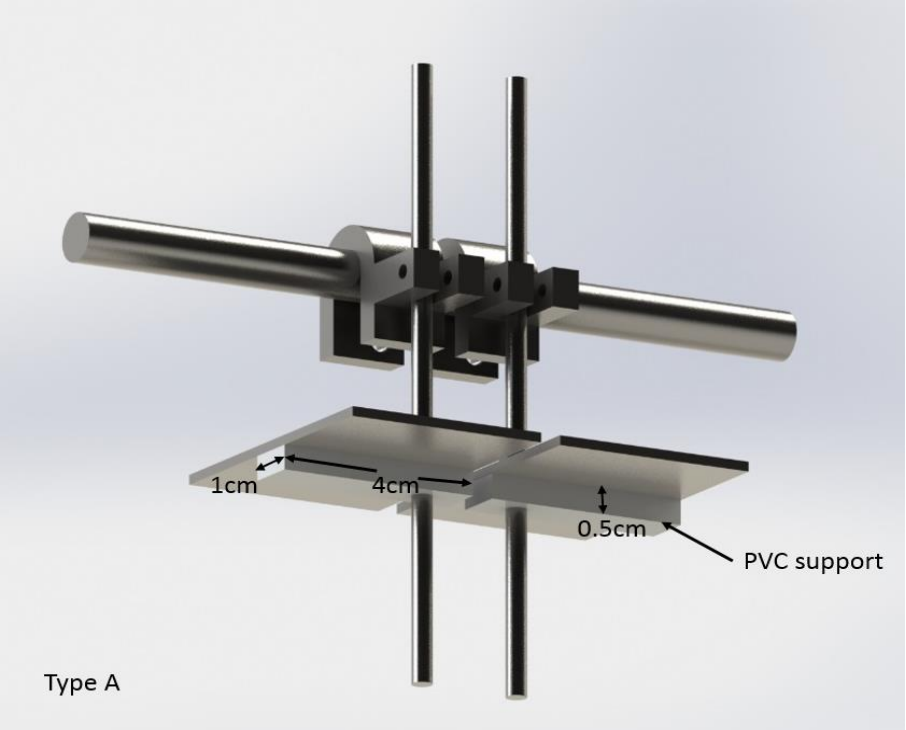

(c)

Figure 4.13: CAD model of Type A external fixator: a) Cross section b) side view c) bottom view

Type B external fixator was designed with greater load bearing capabilities than type A. The coaxial cable of Figure 4.14a was redesigned in order to have an inner conductor of 0.25cm diameter. The length of the cable was 9cm and its impedance was designed to be 50Ohms at the resonance frequency of the monopoles in free space (1.75GHz) for a 2cm monopole separation distance. The SMA launchers and the wire parts of the monopoles were substituted by extending the inner wire of the coaxial cable for 4cm (see Figure 4.14b). Therefore, no SMA launcher was used for the design of the Type B fixator. A comparison between the simulations of the S_{11} and S_{21} of the type A and type B external fixators in free space using CST can be seen in Figure 4.15.

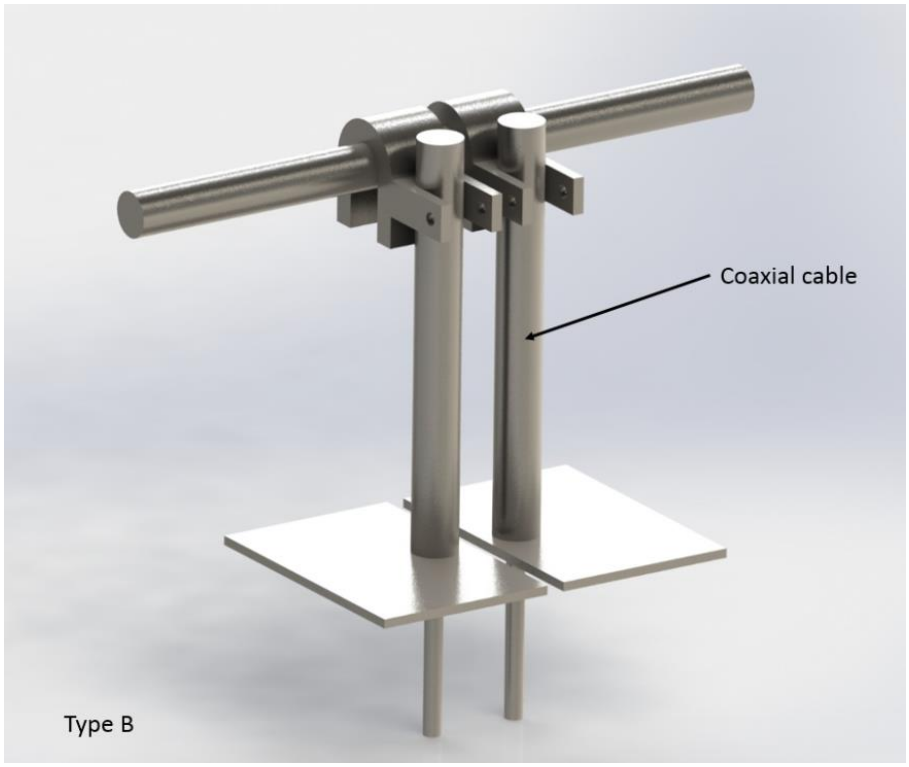

(a)

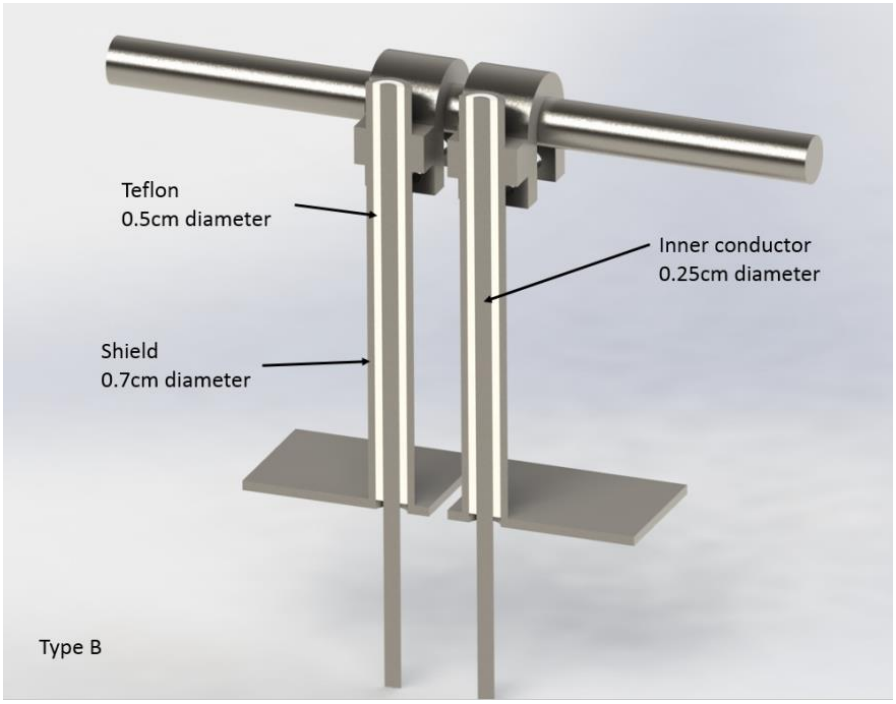

(b)

Figure 4.14: Type B external fixator: a) Top view b) cross section

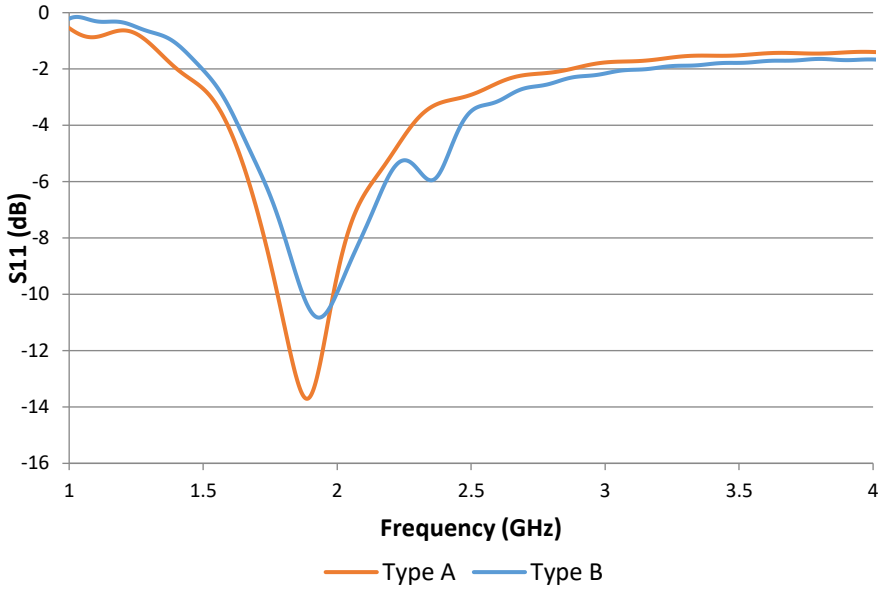

(a)

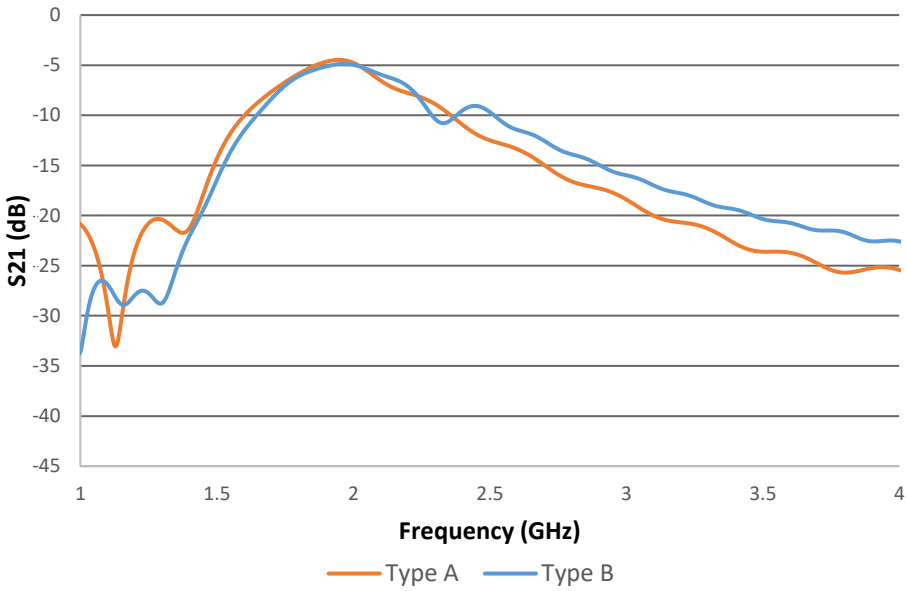

(b)

Figure 4.15: Simulated comparison between type A and type B external fixators in free space using CST: a) S_{11} b) S_{21}

The load bearing capabilities of the two types of external fixators were investigated in simulations using the Solidworks CAD software. The displacement of the wire parts of the monopoles that represent the screws of a real life metal plate was simulated by applying a force of 25N parallel to the direction indicated by the arrows in Figure 4.16.

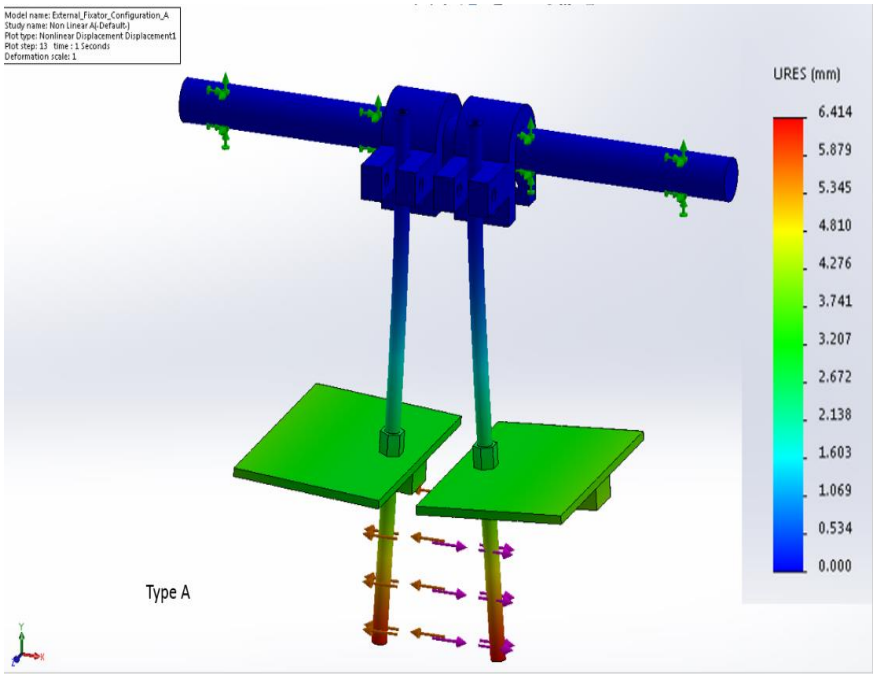

(a)

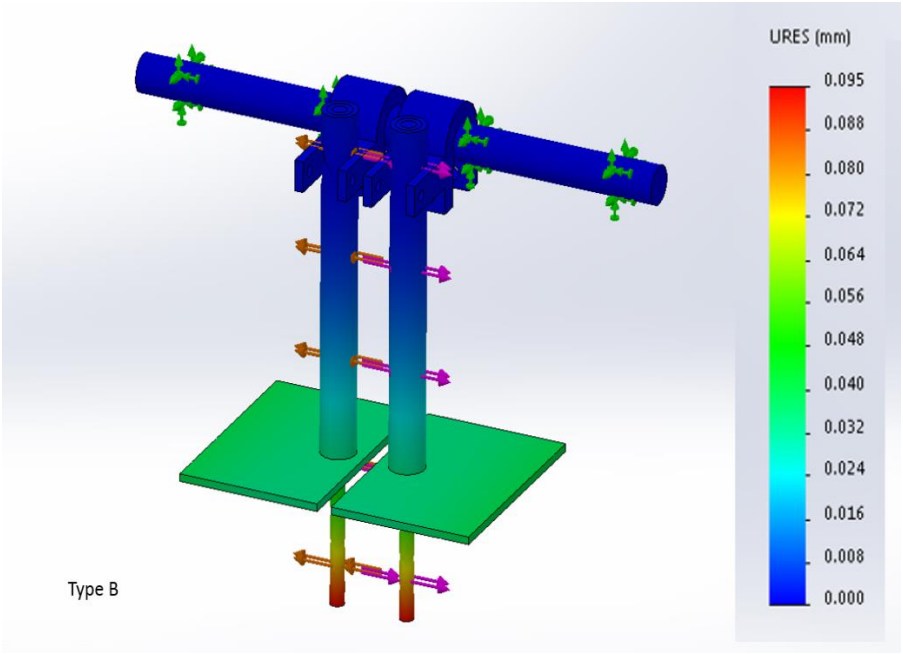

(b)

Figure 4.16: Simulation of displacement (URES) of the external fixator for 25N of applied force: a) Type A fixator b) type B fixator

According to Figure 4.16 the maximum displacement of type A and type B fixator pins is 6.14mm and 0.095mm for 25N of applied force accordingly. Therefore, the type A design is suitable for applications such as the phalange bone in the fingers where lesser amounts of force are applied during fracture healing.

Two more simulations followed in order to further investigate the load bearing capabilities of type B fixators. As it can be observed in Figure 4.17a and Figure 4.17b the maximum displacement of the fixator pins for 300N is 1.159mm and 2.572mm for 500N. Making the design suitable for applications were significant amounts of forces are applied, such as the Tibia bone that is found at the human leg. Further information on the effect of the coupling of the current on the coaxial cable that feeds the monopoles can be found in Appendix C.

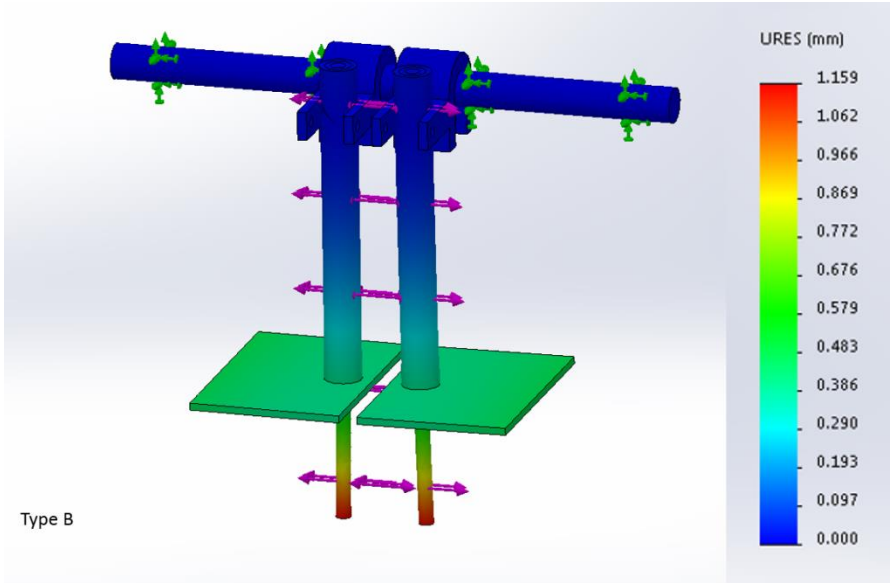

(a)

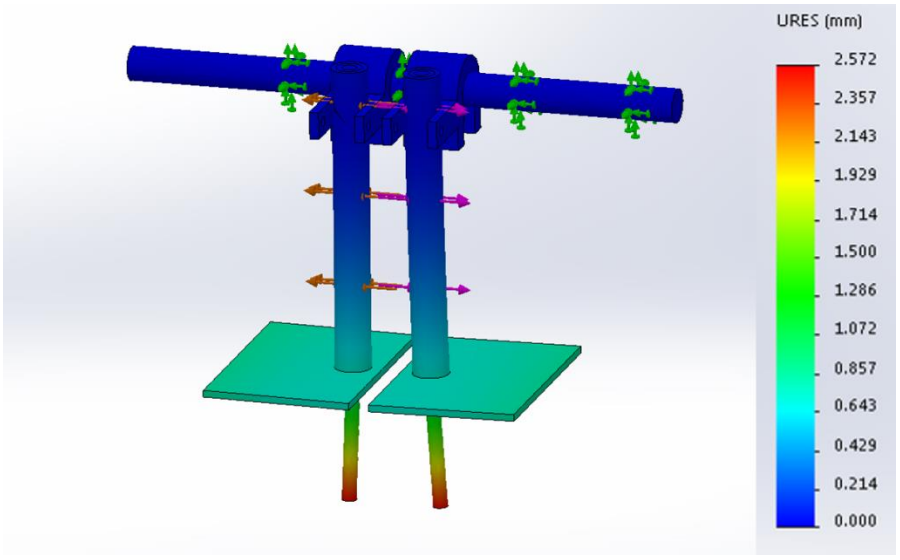

(b)

Figure 4.17: The displacement of the type B fixator for: a) 300N of applied force b) 500N of applied force

4.8 Conclusions

In this chapter, tests with implanted monopoles showed that simulation results can be recreated in measurements with an acceptable level of agreement. Therefore, the presented multi-material phantoms could provide a low cost, repeatable, easy to handle, and hygienic alternative to electromagnetic in-vitro measurements. Furthermore, the flexibility in the design and construction means that the phantom can be adjusted to match the geometry of many bones in the human body. Moreover, the obtained results have shown that the feeding power of 0.3W for the monopole test-bed complies with the SAR specifications for the general public exposure.

Finally, two types of external metal plates featuring the proposed monopoles have been presented. Type A fixator is suitable in applications where lesser amounts of forces are applied into the metal plate, such as the phalange bone, while type B is suitable for applications with greater amounts of loads such as at the radius and tibia bones. The investigated method could provide a fracture monitoring technique during the first 4 weeks after the trauma.

References

[1] IEEE Standards Coordinating Committee 28, *IEEE C95. 1-1992: IEEE Standard for Safety Levels with Respect to Human Exposure to Radio Frequency Electromagnetic Fields, 3 kHz to 300 GHz*, no. April. 1999.

[2] "Specific absorption rate in Canada," *Certification and Engineering Bureau*, 2016. [Online]. Available: https://www.ic.gc.ca/eic/site/ceb-bhst.nsf/eng/h_tt00084.html. [Accessed: 06-Jun-2018].

[3] IEEE International Committee on Electromagnetic Safety (SCC39), *IEEE Standard for Safety Levels With Respect to Human Exposure to Radio Frequency Electromagnetic Fields, 3 kHz to 300 GHz*, no. April. 2006.

[4] L. M. Marshall, T. F. Lang, L. C. Lambert, J. M. Zmuda, K. E. Ensrud, and E. S. Orwoll, "Dimensions and volumetric BMD of the proximal femur and their relation to age among older U.S. men.," *Journal of Bone and Mineral Research*, vol. 21, no. 8, pp. 1197–206, 2006.

[5] R. King, S. Prasad, and B. Sandler, "Transponder antennas in and near a three-layered body," *Microwave Theory and Techniques*, vol. 28, no. 6, pp. 586–596, 1980.

[6] A. K. Skrivervik, "Implantable antennas: The challenge of efficiency," in *7th European Conference on Antennas and Propagation, EuCAP 2013*, 2013, pp. 3627–3631.

[7] J. M. Felício, C. A. Fernandes, and R. Jorge, "Wideband Implantable Antenna for Body-Area High Data Rate Impulse Radio Communication," *IEEE Transactions on Antennas and Propagation*, vol. 64, no. c, pp. 1932–1940, 2016.

[8] H. Khodabakhshi and A. Cheldavi, “Irradiation of a six-layered spherical model of human head in the near field of a half-wave dipole antenna,” *IEEE Transactions on Microwave Theory and Techniques*, vol. 58, no. 3, pp. 680–690, 2010.

[9] “CST Homepage.” [Online]. Available: https://www.cst.com/. [Accessed: 31-Jul-2017].

[10] C. Gabriel, “Compilation of the dielectric properties of body tissues at RF and microwave frequencies,” *Environmental Health*, vol. 1, pp. 1–21, 1996.

[11] M. Gudarzi, B. Marzban, H. Zamanian, and S. Amoozegar, “Investigation of the stress distribution in a bone due to screws pretensions of the bone plate,” in *19th Iranian Conference on BioMedical Engineering (ICBME2012)*, 2012, pp. 1–7.

[12] H. K. Uhthoff, P. Poitras, and D. S. Backman, “Internal plate fixation of fractures: short history and recent developments,” *Journal of Orthopaedic Science*, vol. 11, pp. 118–126, 2006.

[13] G. Konrad *et al.*, “Open Reduction and Internal Fixation of Proximal Humeral Fractures with Use of the Locking Proximal Humerus Plate,” *Journal of Bone and Joint Surgery*, vol. 92–A, no. 1, pp. 85–95, 2010.

[14] A. Goel and V. Laheri, “Plate and Screw Fixation for Atlanto-Axial Subluxation,” *Acta Neurochirurgica*, vol. 129, pp. 47–53, 1994.

[15] S. Banik, S. Bandyopadhyay, and S. Ganguly, “Bioeffects of microwave--a brief review,” *Bioresource Technology*, vol. 87, no. 2, pp. 155–159, 2003.

[16] A. Hirata, H. Sugiyama, and O. Fujiwara, “Estimation of Core Temperature Elevation in Humans and Animals for Whole-Body Averaged SAR,” *Progress In*

Electromagnetics Research, PIER, vol. 99, pp. 53–70, 2009.

[17] N. Kuster and Q. Balzano, “Energy Absorption Mechanism by Biological Bodies in the Near-Field of Dipole Antennas above 300MHz,” *IEEE Transactions on Vehicular Technology*, vol. 41, no. 1, pp. 17–23, 1992.

[18] K. Y. Yazdandoost and R. Miura, “SAR studies for UWB implanted antenna for Brain-Machine-Interface application,” *2016 10th European Conference on Antennas and Propagation, EuCAP 2016*, pp. 3–6, 2016.

[19] “ICNIRP Guidelines for limiting exposure to time-varying electric, magnetic and electromagnetic fields,” *International Commission on Non-Ionizing Radiation Protection, Health Physics*, vol. 74, no. 4, pp. 494 -522;, 1998.

[20] K. Seide, N. Weinrich, M. E. Wenzl, D. Wolter, and C. Jürgens, “Three-dimensional load measurements in an external fixator,” *Journal of Biomechanics*, vol. 37, no. 9, pp. 1361–1369, 2004.

[21] K. Gupta, P. Gupta, G. Singh, S. Kumar, R. Singh, and R. Srivastava, “Change in electrical properties of bone as diagnostic tool for measurement of fracture healing,” *Hard Tissue*, vol. 2, no. 1, pp. 1–8, 2013.

Chapter 5

Bone fracture monitoring using implanted monopoles in three real life bone-equivalent heterogeneous phantoms

---

5.1 Summary

In chapter 4, the measurement setup using two multi-material phantoms was verified. In this chapter a technique for monitoring the healing of severe bone fractures using a pair of RF monopoles implanted in the fractured bone is presented. The bone fracture was modelled as a cylinder residing in the mid distance between the implanted monopoles for the simulations. The technique was tested in the measurement section using three multi-material geometric phantoms. The results between simulation and measurements showed good agreement. In Section 5.2 the two monopole system that is used for the simulations and measurements of this chapter is presented. In Section 5.3, two types of biocompatible 3D printed coatings used for the insulation of the conductive parts of the monopoles are presented. In Section 5.4, the blood distribution inside the fracture of a simple two material phantom is investigated in order to estimate an equivalent approximation of its geometric characteristics for the simulation design of the bone fractures. The bone fracture was modelled inside a voxel model of a 26-year-old female of the Virtual Family using CST Microwave Studio in Section 5.5. The results are compared with measurements inside three novel semi-solid heterogeneous bone phantoms representing the radius (arm), tibia (shin) and phalange (finger) bones in Section 5.6 followed by an ex-vivo measurement of the experiment in a lamb joint in Section 5.7. In Section 5.8 the

simulation and measurement results are compared and discussed. Finally, the concluding remarks of this chapter are presented in Section 5.9.

5.2 The antenna monitoring system

The proposed antenna monitoring system consists of two monopoles and it is based on the simulation and measurement comparisons of Chapter 4. The monopole setup is envisioned to be part of a commercially available external medical metal plate. The wire parts of the monopoles represent the medical screws that are implanted perpendicular to the bone either side of the fracture to provide support of the bone fragments [1]–[4]. Throughout this chapter, the RF power transferred from monopole 1 to monopole 2 in terms of the magnitude of the S_{21} will be investigated as an indicator of the bone's unification – healing progress as its condition will shift gradually from a higher concentration of blood in the initial fractured state, to a lower fraction towards the healed state (see Appendix C). As shown throughout the measurements of phantom recipes of Chapter 3, blood's relative permittivity and conductivity are significantly higher compared to bone's across the frequency spectrum of 1 to 4GHz, i.e ε_{rblood} = 59, σ_{blood}= 2.2 S/m and ε_{rbone} = 11.6, σ_{bone}= 0.31 S/m at 2GHz.

According to Kerns [5], the wavenumber *k* for lossy media is given by:

$$k = \omega\sqrt{\mu_0\mu_r\varepsilon_0(\varepsilon_r - j\frac{\sigma}{\omega\varepsilon_0})} \tag{5.1}$$

Where ω is the angular frequency, μ_0, ε_0 the permeability and permittivity of vacuum respectively, μ_r, ε_r the relative permeability and relative permittivity of the medium respectively, and σ the conductivity of the medium. Therefore, as the amount of blood inside and around the fracture decreases, the total relative permittivity and conductivity inside and

around the area decrease accordingly. Thus, it is expected that the losses of *k* are minimized, resulting in more power being received by the 2nd antenna.

A pair of monopole antennas were simulated and then constructed as shown in Figure 5.1. The monopoles had 0.25cm diameter. For the measurements of tibia and phalange bones located in the shin and fingers of the human body respectively, the monopole lengths were 2.5cm and the groundplanes were 6 × 4cm. However, due to the depth that the Radius bone is found inside the human arm, ranging from 2cm near the elbow to 0.5cm near the wrist, as measured in the voxel model of CST microwave studio a second pair of 4cm length monopoles with 6 × 5.6cm groundplanes were also constructed. As shown in the simulations of Chapter 4, 0.5cm of the length of each monopole was in free space connected to each groundplane and the rest of their length was inside the body placed through the muscle and perpendicularly into the bone. The gap of 0.5cm of free space between the muscle tissue and the groundplanes was used to avoid the groundplane contact with the highly conductive muscle layer. A gap of 0.4cm between the groundplanes was selected as adequate space to apply the needle injections of blood emulating liquid without disturbing the position of the monopoles. The use of two gap-separated groundplanes, one corresponding to each monopole wire, is also necessary for real life applications. This is due to the separation distance between the monopoles (2cm in this investigation) that is dictated by the size of the fracture. It is necessary to use larger monopole separation distances for larger fractures. Therefore, using two groundplanes and not one large groundplane that will host both monopole wires is envisioned to allow easier adjustment of the metal plate by the doctors. An investigation of the scattering parameters effect for larger monopole separation distances is thoroughly investigated in the theoretical model presented in Chapter 6. To maintain the 2cm distance of the monopoles and the 0.4cm gap between the groundplanes, the monopoles were attached to their groundplanes at a 0.8cm distance from the right edge of the x-axis and at the middle of the y-axis of the groundplanes (see Figure 5.1).

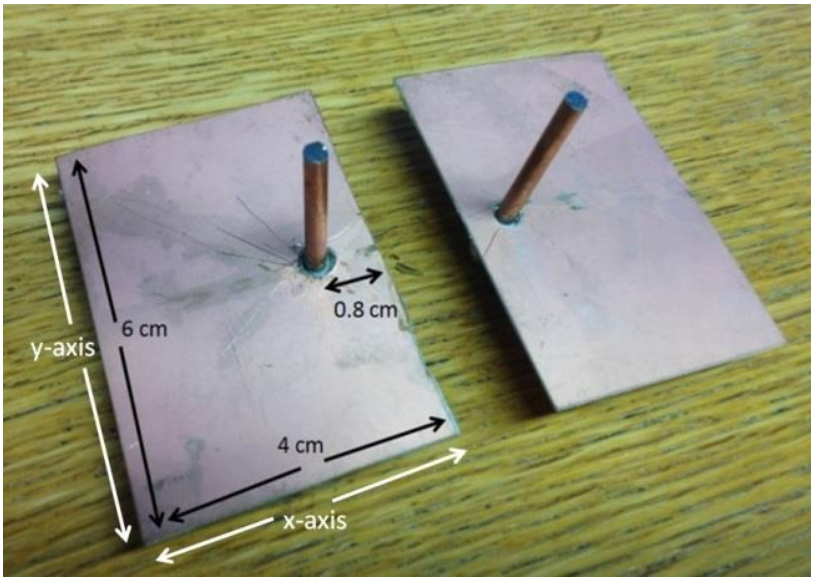

Figure 5.1: Fabricated monopoles of the antenna monitoring system

5.3 The antenna coatings

Plastic tape was used for the insulation of the monopoles in Chapter 4. In this chapter blood emulating liquid will be injected into the phantom to mimic a bone fracture. In order to achieve total isolation of the monopoles from the liquid, two types of coatings were 3D printed in order to insulate them from the surrounding tissues. The outer diameter of each hollow cylindrical coating was set at 0.4cm and was comparable to the average medical screw diameter found in [6]–[8] (see Figure 5.2). The inner diameter was 0.25cm in order to fit the conducting part of each monopole. The type of material used for the first type of coating was acrylonitrile butadiene styrene (ABS) and was printed using a Stratasys Dimension 3D printer (see Figure 5.3). According to Figure 5.2, the helix angle was 30° and the axial channel width was 0.175cm. The root diameter of the screw was 0.3cm and the channel depth was 0.1cm (see Figure 5.3). Due to the fragility of the ABS material, when printed in such small dimensions (0.3cm root diameter), it was only used for demonstration purposes in this thesis. The second coating was made out of biocompatible plastic polymer (PLA) [9]. It was printed using an Ultimaker 2 3D

printer and used in all of the measurements of this chapter (see Figure 5.4). Two pairs of PLA coatings of 4cm and 2.5cm lengths were created in order to match the size of each monopole pair accordingly.

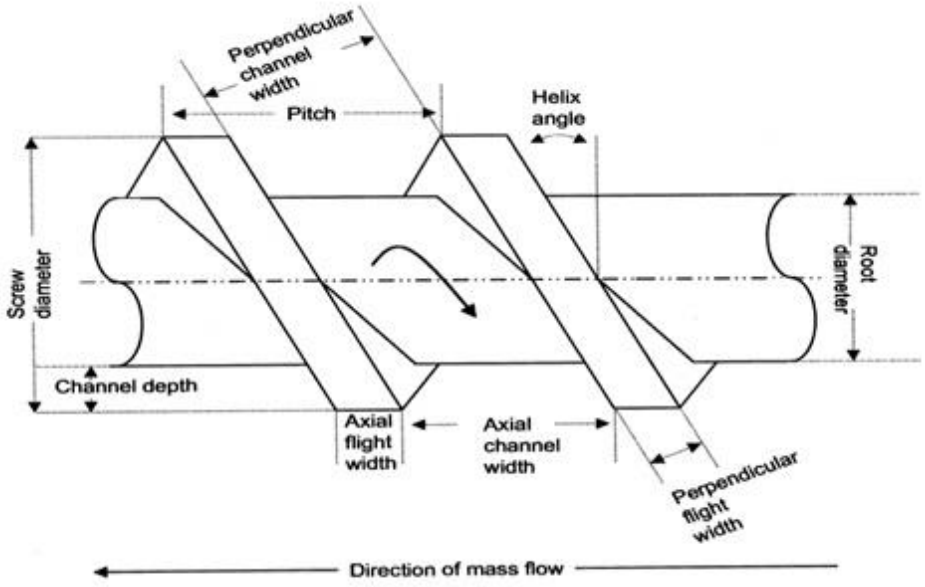

Figure 5.2: Medical screw dimensional map taken from [8]

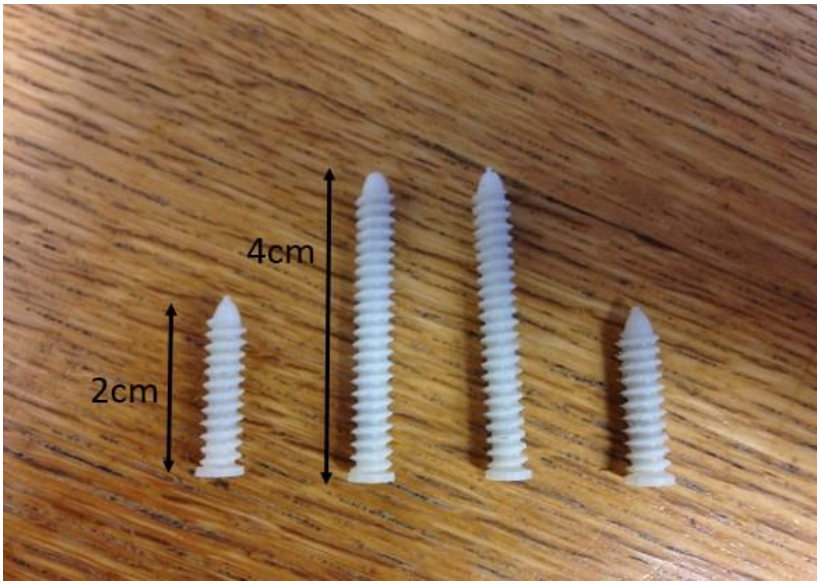

Figure 5.3: Acrylonitrile butadiene styrene 3D printed monopole coatings, corresponding to the 2cm and 4cm monopoles

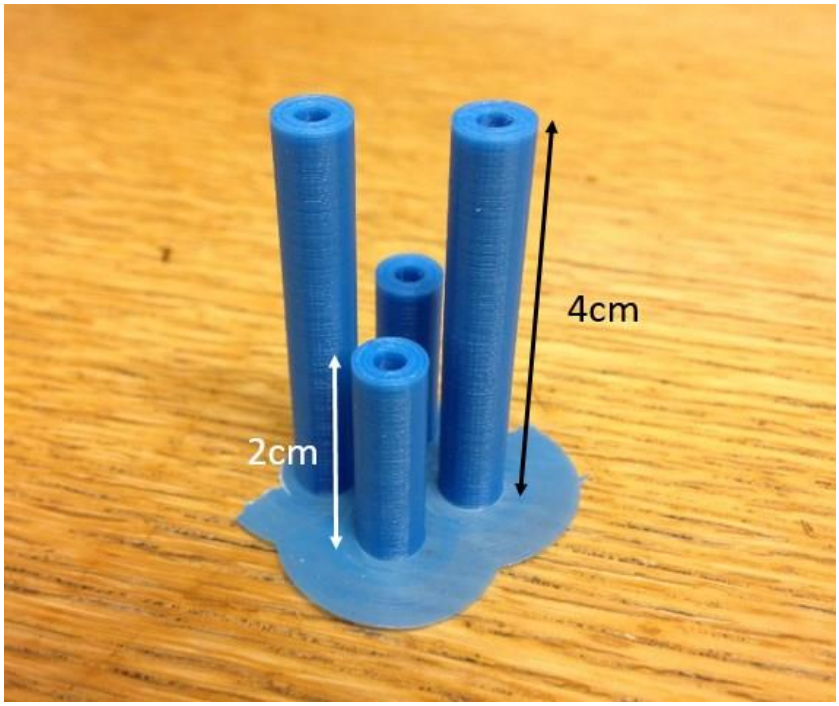

Figure 5.4: Biocompatible plastic polymer 3D printed monopole coatings, corresponding to the 2cm and 4cm monopoles

5.4 Visualisation of the blood distribution inside the fracture

In order to understand the distribution of the blood within a fracture at the stages of inflammation and hematoma where maximum blood is inside and around the fracture, to the healed stage where the blood is minimum and the bone is restored, a measurement was conducted using a transparent gelatine phantom. The phantom was made of tap water and gelatine using the exact water to gelatine ratio (1g of gelatine for 20g of water) as the developed recipes presented in Section 2.3. A layer made of flour and oil was given the dimensions of the phalange bone and was embedded into the gelatine layer (see Figure 5.5a). 10ml of blue coloured cooking liquid was added in the middle of the bone phantom using a syringe gradually with a 2ml injection step.

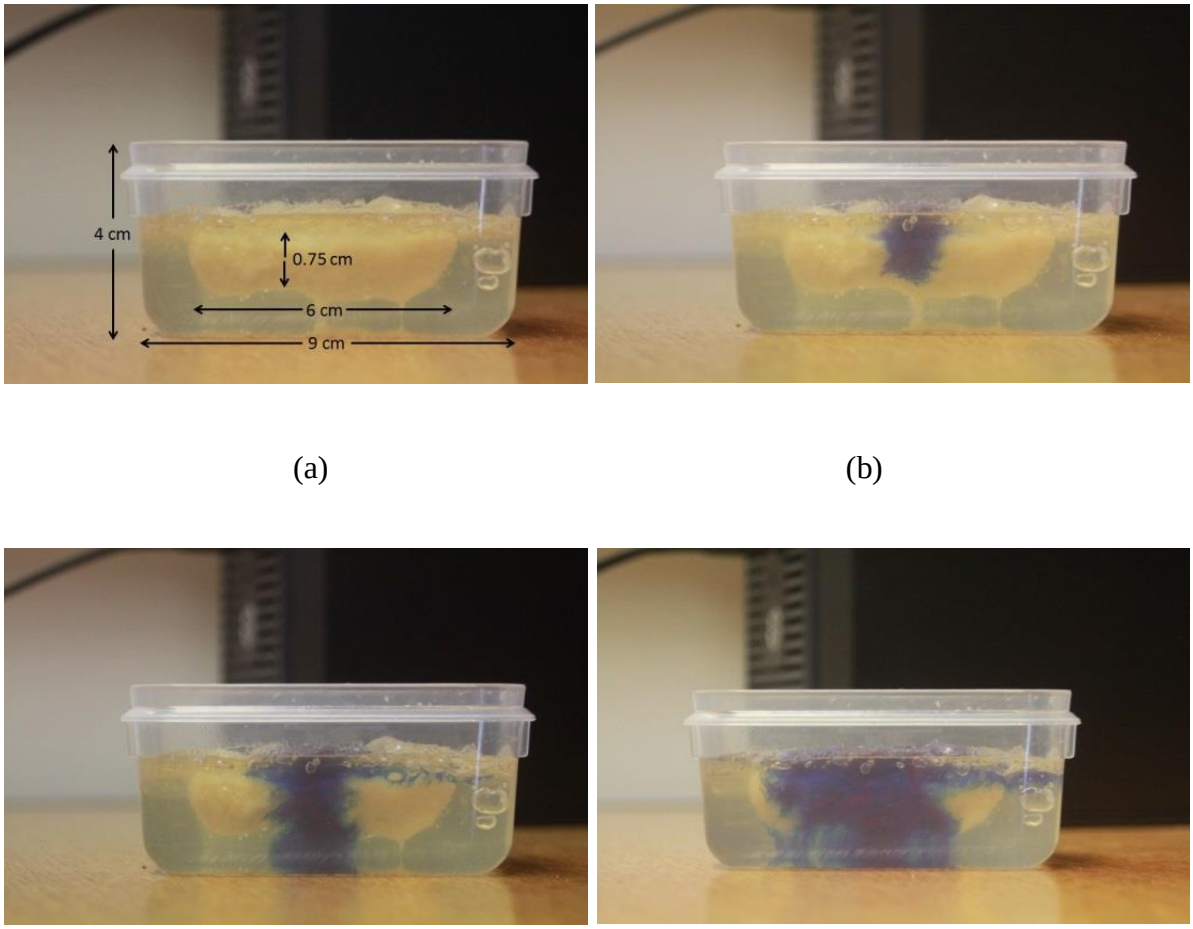

(a) (b)

(c) (d)

Figure 5.5: Photos of the experiment to understand distribution of blood emulating liquid in the phantom a) Dimensions of the test-bed phantom, b) 2ml food colouring injection, c) 6ml food colouring injection, d) 10ml food colouring injection

Figure 5.5 provides an indication on the blood fluid distribution inside a phalange (finger) bone fracture. As presented in Chapter 2, the geometry of a bone fracture and therefore, the geometry of the hematoma, can depend on many factors, such as: The angle of impact, the force of impact, the age of the patient e.t.c. Thus, the blood liquid distribution investigation of the phantom of Figure 5.5 serves as an approximation of the hematoma that will be used for the simulations of Section 5.5. Further on, it was observed that as the amount of food colouring increases in the

middle of the phantom, it surrounds the bone layer approximately in a cylindrical formation. The radius of the cylinder that is composed around the bone by the food colouring is a result of the combination of the radiuses of the existing bone layer cylinder and the food colouring liquid cylinder that surrounds the bone layer. This cylinder combination has a length of 1.5cm and radius of 1.4cm for 2ml of food colouring, 3.4cm length and 1.5cm radius for 6ml and 5cm length and 1.55cm radius for 10ml.

5.5 Simulations of the two monopoles inside a voxel model

For the simulations of the antenna system, the voxel model of a 26 year old female of 58kg weight and 1.60m height of the Virtual Family imported into CST Studio was used [10]. The permittivity and conductivity of the model's tissues were frequency dependent, their values changed for each simulated frequency according to Gabriel's measurement results found in [11] for the range of 1 to 4GHz. According to Figure 5.6, the representation of the fracture was envisioned by two coaxial cylinders. The inner cylinder of the fracture was placed within the 2cm distance between the two monopoles and replaced the bone in that area. The diameter of the inner cylinder was equal to the diameter of the investigated bone and its length was set at 1.6cm. For the replication of bone healing, the dielectric properties of the inner cylinder shifted from a healed state, where no blood was considered at the inner cylinder, therefore the dielectric properties of bone were assigned, to a severed fracture state, where the maximum amount of blood was injected (10ml for the phalange, 30ml for the tibia and radius bone phantom simulations). The total amount of simulation stages were four, 0ml, 2ml, 6ml and 10ml, for the phalange bone and 0ml, 10ml, 20ml and 30ml for the tibia and radius bones. An example of the four stages of the dielectric properties of the inner cylinder for the phalange bone can be found in Table 5.1 at 2.5GHz. The relative permittivity and conductivity values used for the

simulations and measurements of this chapter were frequency dependent at 1 to 4GHz frequency spectrum.

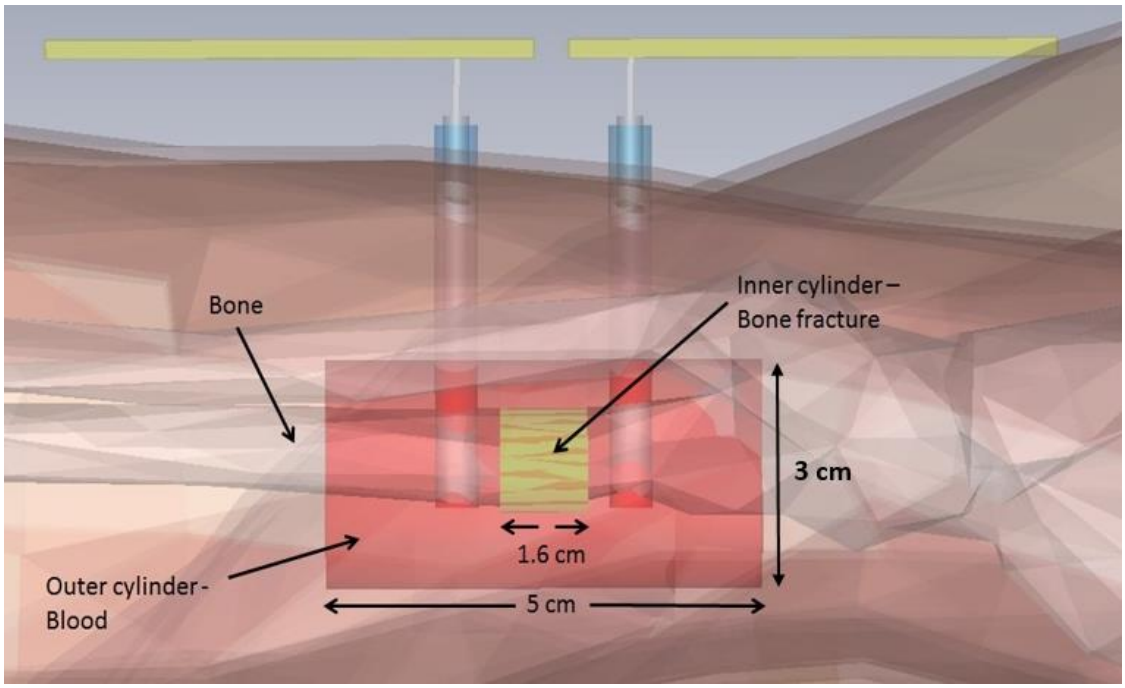

Figure 5.6: Simulation of the bone fracture using two coaxial cylinders inside a voxel model, the topology of the inner and outer cylinders is the same for arm, shin and finger bone fracture simulations

Table 5.1: The simulated values of the dielectric properties of the inner cylinder for 2, 6 and 10ml of blood emulating liquid for the phalange phantom at 2.5GHz

Amount of injected blood emulating liquid (ml)	**Relative Permittivity, ε_r**	**Conductivity, σ (S/m)**
10	29.83	1.25
6	20.62	0.81
2	16.01	0.59
0	11.41	0.38

The outer cylinder that surrounded the fractured bone, was designated the dielectric properties of blood as it represented the hematoma inflammation [12] as reported in Chapter 2. The length and radius of the outer cylinder were given according to the measurements and calculations of blood distribution that were conducted in Section 5.3 (see Figure 5.6). At the initial simulation, the maximum amount of hematoma inflammation was simulated, corresponding to 10ml of blood emulating liquid for the finger (phalange) (see Figure 5.7) and 30ml for the arm (radius) (Figure 5.6) and shin bones (tibia) (Figure 5.8). The length and diameter of the outer cylinder were 5cm and 3cm for the arm bone (radius), for 30ml of blood hematoma of Figure 5.6. For each simulation, the outer cylinder's diameter and length reduced in size until it had equal diameter to the bone. In the final simulation, the fracture was considered healed, the inner cylinder had the dielectric properties of the bone and the outer blood emulating cylinder that corresponded to the inflammation was removed from the simulation.

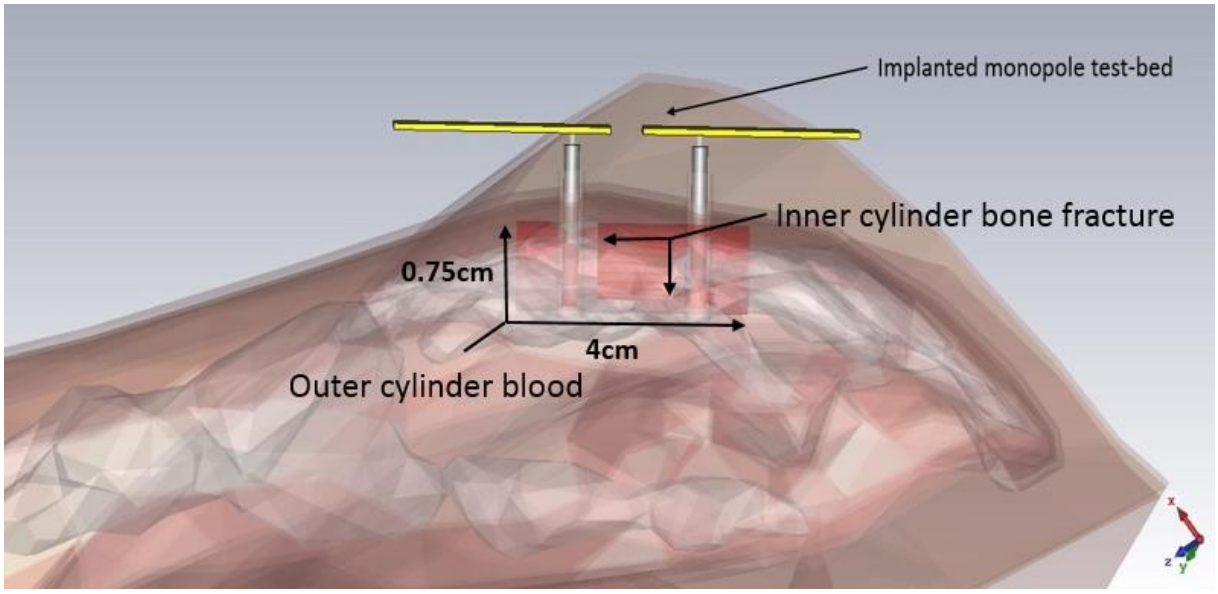

Figure 5.7: Simulated geometry of the bone fracture in the phalange bone (finger)

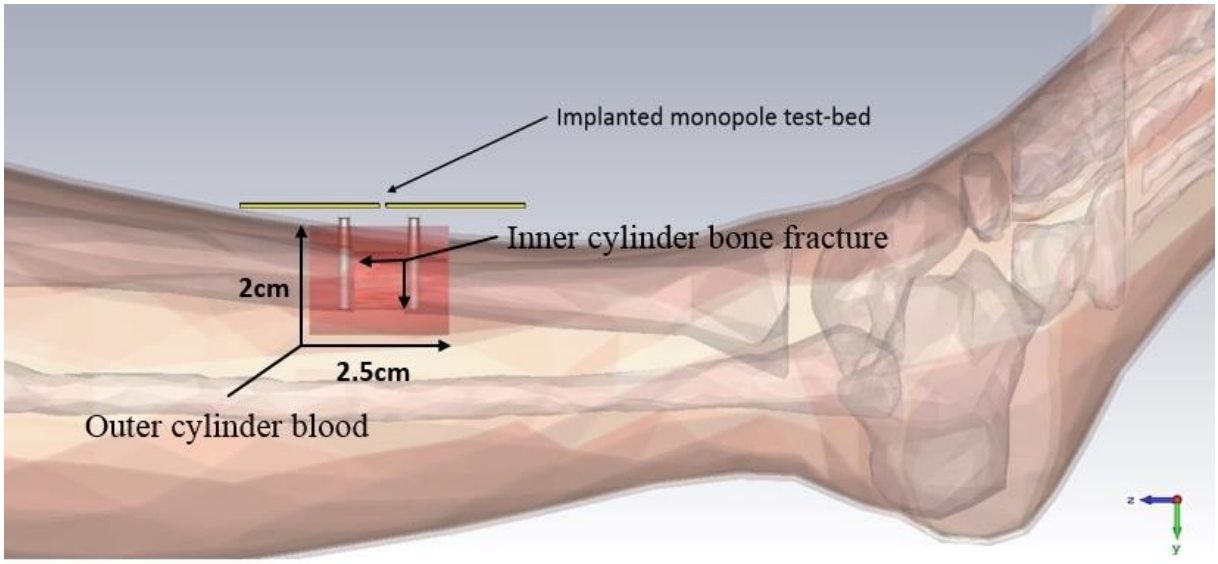

Figure 5.8: Simulated geometry of the bone fracture in the tibia bone

5.6 Measurement setup using a three material phantom

At first, to ensure correct implantation of the monopoles between the skin and the groundplanes the PLA insulators of the monopoles were first implanted into the middle of the bone layer. The coatings were separated by a gap of 2cm from each other (centre to centre); then, the bone emulating tissue was placed inside the muscle phantom and its exposed top surface was carefully covered until all of the air cavities were filled with the muscle phantom (see Figure 5.9). The monopoles were then inserted into the insulating sleeves. The diameters of the bone tissues for all the phantoms presented in Sections 5.6.1 to 5.6.3, were given according to the average diameter of their equivalent bones provided by the voxel model of CST Microwave Studio [10]. The corresponding diameters where 1.5cm for the radius bone (arm), 0.75cm for the phalange (finger) and 2cm for the tibia (shin).

5.6.1 Forearm – radius bone measurement setup

The length of the monopoles for the measurement setup of the radius bone was 4cm. The dimensions of the groundplanes were 6 × 5.6cm. The groundplanes were attached to the exposed parts of the monopoles at the surface of the phantom (see Figure 5.10). The 0.4cm gap between the groundplanes was used as an entry point for the injection of the blood emulating liquid via a sterilized syringe of 1mm diameter. Although the envisioned 0.5cm air gap between the phantom and the groundplanes was followed precisely, the groundplanes were also insulated using plastic sticky tape, thus eliminating the possibility of contact with the highly conductive muscle layer.

(a) (b)

Figure 5.9: a) Bone layer and PLA insulators; b) forearm - radius phantom composed of bone and muscle emulating tissues

The diameter of the bone layer was approximately 1.5cm according to the average diameter of the radius bone found in [13], [14] and its length was 12cm. The muscle layer occupied a plastic box with dimensions of 23 × 8.5 × 5cm.

Figure 5.10: Monopoles implanted into the multi-material forearm - radius phantom

5.6.2 Finger – phalange bone measurement setup

For the phalange phantom, the bone layer had 0.75cm diameter and 6cm length and the muscle layer occupied a plastic box with dimensions of 9 × 6.5 × 4cm (see Figure 5.11). The monopoles had 2cm length and the dimensions of the groundplanes were 6 × 4cm. Due to the smaller size of the phalange bone and its equivalent phantom, the maximum amount of blood emulating liquid that was injected between the monopoles was 10ml in five injections of 2ml.

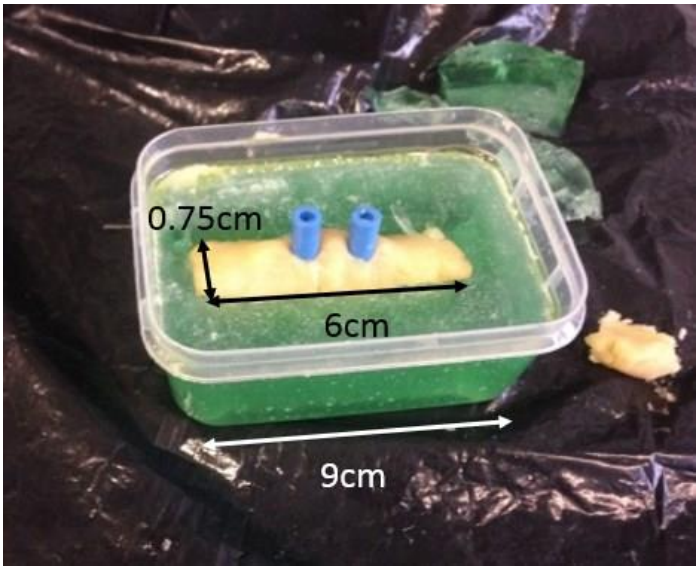

(a)

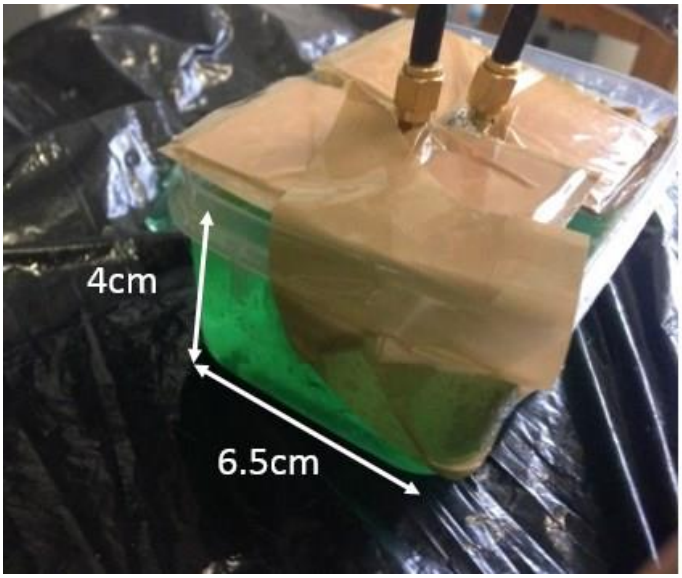

(b)

Figure 5.11: a) Bone layer and PLA insulators, b) monopoles implanted into the finger - phalange phantom composed of bone and muscle emulating tissues

5.6.3 Leg – tibia bone measurement setup

For the measurements of the tibia phantom, the diameter of the bone layer was 2cm and the length was 16cm. The muscle layer occupied a plastic box with dimensions of 23 × 8.5 × 5cm. The length of the monopoles was 2cm and the dimensions of the groundplanes were 6 × 4cm (see Figure 5.12).

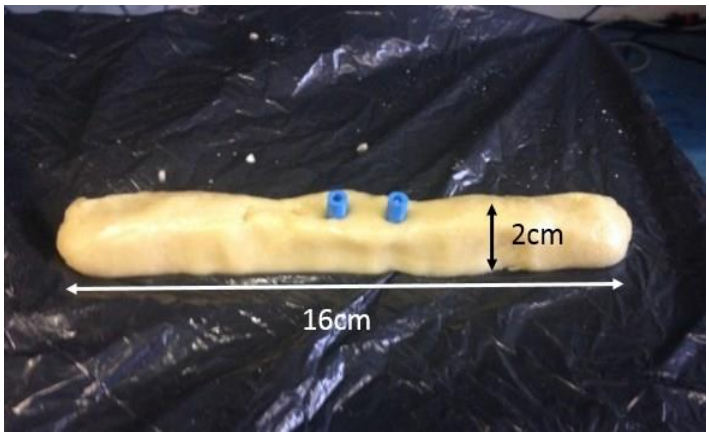

(a)

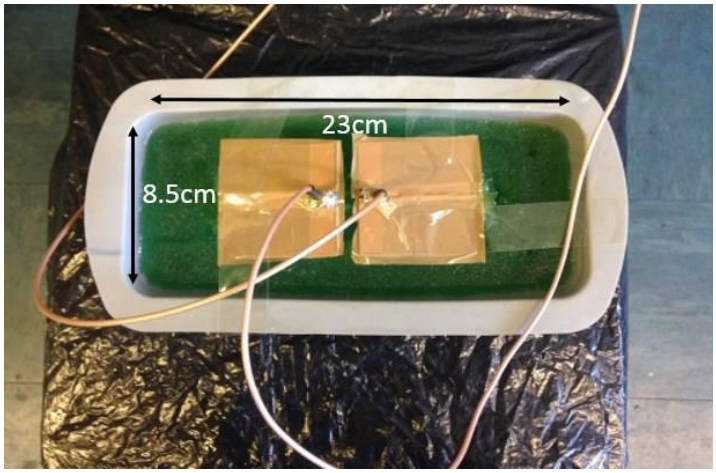

(b)

Figure 5.12: a) Bone layer and PLA insulators; b) Monopoles implanted into the leg - tibia phantom

For each phantom setup presented above, the S_{21} of the monopoles was measured using an Anritsu MS46524A vector network analyzer that was calibrated over the 1 to 4 GHz frequency range. The first measurement was conducted without injecting any blood emulating liquid into the phantom to emulate the fully healed condition of the bone. Each of the next measurements were taken for every 2ml of blood emulating liquid that was injected into each phantom into the bone layer in the mid distance between the monopoles until the maximum amount of millilitres was reached.

5.7 Ex-vivo lamb joint measurement setup

For the ex-vivo measurements, a lamb femur joint that was purchased from a supermarket was used. Two 0.4cm diameter holes were drilled in the top surface of the bone for the monopole insulators to be implanted. The 2.5cm length monopoles that were used in the phalange and tibia phantoms were selected for implantation due to the diameter of the bone joint being approximately 2cm. The monopoles were coated using the 3D printed PLA coatings of Section 5.3. The distance between the holes was measured as 2cm as shown in Figure 5.13. The first S_{21} measurement was conducted without fracturing the bone. For the S_{21} measurements that followed, a 4mm diameter hole was drilled in the mid distance between the monopoles (position 1 in Figure 5.13a) and 2ml of blood emulating liquid was added for each step, up to the amount of 10ml. Then, a second 4mm diameter hole was drilled just to the right of the first hole (position 2 in Figure 5.13a). The liquid injection process continued in 2ml steps with an S_{21} measurement at each step until a total of 20ml had been injected. Finally, a third 4mm hole was drilled just to the left of the first hole (position 3 in Figure 5.13a) and the injection and S_{21} measurement process continued in steps of 2ml until a total of 30ml of liquid was added to the fracture.

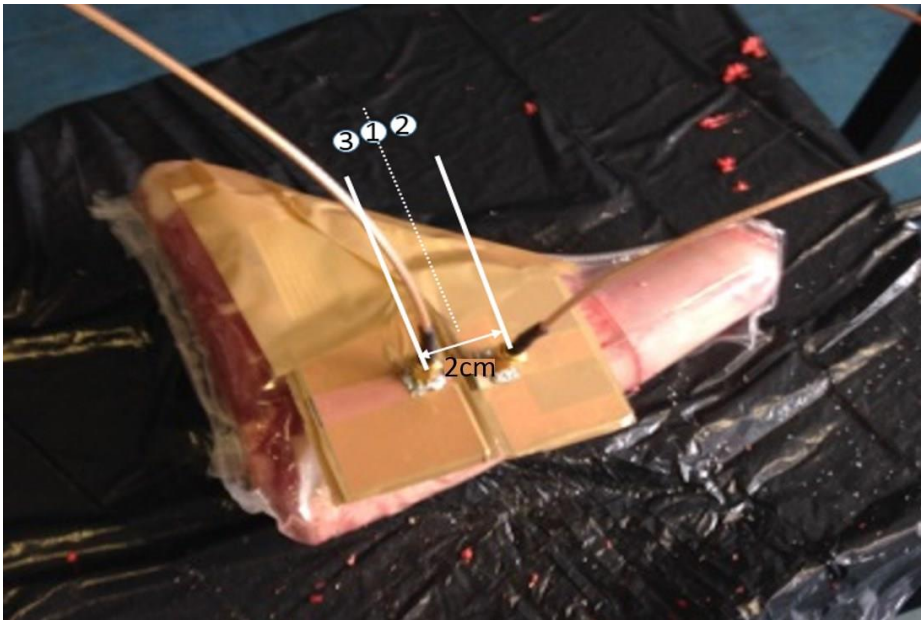

(a)

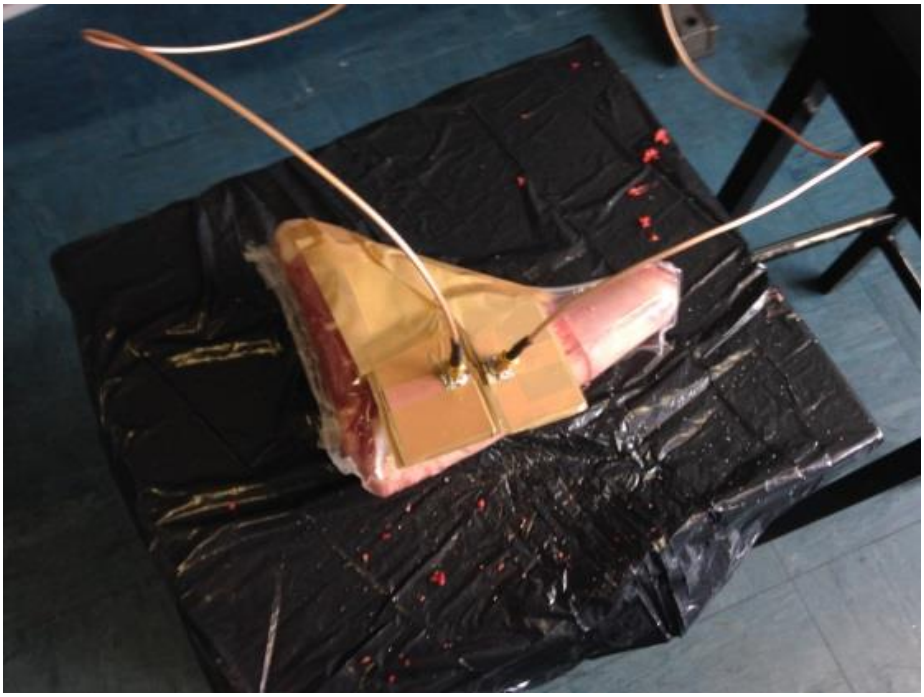

(b)

Figure 5.13: a) PLA insulators implanted into the lamb joint, b) monopoles implanted into the lamb joint

5.8 Measurement results of the three material phantoms and lamb joint test-beds

Dielectric measurements were taken in the centre of the fracture for the same amounts of injected blood emulating liquid using the coaxial probe of Chapter 3. The measurement was conducted in all three phantoms as an additional validation technique. The volume ratio of bone versus blood emulating liquid inside the fractured area was calculated based on the measured relative permittivity of the investigated area compared to the relative permittivity of the bone and the blood tissues. Radius fracture (arm) consisted of 24.1% blood at 10ml, 63.7% blood at 20ml and 97.1% blood at 30ml (see Figure 5.16). Phalange fracture (finger) consisted of 38.2% blood at 6ml, 64.7% blood at 8ml and 90.0% blood at 10ml (see Figure 5.14). Tibia fracture (shin) consisted of 36.9% blood at 10ml, 51.7% blood at 20ml and 91.5% blood at 30ml (see Figure 5.15). According to measurements conducted in [15], the measured relative permittivity of the Trabecular bone callus that signals bone unification varies between 35 and 45 at 1GHz. That range of values show the closest agreement with the 8ml of injected blood emulating liquid measurement for the phalange phantom and with the 20ml for the tibia and radius phantoms.

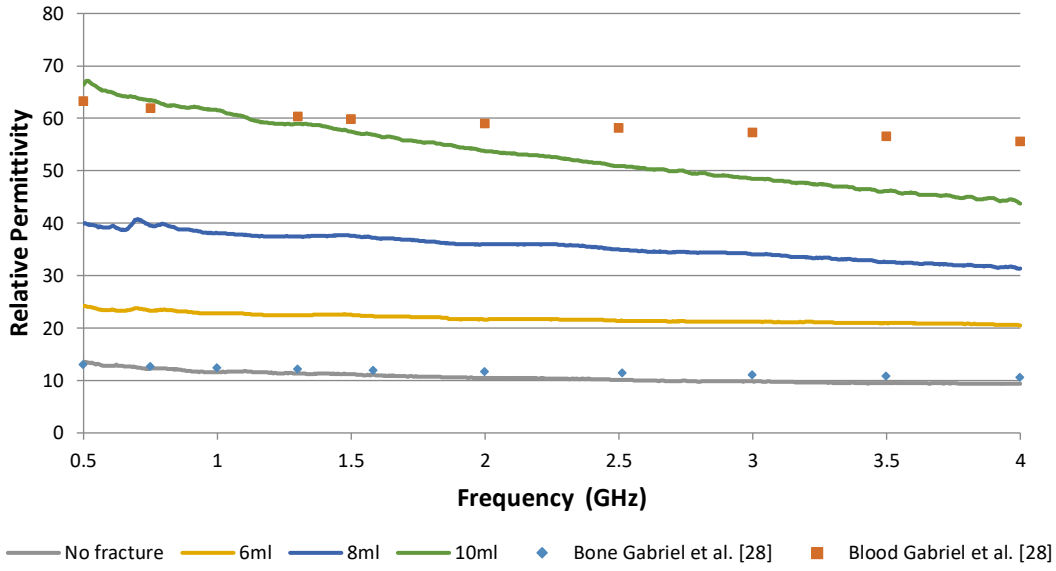

Figure 5.14: Coaxial probe dielectric measurements in the middle of the bone fracture in the phalange phantom

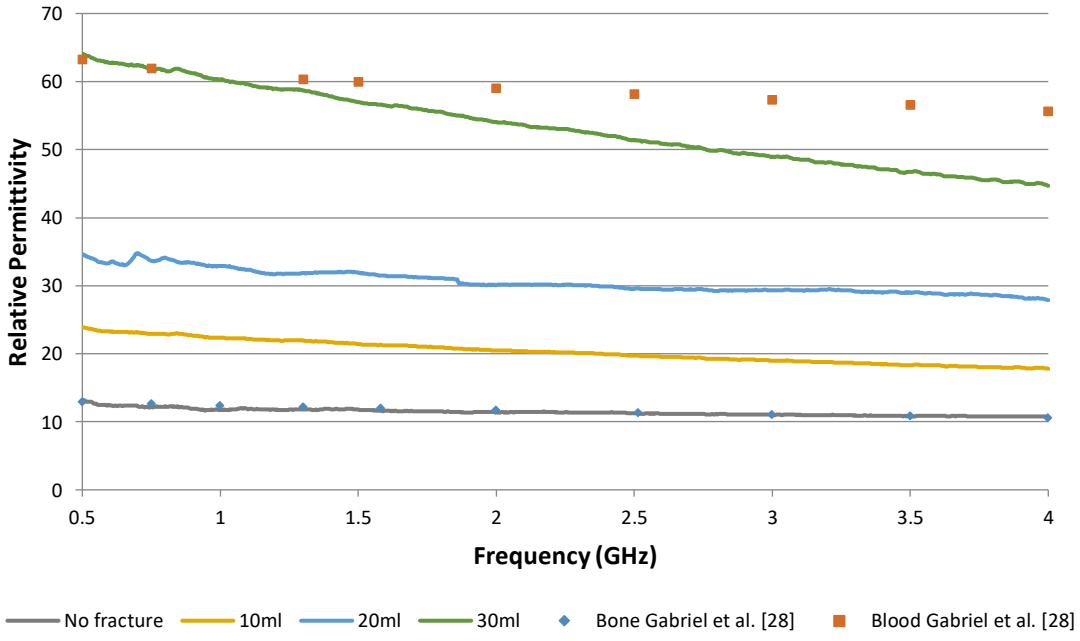

Figure 5.15: Coaxial probe dielectric measurements in the middle of the bone fracture in the tibia phantom

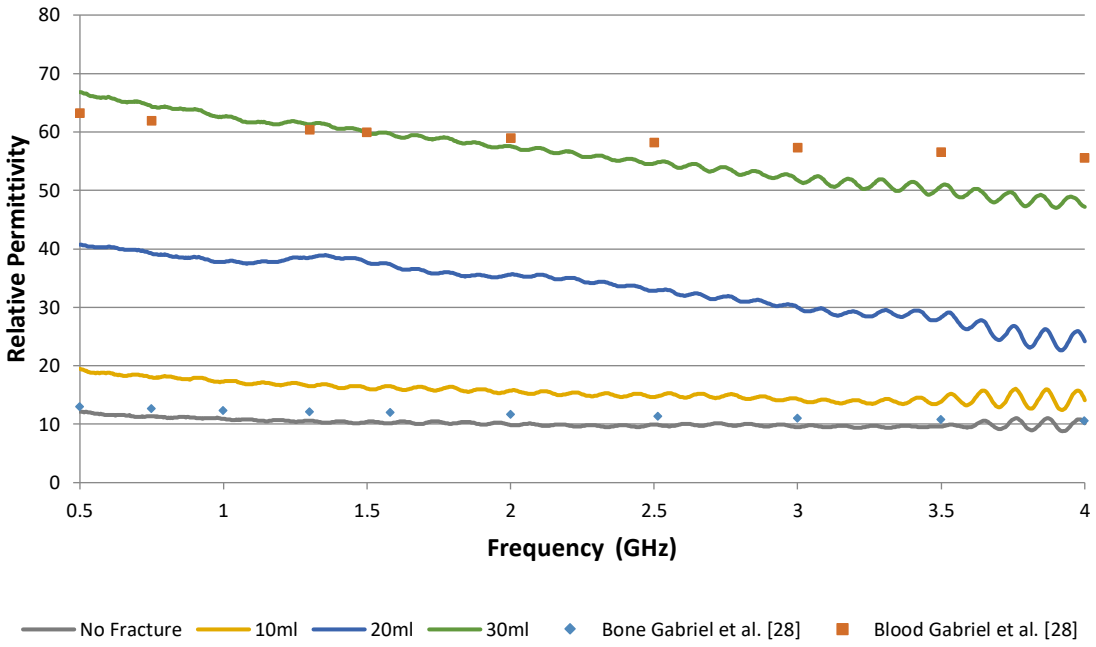

Figure 5.16: Coaxial probe dielectric measurements in the middle of the bone fracture in the radius phantoms

The presented measurement results in Figure 5.17,Figure 5.18 and Figure 5.19, show that by gradually increasing the volume of blood emulating liquid between the monopoles, the magnitude of the S_{21} attenuated in the investigated frequency spectrum. Lamb joint measurements in Figure 5.20 confirm the S_{21} magnitude attenuation in ex-vivo tissues. Several resonances created in the measurements compared to the smoother plots of simulations are due to the complex geometry of the dispersion of the blood emulating liquid inside the phantoms as shown in Figure 5.5. This effect is further analysed at the end of this section with the visualisation of the simulated electric fields of the monopoles inside a geometrical phantom simulated in CST microwave studio.

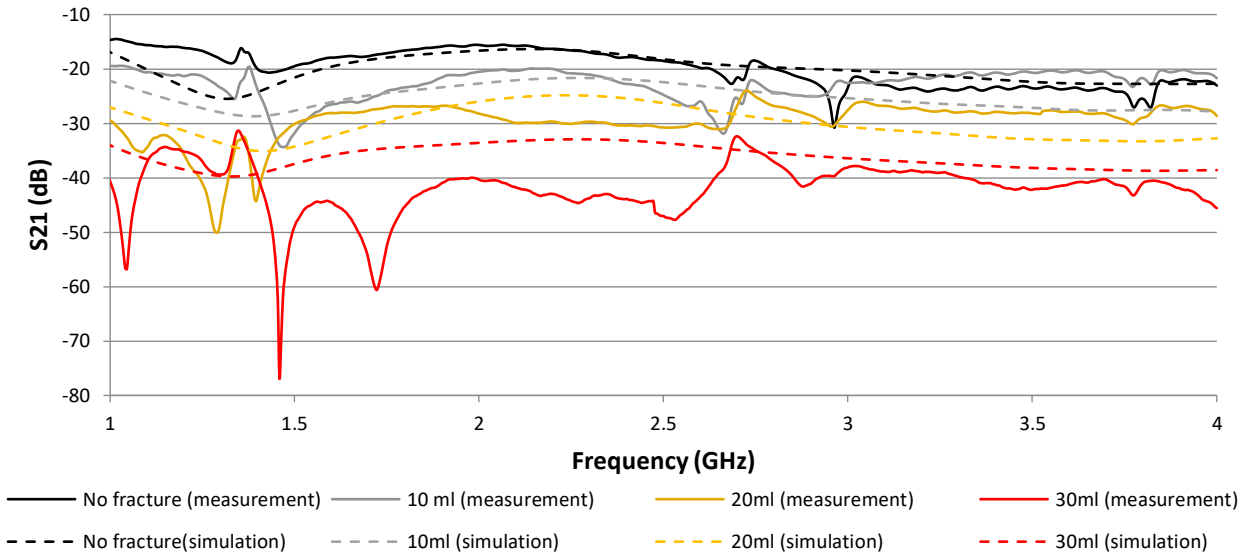

Figure 5.17: The S_{21} measurement and simulation results for the radius phantom with different quantities of blood emulating liquid representing the hematoma

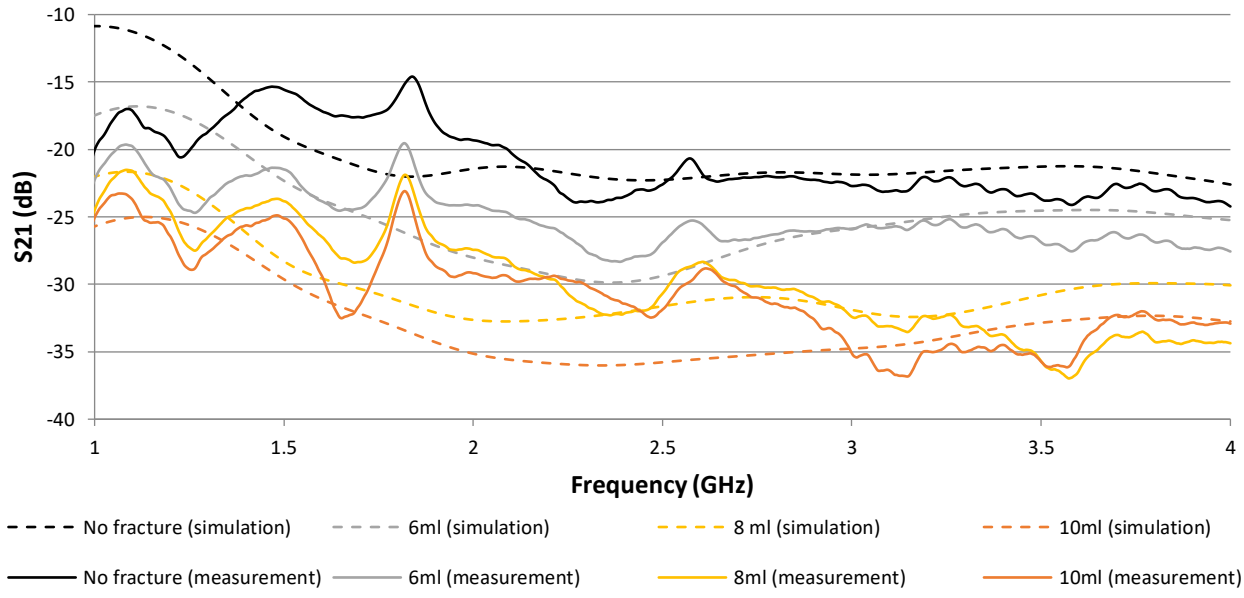

Figure 5.18: The S_{21} measurement and simulation results for the phalange phantom with different quantities of blood emulating liquid representing the hematoma

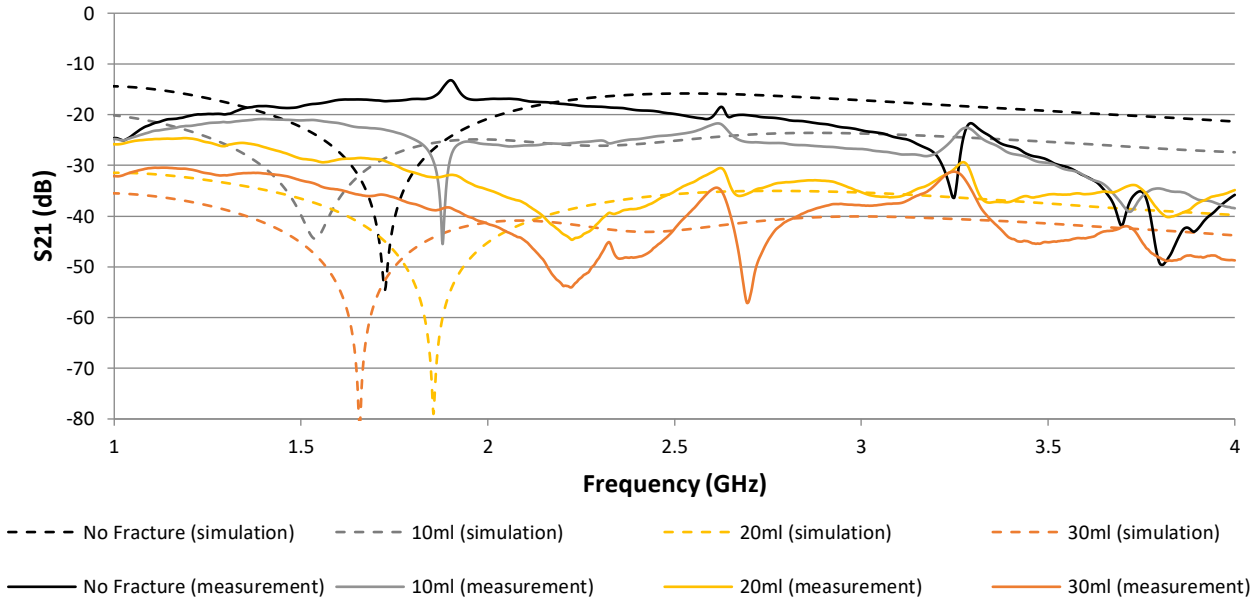

Figure 5.19: The S_{21} measurement and simulation results for the tibia phantom with different quantities of blood emulating liquid representing the hematoma

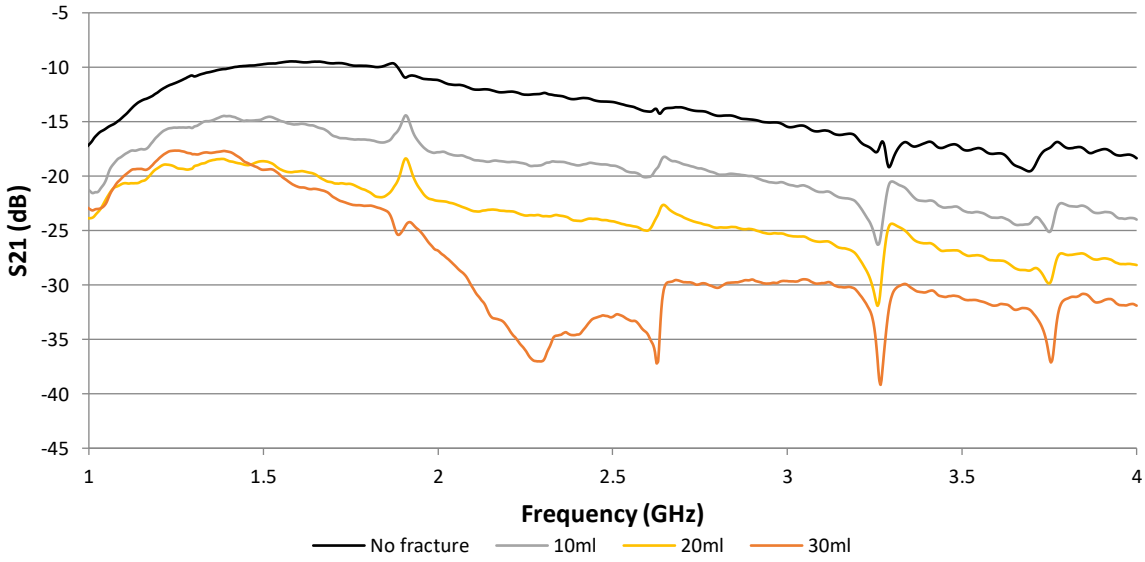

Figure 5.20: The S_{21} measurement results for the lamb joint with different quantities of blood emulating liquid representing the hematoma

According to Figures 5.17 and 5.18, in simulations the relationship between the relative permittivity of the fracture and the amount of injected blood has a linear trend. The reason that such relationship does not exist in measurements is due to the mixing of the ingredients of the phantom's materials. As it was shown in Figures 5.14 to 5.16, during the first two blood emulating liquid injections, the bone (that consists of flour and olive oil), absorbs the injected liquid, this results to a homogenous 'fractured' area where the overall permittivity is a result of the mixture between bone and blood. As the amount of blood emulating liquid in the area increases with more injections, the liquid state of the blood dominates the semi solid form of the bone in the area. Thus, the flour of the bone cannot absorb any more liquid and starts dissolving. This results to the area being inhomogeneous (mainly blood emulating liquid with small pieces of flour), and to the measured permittivity being much closer to that of blood. Therefore, in measurements, as the amount of blood emulating liquid increases, and the losses increase with frequency, the relationship between permittivity and injected blood is expected to exhibit non linearities. This can be observed in Figure 5.21where for 6ml of injected blood liquid the S_{21} at 1GHz is -22.25dB with a step of ≈ -2dB for each frequency sample. As the mount of injected blood liquid increases to 10ml, the difference between the S_{21} at 1 and 2GHz is -6.17dB, at 2 and 3GHz is -5.17dB and at 3 to 4GHZ is -2.1dB with the 3GHz frequency sample exhibiting higher losses by 2.1dB than 4GHz.

This mixing of the ingredients is considered a limitation for phantom measurements often resulting to uncertainties and non linearities in measurements of the S_{21} for frequencies from 3GHz and above. This shows that it is necessary to do additional ex vivo measurements (see Figure 5.20) in order to validate the investigated model of fracture monitoring. This limitation is also mentioned in Section 3.2.7 on page 3-13 of Chapter 3.

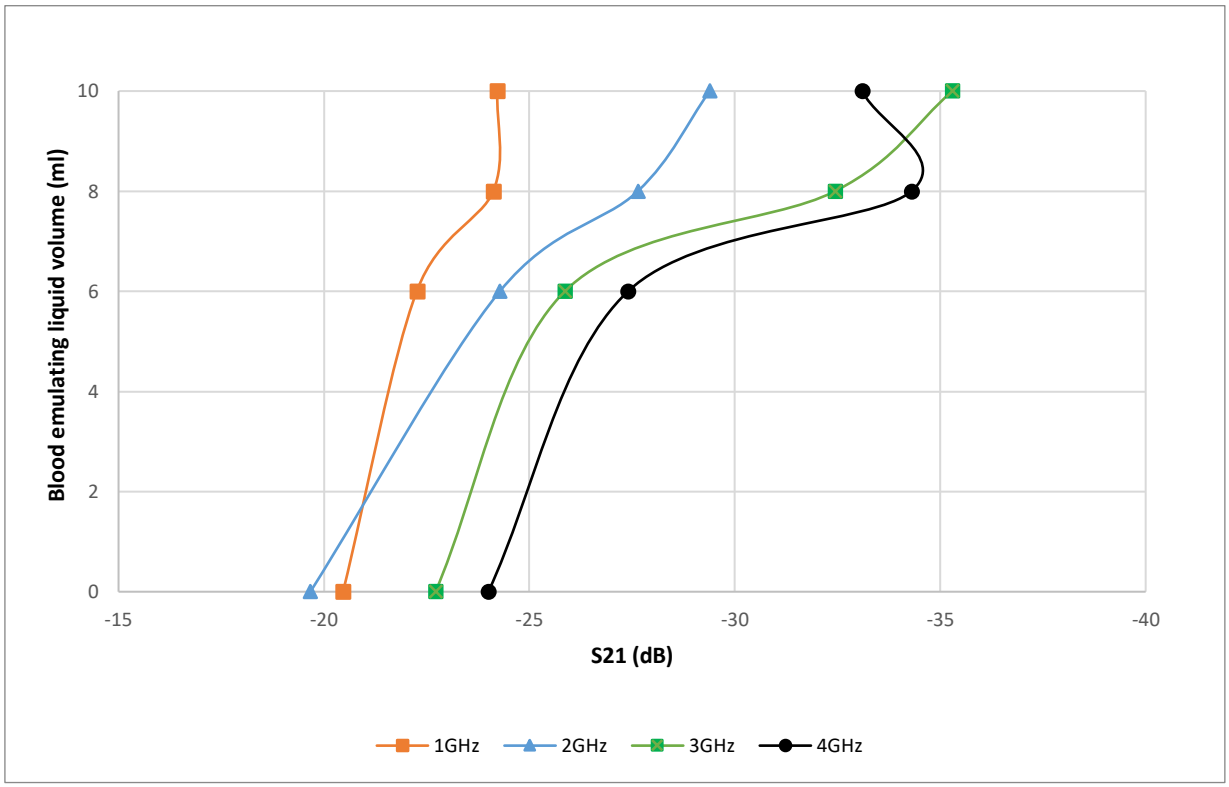

Figure 5.21: Blood emulating liquid volume versus S_{21} for four frequency samples (1 to 4GHz)

The attenuation of the S_{21} due to the losses of blood can be additionally observed in Figure 5.22 where the electric fields of the monopoles are depicted inside a simulated multi-material geometrical phantom that features the exact dimensions of the measured tibia bone phantom of Section 5.6.3 with and without the blood cylinders representing the bone fracture.

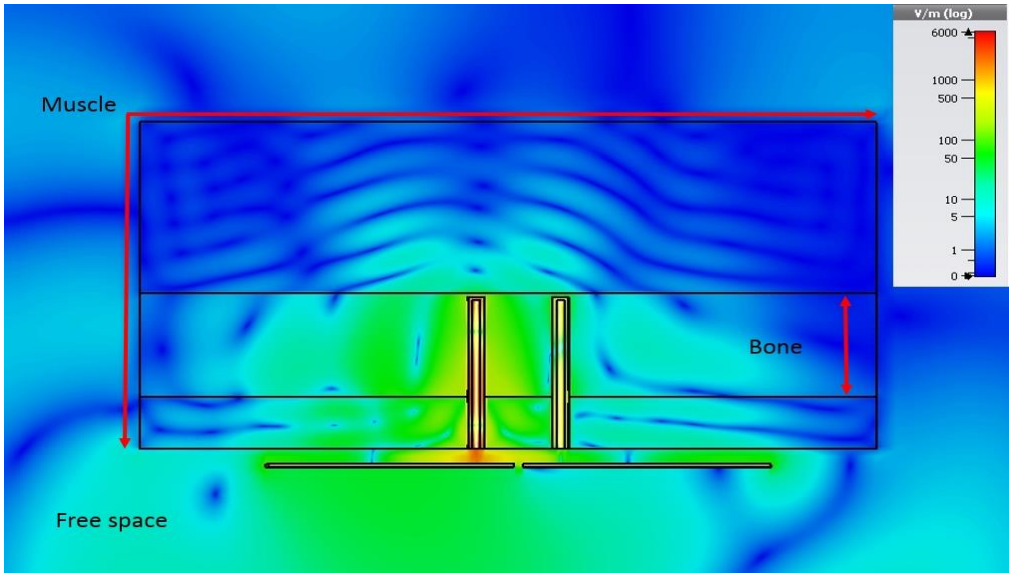

(a)

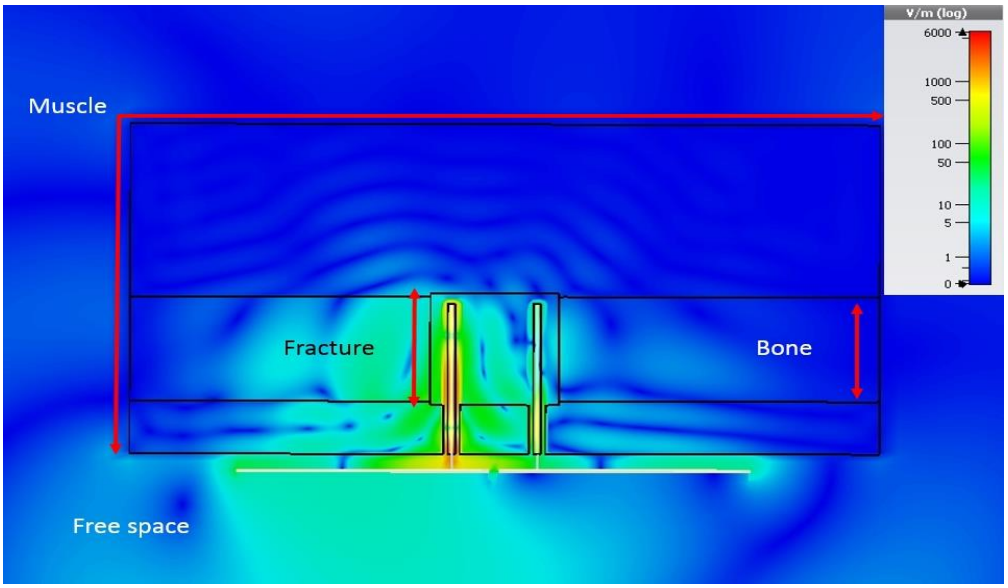

(b)

Figure 5.22: The maximum electric field of the monopoles inside a simulated tibia phantom a) without a blood cylinder, b) with a blood cylinder at 2.5GHz

The comparison between Figure 5.22a and Figure 5.22b shows that the magnitude of the electric field is greatly reduced inside the muscle and in free space when the blood cylinders are introduced by replacing the bone in the structure. The electric field of the monopoles in the Fresnel region ranges between $0.62\sqrt{\frac{D^3}{\lambda}} > R > \frac{2D^2}{\lambda}$ where D is the largest dimension of the

antennas and λ the wavelength. For 4cm monopoles, like the ones simulated in Figure 5.22, at the middle of the investigated frequency spectrum of 1 to 4GHz (2.5GHz), the Fresnel region of the electric field ranges between 1.4cm to 2.6cm. Therefore, the separation distance between the monopoles (2cm throughout this chapter) is located in the Fresnel region of the electric fields. According to [16] the attenuation of the electric field in this region is described by: $e^{-j\vec{k}\vec{r}}/\vec{r}$ where $\vec{k}$ is the wavenumber and $\vec{r}$ is the distance between the field point (x, y, z) and the source. The wavenumber k for lossy media depends on the relative permittivity, ε_r, and conductivity, σ, of each simulated tissue and is given by: $k = |\vec{k}| = \omega\sqrt{\mu_0\mu_r\varepsilon_0(\varepsilon_r - j\frac{\sigma}{\omega\varepsilon_0})}$. The relative permittivity and conductivity of blood are higher than that of bone over the frequency range 1 to 4GHz [17], [18], [38], i.e. ε_{rblood}= 58.1, σ_{blood} = 2.6 and ε_{rbone} = 11.3, σ_{bone} = 0.4 at 2.5GHz . Therefore, k is larger when the blood is present in the separation distance between the monopoles, thus, the attenuation of the electric field is greater when the blood cylinder or blood emulating liquid is introduced inside the phantom for simulations and measurements respectively, having as a result a worsening in the S_{21}magnitude as the volume of the blood increases (see Figure 5.20). The S_{21} attenuation in the simulations was broadly validated in measurements as the amount of blood increased in volume inside the bone, one difference being the additional resonances in the S_{21} seen in the measurements. In the ex-vivo measurements, it is not possible to create perfect geometric cylindrical shapes for the blood-emulating liquid. Creating a fracture with three circular holes only adds to the complexity of the bone's geometry. Furthermore, small bone fragments combined with the blood-emulating liquid and bone marrow of measurements are unlikely to perfectly mimic the homogenous blood properties of the simulation. As a result, the mixture inside the bone is likely to pose multiple different dielectric layers to the propagating wave. These are the likely causes of standing waves and resonances in the S_{21} in the measurements.

Since the relative permittivity and conductivity of blood is significantly higher than that of bone across the microwave frequency range, this behaviour of S_{21} is likely to be observed for much of this frequency range. Therefore, the monopole lengths could easily be adapted to fit the diameter and depth of any human bone likely to have external fixators. However, it is important to bear in mind that microwave attenuation increases dramatically with increasing frequency. So in order to obtain a measureable S_{21} above -40dB, it would be advisable to conduct measurements in the 1 to 4GHz frequency range.

Finally, the reverse process where the magnitude of the S_{21} increases after a bone fracture due to the reduction of blood, can provide an indication of the healing in the fractured area during the first four weeks after the trauma.

5.9 Conclusions

A technique for monitoring the healing of severe bone fractures, using a pair of radio frequency monopoles implanted in the bone has been investigated in this work. The magnitude of change of the S_{21} measurements of two implanted monopoles in the radius, phalange and tibia phantoms has shown to provide a good indication regarding the healing progress of different types of bone fractures that doctors use external metal plates for their treatment. These results have shown that, as the injected blood emulating liquid's volume increased inside the fracture, the transmission between the two monopoles is severely attenuated. This attenuation occurred in simulations using a voxel model of radius, tibia and phalange bones in CST microwave studio and in measurements using three geometrical phantoms of the same bones. This was due to the attenuation of the electric field caused by the high relative permittivity and conductivity of the injected blood emulating liquid. It was shown that since the relative permittivity and conductivity of blood is significantly higher than that of bone across the 1 to 4GHz frequency

range, this behaviour of S_{21} can be observed for much of this frequency range. The results were validated in an ex-vivo measurement of a bone fracture in a lamb joint.

The proposed method could provide a fracture monitoring technique during the first four weeks after the trauma. In a clinical context, no two fractures would ever be identical. The S_{21} that corresponds to a unified fracture 15cm down from the head of the femur in an elderly male is unlikely to be the same as a fracture 25cm down from the head of a femur in a young female. When the size of the fracture, the distance between the monopoles and their lengths are taken into account, there will be considerable variation in S_{21} between patients with consolidated fractures. Therefore, from this study at least, it would not be appropriate to equate an absolute value of S_{21} to consolidated fractures in general. Instead, the focus should be on the rate of change of S_{21} magnitude over time. If a fracture is healing in the normal way, the blood haematoma will reduce over time and there will be an associated continual improvement in the S_{21}. If the healing time can be estimated by the clinicians, then one would expect the rate of change of S_{21} to slow as that period comes to an end. If however, the rate of change of S_{21} drops well in advance of the estimated healing time, this system would indicate healing has stalled and would warrant further investigation by the clinicians. Chapter 6 will present a theoretical model regarding the parametric investigation for monopole separation distances between 1 to 7cm.

References

[1] K. Gupta, P. Gupta, G. Singh, S. Kumar, R. Singh, and R. Srivastava, “Change in electrical properties of bone as diagnostic tool for measurement of fracture healing,” *Hard Tissue*, vol. 2, no. 1, pp. 1–8, 2013.

[2] M. Khan, S. P. S. M. A. Sirdeshmukh, and K. Javed, “Evaluation of bone fracture in animal model using bio-electrical impedance analysis,” *Perspectives in Science*, vol. 8, pp. 567–569, 2016.

[3] T. Yoshida, W.-C. Kim, Y. Oka, N. Yamada, and T. Kubo, “Assessment of distraction callus in rabbits by monitoring of the electrical impedance of bone.,” *Acta Orthopaedica*, vol. 81, no. 5, pp. 628–633, 2010.

[4] S. Symeonidis, W. G. Whittow, M. Zecca, and C. Panagamuwa, “Bone fracture monitoring using implanted antennas in the radius, tibia and phalange heterogeneous bone phantoms,” *Biomedical Physics & Engineering Express*, vol. 4, no. 4, pp. 1–36, 2018.

[5] D. Kerns, “Plane-wave scattering-matrix theory of antennas and antenna-antenna interactions: formulation and applications,” *Journal of Research of the National Bureau of Standards*, vol. 80B, no. 1, pp. 5–51, 1976.

[6] “Reference Chart of Screws , Drill Bits , Taps and Guide Wires.” [Online]. Available: www.synthes.com. [Accessed: 20-Apr-2018].

[7] M. Peter, M. P. Stephan, and S. Norbert, “AO Principles of fracture management,” *AO Foundation*, 2014. [Online]. Available: https://www2.aofoundation.org/wps/portal/!ut/p/a0/04_Sj9CPykssy0xPLMnMz0vMAfGjzOKN_A0M3D2DDbz9_UMMDRyDXQ3dw9wMDAx8jfULsh0VAdAsNSU!/?bon

e=Tibia&segment=Shaft&soloState=lyteframe&contentUrl=srg/popup/further_reading/PFxM2/321_Scrws.jsp. [Accessed: 05-Oct-2017].

[8] M. Maniruzzaman, D. Douroumis, J. S. Boateng, and M. J. Snowden, "Hot-Melt Extrusion (HME): From Process to Pharmaceutical Applications," in *Recent Advances in Novel Carrier Systems*, Intech, 2012, pp. 1–15.

[9] Y. Ramot, M. Haim-Zada, A. J. Domb, and A. Nyska, "Biocompatibility and safety of PLA and its copolymers," *Advanced Drug Delivery Reviews*, vol. 107, pp. 153–162, 2016.

[10] "CST Homepage." [Online]. Available: https://www.cst.com/. [Accessed: 31-Jul-2017].

[11] C. Gabriel, "Compilation of the dielectric properties of body tissues at RF and microwave frequencies," *Environmental Health*, vol. 1, pp. 1–21, 1996.

[12] R. A. D. Carano and E. H. Filvaroff, "Angiogenesis and bone repair," *Drug Discovery Today*, vol. 8, no. 21, pp. 980–989, 2003.

[13] Y. Sheu *et al.*, "Vertebral bone marrow fat, bone mineral density and diabetes: The Osteoporotic Fractures in Men (MrOS) study," *Bone*, vol. 97, pp. 299–305, 2017.

[14] M. Doblaré, J. M. García, and M. J. Gómez, "Modelling bone tissue fracture and healing: A review," *Engineering Fracture Mechanics*, vol. 71, no. 13–14, pp. 1809–1840, 2004.

[15] R. M. Irastorza, S. Valente, F. Vericat, and E. Blangino, "Dielectric properties in fresh trabecular bone tissue from 1MHz to 1000MHz: A fast and non destructive quality evaluation technique," *Materials Science Forum*, vol. 638–642, pp. 730–735, 2010.

[16] M.-K. Hu, “Fresnel region field distributions of circular aperture antennas,” *Journal of Research of the National Bureau of Standards,* vol. 65D, no. 2, pp. 137–147, 1961.

[17] S. Symeonidis, W. G. Whittow, and C. J. Panagamuwa, “Characterisation of an Antenna System Implanted Into a Limb Phantom for Monitoring of Bone Fracture Healing,” in *Loughborough Antennas & Propagation Conference (LAPC)*, 2016.

[18] S. Symeonidis, C. Torres-Sanchez, C. Panagamuwa, and W. G. Whittow, “An Implanted Antenna System for the Monitoring of Bioresorbability of a Biocompatible Scaffold Embedded into a Bone Fracture,” in *MOBIHEALTH’15 Proceedings of the 5th EAI International Conference on Wireless Mobile Communication and Healthcare*, 2015, pp. 1–4.

[19] S. Symeonidis, W. G. Whittow, C. J. Panagamuwa, and M. Zecca, “An Implanted Antenna System for the Monitoring of the Healing of Bone Fractures,” in *2015 Loughborough Antennas & Propagation Conference (LAPC)*, 2015, pp. 1–4.

Chapter 6

An approximate method for calculating the mutual coupling of two monopoles into two-material lossy media

6.1 Summary

In Chapter 3, a detailed approach regarding the development and validation of bone marrow, bone cortical, muscle and blood phantom recipes for the frequency spectrum of 0.5 to 4GHz has been presented. These recipes were used in order to develop the phantom test beds of Chapters 4 and 5. According to the literature [1]–[3] and to the observations made in Chapter 3, blood has higher amount of losses compared to muscle and muscle has higher amount of losses compared to bone. Therefore, of the three investigated tissue types, blood is the lossiest. In Chapter 4 the design of the bone fracture monitoring test bed featuring two monopoles implanted in two multi-material phantoms was thoroughly analysed. In Chapter 5 these multi-material phantoms were given the diameters and tissue layers of a real life human finger, leg, and arm. The resulting analysis of Chapter 5 has shown that the proposed technique for monitoring the healing of severe bone fractures provides a good indication regarding the healing progress of different types of fractured bones. As shown in Chapter 5, the amount of blood that is injected into the phantom to emulate the bone fracture, is crucial to the amount of power transmitted from one monopole to the other. As the injected blood increases, the losses of the phantom also increase, thus, a lesser amount of the transmitted power of monopole A is received by monopole B. Last but not least, it has been shown that according to the average volume of blood that is formed around and inside a real life bone fracture, blood is the dominant loss

mechanism and is the reason why the S_{21} trend of the healing process is observable in the measurements and simulations of Chapter 5. Finally, the separation distance between the monopoles of the investigations of Chapter 5 was 2cm.

The purpose of this chapter is to provide the basis of an analytical method of calculation of the monopoles' S_{21} for any separation distance between 1 to 7cm. This is envisioned to enable doctors to use the proposed fracture monitoring technique of this thesis in bone fractures that require smaller or larger than 2cm spacing between the monopole - screws of an implanted metal plate. This method is based on the modification of an integral formula that is a near field counterpart of the Friis transmission equation. To the authors' best knowledge, this formula has been used in literature for the investigation of the coupling ratio (S_{21}) of two antennas for various separation distances only for free space propagation. In this work, the formula will be modified in order to approximate the S_{21} of a pair of 4cm length RF monopoles implanted into one single material geometric phantom and 2 two-material geometric phantoms with similar dimensions as the ones' investigated in Chapters 4 and 5. Therefore, the suggested modification will allow the formula to be utilized inside frequency dependent lossy media.

The amount of simulations required by CST microwave studio in order to provide the S_{21} for the separation distances of 1 to 7cm for every 1cm are seven. Considering that the monopoles are implanted into a body phantom of complex permittivity, this requires a lot of simulation time and computer resources. The method presented in this chapter will only require the electric far fields simulated in CST at the middle of the 1 to 7cm separation range (4cm) as inputs and will provide the approximated coupling ratios (S_{21}) of the implanted monopoles for all of separation distances in the 1 to 7cm range. Thus, the amount of necessary simulations will be minimized from seven to one.

In Section 6.2 an analysis of the existing literature regarding the integral formula and its application in free space is presented. In Section 6.3 the simulation setup that will be used for the verification of the modified integral formula is outlined. After this, in Section 6.4 the simulation results are discussed and in Section 6.5 the concluding remarks of this chapter are presented.

6.2 Analysis of the existing literature concerning the mutual coupling of antennas

In this section the existing literature regarding the free space approximation of the coupling integral will be examined. Consider a two-port network consisting of arbitrary antennas with a separation distance *d* between each other in free space (see Figure 6.1). The coordinate system is applied such that the origin coincides with the position of the transmitting antenna that is symbolized with subscript *t* (transmitter). The second antenna at distance *d* from the origin is indicated with subscript *r* (receiver). The incident voltage wave at the feedpoint of the transmitting antenna and the reflected voltage wave from the transmitter at the feeding point of the receiving antenna are denoted a_t and b_r respectively (see Figure 6.1). If the system is isolated and the receiving antenna is terminated in a matched load, then $|b_r|^2/|a_t|^2$ is the ratio of received to transmitted power. This power ratio is referred in the literature as the coupling ratio or the mutual coupling between the antennas and it is equivalent to the forward transmission coefficient of the scattering parameters $|S_{21}|^2$ [4]. According to the reciprocity theorem that describes the relations between two antennas, this is likewise equivalent to $|S_{12}|^2$ [5] and $S_{21}dB = 10 * \log(|S_{21}|^2)$.

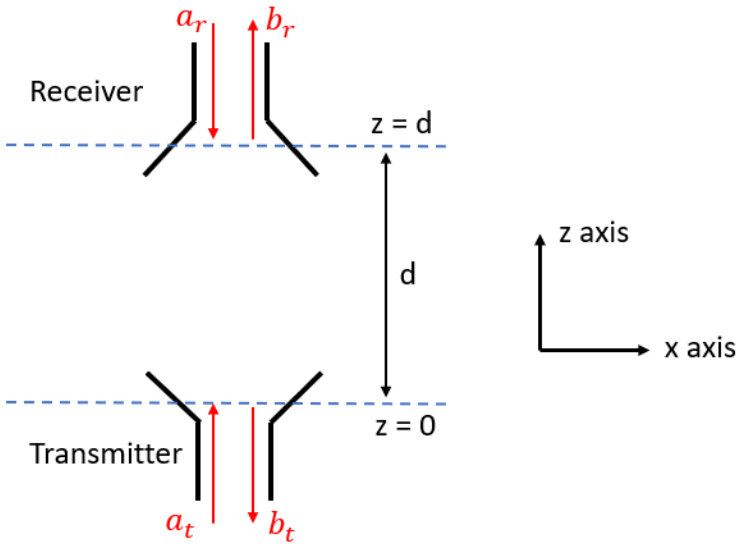

Figure 6.1: A two port network of antennas with complex voltage amplitudes (a_r, b_r, a_t, b_t) oriented along the y axis and separated by a distance d on the z axis

An accurate description of the mutual coupling between two antennas located in each other's far fields in free space is given by the Friis transmission equation [6]:

$$\left|\frac{b_r}{a_t}\right|^2 = G_t(0,0)G_r(\pi,\pi)\left(\frac{\lambda}{4\pi d}\right)^2 |\hat{n}_t \cdot \hat{n}_r|^2 , \tag{6.1}$$

where $\hat{n}_t$ and $\hat{n}_r$ are unit vectors describing the polarization of the receiving and the transmitting antennas and G_t and G_r their realized gain respectively in the system of coordinates of Figure 6.1.

In [6], Yaghjian extended the application of the Friis formula by presenting a near-field transmission integral based on the plane-wave scattering matrix description of antennas by Kerns [7]. This integral formula is a near-field counterpart of the Friis transmission equation that neglects multiple reflections and evanescent modes [8] and is valid for any antenna type used in near-field communication systems.

$$\frac{b_r}{a_t} = -\frac{C'}{k}\int_{K<k} d^2K \frac{\vec{f}_{r1}(-\vec{k})\cdot\vec{f}_{t1}(\vec{k})}{\gamma} e^{-j\gamma d} \tag{6.2}$$

Where C' is the mismatch factor and $\vec{f}_{r1}$, $\vec{f}_{t1}$ are the normalized far fields of the receiver and the transmitter accordingly. The wave vector, $\vec{k}$, is divided into components perpendicular and parallel to the z-axis that is consistent with $\vec{k} = \vec{K} + \gamma\hat{z}$ where $\vec{K} = k_x\hat{x} + k_y\hat{y}$ and $\gamma = \sqrt{k^2 + K^2}$, where $k = {2\pi}/{\lambda}$ is chosen to be real and positive for $K < k$ in free space. In Figure 6.1 the forward transmission of the antennas that is required for the calculation of the mutual coupling is parallel to the z axis, thus the components $k_x\hat{x}$ and $k_y\hat{y}$ are equal to zero. Therefore, $\vec{K} = 0$ and $\gamma = k$. The mutual coupling can then be calculated using Yaghjian's near-field transmission integral (6.2) from [6].

Since 1982, several authors have suggested modifications on Yaghjian's formula in order to achieve satisfactory adaptations depending on their envisioned context. Such a modification based on a version of Yaghjian's formula was presented by Frid et al in [9]. This method only needs the antenna far fields and the distance between the antennas to achieve a solution. Frid's equation will be used for the mutual coupling calculation throughout this chapter and its derivation is explained below [9]:

It is well known from the literature that the electric far-field of an antenna placed at the origin decays as $\frac{e^{-ikr}}{r}$ in the far-field region [10]; consequently, it is possible to describe the electric far-field using the vector far-field amplitude [9], using:

$$\vec{f}_{V_0}(\theta,\varphi) \equiv \frac{1}{V_0}\lim_{r\to\infty} re^{+jkr}\vec{E}(\vec{r}), \tag{6.3}$$

Where V_0 is a normalization constant of voltage. Function f is commonly denoted by $\vec{f}(\hat{r})$, $\vec{f}(\vec{k})$ or $\vec{f}(\theta,\varphi)$ in the literature depending on the context. All of the above notations refer to the far-

field that is normalized by V_0 as function of the spherical angles for one choice of angular frequency.

The normalized far-fields $\vec{f}_{r1}$ and $\vec{f}_{t1}$ of Yaghjian's equation (6.2) are denoted with index 1 by Frid et al. [9] in order to clarify that the choice of normalization constant V_o from [6] is used. The application of V_o from [6] requires the reflection coefficient and the characteristic impedance in the feeding port of the antenna to be known for the estimation of the mismatch factor $C' = \frac{Z_{RFeed}}{\eta(1-\Gamma_R\Gamma_L)}$ found in the integral equation (6.2). Where η is the intrinsic impedance of free space ($\simeq 377\ \Omega$), Z_{RFeed} is the characteristic impedance of the feedline of the receiving antenna and Γ_R and Γ_L are the reflection coefficients of the receiving antenna and its passive termination, respectively.

The integrand found in (6.2) has a singularity on or near the boundary of the integration domain ($K < k$) where γ =0, rendering a numerical evaluation difficult, thus, it was recommended to truncate the domain of integration closest to the singularity in the integrand [11], [12].

Frid et al. [9] suggested a method to improve the numerical properties of integrals that have singularities on the boundary of the integration domain by removing the singularity with a change of variables [11]. This was realized by the change of variables $K^2 + \gamma^2 = k^2$ and $\gamma = k\cos\theta$, thus according to the derivative equation in [13]: $d^2\mathrm{K} = KdKd\varphi = -\gamma d\gamma d\varphi = \gamma \sin\theta d\theta d\varphi$, therefore, it was shown to be possible for the integration to be calculated over the azimuthal (φ) and polar (θ) angles in the spherical system of coordinates:

$$\frac{b_r}{a_t} = \int_0^{\pi/2} d\theta \int_0^{2\pi} d\varphi\, \vec{f}_r(\pi-\theta,\ \pi+\varphi)\cdot \vec{f}_t(\theta,\ \varphi) e^{-j\gamma d}\sin\theta \qquad (6.4)$$

In order to avoid the calculation of C' found in equation (2), Frid et al. in [9] have derived an alternative choice of V_0 by embedding the coupling quotient $-C'$ to the dot product of the normalized far-field function.

$$\vec{f}_r(-\vec{k}) \cdot \vec{f}_t(\vec{k}) \equiv -C'\vec{f}_{r1}(-\vec{k}) \cdot \vec{f}_{t1}(\vec{k}) \tag{6.5}$$

To maintain consistency of [6] with [9], Frid et al. have based their alternative normalization of the far-fields on the method of stationary phase found in [5], [8]:

$$\left|\vec{f}(\theta,\varphi)\right|^2 = \frac{G(\theta,\varphi)}{4\pi} \tag{6.6}$$

Therefore, the antenna far-fields are given by:

$$\vec{E}(\mathrm{r},\theta,\varphi) = \vec{F}_p(\theta,\varphi)e^{-jkr}/r \tag{6.7}$$

And can be calculated for some known feeding power *P* in CST microwave studio [14]. Based on the equations (6.6) and (6.7), $\vec{f}$ in the system of coordinates of Figure 6.1 is calculated by Frid et al [9] as:

$$\vec{f}(\theta,\varphi) = \frac{\vec{F}_p(\theta,\varphi)}{\sqrt{P|\eta|}} \tag{6.8}$$

Thus, the corresponding choice of normalization variable for *Vo* of equation (6.3) is equal to $\sqrt{P|\eta|}$. The benefit of normalization formula (6.8) is that it only requires the normalized antenna far-fields, the feeding power of the antenna and the geometrical separation *d* as input. Hence, in equation (6.4) there is no need to determine the reflection coefficients which would otherwise have been required for calculating C'.

According to the system of coordinates of Figure 6.1 the forward transmission of the antennas that is required for the calculation of the mutual coupling is parallel to the z axis. Therefore, $\vec{K}$ = 0 and $\gamma = k$. Thus, for the condition that both the receiving and transmitting antennas are parallel to the y axis and separated by a distance *d* that is parallel to the z axis (see Figure 6.1) the formula found in (6.4) can be re-written as:

$$\frac{b_r}{a_t} = \int_0^{\pi/2} d\theta \int_0^{2\pi} d\varphi \, \vec{f}_r(\pi - \theta,\ \pi + \varphi) \cdot \vec{f}_t(\theta,\ \varphi) e^{-j|k|d sin\theta} \tag{6.9}$$

The origin and orientation of $\theta,\ \varphi$ angles of the far fields simulated in CST microwave studio is shown in Figure 6.2. The term $\vec{f}_r(\pi - \theta,\ \pi + \varphi)$ indicates the part of the normalized far field hemisphere of the receiver and the term $\vec{f}_t(\theta,\ \varphi)$ the part of the normalized far field hemisphere of the transmitter that are required for the calculation of the mutual coupling. The integration of the receiver's and the transmitter's far field hemispheres are taken in the domain of $\theta \in [0, \frac{\pi}{2}]$ and $\varphi \in [0, 2\pi]$ (see Figure 6.3).

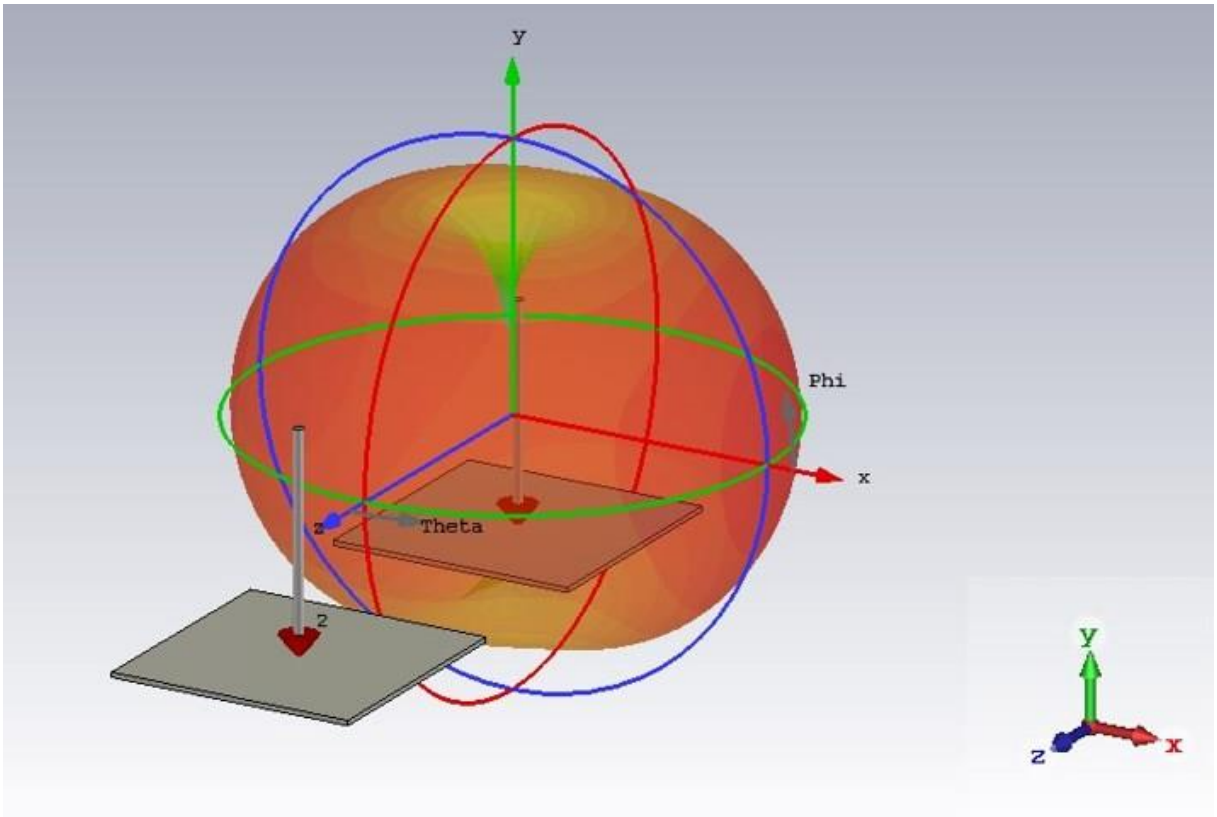

Figure 6.2: The orientation of theta (θ) and phi (φ) angles of the far field

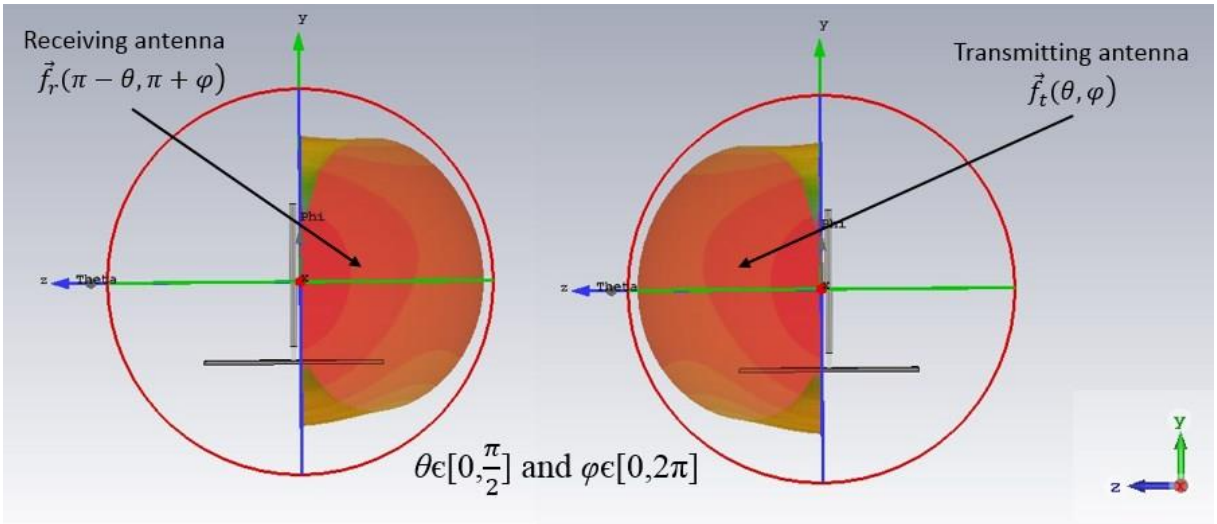

Figure 6.3: The normalized far field hemispheres$\vec{f}_t$, $\vec{f}_r$ used in equation (6.9)

It is worth mentioning that the integral relations (6.4) and (6.9) are derived by neglecting multiple reflections, however, these reflections are calculated when the normalized far fields from the CST Microwave studio are used as inputs to the equations [15]. The time-dependence $e^{j\omega t}$ in formulas (6.4) and (6.9) was assumed throughout all of the calculations.

6.3 The modified integral equation for lossy media

As stated in this Section 6.2, the integral equations (6.4) and (6.9) are used in literature for free space calculations, thus the wavenumber is $k = {}^{2\pi}/_{\lambda}$. The integral relation (6.9) will be used in this chapter for the evaluation of the mutual coupling between two monopoles inside 2 two-material phantoms. Therefore, the wavenumber of free space in equation (6.9) will be replaced by the wavenumber of lossy media that is: $k_{lossy} = \omega\sqrt{\mu_0\mu_r\varepsilon_0(\varepsilon_r - j\frac{\sigma}{\omega\varepsilon_0})}$ [7].

Additionally, the impedance of the phantom given by: Z = $\sqrt{j\omega(\frac{\mu_0}{\sigma} + \varepsilon_r\varepsilon_0)}$ [5] will be used instead of the impedance of free space, η, in the normalization equation (6.8). Thus, the normalization equation (6.8) will be re-written as:

$$\vec{f}(\theta,\varphi) = \frac{\vec{F}_p(\theta,\varphi)}{\sqrt{P|Z|}} \tag{6.10}$$

The wavenumber of lossy media, k_{lossy}will be assigned to the mutual coupling integral equation (6.9) that will be re-written as:

$$\frac{b_r}{a_t} = \int_0^{\pi/2} d\theta \int_0^{2\pi} d\varphi \, \vec{f}_r(\pi - \theta,\ \pi + \varphi)\cdot \vec{f}_t(\theta,\ \varphi) e^{-j|k_{lossy}|d sin\theta} \tag{6.11}$$

Hereafter, (6.11) will be referred to as the modified equation (6.11).

As a proof of concept, the modified equation (6.11) will be used to calculate the mutual coupling of two monopoles inside an one layer phantom consisting of muscle a) for a separation distance of 4cm over the frequency spectrum of 1 to 4 GHz; and b) for the separation distance range of 1 to 7cm at 2.5GHz. After this, a) and b) will be repeated by placing the two monopoles inside 2 two-material phantoms. In order to contain the maximum possible electric far field inside the phantom, its dimensions in terms of length, width and height will be the maximum achievable for processing by a computer with an i5 processor and 16GB of RAM. The results will be compared with the simulations of the scenarios a) and b) using the time domain solver of the CST electromagnetic simulator. Matlab will be used for the importing of the far field data into the modified equation (6.11).

This section will address the validation of the modified integral equation (6.11). For this validation, the two RF monopoles of Chapter 5 will be used (see Figure 6.4). The monopoles will be separated by a 4cm distance and implanted into 2 two material phantom test-beds with

identical geometries, consisting of muscle and bone (see Figure 6.6) and muscle and blood (Figure 6.7) in CST.

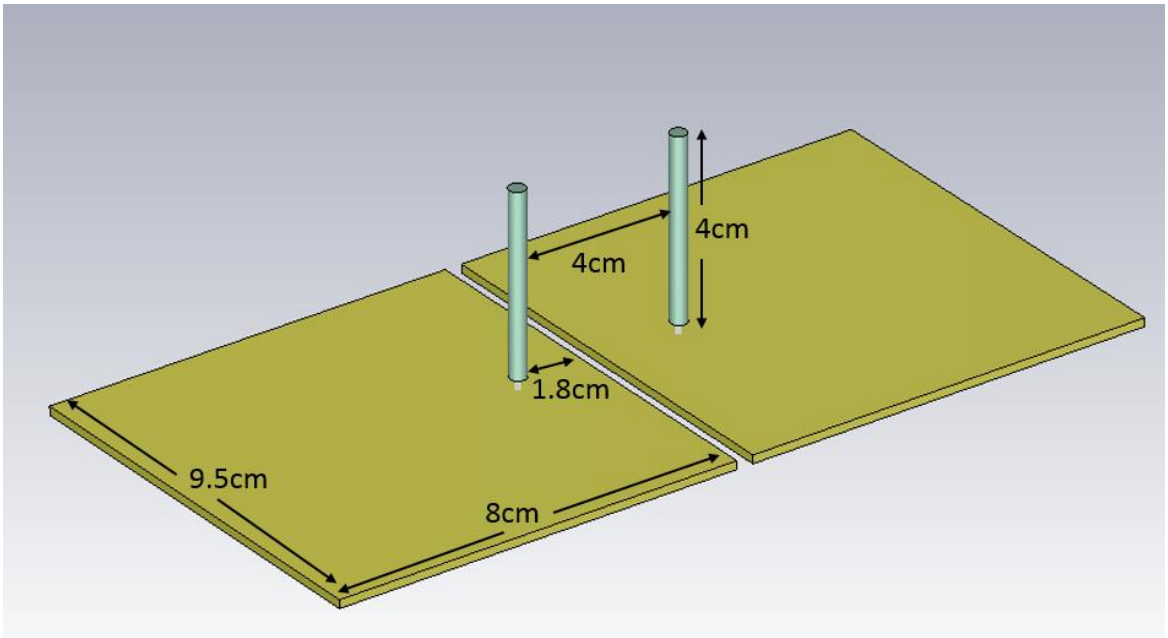

Figure 6.4: The geometric parameters of the two port monopole network for the frequency spectrum simulations at 4cm separation distance

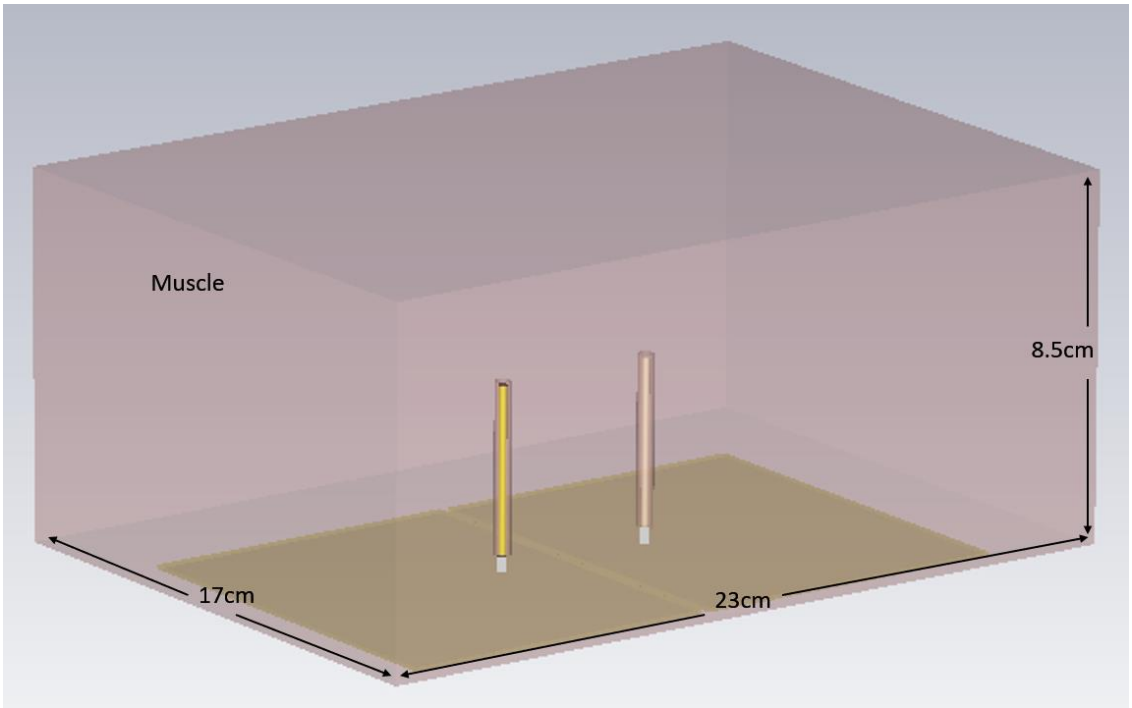

Figure 6.5: The geometric parameters of the one material phantom test-bed consisting of muscle for a 4cm monopole separation distance

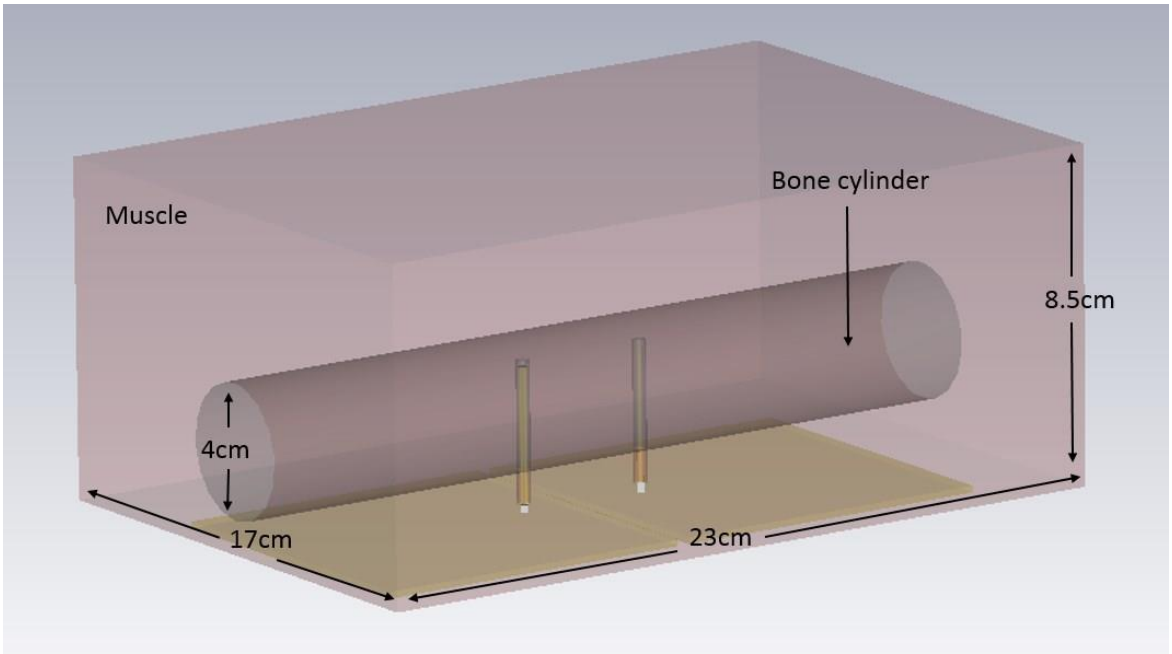

Figure 6.6: The geometric parameters of the two material phantom test-bed consisting of bone and muscle tissues for a 4cm monopole separation distance

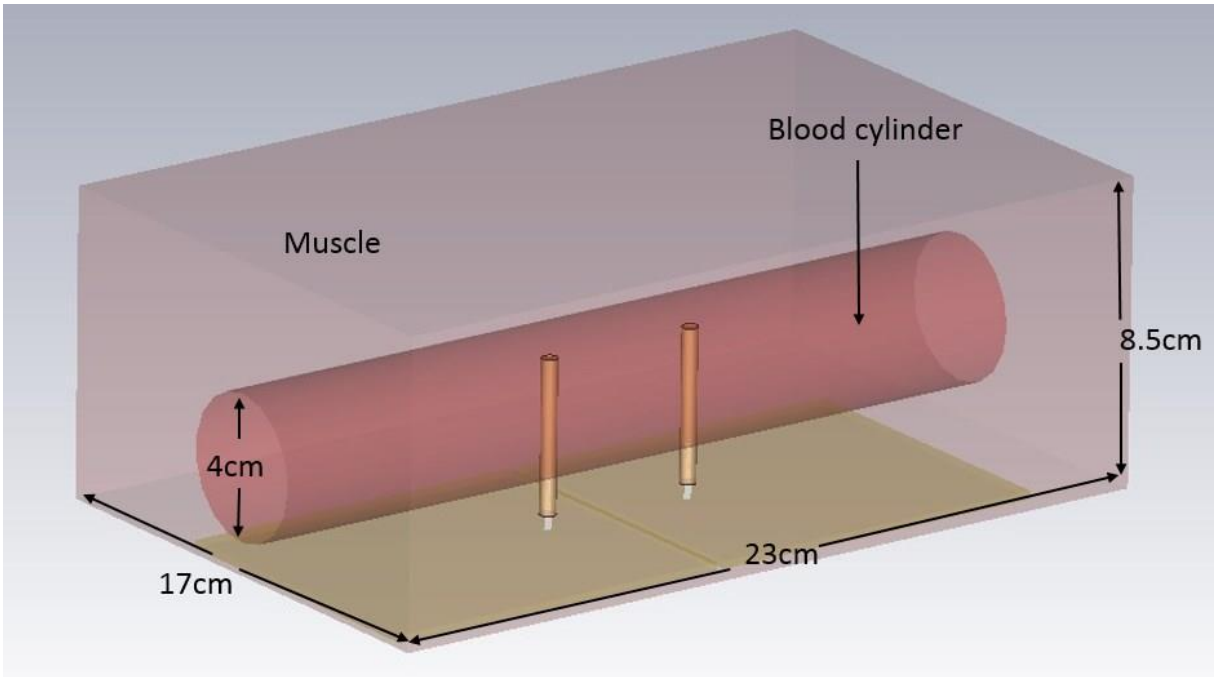

Figure 6.7: The geometric parameters of the two material phantom test-bed consisting of blood and muscle tissues for a 4cm monopole separation distance

The dielectric parameters of the simulated phantom layers were frequency dependent over the frequency range of 1 to 4GHz [1]. The dimensions of the muscle layer were 8.5 × 17 × 23cm (H × W × L). For the two material phantoms of Figure 6.6Figure 6.7, the bone and blood cylinders were 23cm long with 4cm diameter and the height of the bone cylinder from the bottom surface of the muscle is 0.5cm. The monopoles' groundplanes were positioned at 2mm distance from the bottom of the muscle's surface in order to avoid contact with the muscle layer.

The two monopoles used in the simulation had a diameter of 0.25cm and the material used for the insulation of their conducting parts was Teflon. The diameter of the coating was 0.35cm. This dimension was selected in order to insulate the monopole from the bone and muscle layers but sufficiently minimize the effect of Teflon's relative permittivity ($\varepsilon_r = 2.1$) on the wave propagation. The far-fields of the monopoles were calculated in CST Microwave studio, normalized using equation (6.10) and imported into the modified integral equation (6.11). The Matlab code used can be found in [16]. Thus, the notation $\vec{f}_r$ and $\vec{f}_t$ refers to the far fields of

the receiving and the transmitting monopoles respectively after they were normalized for a feeding power P = 1W and the impedance of the phantom given by Z. In order to calculate the impedance, Z, and the wavenumber, k, the volume ratio between the materials of each of the 2 two-material phantoms was used as an approximate method. According to Figure 6.6, 91.31% of the muscle – bone phantom consists of muscle and 8.69% of bone, therefore, $Z = 0.91*Z_{muscle} + 0.087*Z_{bone}$ and $k = 0.91*k_{muscle} + 0.087*k_{bone}$. The same process was applied for the muscle – blood phantom, using Z_{blood} instead of Z_{bone} and k_{blood} instead of k_{bone}.

The time-domain solver (FDTD) was selected as the electromagnetic solver. The benefit of using the FDTD solver is that the scattering parameters are computed as a function of frequency in comparison to other methods where only one frequency sample at a time is produced i.e. the integral solver. The main disadvantages of using FDTD is that the amount of mesh shells increases if the antenna separation is large, consequently, the computation time is also increased. In addition to that, the boundaries of each frequency monitor need to be set for each frequency monitor contrary to the integral solver that does not require user defined boundary conditions. Since the largest separation distance of the application presented in this chapter was 7cm, the FDTD was selected and used for all the problems in this chapter. In order to take into account the effects of the near field coupling between the monopoles for distances smaller than 4cm, two monopoles were used in the simulations at all times. The far-fields of both monopoles were used as inputs to the integral formula (6.9).

6.4 Simulated results and discussion

6.4.1 Free space simulations to compare with original equations

Initially, for validation purposes of the Frid et al. [9] formula (6.9), the two 4cm monopoles were simulated in free space, a) For a 4cm separation distance at the frequency spectrum of 1 to 4GHz and b) for the separation distances of 1 to 7cm. For these simulations, found in Figure 6.8 and Figure 6.9 respectively, the impedance of free space, $|\eta|$, was used and the wavenumber was: $|k| = \left|\frac{2\pi}{\lambda}\right|$. The far fields of each frequency monitor in a) and each separation distance simulation in b) were imported to the coupling integral equation (6.9). It will be shown later in this section that it is possible to calculate the S_{21} for b) with the modified integral equation (6.11) using only one frequency for the extraction of the monopole far fields. In addition to that, Figure 6.8 shows the comparison between the S_{21} produced by the integral equation (6.9) using as an input the whole far field spheres versus the hemispheres of the monopoles' far fields. As observed in Figure 6.8, the root mean square error of the magnitude of the S_{21} when compared to the CST simulation is 6.2% for the hemisphere input and 12.7% for the sphere input, therefore, as showed in [9] and [6] the hemispheres will be used as inputs throughout the rest of this chapter. It is worth mentioning that the best agreement between the CST simulation and the coupling integral calculation of S_{21} for the hemisphere input is found at 2.5GHz (see Figure 6.8). Therefore, the far field monitors of the monopoles obtained at that frequency will be used for the calculation of the separation distances of 1 to 7cm.

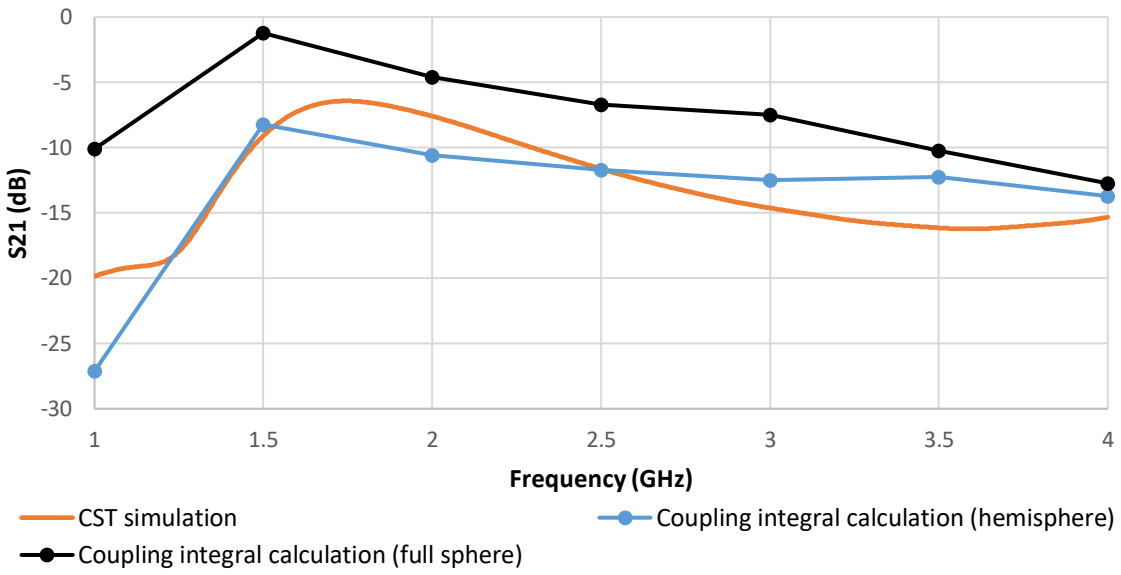

Figure 6.8: Monopole antennas comparison between CST simulations and coupling integral (6.9) calculations for the separation distance of 4cm in free space

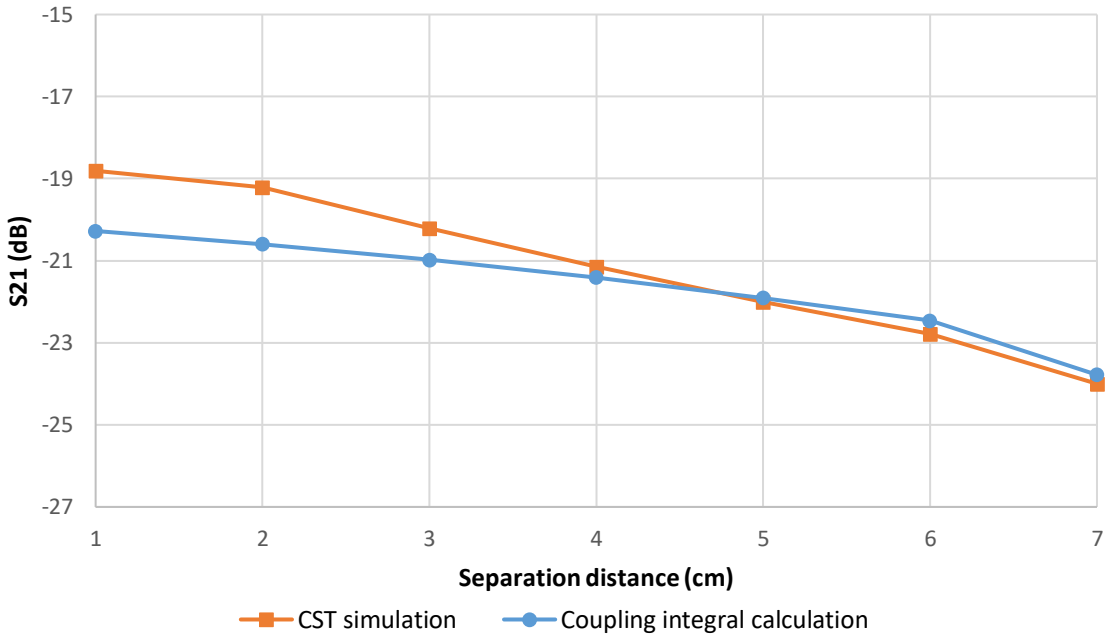

Figure 6.9: Monopole separation distance comparinson between CST simulations and coupling integral (6.9) calculations in free space at 2.5GHz

Figure 6.9 shows the separation distance comparinson between CST simulations and coupling integral calculations in free space. For these calculations the far fields obtained by CST for every 1cm of separation distance at 2.5GHz were used as inputs to the coupling integral equation (6.9) of Henrik Frid et al. [9]. Less than 0.5dB disagreement between the results can be observed at the 4cm separation distance and beyond. According to [6] the coupling integral equation produces more accurate results when the antennas are closer to the far-field region limit, defined by $kd >> 1$, with k being the wavenumber and d the separation distance. Due to the relatively small investigated separation distances compared to the far field limit, it is necessary to mention that the monopoles were placed in the Fresnel zone of the electric field ($kd > 1$). For instance, for a monopole separation distance of 4cm in free space, kd satisfies the Fresnel zone limit by being equal to 2.09 at 2.5GHz. Therefore, it is expected that the results of the coupling integral equation may not provide adequate accuracy as the monopole separation distance decreases. The wavenumber k for lossy media, such as the human tissues, has larger values compared to k in the free space. This is due to the higher relative permittivity and conductivity of these tissues when compared to the dielectric parameters of free space. For instance, at 2.5GHz for d = 4cm, the far field limit is $|kd| \approx 15.42$ inside a homogenous muscle phantom and 2.09 in free space. Therefore, the far-field relation $kd >> 1$ is better satisfied when the antennas are implanted into high permittivity lossy media.

6.4.2 Phantom simulations using the modified integral equation

The following simulation comparisons will be conducted inside an one material geometrical phantom consisting of muscle and 2 two-material geometrical phantoms with the exact same muscle layer geometries, one consisting of muscle and bone and the other of muscle and blood. The composition of the selected two material phantoms were chosen to represent the totally healed state (muscle - bone) and the totally fractured state (muscle - blood), it is envisioned that

future work will include in-between states like the ones investigated in Appendix C. In addition to that, the modified coupling integral formula (6.11) will be used for the calculations.

Figure 6.10 represents the comparison between the CST simulation and the modified equation (6.11) over the 1 to 4GHz frequency spectrum for the muscle phantom and Figure 6.11 represents the same comparison for the separation distances of 1 to 7cm for the at 2.5GHz. The root mean square error is 4.3% for the compared plots of Figure 6.10 and 3.6% for the plots of Figure 6.11. This small relative error shows that it is possible to calculate the $S_{21}$of the two monopoles inside an one layer lossy medium using the CST simulation results as inputs to the modified equation (6.11). In order to adequately represent a human limb, the investigation will continue with comparisons between simulations and calculations inside 2 two material phantoms.

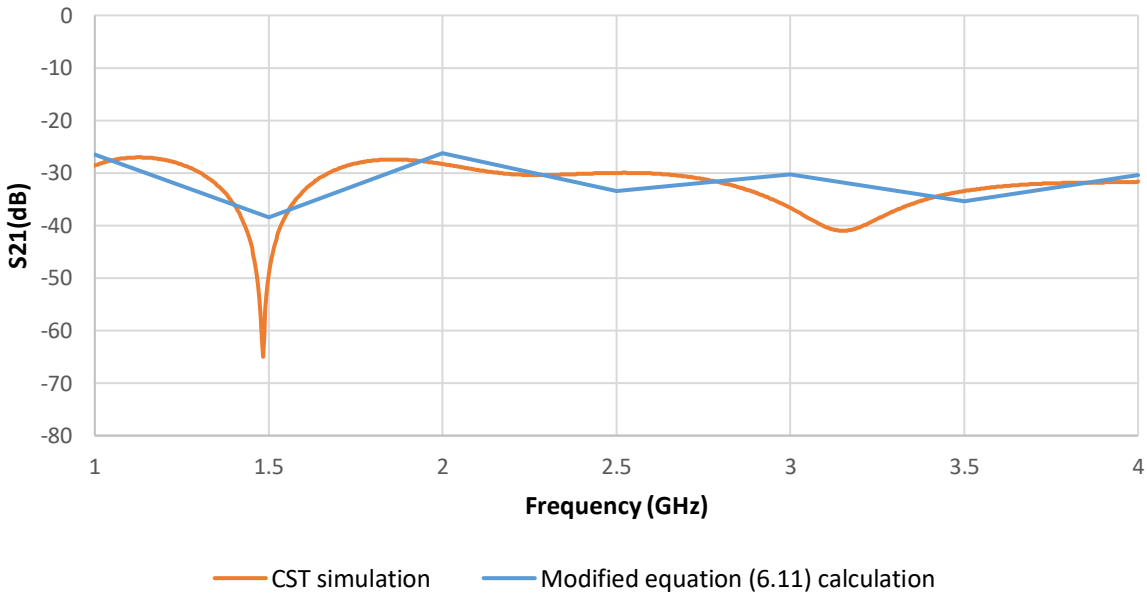

Figure 6.10: Comparison between the CST simulation and the modified equation (6.11) over the 1 to 4GHz frequency spectrum for the muscle phantom

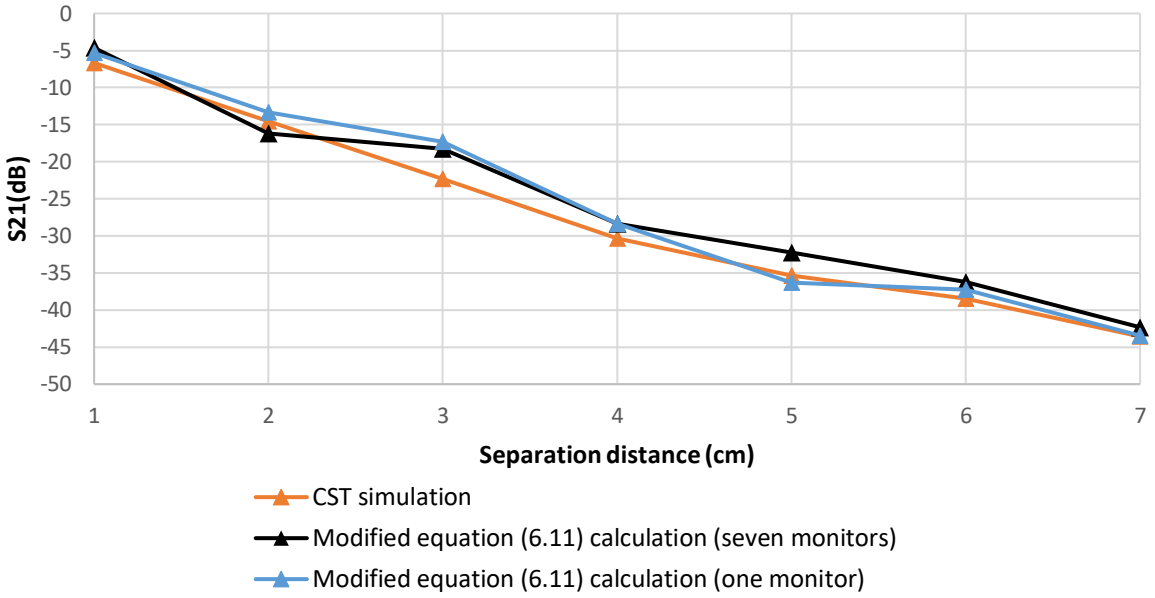

Figure 6.11: Comparison between the CST simulation and the modified equation (6.11) calculations for the separation distances of 1 to 7cm for the bone - muscle phantom at 2.5GHz

A possible way to increase the accuracy of the modified equation (6.11) is to increase the angular sample spacing of the imported far fields. This is achieved by changing the angle step width of the θ and φ angles in the far field plot properties in CST Microwave Studio from the default value in degrees to the desired one. In order to test this hypothesis, Figure 6.12 shows the comparison between 0.25° and 1° angle step width (angular sample spacing) simulated inside the bone – muscle phantom at the frequency spectrum of 1 to 4GHz. The far fields for each frequency of the monopoles were used as inputs to the modified equation (6.11) for the angular sample spacing of 0.25° and 1° as shown in the legend of Figure 6.12. The sample rate of 0.25° was the smallest obtainable sample by CST. It has shown to provide better accuracy of the S_{21} calculation compared to the 1° sample rate having a root mean square error of 3.3% between the CST simulation and the 0.25° calculation and 6.8% error for the 1°.

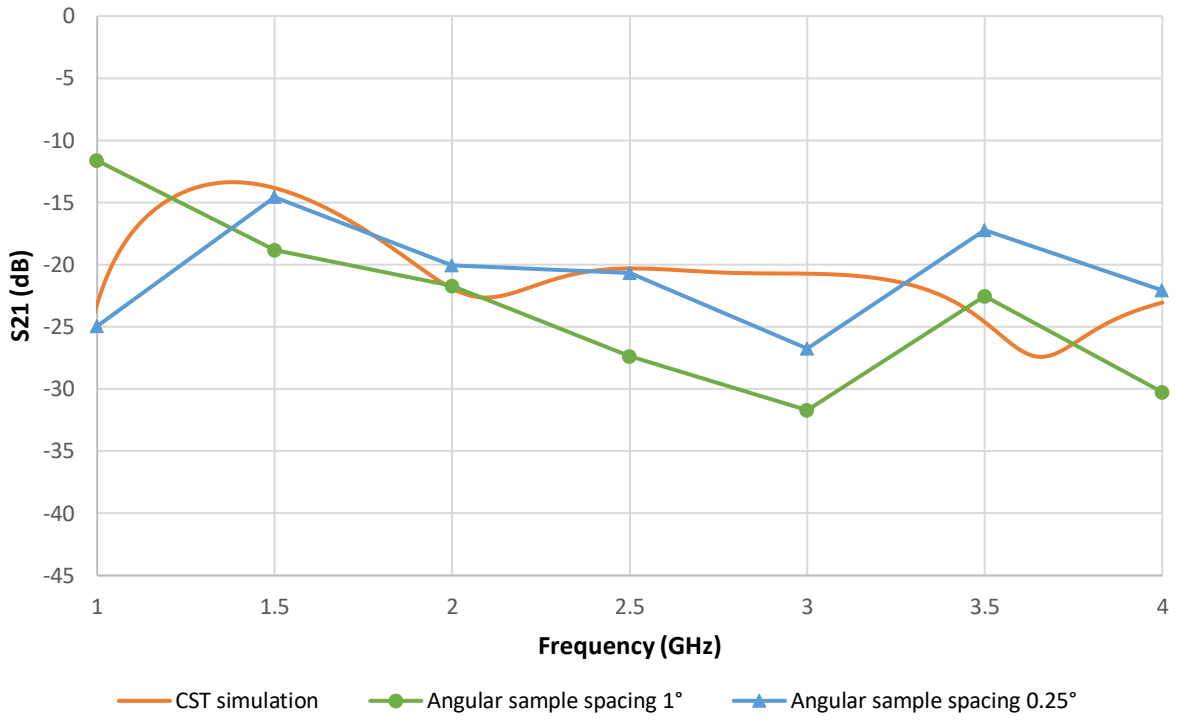

Figure 6.12: Comparison between the CST simulation and the modified equation calculations for the far field angular sample spacing's of 1° and 0.25° inside the muscle – bone phantom with a monopole separation distance of 4cm

In Figure 6.13 the two material phantom consisting of blood and muscle was used (see Figure 6.7). This was done for the reproduction of the conditions of a fully fractured bone. As in the previously reported experiments, the monopole length and separation distance was set at 4cm. The angular sample spacing of 0.25° was used for the calculation of the modified equation (6.11). The impedance of blood was used for the normalisation of the far field components that were located in the blood layer.

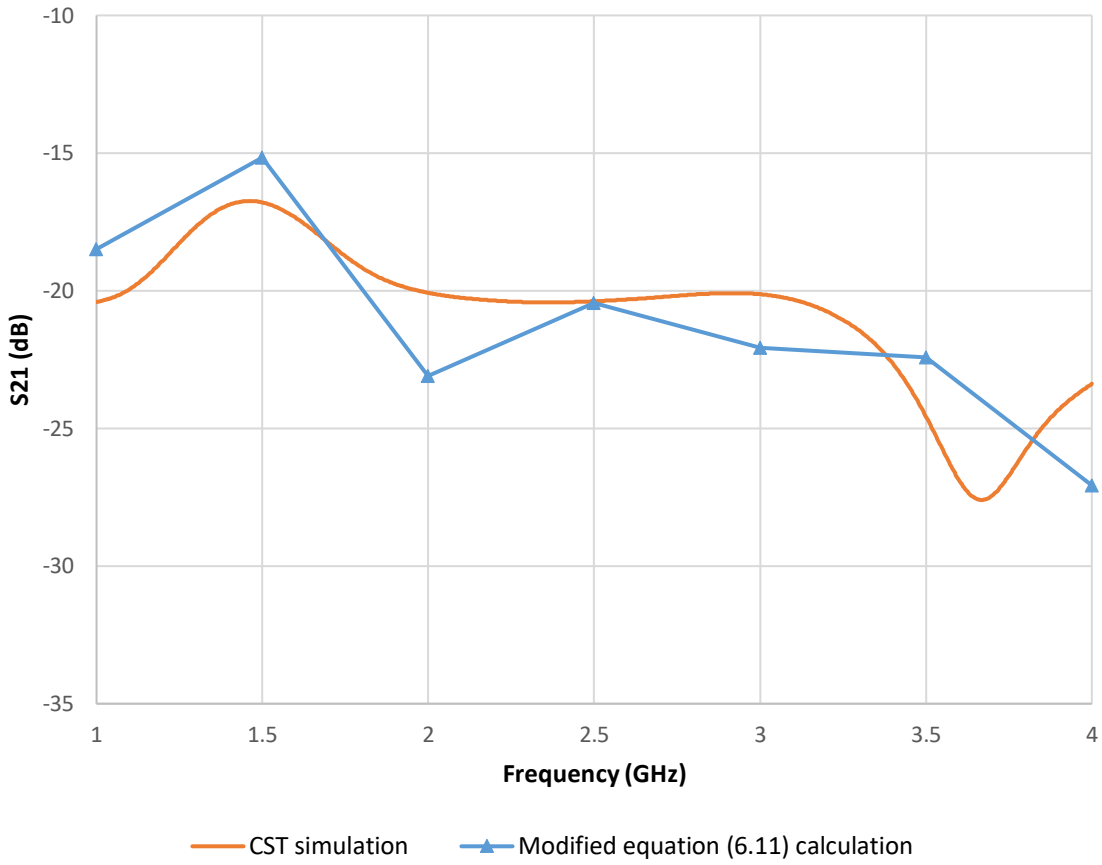

Figure 6.13: Comparison between the CST simulation and the modified equation (6.11) over the 1 to 4GHz frequency spectrum for the muscle – blood phantom with a monopole separation distance of 4cm

Figure 6.13 shows a 3.6% root mean square error of S_{21} magnitude between the CST and the modified equation calculations for the muscle – blood phantom. This is due to the close values of relative permittivity and conductivity of blood and muscle layers [2]. This, results in less reflections of the propagated wave at the interface of the phantom's layers, thus, less frequency mismatches [3]. As a consequence to that, closer agreement between the modified equation (6.11) results and the measured S_{21} can be expected for severe fractures in real life situations.

The comparison between the modified equation (6.11) and the CST simulations for the monopole separation distances of 1 to 7cm inside the 2 two material phantoms was investigated. The far fields were exported from CST at 2.5GHz. This frequency was selected due to the close match provided between the comparisons of Figure 6.12 for the bone and Figure 6.13 for the blood phantoms respectively at 2.5GHz. Figure 6.14 shows the comparison between the monopoles separation distances of 1 to 7cm. The seven CST simulations, one of each separation distance, were compared to the modified equation (6.11) results using a far field monitor for each separation distance (7 monitors total) and the modified equation (6.11) results using only one monitor at 4cm. The 4cm monitor was selected as it was at the middle of the investigated separation distance range. This comparison was repeated in Figure 6.15 following the exact same process at the blood – muscle phantom.

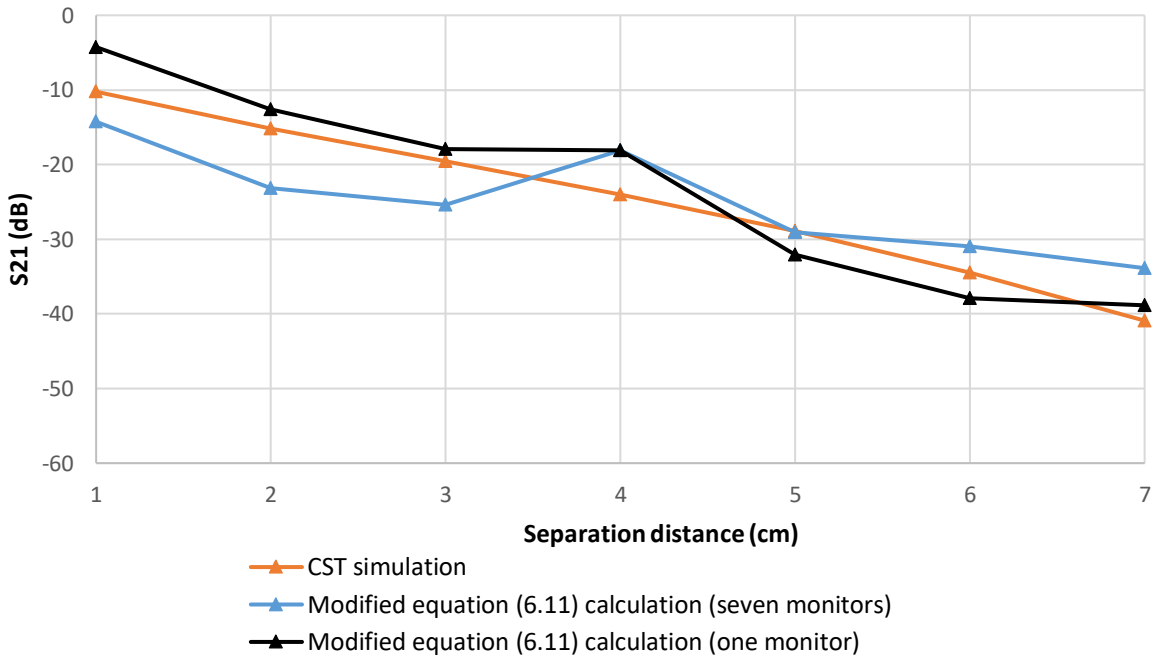

Figure 6.14: Comparison between the CST simulation and the modified equation (6.11) calculations for the separation distances of 1 to 7cm for the bone - muscle phantom at 2.5GHz

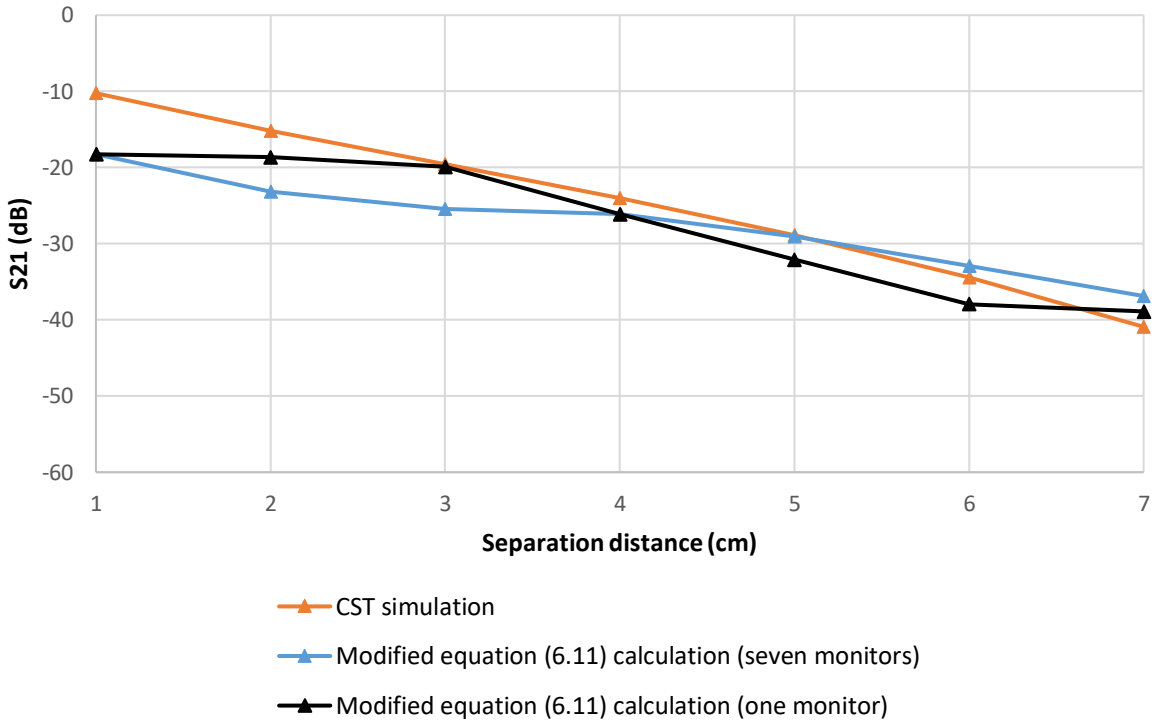

Figure 6.15: Comparison between the CST simulation and the modified equation (6.11) calculations for the separation distances of 1 to 7cm for the blood - muscle phantom at 2.5GHz

A 6.4% and 8.9% root mean square error between the CST simulations and the modified equation (6.11) calculations using one far-field monitor and seven monitors respectively has been shown in Figure 6.14 for the bone – muscle phantom. Figure 6.15 shows a 5.3% and 6.8% root mean square error between the CST simulations and the modified equation (6.11) calculations using one far-field monitor and seven monitors respectively for the blood – muscle phantom. Due to the coupling effect between the monopoles at near field distances ($|kd| \approx$ 19.27 for the separation distance of d = 5cm at 2.5GHz) the far field monitor samples taken at distances smaller than 5cm can add to the error of the modified integral calculations. Thus, the calculations made using one monitor at 4cm show a smaller error by approximately 1.5% for distances smaller than 4cm.

At 5cm and beyond, both seven and one monitor calculations provided better agreement with the CST simulations of the two investigated phantoms compared to distances smaller that 4cm, with the exception of 3cm of the bone – muscle phantom of Figure 6.14 and 1cm of the blood – muscle phantom of Figure 6.15 there was significant disagreement. As explained in the beginning of this section, the modified equation (6.11) produces more accurate results when the antennas are closer to the far-field region limit *(kd* >> 1) [6]. Therefore, as the separation distance reduces and the Fresnel region limit is satisfied (*kd* > 1), the accuracy of (6.11) also reduces. Despite that, the modified equation (6.11) provides good results for separation distances over 4cm. In addition to that, the overall accuracy of the modified equation (6.11) was shown to be least affected by the number of far field monitors. Therefore, using the modified equation (6.11) to approximate the monopole separation distances at the 1 to 7cm range with only one far field monitor taken at the midpoint of the separation range can greatly reduce the calculation time of the S_{21}.

6.5 Conclusions

In this chapter an analytical model for the calculation of the S_{21} of two monopoles inside a single material muscle phantom and 2 two-material phantoms has been demonstrated. A coupling integral equation found in the literature that approximates the S_{21} of two antennas in free space has been modified for lossy media implementation. The modified integral equation is a near field counterpart of the Friis transmission formula. The S_{21} results of the modified integral equation were validated at the frequency spectrum of 1 to 4GHz by comparisons with CST Microwave Studio simulations into 2 two-material phantoms. The two phantoms had identical geometries consisting of bone - muscle and blood – muscle accordingly. In addition to that, the modified equation can be used for the approximation of the S_{21} of two monopoles

for the separation distances of 1 to 7cm. It was shown that the modified equation produces more accurate results when the monopoles are closer to the far-field region limit *(kd* >> 1). As the separation distance reduced and the Fresnel region limit was satisfied (*kd* > 1), the accuracy of equation reduced accordingly. Despite that, the modified equation approximated the S_{21} by using one far field monitor obtained in the middle of the 1 to 7cm separation distance as an input from CST. This significantly decreased the required simulation time by reducing the amount of necessary simulations from seven to one.

References

[1] C. Gabriel, "Compilation of the dielectric properties of body tissues at RF and microwave frequencies," *Environ. Heal.*, vol. 1, pp. 1–21, 1996.

[2] R. W. Lau and C. Gabriel, "The dielectric properties of biological tissues: III. Parameteric models for the dielectric spectrum of tissues," *Phys. Med. Biol.*, vol. 41, pp. 2271–2293, 1996.

[3] F. Merli, "Implantable Antennas for Biomedical Applications," PhD Thesis, Ecole Polytechnique Federale de Lausanne, 2011.

[4] Robert E. Collin, *Foundations for Microwave Engineering, 2nd Edition*. Wiley-IEEE Press, 2000.

[5] C. A. Balanis, *Modern Antenna Handbook*. New York, NY, USA: Wiley-Interscience, 2008.

[6] A. D. Yaghjian, "Efficient computation of antenna coupling and fields within the near-field region," *IEEE Trans. Antennas Propag.*, vol. 30, no. 1, pp. 113–128, 1982.

[7] D. Kerns, “Plane-wave scattering-matrix theory of antennas and antenna-antenna interactions: formulation and applications,” *J. Res. Natl. Bur. Stand. (1934).*, vol. 80B, no. 1, pp. 5–51, 1976.

[8] Y. S. Chen, S. Y. Chen, and H. J. Li, “Analysis of antenna coupling in near-field communication systems,” *IEEE Trans. Antennas Propag.*, vol. 58, no. 10, pp. 3327–3335, 2010.

[9] H. Frid, H. Holter, and B. L. G. Jonsson, “An Approximate Method for Calculating the Near-Field Mutual Coupling between Line-of-Sight Antennas on Vehicles,” *IEEE Trans. Antennas Propag.*, vol. 63, no. 9, pp. 4132–4138, 2015.

[10] J. D. Jackson, *Classical Electrodynamics*, 3rd ed. New York, NY, USA: Wiley, 1999.

[11] G. Monegato and L. Scuderi, “Numerical integration of functions with boundary singularities,” *J. Comput. Appl. Math.*, vol. 112, no. 1–2, pp. 201–214, Nov. 1999.

[12] E. Lutz, “Exact Gaussian quadrature methods for near-singular integrals in the boundary element method,” *Eng. Anal. Bound. Elem.*, vol. 9, no. 3, pp. 233–245, Jan. 1992.

[13] T. Hansen and A. D. Yaghjian, *Plane-wave theory of time-domain fields: near-field scanning applications*. New York, NY, USA: IEEE Press, 1999.

[14] “CST Homepage.” [Online]. Available: https://www.cst.com/. [Accessed: 31-Jul-2017].

[15] H. Frid, “Efficient computation of the near-field mutual coupling between antennas on vehicles,” MSc Thesis, KTH Electrical Engineering, 2014.

[16] Symeon Symeonidis, “CST Microwave Studio - Matlab API,” 27-Sep-2018. [Online]. Available: https://doi.org/10.5281/zenodo.1237969. [Accessed: 06-Feb-2019].

Chapter 7

Conclusions

7.1 Summary of research and novelty

This thesis has investigated bone fracture monitoring using a pair of radiofrequency monopoles that will also act as the screws of an external medical metal plate used by surgeons for stability and alignment of the bone fragments. The research was conducted by producing body phantom recipes of bone marrow, bone cortical, blood and muscle and developing them into several heterogeneous geometrical body phantoms constituting an arm (radius), a finger (phalange) and a leg (tibia). The power transmitted from one monopole to the other (S_{21}) was measured and evaluated as an indicator for fracture healing as blood emulating liquid was injected inside the phantom emulating the conditions of a bone fracture. The conducted experiments showed that the power transmitted from one monopole to the other through the fracture decreased significantly by 15dB in total as the volume of the blood representing the fracture increased, thus providing doctors with a valuable monitoring tool regarding the state of a fractured bone during the first two to four weeks after the trauma which are critical for bone restoration. Additionally, the technique was shown to be fit for any monopole length, thus, screw length of the external metal plate that covers the entire diameter of the fractured bone. The results were validated in simulations using a voxel model in CST microwave studio and measurements using three multi-material geometrical phantoms and a lamb joint. The change in the S_{21} magnitude for each blood simulating liquid injection has been shown to be at least 3 dB averaged over the frequency spectrum of 1 to 4GHz for both voxel model simulations and phantom measurements.

As reviewed in Chapter 2 there is a limited amount of authors who have investigated similar techniques in literature, mainly focusing on measuring the impedance of the fracture using alternating current on the pins of a metal plate at the frequency spectrum of 2 to 50Hz with varying and contradictory results. This thesis has considered the novel area of using the screws of an external metal plate as monopoles at the frequency spectrum of 1 to 4GHz. This allowed the use of the knowledge obtained by the well-researched dielectric properties of the human body at the investigated spectrum that formulated the basis for the interpretation of the S_{21} magnitude behavior at different states of fracture healing. This, to the author's best knowledge has not been investigated in literature yet.

In Chapter 6, preliminary research for an approximate method for the near field coupling calculation inside multilayer phantoms was investigated. The analytical model was based on the near-field counter part of the Friis transmission equation and utilized the electric far-fields of the monopoles in order to approximate their mutual coupling in terms of S_{21} in the near field region. The mutual-coupling formula allowed the estimation of the S_{21} for monopole separation distances of 1 to 7cm and for a fixed separation distance of 4cm at the frequency spectrum of 1 to 4GHz and limited the need for simulations, thus allowing faster calculation time. The comparisons of the modified integral formula of Chapter 6 have shown a root mean square error of 3.3% between the CST simulations and the formula calculations for the muscle - bone phantom and a 3.6% error for the muscle – blood phantom over the 1 to 4GHz frequency spectrum for the 4cm monopole separation distance. In addition, the root mean square error for the monopole separation distances of 1 to 7cm between CST simulations and integral formula calculations was shown to be 6.4% for the muscle – bone phantom and 5.3% for the muscle – blood phantom. Previously, authors had only considered using this formula for the estimation of near coupling of antennas in free space. This thesis used the equation for complex wavenumbers that describe the lossy nature of human tissues while introducing an angle modification that

allowed more accurate results when more than one tissue occurs along the longest diameter of the implanted antennas.

7.2 Summary of results

The recipes developed in this thesis showed less than ± 5% error compared to their real-life tissue equivalent values according to the IEEE standards for phantom development [1] over the frequency spectrum of 0.5 to 4GHz, thus, they could be confidently used in novel body phantom applications. Using these recipes several phantoms were designed that possessed the versatility of emulating the anatomy and the geometry of any selection of human bones. The created phantoms also showed good agreement in comparisons of CST simulations and measurements of the S_{11} and S_{21} of two implanted monopoles.

Further on, a bone fracture was modelled as a varying percentage of blood emulating liquid and bone. The monopoles were used as the screws of an external medical metal plate and were placed perpendicularly at the left and right of the fracture. The rate of change of the S_{21} was shown to provide a tool that allowed the estimation of the amount of blood (hematoma) inside any bone fracture, having at least 3dB difference for each blood emulating liquid injection step. As the dielectric properties of the investigated fractured area shifted from the relative permittivity and conductivity of blood towards the relative permittivity and conductivity of bone, the losses of the region surrounding the monopole - screws were reduced and the magnitude of the S_{21} of the monopoles increased, thus, indicating bone healing.

The results were validated by taking dielectric measurements in the middle of the fracture using a semi-rigid coaxial probe and comparing the data to the estimated relative permittivity values of bone callus stages that reflect the progress of healing after a bone fracture. For additional

validation, measurements were conducted by injecting blood emulating liquid into a real lamb joint.

Finally, an analytical model on the approximation of the S_{21} of the monopoles in the near field inside multi-material phantoms was created. The results showed an agreement at the frequency spectrum of 0.5 to 4 GHz and on the parametric investigation of separation distance between them (1 to 7cm). This will allow application of the proposed technique for special types of fractures where the screws of the external fixation are separated by large distances. Last but not least, it was shown that this method approximated the S_{21} by using one far field monitor obtained in the middle of the 1 to 7cm separation distance as an input from CST. This significantly decreased the required simulation time by reducing the amount of necessary simulations from seven to one.

7.3 Perspectives for industry

Throughout this thesis it has been shown that the S_{21} of two monopoles embedded into an external metal plate can provide an indicator of the hematoma reduction that signifies fracture healing. This monitoring technique can be provide accurate results the first four weeks after a severe bone fracture and has been shown through the measurements of Chapter 5 that this period can be extended up to the point of complete bone healing if necessary. Besides the monitoring capabilities of the proposed technique the initial four weeks that X-ray and CT scanning cannot be implemented if the metal plates are ferromagnetic; it can greatly reduce the yearly cost of maintenance of X-ray and CT scanning machines, that ranges from £6,680 to £28,200 for X-ray scanners [2] and from £59,000 to £77,973 for CT scanners [3] for each device, considering that the monitoring period is extended. According to NHS statistics of the year of 2016, over 65,000

people aged 60 or older attended to 177 hospitals in England, Wales and Northern Ireland for just osteoporotic bone fractures, raising the cost of social care to £1 billion per year [4]. It is estimated that Britain being the country with the less amount of diagnostic imaging machines per hospital has at least one to two CT and X-ray scanners per hospital and France being the most has at least three to four [5]. Therefore, the implementation of the proposed RF technique can greatly reduce the yearly cost of maintaining these imaging devices and allow the funds intended for this purpose to be utilized for other purposes, such as the improvement of the quality of treatment of patients and the recruitment of additional medical personnel.

7.4 Future work

This thesis has produced multiple new results regarding bone fracture monitoring in the radiofrequency spectrum. However, there are improvements and open issues that should be further investigated. Future work will include the design of a real-life external metal plate that will feature the embedded monopoles investigated in this thesis. The monopole screws will be insulated using 3D printed biocompatible coatings with the exact geometries of commercially available medical screws. Further on, in vivo measurements will be conducted in lambs for further adjustment of the results until the method is validated for human trials. Due to the variety of bones and bone fractures and the validity of the technique for any monopole length that is proportional to the diameter of the fractured bone, the method has the potential to be tested in any bone fracture location that surgeons use external metal plates as a preferable treatment strategy. In addition to that, several muscle-bone phantom size ratios that correspond to different human body types will be investigated.

The relative permittivity and conductivity of the soft bone (callus) that is formed after the initial stage of hematoma and triggers the bone healing process after a fracture, has not been adequately reported in literature yet. Several in vivo and vitro dielectric measurements are necessary in order to obtain samples of the callus at its initial stage of formation after the hematoma until the stage of healthy bone formation. This information will provide an additional tool in fracture monitoring allowing the identification of the state of a fracture by comparing its dielectric properties to the will - known properties of each callus stage. Therefore, the utilization of non-invasive techniques, such as measuring the relative permittivity and conductivity using microwave imaging techniques might be possible.

Further research will be done using the analytical model of the antenna coupling presented in Chapter 6. Future work will include a technique using a modification angle that dictates the ratio of normalization of the propagated monopole far fields according to their location inside 2 two-material phantoms. It will be investigated whether it is possible for this angle to be used for the improvement of the agreement between the CST simulations and the modified integral equation calculations inside the 2 two-material phantom test beds. In addition to that, the design of a model using the Fresnel equations instead of the far-field, for implanted radiators with separation distances that vary between $0.62 \cdot {}^{D^3}/_{\lambda} < R \leq 2 \cdot {}^{D^2}/_{\lambda}$ where D is the largest physical linear dimension of the antenna and R the separation distance; will provide greater accuracy upon conducting parametric calculations of the coupling ratio on varying distances inside R. These calculations will be crucial for the optimization of applications such as the RF ingestable pills that feature antennas communicating with base stations out of the body while their depth varies inside the body and exhibit limited radiation capabilities due to their size.

References

[1] IEEE Standards Coordinating Committee 34, *IEEE Recommended Practice for Determining the Peak Spatial-Average Specific Absorption Rate (SAR) in the Human Head from Wireless Communications Devices: Measurement Techniques*, no. February. The Institute of Electrical and Electronics Engineers, Inc., 2003.

[2] Stephen Loomis, "X-Ray Equipment Service Cost Price Info," *Block Imaging*, 2016. [Online]. Available: https://info.blockimaging.com/x-ray-equipment-service-cost-price-info. [Accessed: 11-Jan-2018].

[3] Stephen Loomis, "CT Scanner Service Cost Price Info," *Block Imaging*, 2016. [Online]. Available: https://info.blockimaging.com/bid/95421/ct-scanner-service-cost-price-info. [Accessed: 11-Jan-2018].

[4] Royal College of Physicians, "National Hip Fracture Database (NHFD) Annual Report," Oxford, 2017.

[5] "Healthcare resource statistics - technical resources and medical technology - Statistics Explained," *Eurostat*, 2017. [Online]. Available: http://ec.europa.eu/eurostat/statistics-explained/index.php?title=Healthcare_resource_statistics_-_technical_resources_and_medical_technology&oldid=280129. [Accessed: 11-Jan-2018].

Appendix A

This appendix describes the simulated comparison of the dielectric properties of muscle tissue using the coaxial probe technique of Chapter 3, Section 3.4 versus the relative permittivity and conductivity values measured by Gabriel et al. [1]. Figure A.4 shows the geometry of the simulated test bed. The probe used for the simulation is identical to the probe used for the measurements of the recipes of Chapter 3 (9.5cm length, 3mm diameter). The pink box was given the dielectric properties of muscle over the frequency spectrum of 0.5 to 4GHz. As explained in Chapter 3 the open – short – deionized water calibration was followed. For the open measurement, the S_{11} of the probe was captured in free space. For the short calibration, a sheet of copper was placed in contact with the sliced end of the coaxial cable uniting its inner conductor with the outer. Finally, for the load calibration, the probe was immersed in a box with the dielectric properties of deionized water (see Figure A.1). Figure A.2 and Figure A.3 show the linear magnitude and phase of the open, short and load measurements of the coaxial cable. The phase difference between the open and the short calibration measurement is 180° (Figure A.3), this is also stated by Balanis in [2]. After the open – short – load calibration, the coaxial probe has been immersed into the muscle box. Figure A.4b shows the three points of entry of the coaxial probe into the muscle box, with 2 being at the centre of the box's top surface. Location 1 is in the mid distance between the left end of the box and location 2 and location 3 is in the mid distance between the right end of the box and location 2.

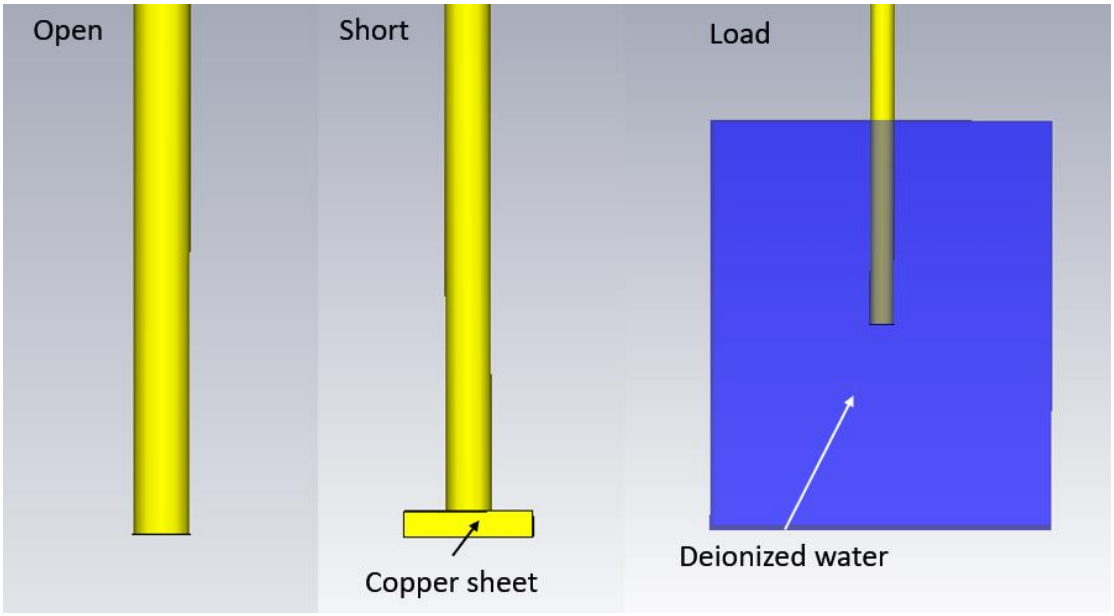

Figure A.1: The open – short - load calibration of the coaxial cable

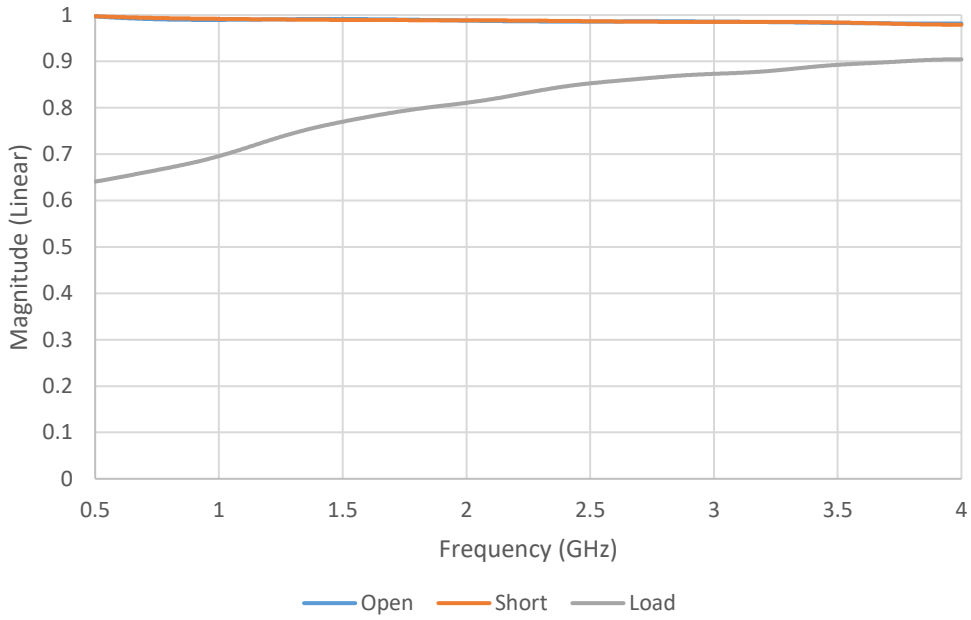

Figure A.2: The linear magnitudes of the open – short – load measurements

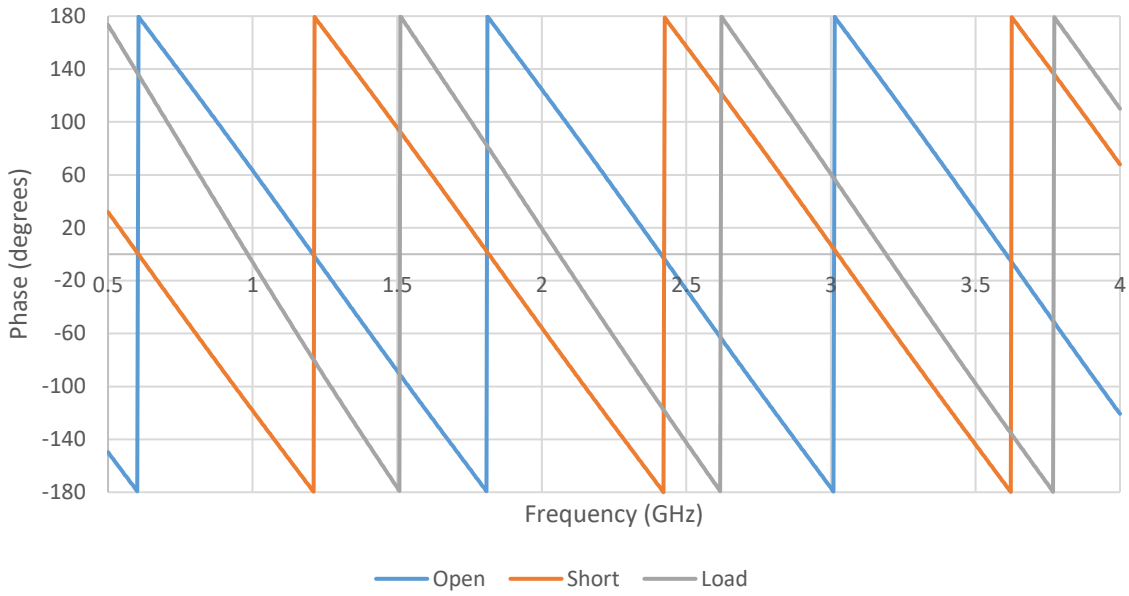

Figure A.3: The phases of the open – short – load measurements

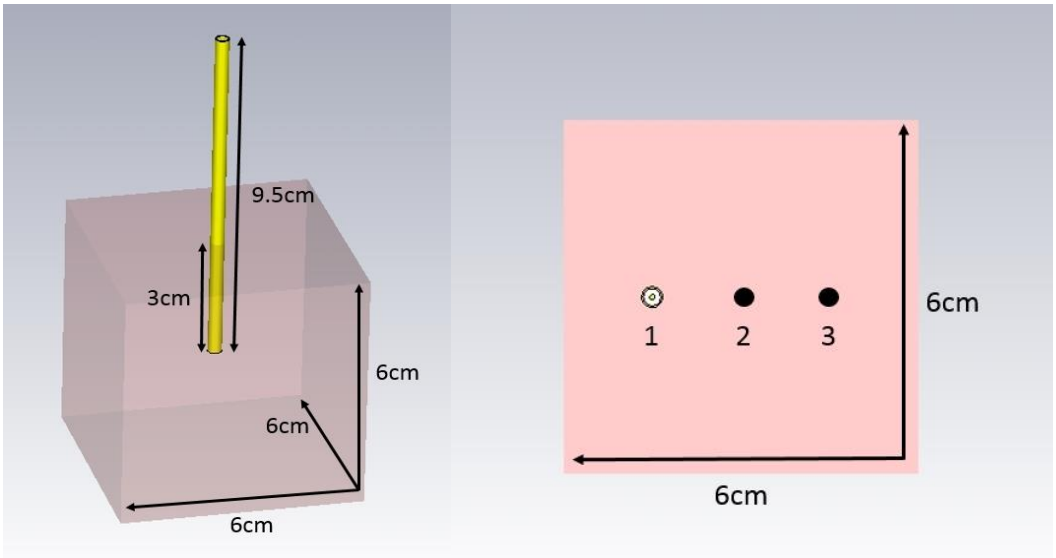

Figure A.4: Muscle tissue box dimensions with the probe being implanted in the middle of the box (left), with the three points of entry of the probe for the three samples taken (top view) (right)

Figure A.6 shows the S_{11} of the coaxial probe implanted into the muscle box over the frequency spectrum of 0.5 to 4GHz for each of the three locations shown in Figure A.4. Figure A.7Figure A.8 show the relative permittivity and conductivity calculated using the S_{11} of Figure A.6 as input to the Microsoft© Excel spreadsheet produced by the authors of [3], versus the muscle tissue values of CST Studio 2017 that are identical to the values measured by Gabriel et al [1]. The mean square error of the probe's measurements is equal to 0.46 for relative permittivity and 0.018 for conductivity over the frequency spectrum of 0.5 to 4GHz. The formulas used for the calculation of the relative permittivity and conductivity of the investigated material from the S_{11}can be seen in Chapter 3 pages 3-16 and 3-17. Figure A.5 shows the Matlab code that was built

for demonstration purposes using the formulas (3.1) – (3.4) for the calculation of the relative permittivity and conductivity of muscle at 1.5GHz.

```
1
2       % The measurement frequency in GHz
3 -     Frequency = 1.5;
4
5       % The complex S11 value of the probe immersed
6       % into a liquid of unknown dielectric properties
7 -     UnknownLiquid = 0.185392 + 1j*0.680845;
8
9       % The complex S11 value of the probe in Open Circuit
10 -    OpenCircuit = -0.984988 -1j*0.0443363;
11
12      % The complex S11 value of the probe in Short Circuit
13 -    ShortCircuit = 0.979135 +1j*0.110103;
14
15      % The complex S11 value of the probe immersed
16      % in deionized water
17 -    DeionizedWater = 0.437041+ 1j*0.756004;
18
19      % The calculations of Chapter 3 page 3-16
20 -    N = UnknownLiquid - OpenCircuit;
21 -    O = ShortCircuit - DeionizedWater;
22 -    P = UnknownLiquid - ShortCircuit;
23 -    Q = DeionizedWater - OpenCircuit;
24 -    R = UnknownLiquid - DeionizedWater;
25 -    S = OpenCircuit - ShortCircuit;
26
27 -    U = 2*1j*Frequency*pi*(10^9)*9.31*10^-12;
28 -    V = exp((log(U)*0.986)) + 1;
29 -    W = (V^-1)*(78 - 4.6) + 4.6;
30 -    X = ((P*Q)^-1)*O*N*W*(-1);
31
32      % The complex permittivity
33 -    Permittivity = X -((P*Q)^-1)*R*S;
34      % The relative permittivity
35 -    RelativePerm = real(Permittivity)
36      % The conductivity
37 -    Conductivity = imag(Permittivity)*8.854*(10^-12)*Frequency*(10^9)*pi*2*(-1)
38
```

Figure A.5: The matlab code used for the extraction of the relative permittivity and conductivity from S_{11}

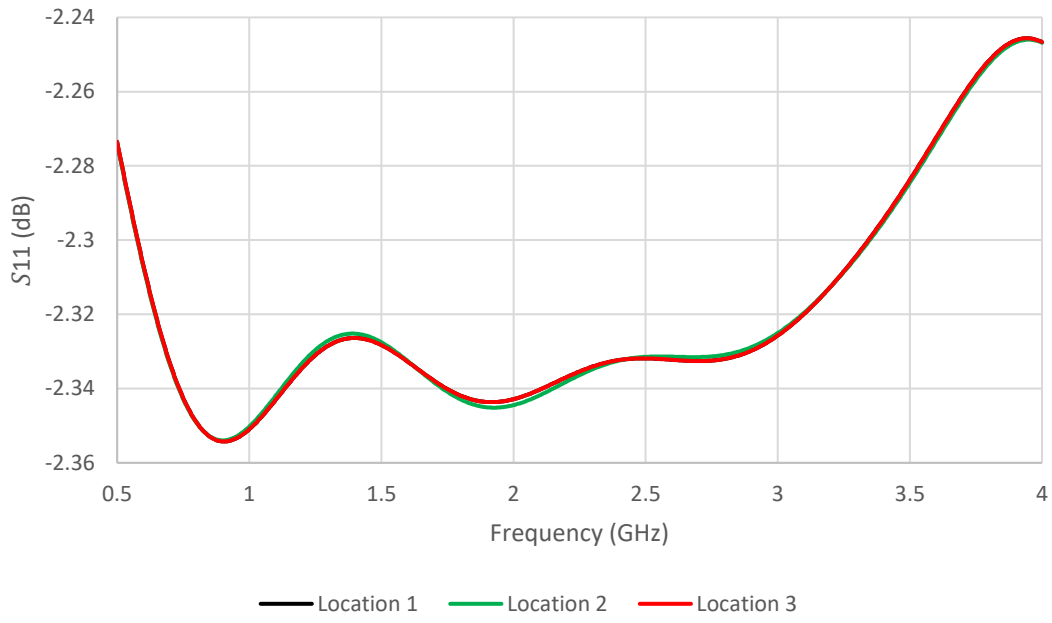

Figure A.6: The return loss of the coaxial probe taken at the three locations indicated in Figure A.1b

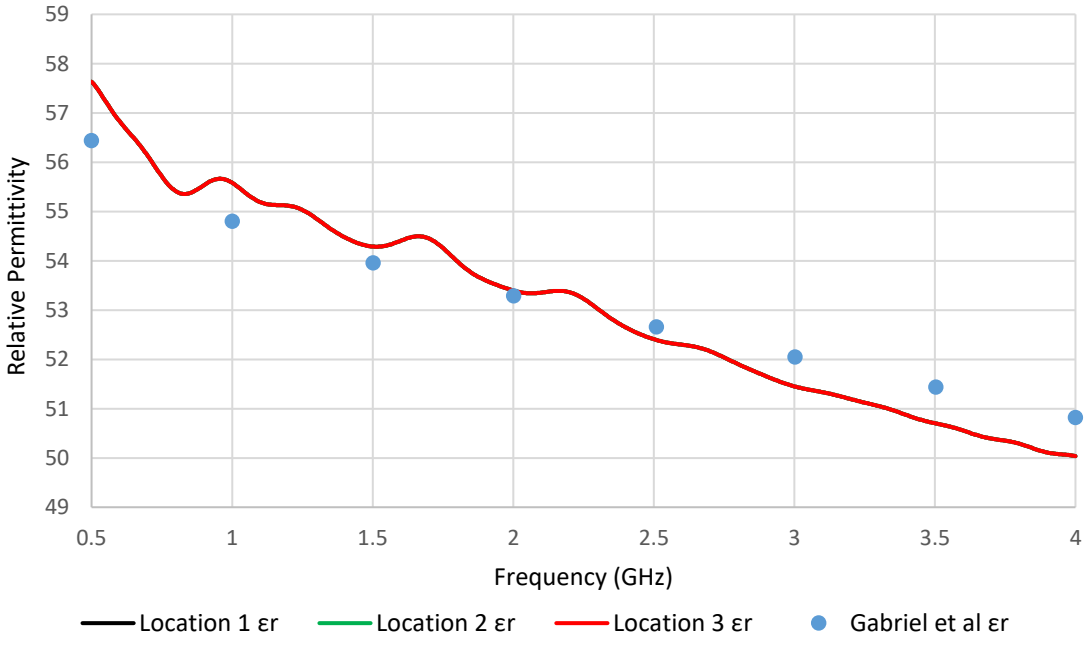

Figure A.7: The relative permittivity of the muscle box calculated using the probe versus the relative permittivity of muscle tissue according to Gabriel et al [1].

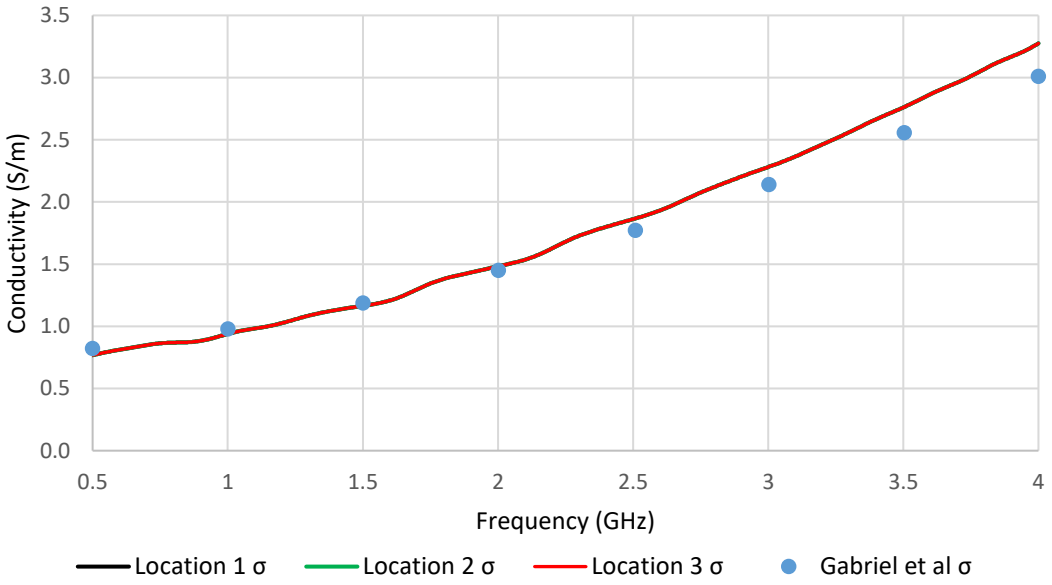

Figure A.8: The conductivity of the muscle box calculated using the probe versus the conductivity of muscle tissue according to Gabriel et al [1].

References

[1] C. Gabriel, "Compilation of the dielectric properties of body tissues at RF and microwave frequencies," *Environ. Heal.*, vol. 1, pp. 1–21, 1996.

[2] C. A. Balanis, *Antenna Theory*, 4th editio. Wiley, 2016.

[3] C. J. Panagamuwa, I. Howells, and W. G. Whittow, "Conductivity and permittivity measurements of children and adult's hands covering mobile communications frequency bands," in *Progress In Electromagnetics Research Symposium (PIERS)*, 2013, pp. 1–5.

Appendix B

The standard deviation between the nine sets of relative permittivity and conductivity curves for bone marrow, bone cortical, blood and muscle materials see Chapter 3: Pages (3-33) to (3-36).

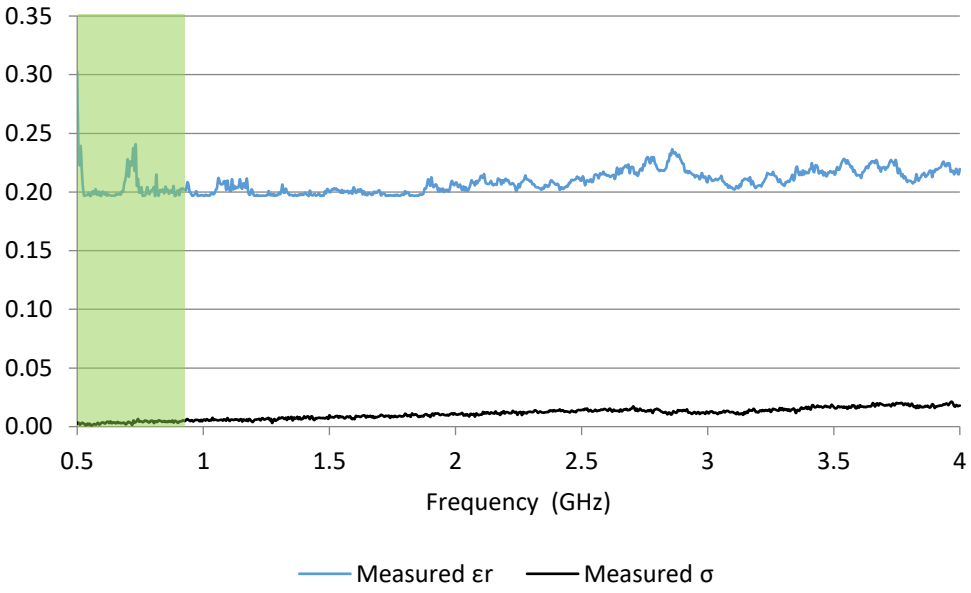

Figure B.1: The standard deviation of the nine measurements taken in bone marrow between 0.5 to 0.8GHz

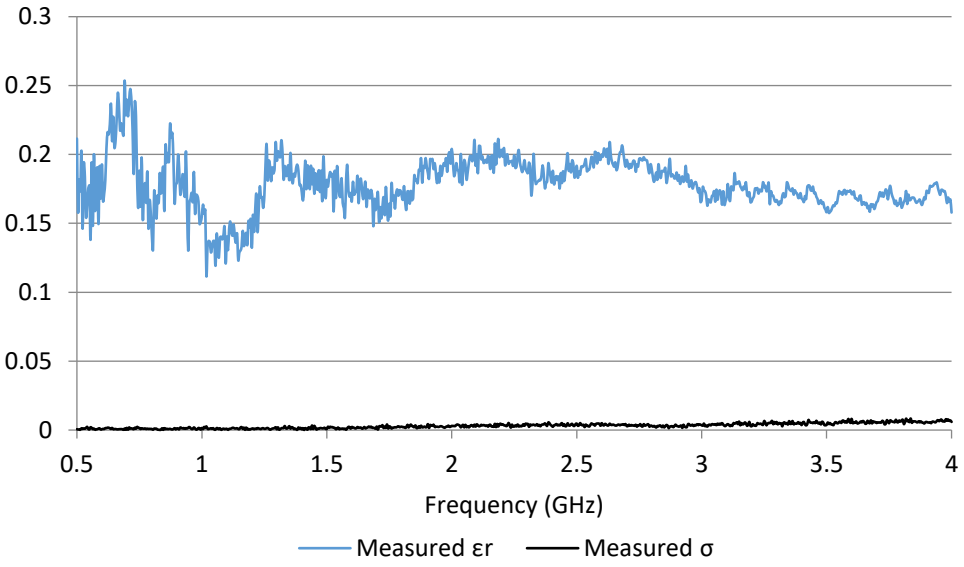

Figure B.2: The standard deviation of the nine measurements taken in bone marrow between 0.5 to 4GHz

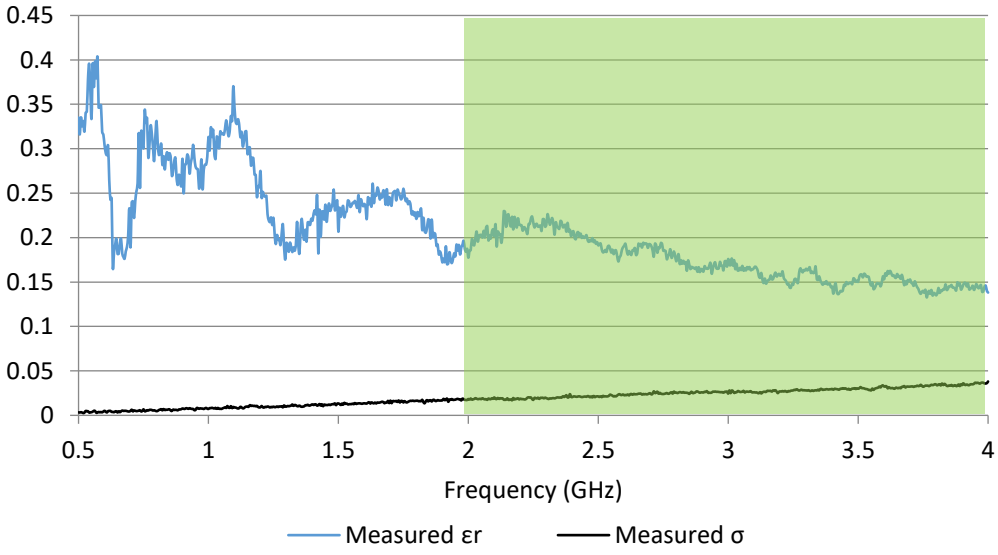

Figure B.3: The standard deviation of the nine measurements taken in bone marrow between 2 to 4GHz

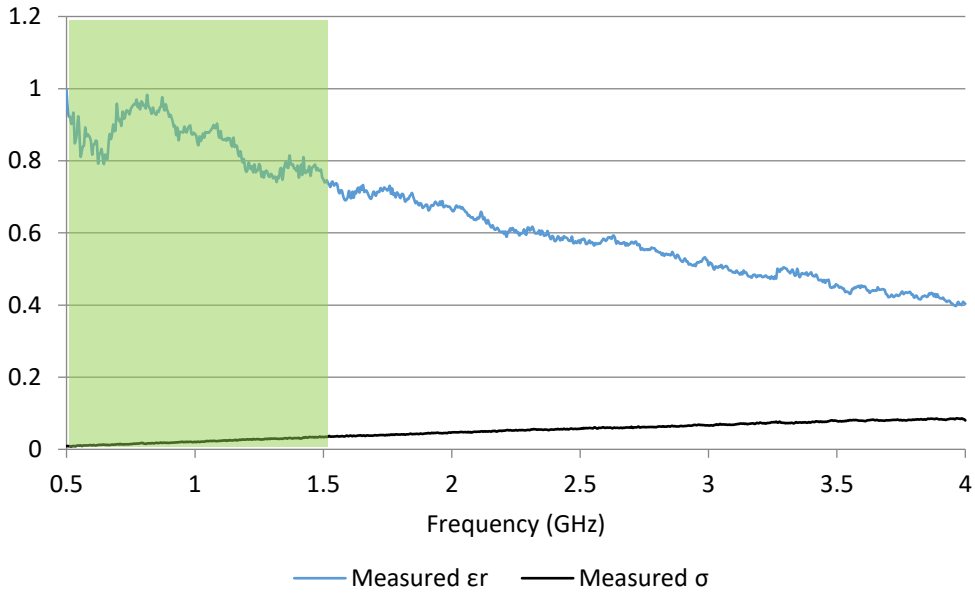

Figure B.4: The standard deviation of the nine measurements taken in bone cortical between 0.5 to 1.5GHz

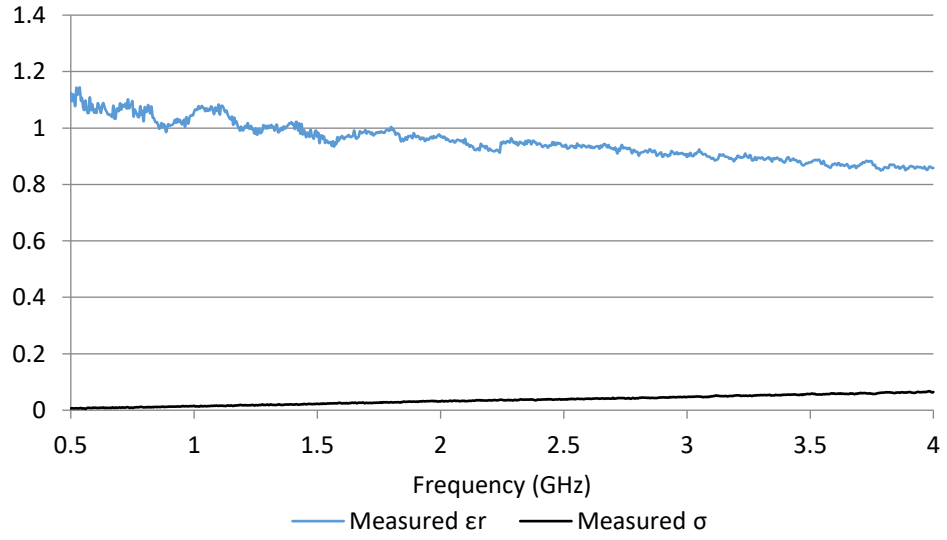

Figure B.5: The standard deviation of the nine measurements taken in bone cortical between 0.5 to 4GHz

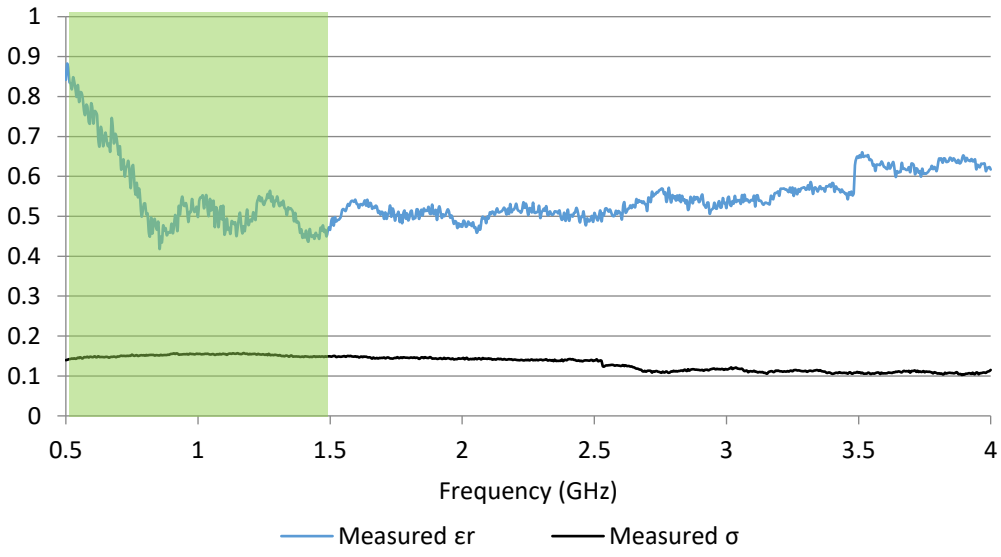

Figure B.6: The standard deviation of the nine measurements taken in blood between 0.5 to 1.5GHz

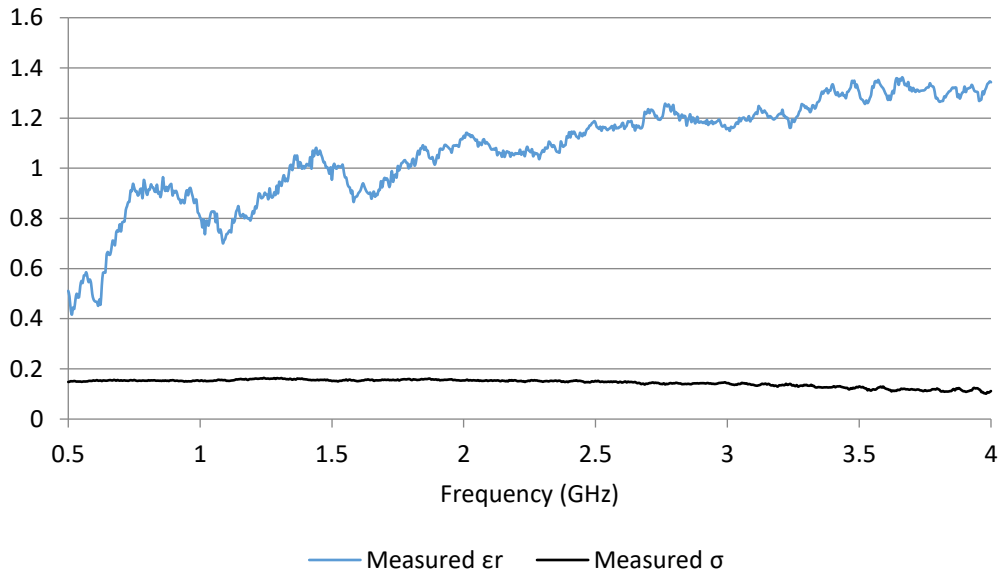

Figure B.7: The standard deviation of the nine measurements taken in blood between 0.5 to 4GHz

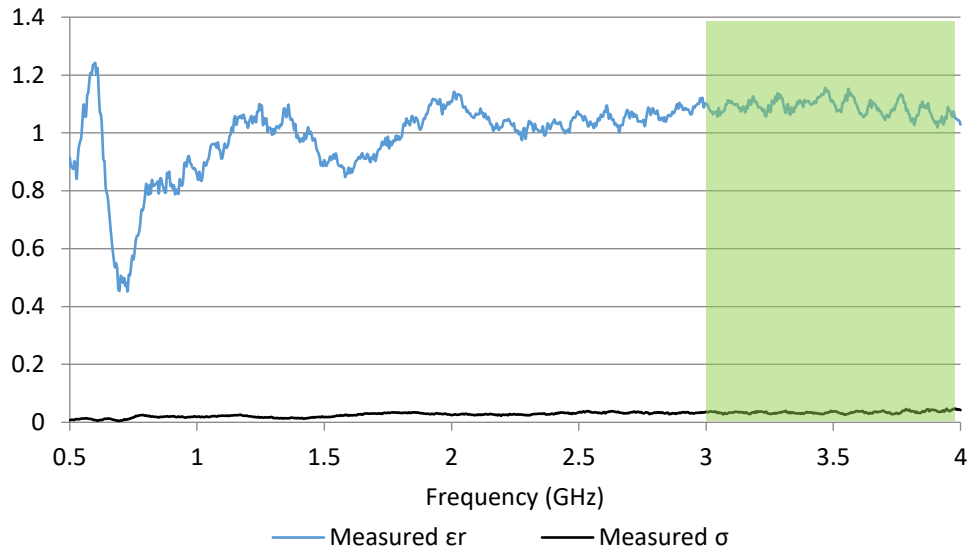

Figure B.8: The standard deviation of the nine measurements taken in bone blood 3 to 4GHz

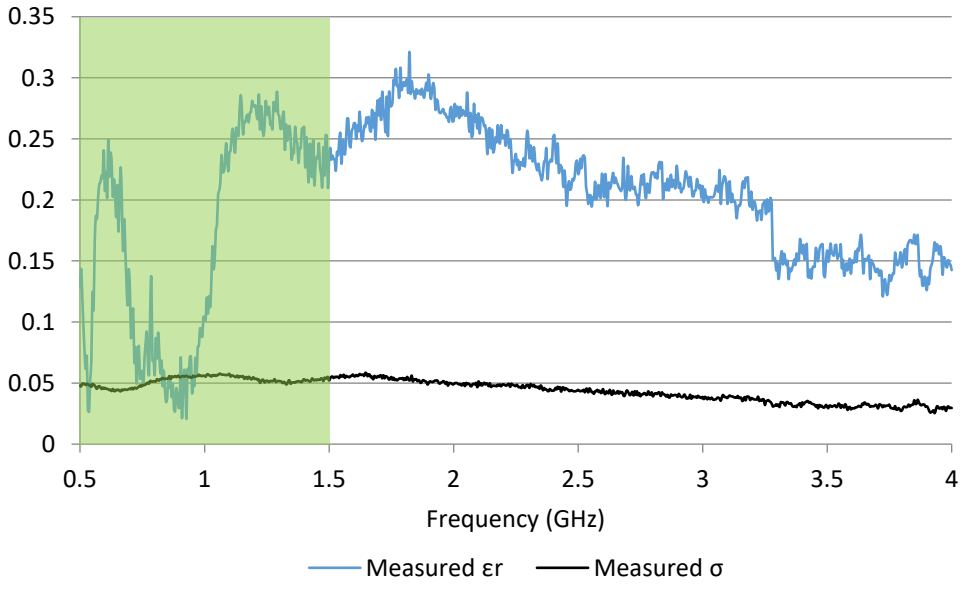

Figure B.9: The standard deviation of the nine measurements taken in muscle between 0.5 to 1.5GHz

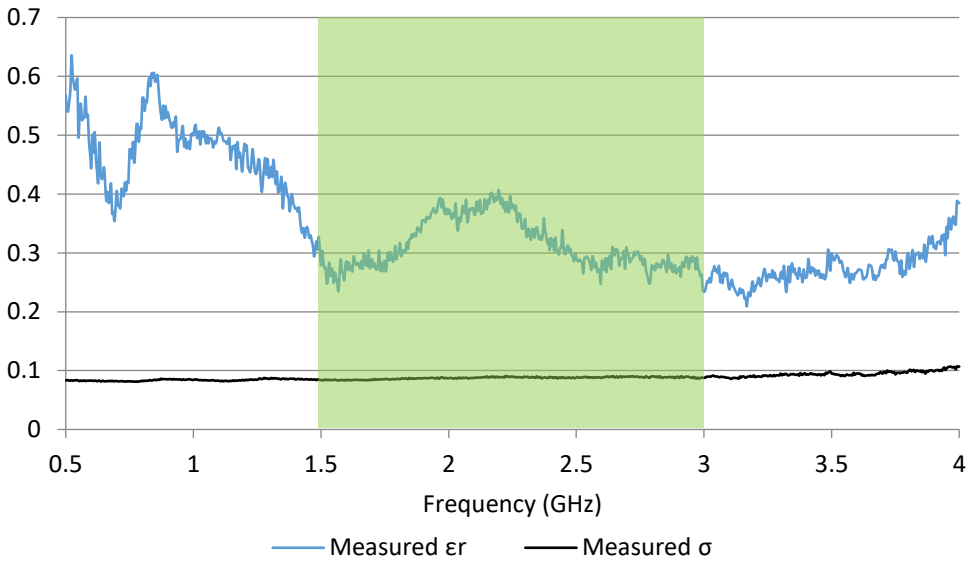

Figure B.10: The standard deviation of the nine measurements taken in muscle between 1.5 to 3GHz

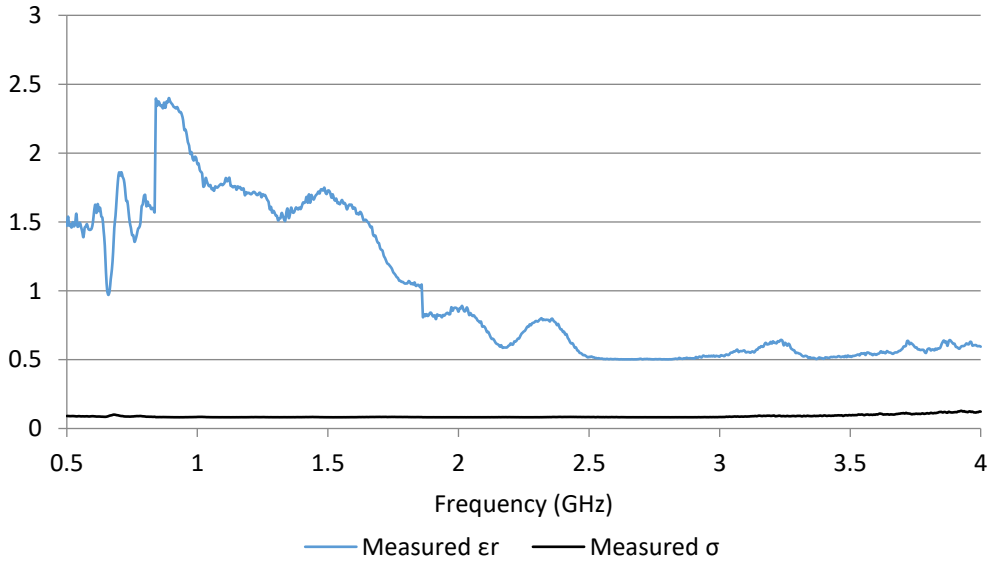

Figure B.11: The standard deviation of the nine measurements taken in muscle between 0.5 to 4GHz

Appendix C

In Figure C.1 a simple one layer phantom consisting of muscle has been simulated. Figure C.2 shows the S_{11} of the implanted monopoles and Figure C.3 shows the S_{21} where effect of any mismatches has been removed by normalizing it with the S_{11}. Finally, in Figure C.4 the muscle phantom has been plotted against itself with 10% lower relative permittivity in order to highlight the amount of changes in the S_{21} for a 10% error in ε_r. As it can be observed in Figure C.4 the amount of change in the $S_{21}$is less 1dB for a 10% error in the ε_r of the muscle layer.

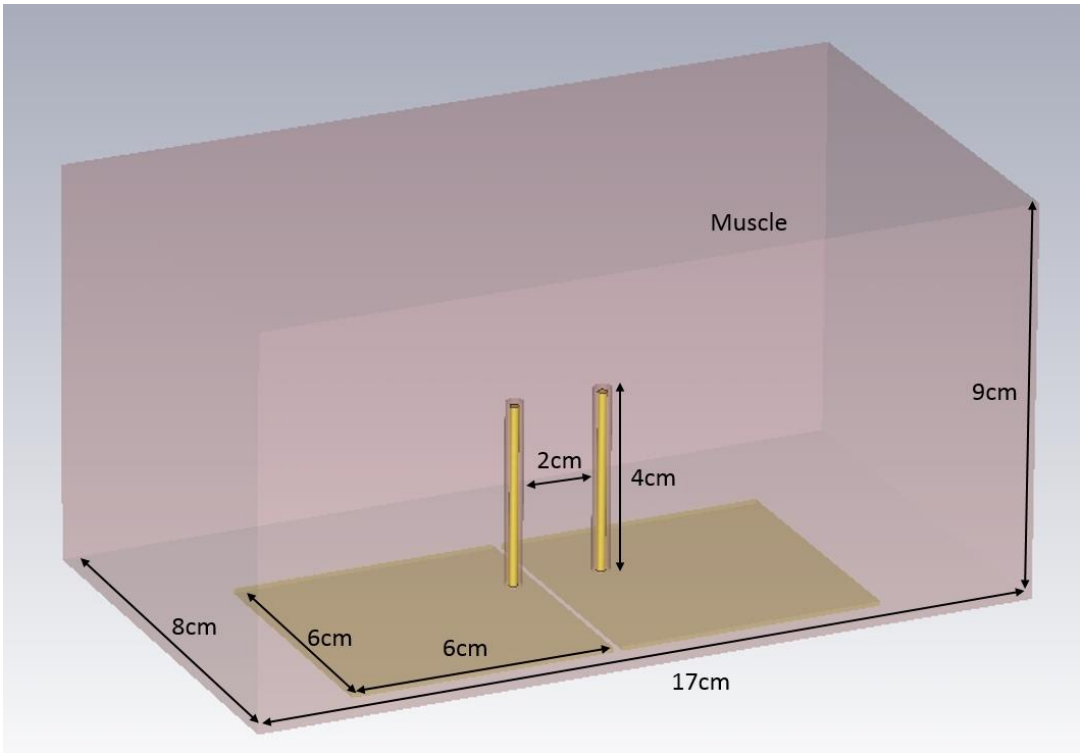

Figure C.1: One layer muscle phantom

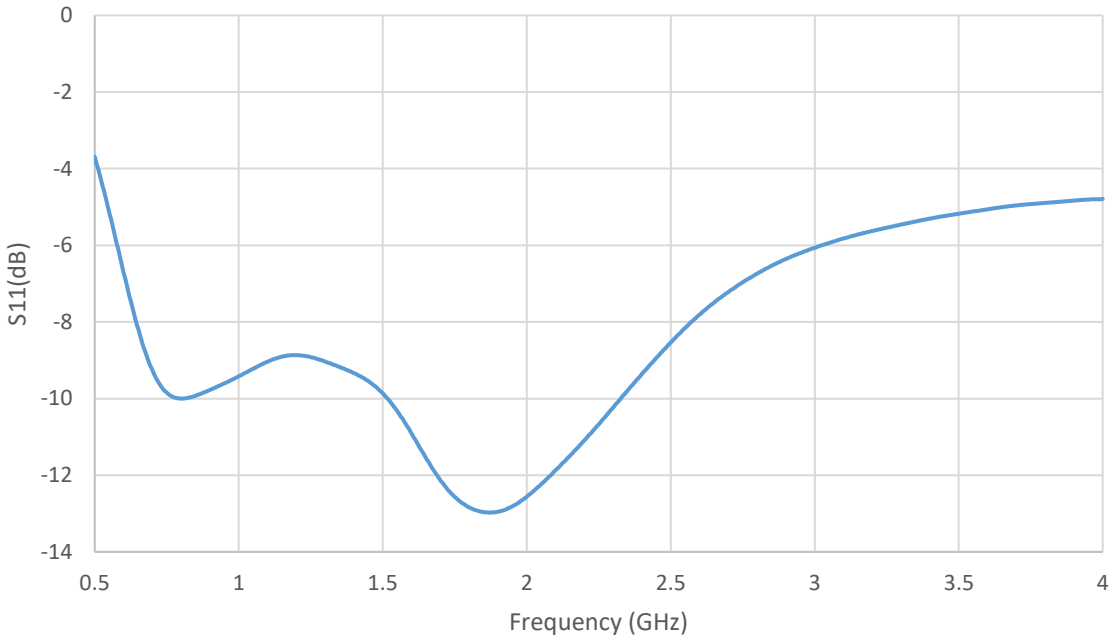

Figure C.2: The S_{11} of the Muscle phantom

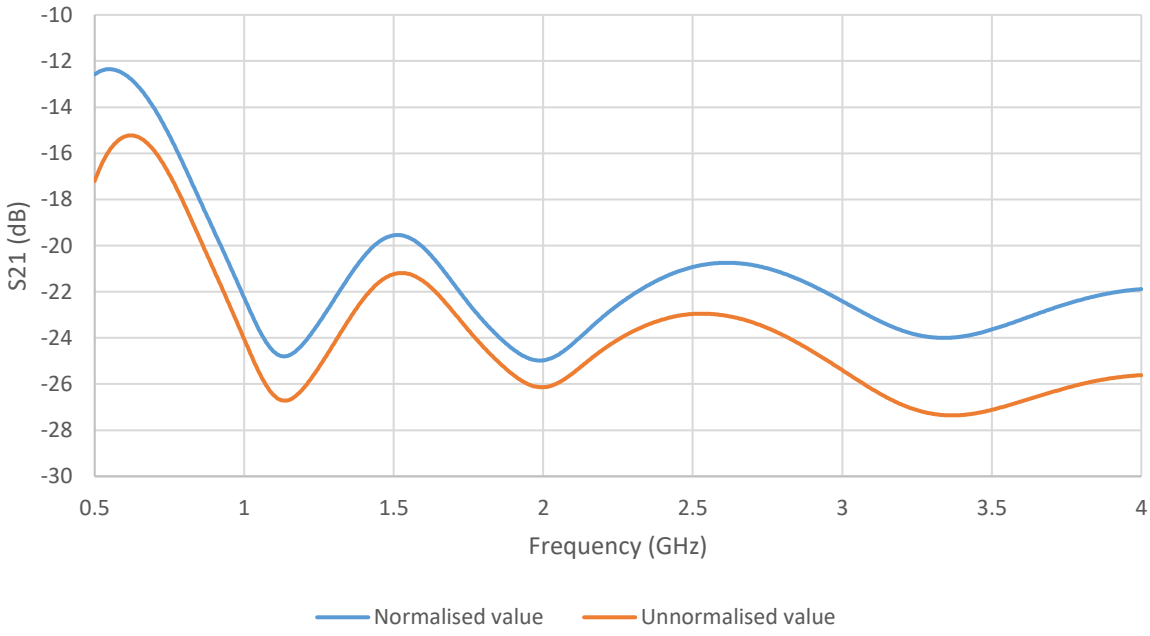

Figure C.3: The S_{21} of the muscle phantom

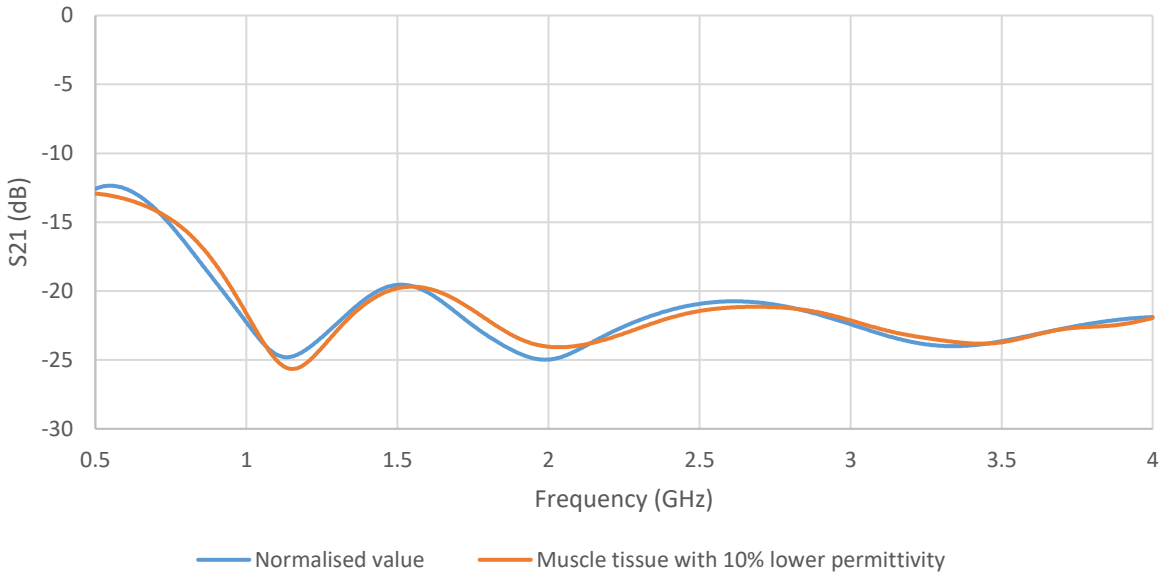

Figure C.4: Comparison between the normalized values of S_{21} of the muscle phantom and the same phantom with 10% lower ε_r

Figure C.5Figure C.6 show the current on the surface of the monopoles with and without a coaxial cable feed respectively. It can be observed that feeding the monopoles using waveguide ports underneath their groundplanes (see Figure C.5) or attaching the waveguide ports onto a coaxial cable (see Figure C.6) has a minimum effect on the surface current. The highest magnitude of the surface current can be observed on the groundplane around the wire part of the monopoles and along the length of the wire parts in both figures.

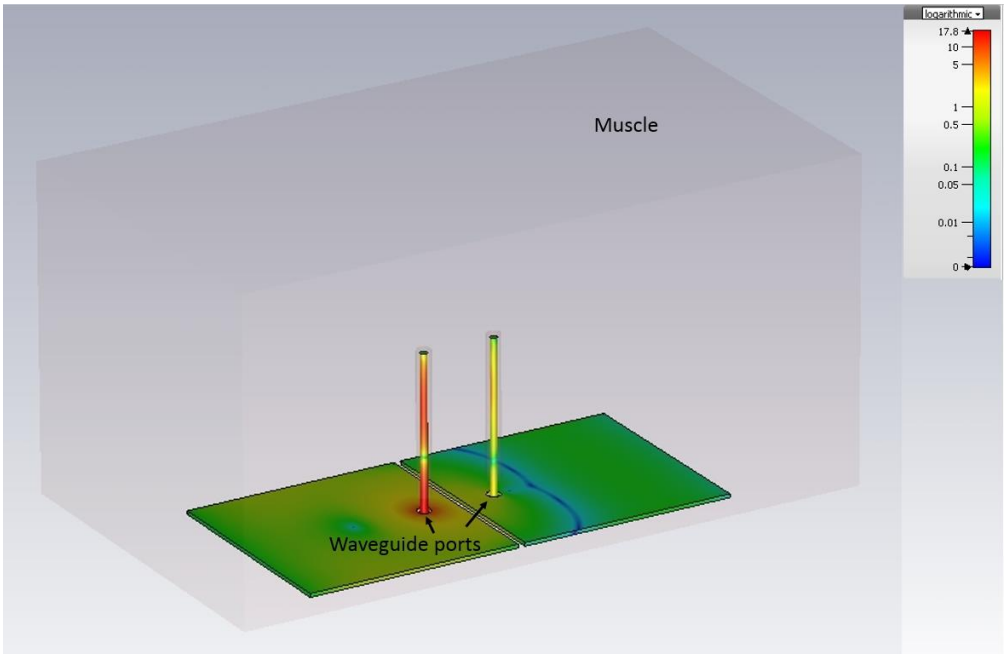

Figure C.5: The surface current of the monopoles fed with two waveguide ports at 2GHz

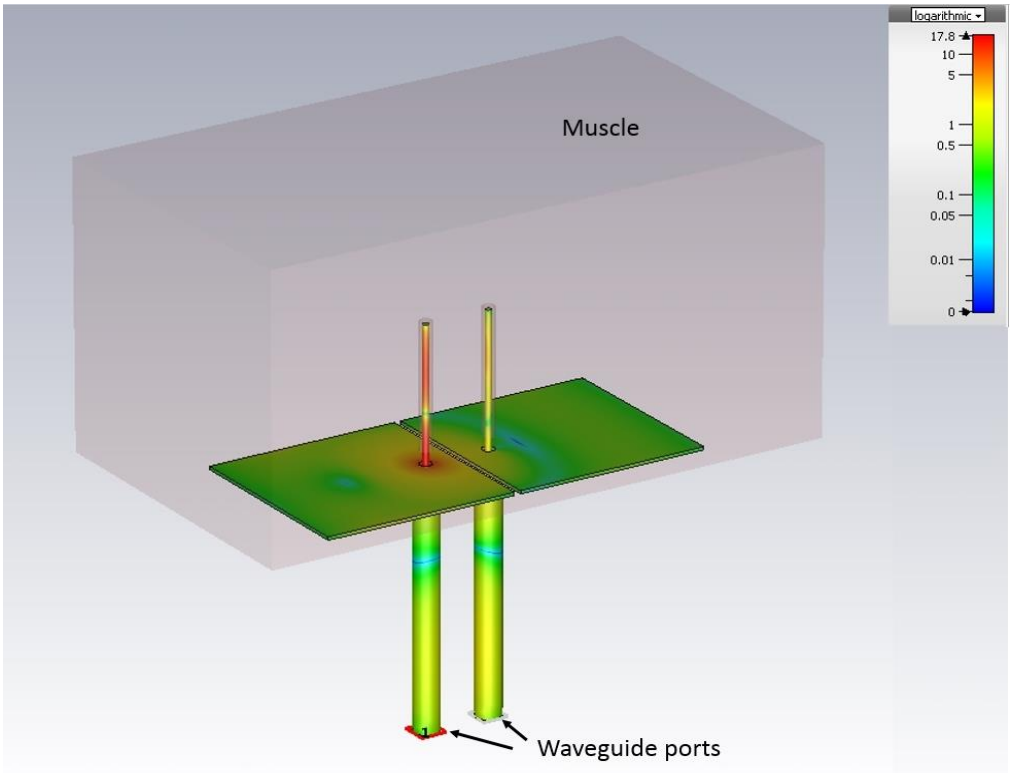

Figure C.6: The surface current of the monopoles fed with two 50Ohm coaxial cables terminated to two waveguide ports at 2GHz

A three layer phantom consisting of muscle, bone and a fractured area was simulated in Figure C.7. In order to further highlight the effects of the dielectric properties change in the S_{21} of the monopoles, the fracture area of the phantom changed from 100% the dielectric properties of blood and 0% the dielectric properties of bone towards 100% the dielectric properties of bone and 0% the dielectric properties of blood in five steps. An example of the dielectric properties change at 2GHz can be seen in Table C.1.

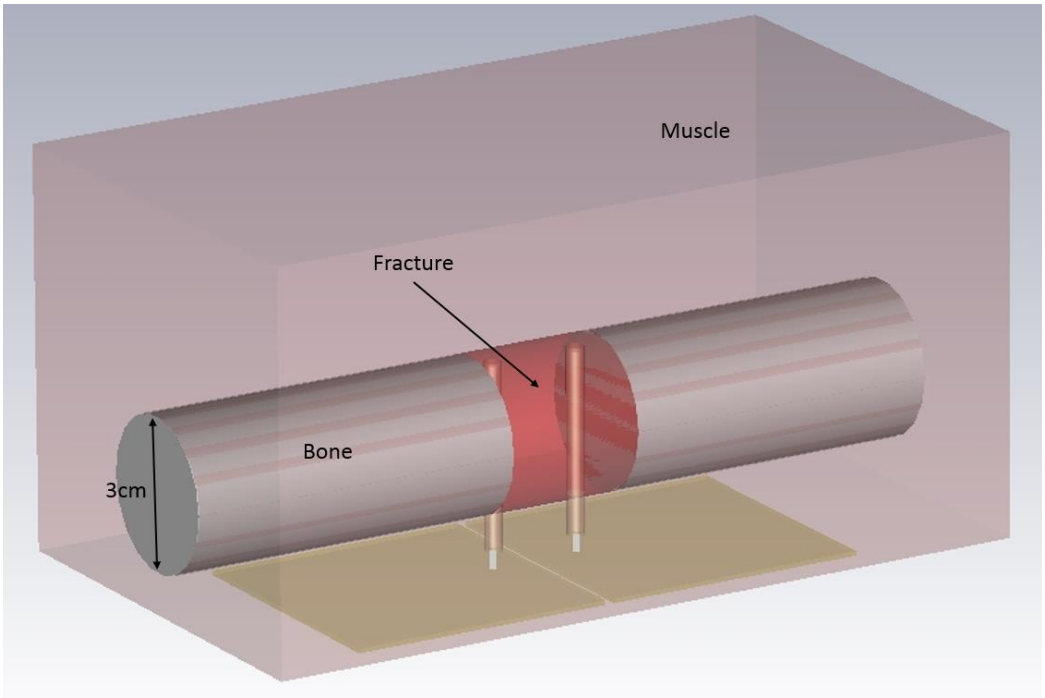

Figure C.7: A three layer phantom consisting of muscle, bone and a fractured area

Table C.1: The dielectric properties of the fracture during the healing process at 2GHz

	Fracture cylinder	
Dielectric properties of blood	**Relative Permittivity, ε_r**	**Conductivity, σ (S/m)**
100%	59	2.18
75%	47.05	1.7
50%	35.25	1.24
25%	23.45	0.31
0%	11.65	0.08

Figure C.8Figure C.9 show the S_{11} and the S_{21} of the monopoles inside the three material phantom of Figure C.7. The dielectric properties of the fracture changed according to Table C.1. As it can be observed, the amount of change in the S_{11} is less than 1.5dB over the frequency spectrums of 0.5 to 1GHz and 1.5 to 2GHz for the first four steps of Table C.1. Therefore the S_{11} was not used as a fracture healing indicator in this thesis. The phase of the S_{21} was not used either, this was due to the change in the angle being less than 5 degrees at 1.6GHz for the first four steps of Table C.1 (see Figure C.10). The change in the S_{21} is at least 3 dB in average between each step over a much broader frequency spectrum (0.5 to 2.5GHz). Additionally, this 3dB change in the S_{21} for each step that the bone cylinder's dielectric properties shift closer to the properties of blood, shows that it is the dominant medium of propagation for distances as large as 2cm. Therefore, throughout this thesis, the magnitude of the S_{21} has been used as an indicator for the change of dielectric properties of the fractured area of the bone.

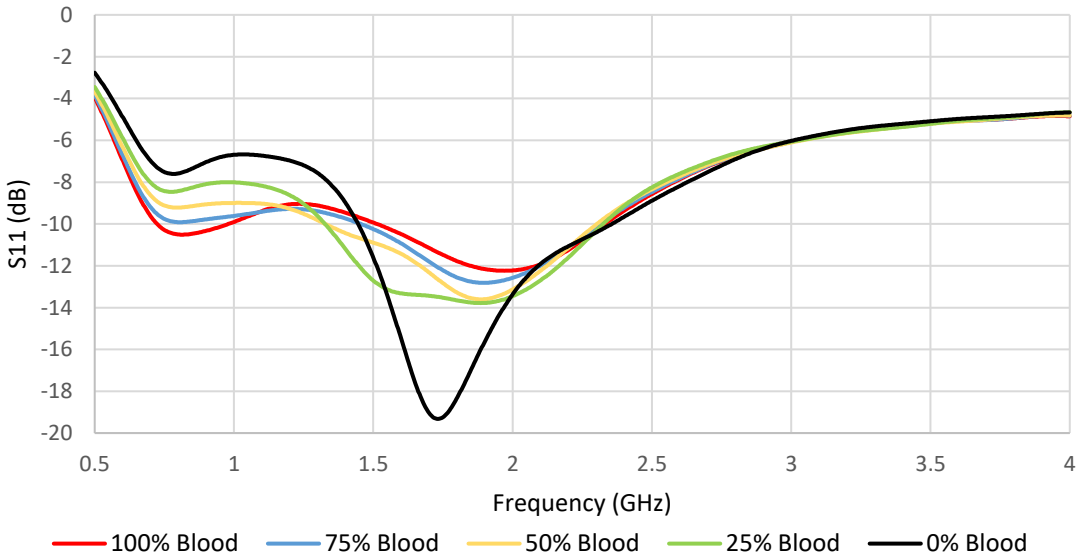

Figure C.8: The corresponding S_{11} for the five steps indicated in Table C.1 of the three material phantom

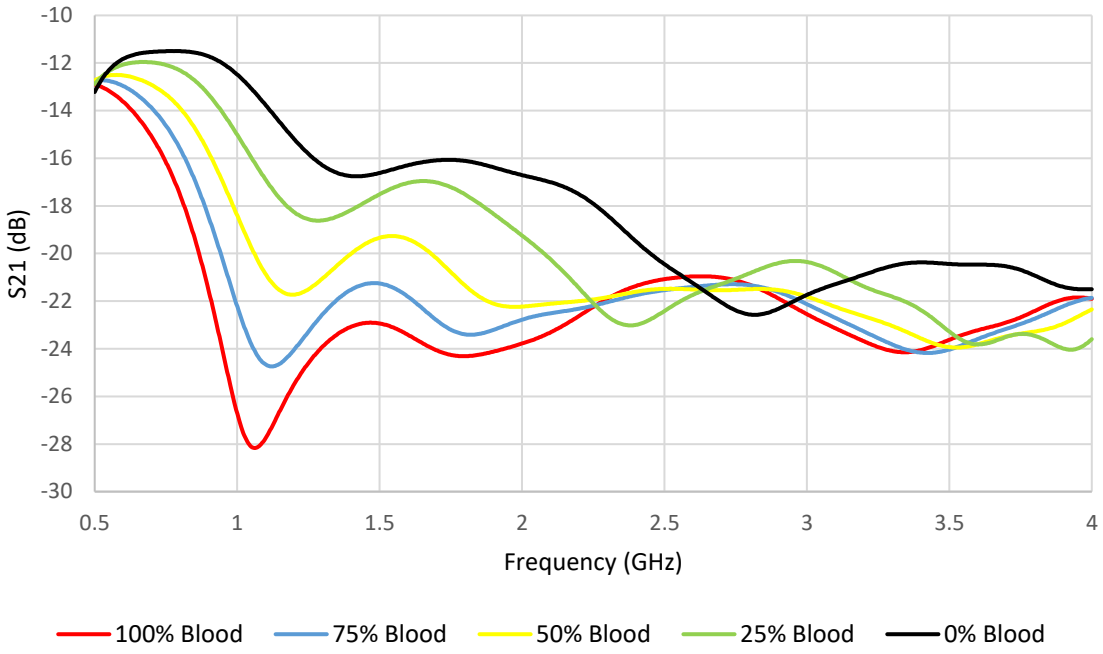

Figure C.9: The corresponding normalised S_{21} for the five steps indicated in Table C.1 of the three material phantom

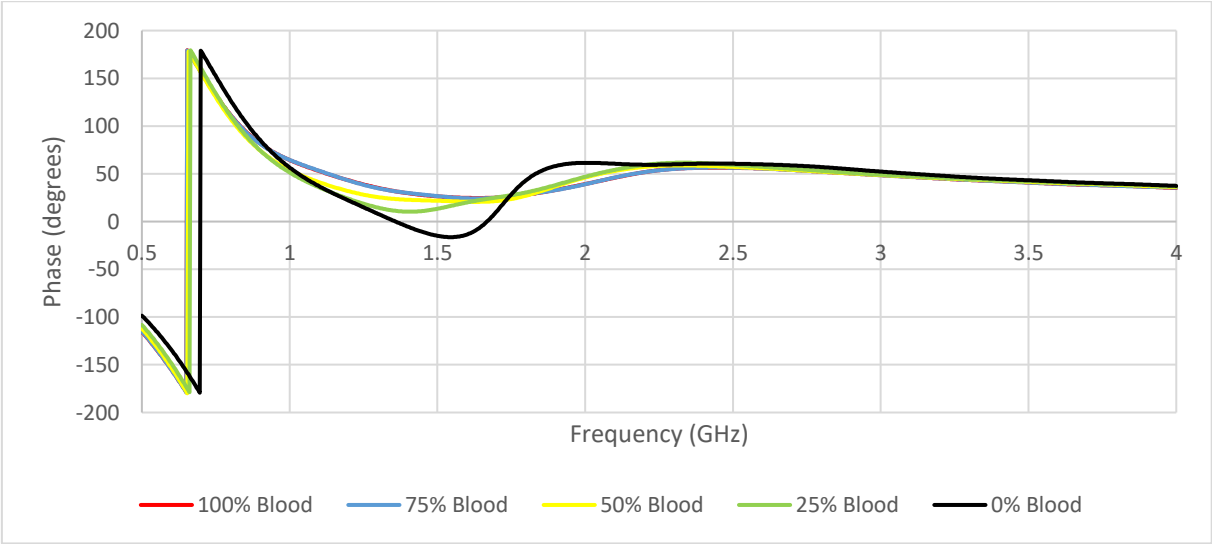

Figure C.10: The corresponding phase of the S_{21} for the five steps indicated in Table C.1 of the three material phantom